CALIFORNIA INSTITUTE OF TECHNOLOGY

EARTHQUAKE ENGINEERING RESEARCH LABORATORY

MECHANISM OF COLLAPSE, SENSITIVITY TO GROUND MOTION FEATURES, AND RAPID ESTIMATION OF THE RESPONSE OF TALL STEEL MOMENT FRAME BUILDINGS TO EARTHQUAKE EXCITATION

BY

SWAMINATHAN KRISHNAN
MATTHEW MUTO

REPORT NO. EERL 2011-02

PASADENA, CALIFORNIA

JANUARY 2011

A REPORT ON RESEARCH SUPPORTED IN PART BY THE NATIONAL EARTHQUAKE HAZARD REDUCTION PROGRAM (NEHRP) UNDER THE SUPERVISION OF SWAMINATHAN KRISHNAN

Acknowledgements

The authors would like to express their deep gratitude to Professor Paul Jennings of the California Institute of Technology for his thorough review of this work. His insightful comments have helped refine this report appreciably. This study was funded in part by the U.S. National Earthquake Hazard Reduction Program (NEHRP award number G09AP00063). Financial support from NEHRP is gratefully acknowledged. The first author is also grateful to the National Science Foundation (NSF), the Southern California Earthquake Center (SCEC), and the United States Geological Survey (USGS) for their continued support to his research program. Recent grants include NSF award no. CMMI-0926962, and unnumbered awards by the USGS and SCEC.

Abstract

This study explores the behavior of two tall steel moment frame buildings and their variants under strong earthquake ground shaking through parametric analysis using idealized ground motion waveforms. Both fracture-susceptible as well as perfect-connection conditions are investigated. Ground motion velocity waveforms are parameterized using triangular (sawtooth-like) wave-trains with a characteristic period (T), amplitude (peak ground velocity, PGV), and duration (number of cycles, N). This idealized representation has the desirable feature that the response of the target buildings under the idealized waveforms closely mimics their response under the emulated true ground motion waveforms. A suite of nonlinear analyses are performed on four tall building models subjected to these idealized wave-trains, with T varying from 0.5s to 6.0s, PGV varying from 0.125 m/s to 2.5 m/s, and N taking the values of 1 to 5, and 10. This range of parameters should be adequate to characterize the ground motions that can be expected to occur during earthquakes in the 6–8 magnitude range at some distance (say, $>$ 2km) away from the fault. Databases of peak transient and residual interstory drift ratio (IDR), and permanent roof drift are created for each model. The sensitivity of structural response to T, PGV, and N is studied. Severe dynamic response is induced only in the long-period, large-amplitude excitation regime. Through a simple examination of the energy balance during earthquake shaking, it can be shown that the input excitation energy is small for excitation with periods shorter than the structural period, whereas it is proportional to the square of the ground velocity if the excitation periods are much longer than the structural periods. Thus, collapse-level response can be induced only by long-period, moderate to large PGV ground excitation. The collapse initiation regime expands to lower ground motion periods and amplitudes with increasing number of ground motion cycles. It should be noted that the energy balance analysis is not appropriate for excitation velocities that are extreme where conservation of momentum may be more applicable. However, peak ground velocity from earthquakes seldom exceeds 2.5m/s and energy balance would generally be applicable.

The close examination of one instance of collapse shows damage (yielding and/or fracture) localizing in a few stories in the form of a "quasi-shear" band (QSB) comprising of plastic hinges at the top of all columns in the uppermost story of the band, at the bottom of all columns in the lowermost story of the band, and at both ends of all beams in the intermediate stories. Such a pattern of hinging results in shear-like deformation in these stories, resembling plastic shear bands in ductile solids. Most of the lateral deformation due to seismic shaking is concentrated in this band. When the overturning 1^{st}-order and 2^{nd}-order ($P-\Delta$) moments from the inertia of the overriding block of stories exceed the moment-carrying capacity of the quasi-shear band, it loses stability and collapses. This initiates gravity-driven progressive collapse of the overriding block of stories. Thus, the collapse mechanism initiates as a sidesway mechanism that is taken over by gravity once the quasi-shear band is destabilized. There are $\frac{N_s(N_s+1)}{2}$ possible quasi-shear bands (and an equal number of sidesway collapse mechanisms) in either principal direction of an N_s-story moment frame building. More than one quasi-shear bands could occur during the entire duration of strong earthquake shaking. The band exhibiting the greatest distress (termed the "primary" quasi-shear band)

ultimately evolves into a sidesway collapse mechanism.

The formation of the quasi-shear band under single-cycle excitations is explained through the classical uniform shear-beam analogy to moment frame buildings. Under low-intensity motions ($PGV < 0.25m/s$) with periods in the 0.5s–6s range excitation energy is low. As a result, structural response is predominantly elastic and is analogous to that of a uniform elastic shear-beam through which a shear wave propagates. For moderate-intensity excitations ($0.25m/s \leq PGV < 1.5m/s$), the reverse phase of the incident pulse constructively interferes with the reflected forward phase causing yielding in the region of positive interference, very similar to what would occur in a uniform inelastic shear-beam. The primary quasi-shear band migrates down the building with increasing pulse period. However, this migration slows down with increasing period and gets arrested nominally between floors 3 and 9 for the existing building, and between floors 3 and 8 for the redesigned building, whereas the peak strain in the corresponding inelastic uniform shear-beam continues to migrate to the very bottom. This is a direct result of the non-uniformity of the buildings. Going from the top of the building to the bottom, there is a gradual increase in the strength and stiffness of the structure. The increased strength at the bottom does not allow yielding to permeate into those stories. Now, excitation energy imparted to the structure can be large enough only under long-period ground motion in the context of the target buildings. Therefore, collapse-level response must be accompanied by the formation of the primary quasi-shear band in the vicinity of the stories where the downward migration of the QSB (with increasing T) is arrested.

For high-intensity excitations ($PGV > 1.5m/s$) that are sufficiently long-period, the pulse may yield the structure on its way up the building. The strength of the building drops as the pulse travels up the building. However, inertial forces drop as well, as a result of fewer stories above contributing to the mass. The narrow band of stories with an optimal combination of low-enough strength and high-enough inertial force demand is where peak yielding occurs. This region is identical to the region where the downward migration of the primary quasi-shear band is arrested under moderate-intensity, long-period excitation. This is because the governing factor dictating the location of the band in both cases is strength non-uniformity. As the wave travels up the building, it is reflected off the roof with a change in sign. Because the period of the incident wave is sufficiently long (a necessary condition for large input excitation energy), the reverse phase of the incident pulse constructively interferes with the reflected forward phase causing greatest yielding in the same region as the pre-reflection yielding. To summarize, under both moderate-intensity and high-intensity ground motions, input excitation energy large enough to collapse the building requires long-period excitation. Such long-period excitation always causes the formation of the primary quasi-shear band in an optimal set of stories governed by the mass and strength distribution of the building over its height, which are characteristics solely of the structure and not the ground motion. When T and PGV are large enough, it is this band that evolves into a collapse mechanism. This points to the existence of a "characteristic" collapse mechanism or only a few preferred collapse mechanisms (out of the $\frac{N_s(N_s+1)}{2}$ possible mechanisms) in either principal direction of the building. If multiple preferred collapse mechanisms exist, they would be clustered together with significant story-overlap amongst them.

The simulations of the four models under idealized ground motion waveforms where collapse occurs do not show the formation of a single (unique) collapse mechanism. However, in each model only one to five

collapse mechanisms occur out of a possible 153 mechanisms in each principal direction of the building. Furthermore, if two or more preferred mechanisms do exist, they have significant story-overlap, typically separated by just one story. For example, the strongly preferred collapse mechanisms in the existing building model (perfect connections) under X direction excitation occur between floors 3 and 9, and floors 4 and 9, while the weakly preferred mechanisms occur between floors 3 and 8, and floors 4 and 8 (four preferred mechanisms out of 153 possible mechanisms, all clustered together within a narrow story zone; two of these mechanisms are in fact a subset of the other two mechanisms).

The characteristic and/or preferred collapse mechanisms can be identified by applying the Principle of Virtual Work to all possible quasi-shear bands in a building. Based on plastic analysis principles, the band that is destabilized by the smallest acceleration of the over-riding block of stories is the characteristic collapse mechanism. If one or more bands exist that have destabilizing accelerations close to that of the characteristic collapse band, say within 5%, then these bands may evolve into collapse mechanisms as well. This method identifies all the preferred collapse mechanisms in all four building models satisfactorily.

One application of the structural response database built for the sensitivity study is the rapid estimation of structural response immediately following an earthquake if the ground motion records become available. The best fit of the idealized wave-trains in the database to the ground motion record can be determined using the least absolute deviation method. The corresponding key structural response metrics can be extracted from the database using a simple table look-up approach. Such a method, when applied to a suite of near-source records, predicts peak transient IDR remarkably well. Gaussian mean estimation error on the peak transient IDR is 0.0006, with a standard deviation of 0.0069. A minor modification to this approach is needed when applying it to multi-cycle far-field records. This modified approach is used to estimate the peak transient IDR response of the buildings under synthetic waveforms from a large hypothetical San Andreas fault earthquake. The Gaussian mean error for this estimation is 0.0011, with a standard deviation of 0.0209, slightly worse than for the near-source records, nevertheless within one "performance level" – good enough for emergency response decision-making. The same approach can be used for ball-park estimation of structural response under any given earthquake record, in lieu of comprehensive nonlinear analysis.

Contents

List of Figures

List of Tables

Chapter 1 Introduction

1.1 Objectives of the Study

There are three key objectives of this study:

1. To determine the sensitivity of the collapse regime of tall steel moment frame building response to three ground motion features– frequency content, intensity, and duration.

2. To determine the mechanism(s) of collapse of these structures under various types of earthquake ground motion waveforms.

3. To develop a rapid estimation procedure for tall building earthquake response to a given ground motion waveform, immediately following an earthquake or otherwise.

1.2 Basic Approach

A straightforward approach to achieving all three objectives is to:

1. develop a simplified (idealized) representation scheme for seismic ground motion waveforms using three parameters to characterize ground motion frequency content, intensity, and duration;

2. conduct a parametric nonlinear response history analysis sweep of selected tall building models by varying the parameters of the idealized waveforms; such a suite of analyses can help to systematically and uniformly explore structural response to ground motions with features spanning a broad spectrum, covering earthquakes of all kinds.

3. create a database of key structural response metrics as a function of ground excitation waveform parameters.

This response database can be used in the following ways to achieve the aforementioned objectives of the study:

1. mapping the key structural response metrics that track collapse (transient and peak residual interstory drift ratio) against the idealized waveform parameters;

2. determining the closest match of a given ground motion waveform to any one of the idealized waveforms in the database and extracting the corresponding structural response metrics to estimate the post-earthquake condition of the structure as being immediately occupiable (IO), life-safe (LS), collapse prevented (CP), red-tagged (RT) or collapsed (CO);

3. tracking the evolution of the collapse mechanisms as a function of the idealized waveform parameters by mapping the damage localization region (i.e., extent and distribution of plastic rotations in beams, columns, and panel zones).

A necessary condition for the findings to be equally applicable to real seismic ground motion is that the structural response under the best-fit idealized ground excitation must closely mimic that under the true waveform being emulated. This condition forms the basis for the selection of the ground motion idealization scheme.

1.3 Buildings Considered

Here, we focus on two tall steel moment frame buildings and their variants. The first building is an existing 18-story office building, located within five miles of the epicenter of the 1994 Northridge earthquake. An isometric view of its FRAME3D model is shown in Figure 1.1(a). It was designed according to the 1982 UBC and completed in 1986-87. The height of the building above ground is 75.7 m (248' 4") with a typical story height of 3.96 m (13' 0") and taller first, seventeenth, and penthouse stories. The lateral force-resisting system consists of two-bay welded steel moment-frames, two apiece in either principal direction of the structure as shown in Figure 1.1(c). The location of the north frame one bay inside of the perimeter gives rise to some torsional eccentricity. Many moment-frame beam-column connections in the building fractured during the Northridge earthquake, and the building has been extensively investigated since then by engineering research groups [26]. Fundamental periods, computed assuming 100% dead load and 30% live load contribution to the mass, are 4.52s (X-translation), 4.26s (Y-translation) and 2.69s (torsion). We consider two models of the existing building, one with connections susceptible to fracture, and the other with perfect connections. Two orthogonal orientations (with respect to the strong component of the ground motion) are considered for the model with perfect connections.

The second building, a FRAME3D model of which is shown in Figure 1.1(b), is similar to the existing building, but the lateral force-resisting system has been redesigned according to the 1997 UBC. It has been designed for larger earthquake forces and greater redundancy in the lateral force-resisting system, with 8 bays of moment-frames in either direction (although lateral resistance will likely be dominated by the three-bay moment frames shown in Figure 1.1(d) as opposed to the single-bay moment frames). The frame located in the interior of the existing building has been relocated to the exterior, eliminating the torsional eccentricity. Fundamental periods, computed assuming 100% dead load and 30% live load contribution to the mass, are 4.06s ([X+Y-] translation), 3.85s ([X+Y+] translation) and 2.60s (torsion). Note that the fundamental translational modes are oriented approximately along diagonals on the building plan view. Detailed floor plans, beam and column sizes, and the gravity, wind and seismic loading criteria for the two buildings can be found in [20] and [21]. Only one variant of the redesigned building is modeled here, that with perfect connections.

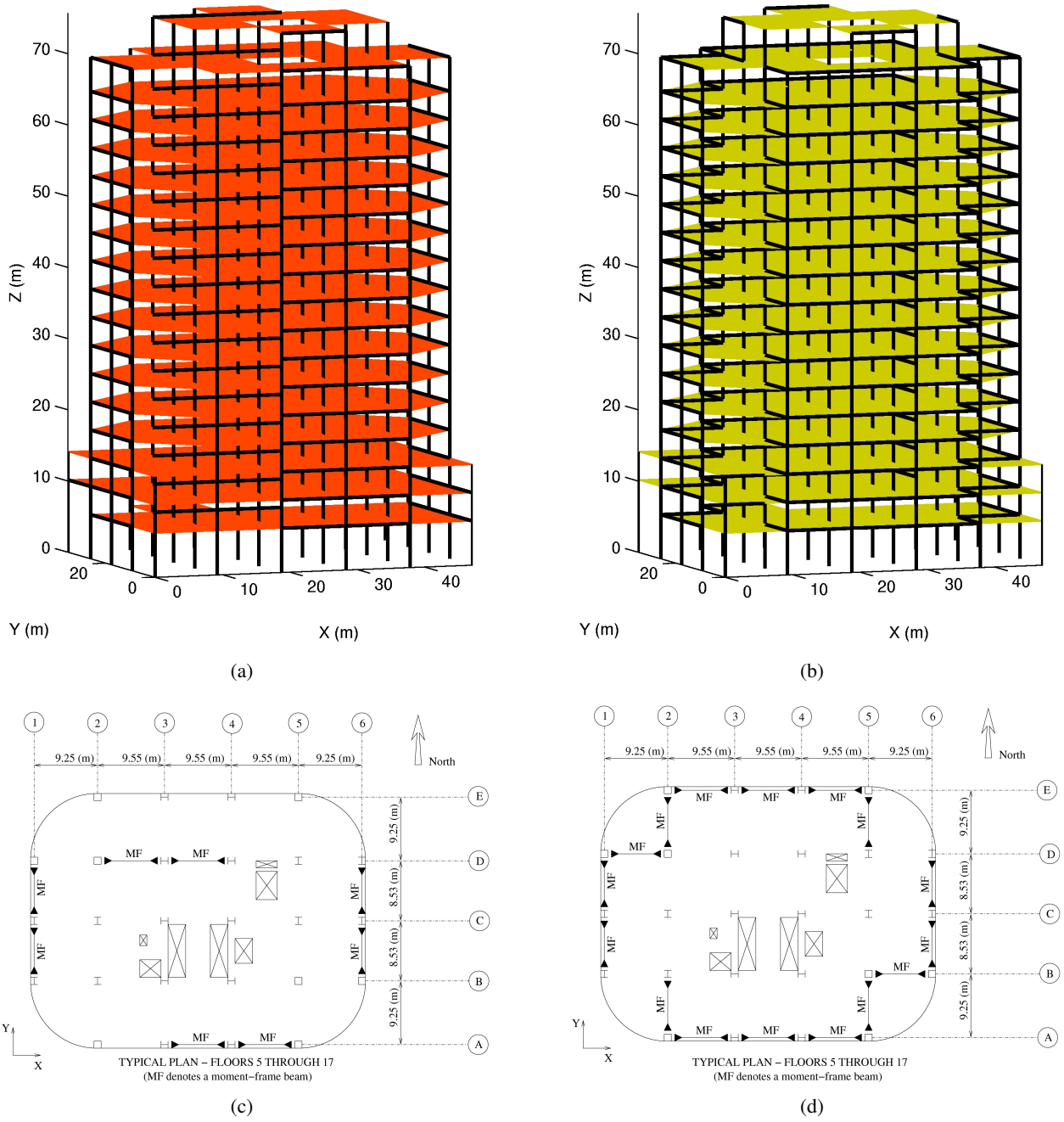

Figure 1.1: Structural models of the two 18-story steel moment frame buildings: (a) Isometric view of the existing building (designed using the 1982 UBC). (b) Isometric view of the new building (redesigned using the 1997 UBC). (c) Plan view of a typical floor of the existing building showing the location of columns and moment-frame (MF) beams. (d) Plan view of a typical floor of the redesigned building.

1.4 Specifics of Structural Modeling

Nonlinear damage analyses of the building models subjected to the simulated ground motion in this study are carried out using the program FRAME3D (http://www.virtualshaker.caltech.edu) that is based on the

finite-element method and is capable of performing three-dimensional nonlinear time-history analysis under 3-component ground motion. A three-dimensional structural model of a framed building using this program consists of grids of beams and columns (Figure 1.2). The setup of the model is comprised of three element classes: panel zone elements for joints, beam elements for beams and columns, and diaphragm elements for floor and roof slabs. The elastofiber beam element is divided into three segments – two end nonlinear segments and an interior elastic segment, as shown in Figure 1.3. The cross-sections of the end segments are subdivided into fibers. Associated with each fiber is a nonlinear hysteretic stress-strain law, proposed by [11], for axial stress, σ_n, and axial strain, ϵ_n, where n denotes the n^{th} fiber. This hysteresis model defines a backbone curve (Figure 1.4(a)) consisting of a linear portion, a yield plateau, a strain-hardening region which is described by a cubic ellipse, and a strain softening region described by a continuation of the same cubic ellipse. The backbone curve is characterized by seven parameters: yield stress σ_y, ultimate stress σ_u, Young's modulus E, strain at initiation of strain hardening ϵ_{sh}, strain at ultimate stress ϵ_u, rupture strain ϵ_r, and the tangent modulus at initiation of strain hardening E_{sh}. Hysteresis loops (Figure 1.4(b)) consist of linear segments and cubic ellipse segments, and the hysteretic rules to define the cyclic response of each panel are given by [3]. A fiber fracture capability, in the form of a general probabilistic description of the fracture strain, has been added to approximately represent fracture of welded beam-to-column connections [9, 10]. When the fiber strain reaches the fracture strain, it fractures and can no longer take tension, but upon reversal of loading the fractured and separated parts can come in contact, and the fiber is able to resist compression again. The fiber segment is based on the finite element method, wherein the beam translations and rotations are interpolated linearly and independently from their nodal values, requiring a one-point integration on the shear terms to prevent locking.

The panel zone element models nonlinear shear deformation in the region of the joint where the beams and columns intersect. The joint region consists of a length of column within the depth of the connecting beams. Shear deformation is due, primarily, to opposing moments from the beams and columns at the joint caused by the frame being subjected to lateral loads. The joint is modeled by two planar orthogonal panels forming a cruciform section. Edges of these panels contain attachment points a, b, c, and d where beams attach, and e and f on the top and bottom,respectively, where columns attach (Figure 1.5(a)). Each panel may yield and strain harden in shear. Material nonlinearity in each panel is included by assuming a linear-quadratic shear stress-strain backbone behavior until ultimate shear stress is reached, and perfectly plastic behavior thereafter, as first proposed by [11]. Hysteresis loops, defined by linear segments and quadratic ellipse segments, and hysteresis rules, based on an extended Masing's hypothesis, are used to model the cyclic response of each panel (Figure 1.5(b)).

A diaphragm element is used to model the in-plane stiffness of floor slabs. It is essentially a 4-noded plane-stress element that remains elastic at all times. Refer to [17] for the detailed theory of each of these element types. A key feature of FRAME3D is that full geometric updating is included in both static and dynamic analyses to accommodate large nodal translations and rotations. This automatically accounts for the $P-\Delta$ effects and allows the analysis to follow a building's response well into collapse. It involves updating the locations of the joint nodes, attachment points, and the local beam nodes, as well as the orientations of the local element coordinate systems [16, 18, 19] and ensuring equilibrium in the updated configuration. The

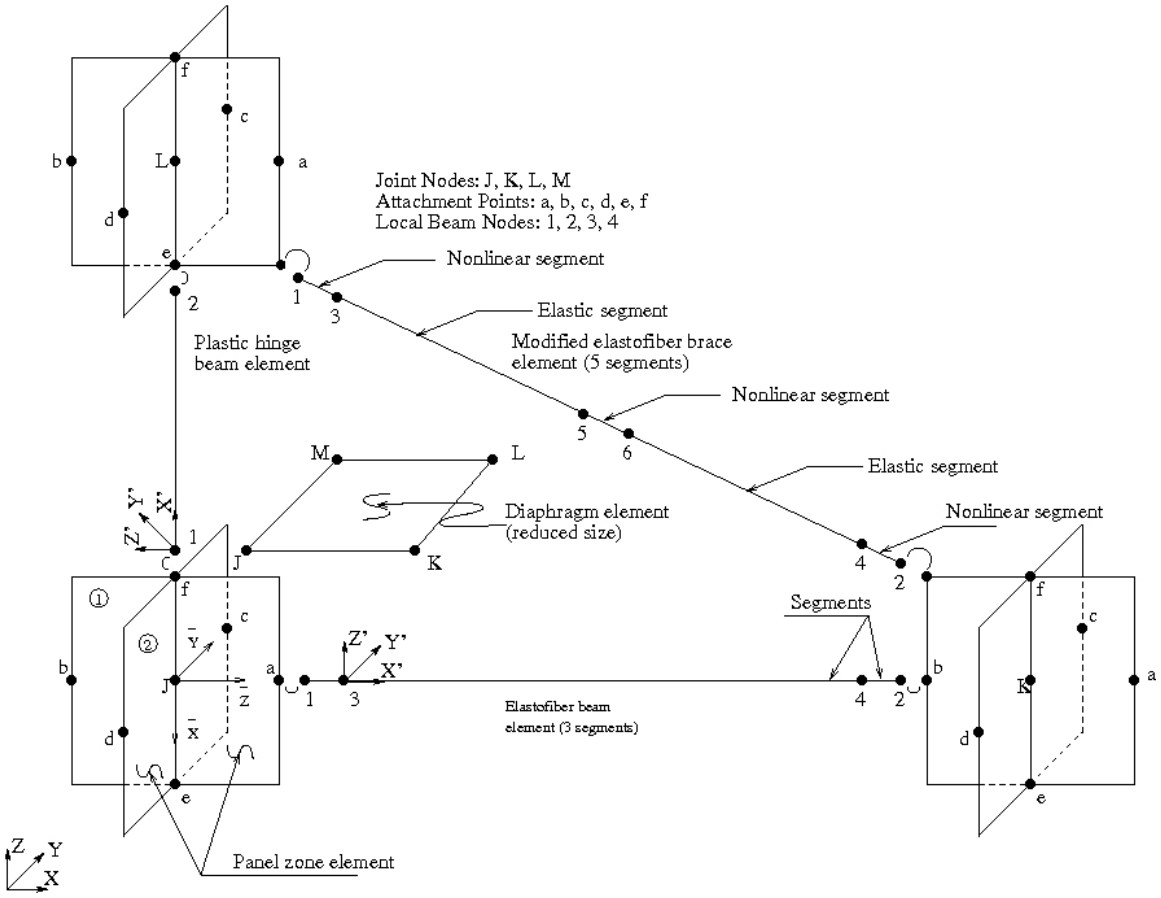

Figure 1.2: Element arrangement in the FRAME3D modeling framework, showing joint nodes, attachment points, beam internal nodes the plastic hinge and elastofiber elements for beam/column modeling, the 5-segment modified elastofiber element for brace/slender-column modeling, the panel zone element for joint modeling, and the diaphragm element for floor slab modeling.

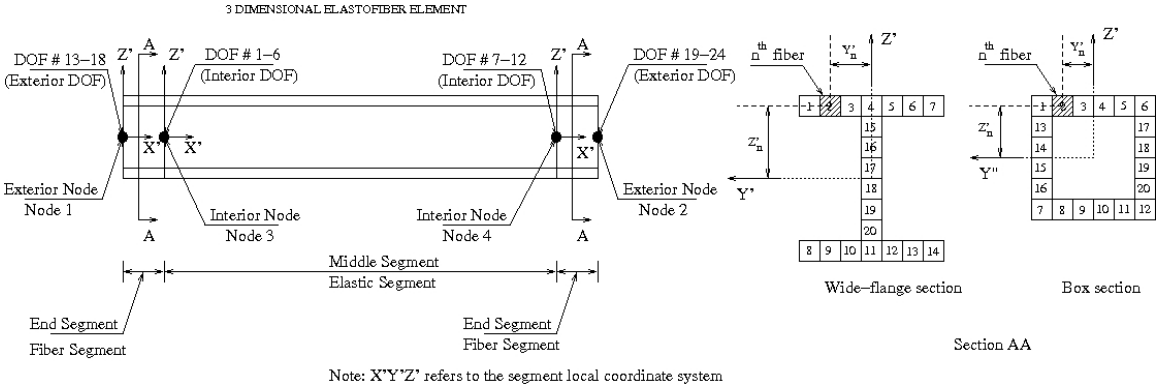

Figure 1.3: Schematic representation of the elastofiber beam element used to model columns and beams. Each element is divided into a linear elastic middle segment and two non-linear fiber segments. The fiber segments are composed of 20 non-linear fibers that run the length of the segment, as shown in section view A-A.

program utilizes an iteration strategy applied to an implicit time-integration scheme to solve the nonlinear equations of motion at each time-step.

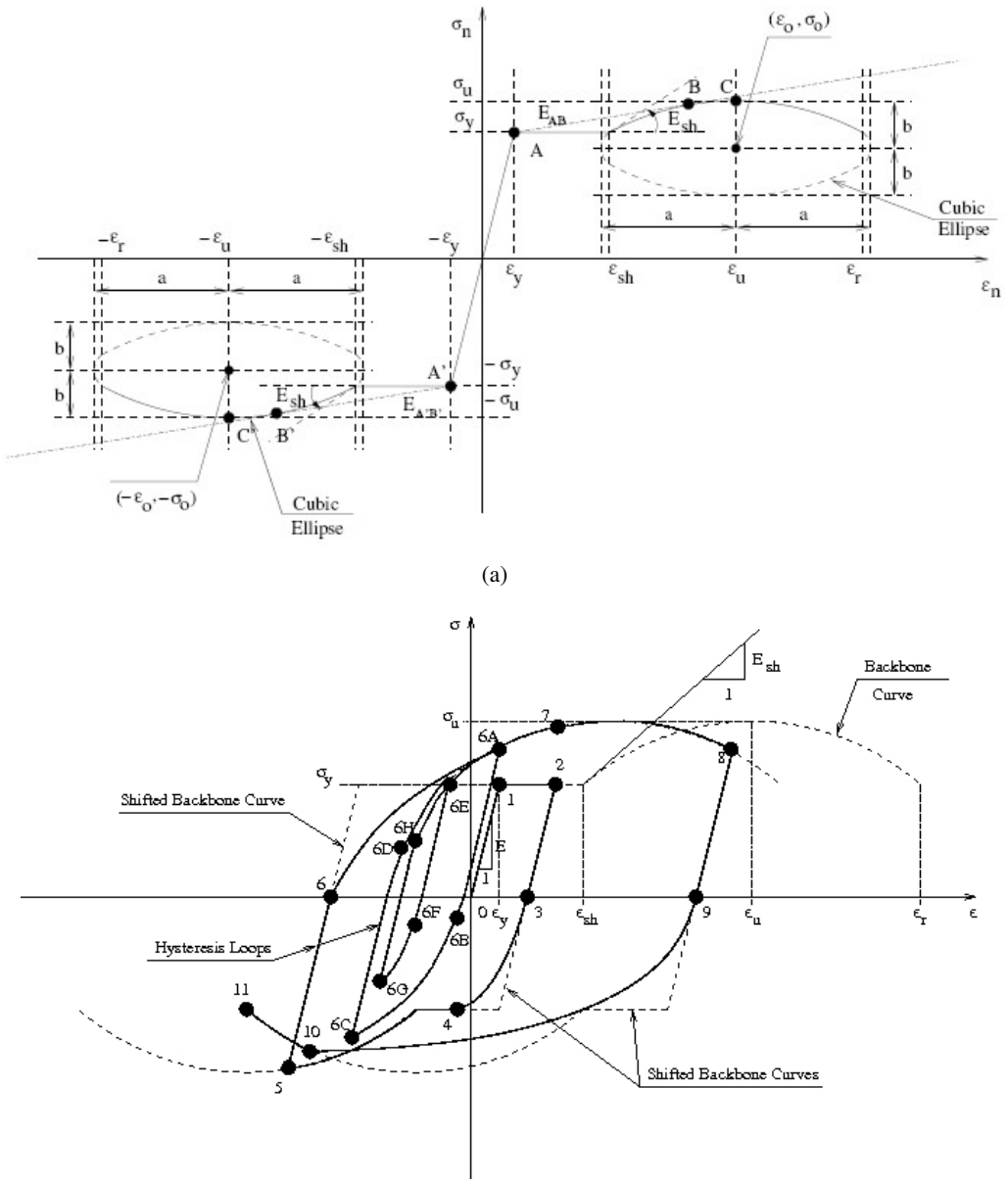

Figure 1.4: (a) Backbone curve for the fiber stress-strain relationship. (b) An example of how curve combined with hysteretic laws to determine the fiber response.

The FRAME-3D models for the two buildings use panel zone elements and elastofiber elements to model the structural frame, and plane stress elements to represent the floor diaphragms. The story masses are lumped at the column locations based on plan tributary area. Composite action due to the connection between the floor slabs and the moment-frame beams is not considered. A rigid foundation is assumed, with the base of all columns fixed. Soil-structure interaction is not included.

There is great uncertainty in the performance of the beam-to-column connections in older welded steel moment frame buildings as evidenced in the 1994 Northridge earthquake, where brittle behavior was ob-

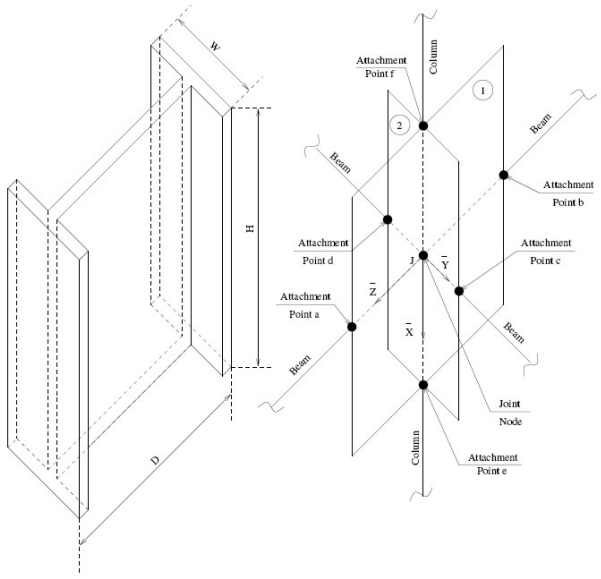

(a)

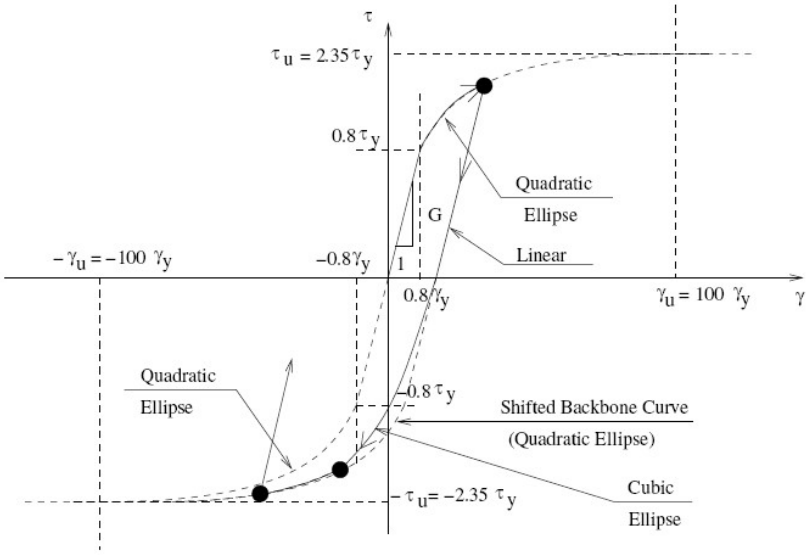

(b)

Figure 1.5: (a) Idealization of the beam-column connection into a panel-zone element. (b) Backbone curve for the nonlinear hysteretic stress-strain relationship in the panel-zone element.

served in many of these connections. To take into account this vulnerability of older steel moment-frames to fracture, FRAME3D allows for a user-specified probabilistic description of the fracture strain of fibers in elastofiber elements. This feature is used in modeling the existing building. Two susceptibility models are considered, one with perfect connections representing the best-case scenario in as far as system ductility is concerned, and the other with susceptible connections representing a less optimistic and perhaps more realistic assumption in this regard. Since there were significantly greater number of fractures observed in the bottom flanges of beams during the Northridge earthquake, a more susceptible probability distribution

is assumed for the fibers in the beam bottom flange when compared against that assumed for the fibers in the top flange and the web. The fracture strain for the fibers in the bottom flanges of moment frame beams, represented by fibers 8 to 14 in Figure 1.3, is drawn from the distribution shown in Figure 1.6(a) (probability is 20% that the fracture strain is 0.9 times the yield strain, ϵ_y; 20% that it is $2\epsilon_y$; 20% that is $5\epsilon_y$; 20% that is $15\epsilon_y$; and 20% that it is $40\epsilon_y$). For the top-flanges, represented by fibers 1-7 in Figure 1.3, and the webs of the beams, represented by fibers 15-20 in the figure, fracture strains are drawn from the distribution shown in Figure 1.6(b) (with a 30% probability that the fracture strain is $10\epsilon_y$; 30% that it is $20\epsilon_y$; 20% that it is $40\epsilon_y$; and 20% that it is $80\epsilon_y$). At each connection, the fracture strain in all the beam bottom flange fibers is taken to be a random variable. At the beginning of the time-history analysis, a single realization of this random variable is generated from the corresponding distribution and assigned to the fracture strain of all the beam bottom flange fibers at that connection. This is repeated for the bottom flange fibers as well as the web and the top flange fibers at either segment of each beam. For column flange and web fibers, it is assumed that the fracture strains are far greater than the rupture strain, thus precluding the occurrence of fractures.

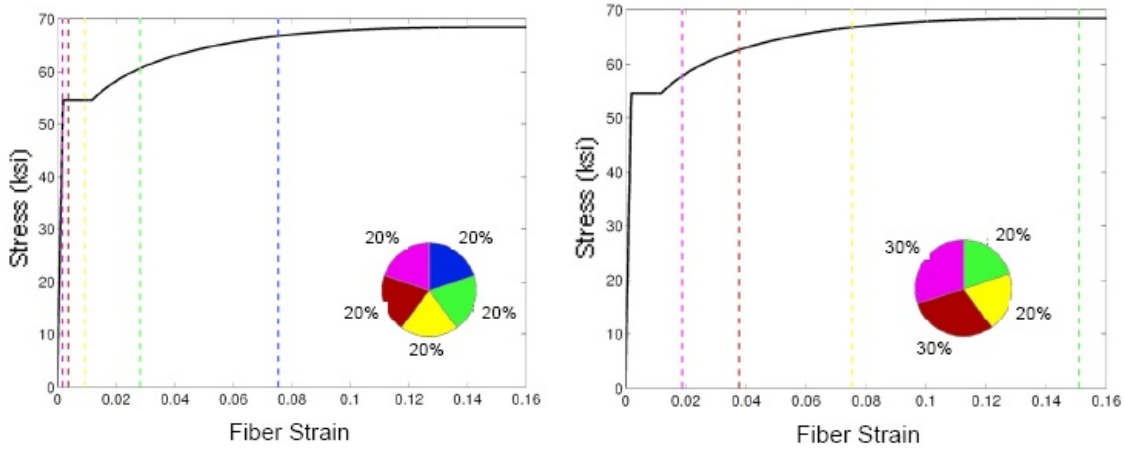

(a) (b)

Figure 1.6: Marked on the backbone axial stress-strain curves of the elastofiber element fibers is the distribution of fracture strain assumed for the susceptible connection case of the existing building: (a) beam bottom flange, and (b) beam web and top flange. The pie chart shows the probability of assigning one of the five fracture strains marked on the backbone curve of a given fiber, for e.g., in (a) there is a 20% chance that the fiber fracture strain is about 0.028 as indicated by the green dashed line and the green colored pie in the pie chart.

The specifications [6] developed by the Federal Emergency Management Agency (FEMA) for moment-frame construction following the Northridge earthquake should result in superior connection performance. Hence, the connections in the redesigned building (designed according to UBC97) are assumed to be flawless, and the fracture-susceptible case is not considered in this study.

Chapter 2 Ground Motion Idealization

Tall buildings of the kind targeted in this study are long-period structures and are generally more responsive to long-period ground excitation. High frequency content in the ground motion has little influence on their collapse behavior [21]. The power in the long-period regime is more apparent in ground velocity and displacement waveforms than in the ground acceleration waveform that is dominated by the higher frequencies. Thus, structural damage to tall buildings is better correlated with peak ground velocity (PGV) and peak ground displacement (PGD) than with peak ground acceleration (PGA). The collapse of tall buildings in Mexico City at a distance of over 350km from the epicenter of the Mexico City earthquake of 1985 is testament to this fact. The amplitudes of high-frequency ground accelerations had attenuated significantly due to the large propagation distance. However, the seismic waves retained significant energy at longer periods. What caused these buildings to collapse is the amplification of this long-period excitation (growth of PGD and PGV in the 2s–3s period range) as the waves propagated through the thick clay layer just beneath the surface upon which they were located [1]. This sensitivity of tall building response to PGV and PGD (in addition to duration) suggests that ground velocity and displacement waveforms are best candidates for parameterization, as far as applicability to tall buildings is concerned. Displacement waveforms have one drawback however. They can have static offsets that may (if they occur quickly) or may not (if they occur slowly) have a significant influence on tall building response. Characterizing the static offset may require one or two additional parameters, increasing the complexity of the parameterization scheme. Residual ground velocities following an earthquake are always zero, making ground velocity waveforms the best candidate for parameterization. Here, ground velocity waveforms are idealized as triangular (sawtooth-like) wave-trains as shown in Figure 2.1(b). This ground motion representation scheme was first used by Hall et al. [12] to study the effects of near-source ground motion on tall building response. The displacement history in this representation closely mimics the displacement pulse that would result from the rupture of a penny-shaped crack on a fault surface (point-source) in the vicinity of the crack [4]. Although a single cycle is shown in the figure, multi-cycle extensions with identical period and amplitude are also used to represent long-duration ground motion waveforms. The acceleration waveform corresponding to this velocity history is a rectangular wave-train (Figure 2.1(c)), while the displacement is a one-sided parabolic wave-train (Figure 2.1(a)). The one-sided nature of the displacement should not be of concern. For multi-cycle excitation, displacement is cyclic but always has a positive sign. This is an artefact of the idealization scheme, mathematically equivalent to shifting the origin of the frame of reference, and should have little or no effect on the dynamics of the structure.

Three parameters are used to characterize the ground velocity waveform: period T, amplitude PGV (peak ground velocity), and number of cycles N. The ability of this ground motion representation to accurately emulate the true seismic ground motion waveforms in as far as impacts on the buildings of interest are concerned must be ensured. Toward this end, the best-fitting single-cycle idealized waveform from a suite of idealized waveforms to the strong component of 18 near-source records (velocity histories) is deter-

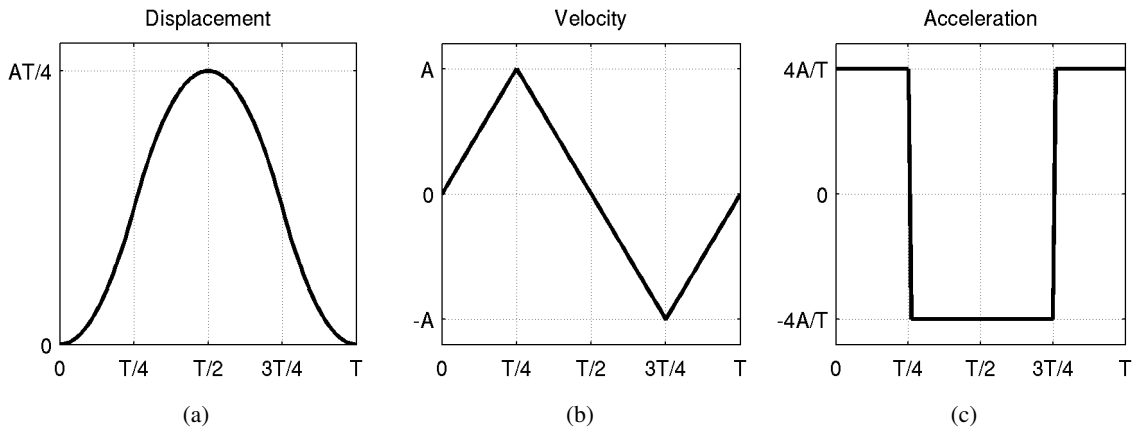

(a) (b) (c)

Figure 2.1: Waveforms for the (a) displacement, (b) velocity, and (c) acceleration of the idealized pulses used as input ground motions.

mined using the Least Absolute Deviation method (L_1 norm). The idealized waveform suite comprises of waveforms with period varying between 0.5s and 6.0s at 0.25s intervals, PGV varying between 0.125m/s and 2.5m/s at 0.125m/s intervals, and the number of cycles ranging from 1 to 5 as well as 10 to emulate long duration records. The near-source records are from the 1992 Cape Mendocino, the 1999 Chi-Chi, the 1979 Imperial Valley, the 1978 Iran, the 1995 Kobe, the 1989 Loma Prieta, the 1992 Landers, the 1994 Northridge, the 1971 San Fernando, and the 1987 Superstition Hills earthquakes. The idealized waveform fits are shown in Figures 2.2 through 2.4. Best-fitting 2-, 3-, 4-, 5-, and 10-cycle waveforms are shown as well. These are not utilized in the forthcoming analysis since all the records have a prominent near-source pulse that is likely to dominate the structural response. They are, however, used in characterizing ordinary multi-cycle ground motion in later sections.

The FRAME3D models of the existing building (perfect and susceptible connections), and the redesigned building (perfect connections) are analyzed under the 18 three-component near-source records. For the existing building model with susceptible connections and the redesigned building model with perfect connections, the strong component of ground motion is oriented in the building X direction. For the existing building model with perfect connections, two cases are considered: strong component oriented in the building X and Y directions. The peak transient interstory drift ratio (IDR), which is the peak value for all stories of the relative displacement between the top and bottom of a story normalized by its height, is used as a measure of structural performance. The same models are also analyzed under the one-component best-fitting single-cycle idealized waveforms. Shown in Figures 2.5 and 2.6 is the comparison of the profiles of peak transient IDR over the height under the actual and idealized motions for the existing building (susceptible connections) and the redesigned building (perfect connections) models. The consistently good match of the profiles indicates that the particular idealization adopted here to characterize the ground motion can be very effectively used in studying the response of the target buildings. Notable exceptions are the results for the Lexington dam record from the Loma Prieta earthquake and the Pacoima Dam record from the San Fernando earthquake. The average error in the peak transient IDR estimate exceeds 30%. The L_1 norm (least absolute deviation) accords equal weightage to the amplitude as well as period of ground motion during the

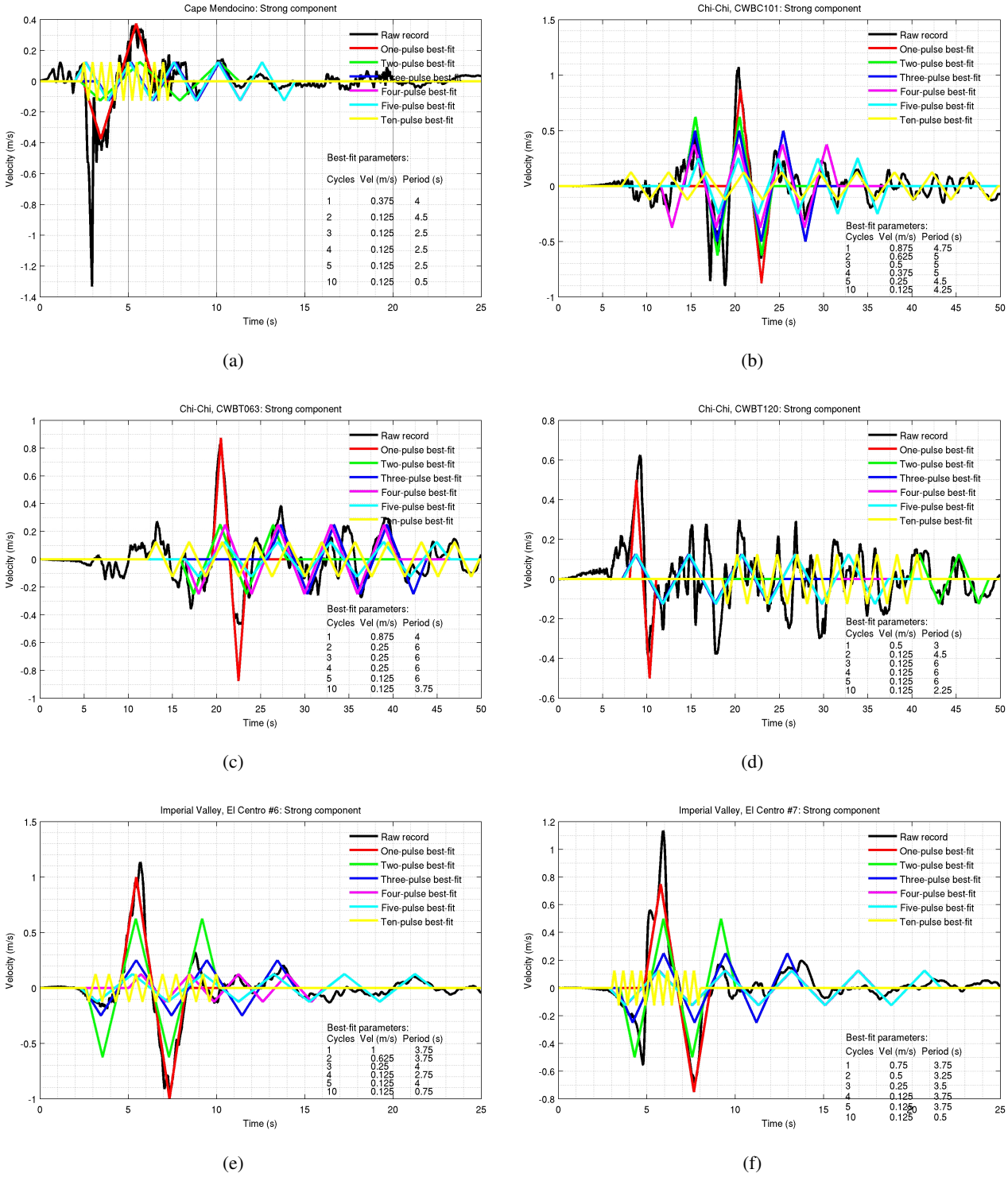

Figure 2.2: Near-source ground motion records from the Cape Mendocino, Chi-Chi, and Imperial Valley earthquakes. Also shown are the idealized 1-, 2-, 3-, 4-, 5-, and 10-cycle saw-tooth waveforms with the least absolute deviation (L_1 norm) from the corresponding record.

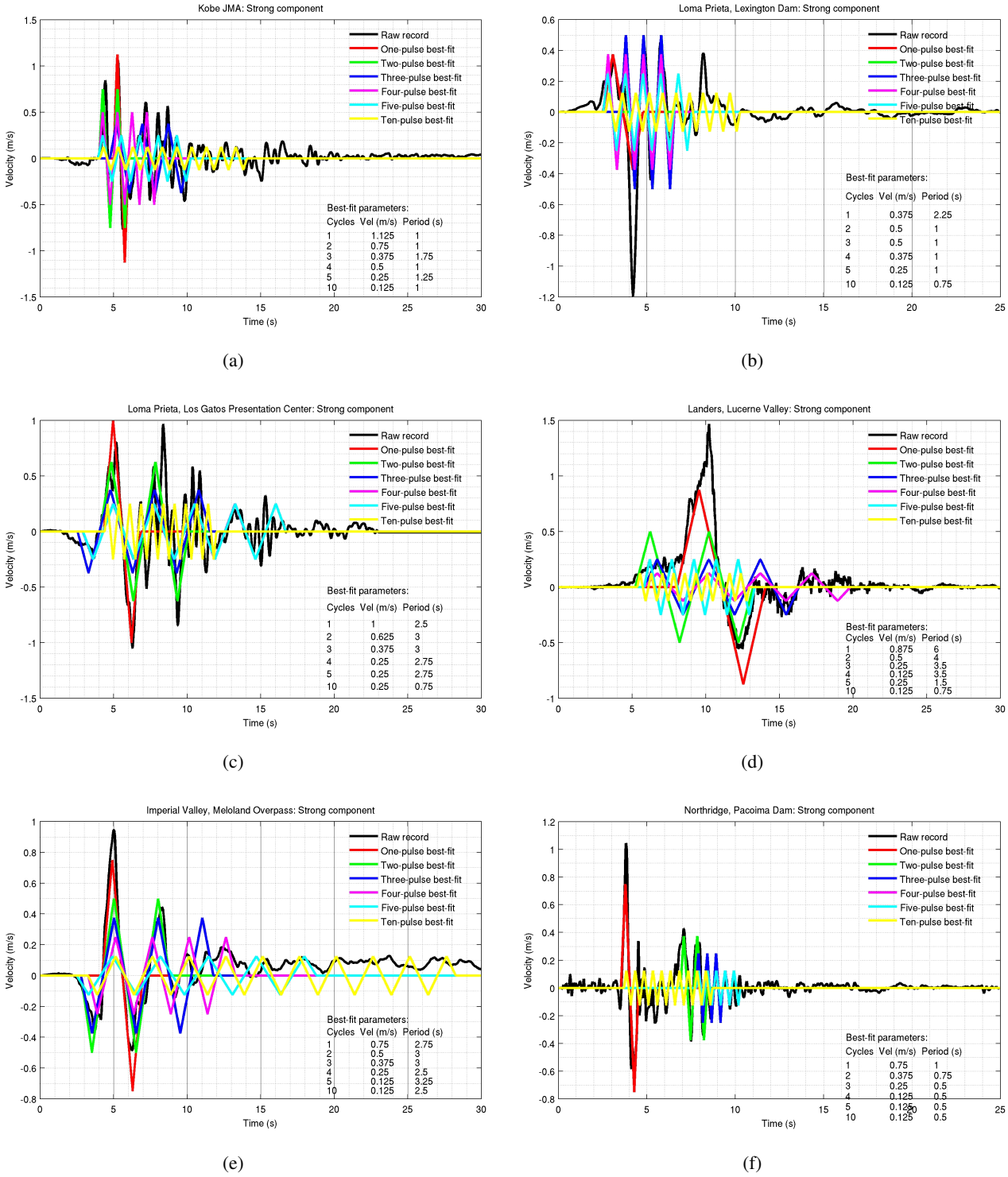

Figure 2.3: Near-source ground motion records from the Kobe, Loma Prieta, Landers, Imperial Valley, and Northridge earthquakes. Also shown are the idealized 1-, 2-, 3-, 4-, 5-, and 10-cycle saw-tooth waveforms with the least absolute deviation (L_1 norm) from the corresponding record.

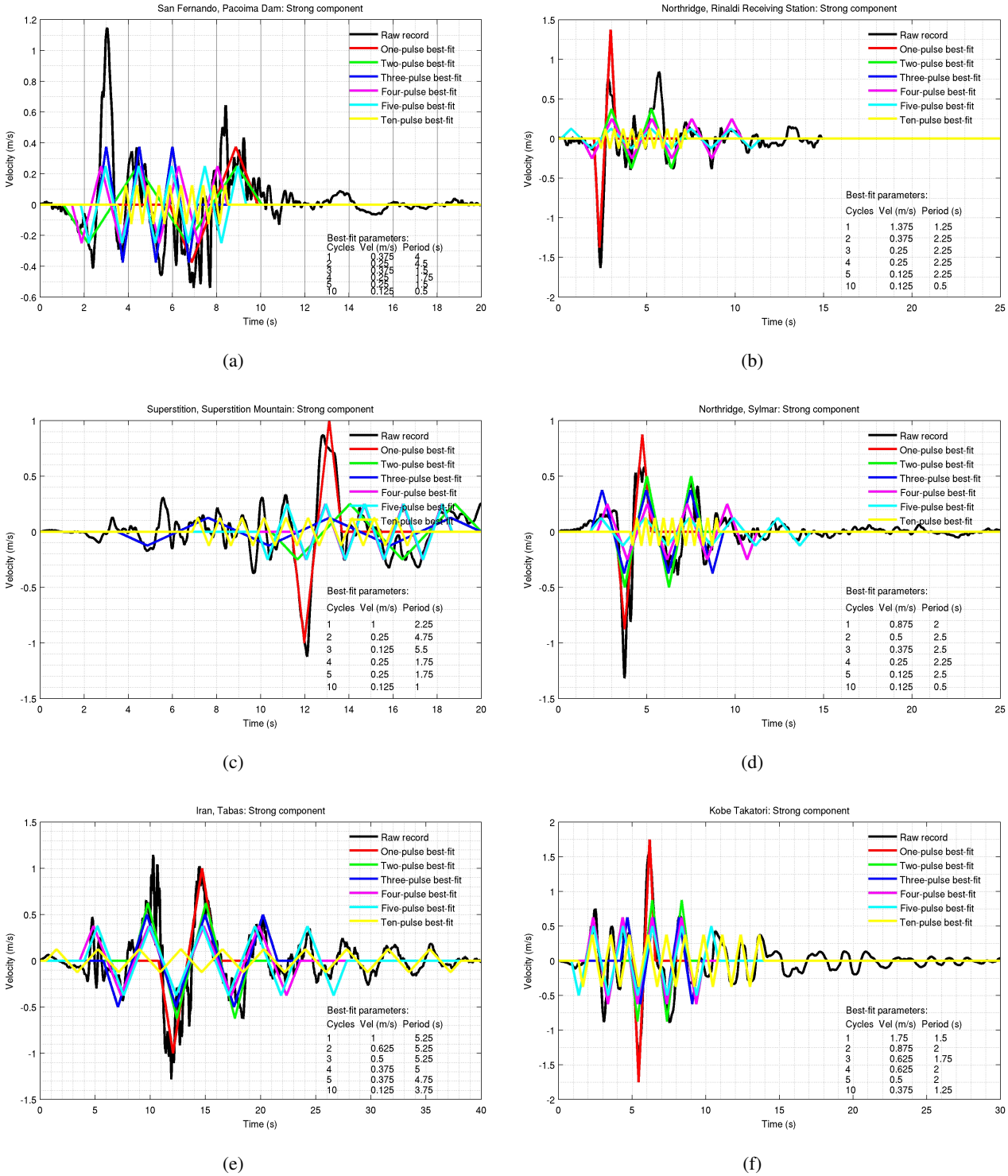

Figure 2.4: Near-source ground motion records from the San Fernando, Northridge, Superstition, Iran, and Kobe earthquakes. Also shown are the idealized 1-, 2-, 3-, 4-, 5-, and 10-cycle saw-tooth waveforms with the least absolute deviation (L_1 norm) from the corresponding record.

minimization process, unlike the L_2 norm (least squares) which would accord far greater weightage to the amplitude than the period. In cases where there is a high-amplitude moderate-period one-sided pulse and a moderate-amplitude long-period two-sided pulse, such as in the Pacoima Dam record from the San Fernando earthquake (Figure 2.4(a)), the L_1 norm picks the moderate-amplitude long-period two-sided pulse over the one-sided high-amplitude moderate-period pulse. The reverse would be true for the L_2 norm. Since tall building structural response is sensitive to both periods and amplitudes, the L_1 norm is used despite large errors in some instances. In the Lexington Dam record from the Loma Prieta earthquake (Figure 2.3(b)), the stronger forward phase of the record has a shorter period than the reverse phase. Since the idealized waveforms have the same amplitude for both forward and reverse phases, the features of only one of the two phases can be picked by the optimization algorithm. The L_1 norm picks the period and amplitude of the longer period reverse phase. The L_2 norm would pick the period and amplitude of the forward phase. In these two examples, the L_2 norm would do better, but in most other cases the L_1 norm does better in the context of structural response predictions. The peak values of IDR in all four building models from the two sets of analysis are compared against each other and the errors are quantified in Figure 2.7. The IDR errors have a Gaussian mean of 0.00056 and standard deviation of 0.0069.

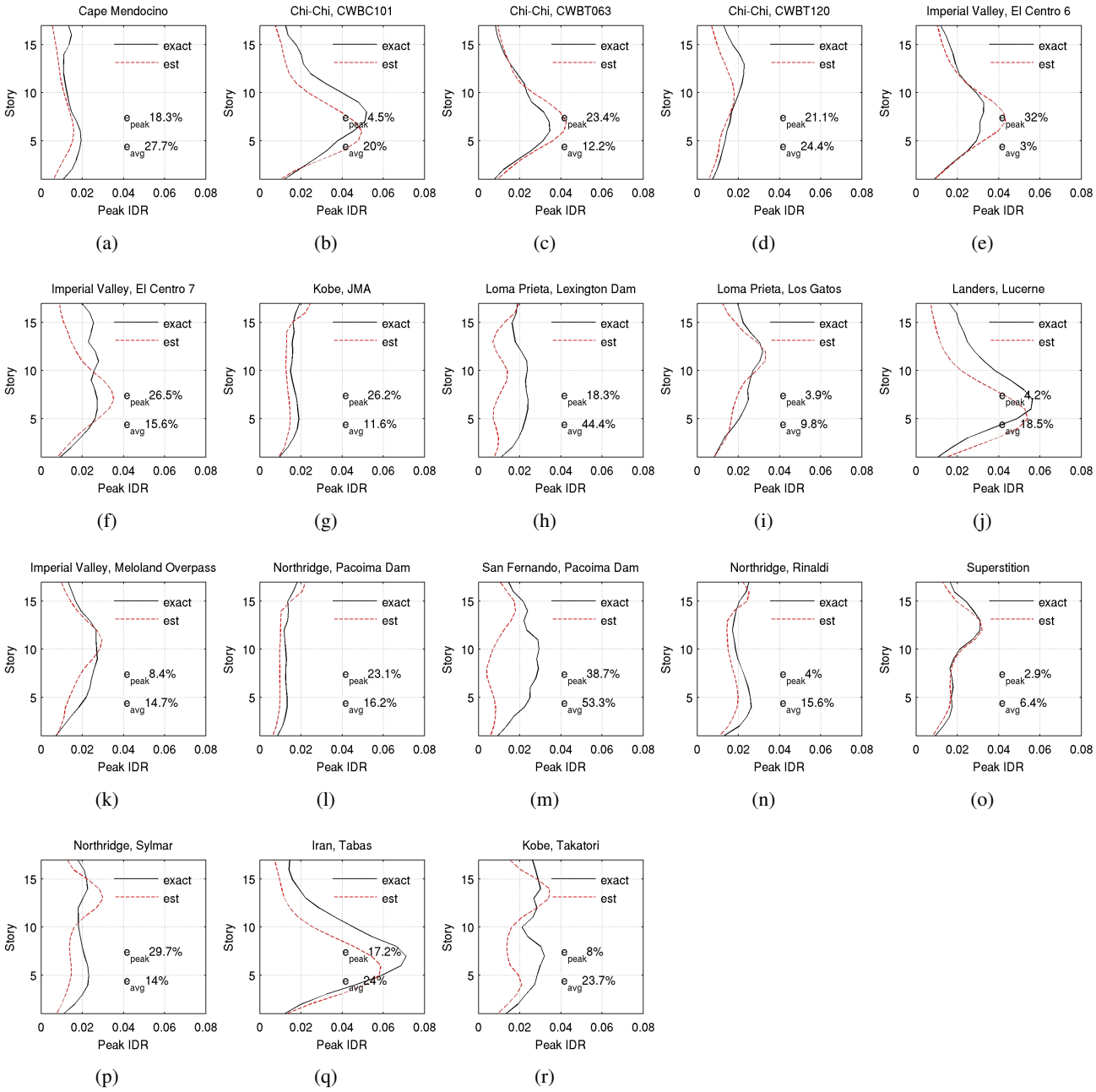

Figure 2.5: Comparison of peak transient interstory drift ratio (IDR) profile over building height computed using real record against that computed using the best-fit idealized 1-cycle saw-tooth waveform: Existing building (susceptible connections).

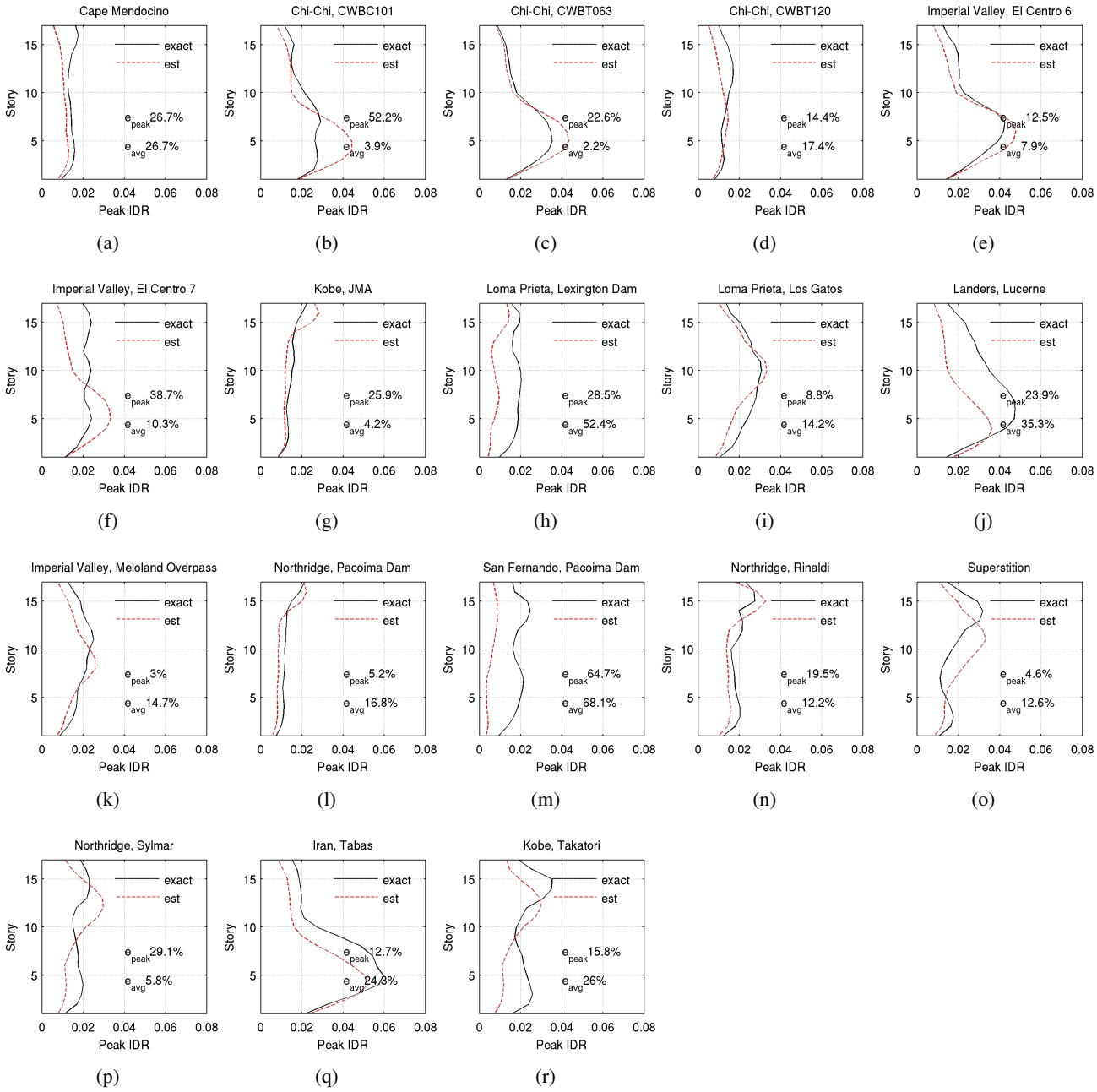

Figure 2.6: Comparison of peak transient interstory drift ratio (IDR) profile over building height computed using real record against that computed using the best-fit idealized 1-cycle saw-tooth waveform: Redesigned building (perfect connections).

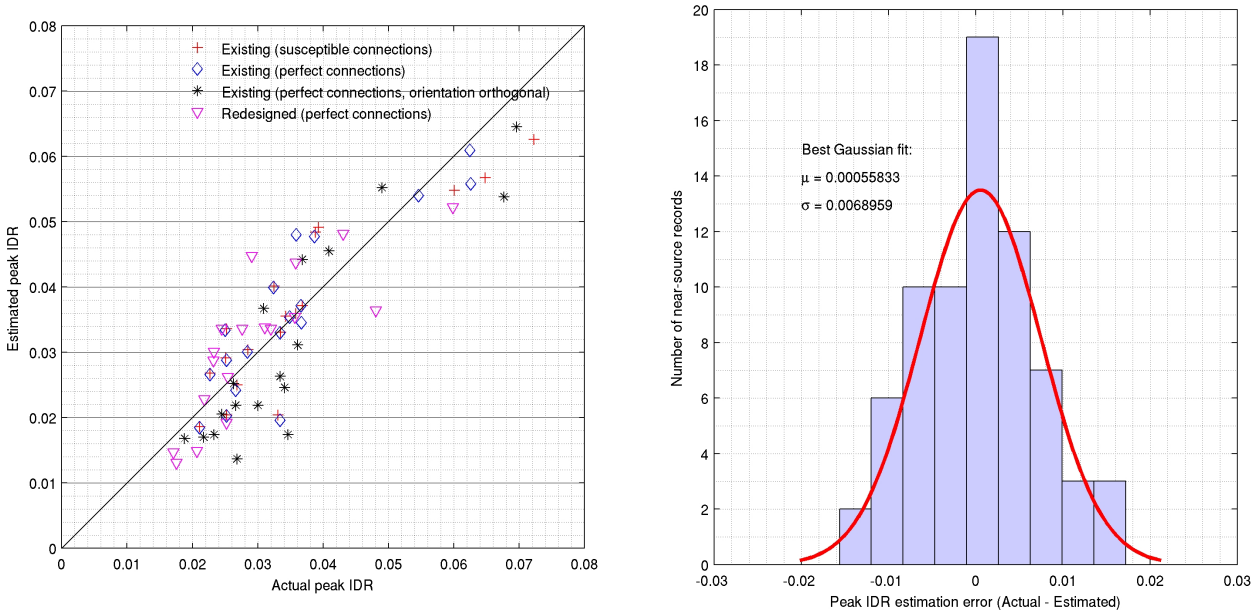

(a) (b)

Figure 2.7: (a) Peak transient interstory drift ratio (IDR) in all the building models computed using the near-source records plotted against that computed using best-fit idealized 1-cycle waves. The diagonal line represents identical results from the two analyses. (b) Histogram of the error in determining the peak transient IDR from the idealized waveform as opposed to the actual record. The best-fit Gaussian is also shown.

Chapter 3 Tall Building Response Sensitivity to Ground Motion Features

To assess the sensitivity of structural response to ground motion features, a series of 3-D nonlinear response history analyses are conducted on the four building models: (a) Existing building (susceptible connections) under X direction excitation, (b) Existing building (perfect connections) under X direction excitation, (c) Existing building (perfect connections) under Y direction excitation, and (d) Redesigned building (perfect connections) under X direction excitation. The models are subjected to the idealized 1-component ground motion waveforms introduced in the last chapter with ground motion period T varying between 0.5s and 6.0s at 0.25s intervals, PGV varying between 0.125 m/s and 2.5 m/s at 0.125 m/s intervals, and the number of cycles N taking the values of 1 to 5 and 10. Key response metrics are computed and stored in a database. These include the peak transient inter-story drift ratio (IDR) and its location over the building height, the peak residual IDR and its location, permanent roof drift (or tilt) following seismic shaking, plastic rotations in beams, columns, and joints (panel zones), and locations of fractures in the model with fracture-susceptible connections. The peak residual IDR is computed by lowpass-filtering the interstory drift ratio histories and averaging the points within a 5s time-window that has the lowest variance of all such time-windows in the record. A two-pass Butterworth filter with a corner at 10s is employed. A similar approach is adopted for computing the permanent roof drift which is the roof residual displacement normalized by building height. The penthouse is excluded from the peak IDR calculations. It has a much smaller floor-plate than the typical floor of the two buildings. Moreover, the primary moment frames are terminated at the 17^{th} story.

In order to unravel the structural response sensitivity from all perspectives, the following maps and/or figures are generated for each building model:

1. color maps with contours of peak transient IDR (and its story location) on the T-PGV plane, one map for each N;
2. peak transient IDR (and its story location) maps on the PGD-PGV plane, one map for each N;
3. peak residual IDR (and its story location) maps on the T-PGV plane, one map for each N;
4. peak residual IDR as a function of peak transient IDR, one map for each N;
5. permanent roof drift (roof residual displacement normalized by building height) maps on the T-PGV plane, one map for each N;
6. permanent roof drift as a function of peak transient IDR, one map for each N;
7. curves of peak transient IDR (with story locations) as a function of T, one curve for each PGV and N;

S.No.	Performance Level		Transient IDR Upper Limit	Post-Earthquake Damage State
	Label	Description		
1	IO	Immediate Occupancy	0.007	Very light/limited structural damage No permanent drift, minor repairs Immediately occupiable
2	LS	Life Safety	0.025	Moderate damage, but structure retains a margin against partial collapse 1% residual drift, structure repairable, but may be economically impractical Building likely to be shut down for repairs
3	CP	Collapse Prevention	0.050	Severe damage, on the verge of partial collapse 5% residual drift, structure may be irrepairable Building may need to be demolished
4	RT	Red-Tagged	0.075	Partial collapse may have occurred Building is red-tagged; needs to be demolished
5	CO	Collapsed	0.100	Partial collapse near-certain; complete collapse likely Near-certain complete collapse beyond IDR of 0.100

Table 3.1: Structural performance levels, associated response metrics, and post-earthquake damage states.

8. curves of peak transient IDR (with story locations) as a function of PGV, one curve for each T and N;

9. curves of peak transient IDR (with story locations) as a function of N, one curve for each T and PGV.

Results for the existing building (susceptible connections) under X direction excitation are presented in Appendix A; for the existing building (perfect connections) under X direction excitation in Appendix B; for the existing building (perfect connections) under Y direction excitation in Appendix C; and for the re-designed building (perfect connections) under X direction excitation in Appendix D. For the contour maps, the data from the parametric analysis is interpolated on a fine parameter grid using a triangle-based linear interpolation technique and filtered using a disk-shaped correlation filter to smoothen sharp transitions in the contours. Also plotted on the peak transient IDR maps are contours corresponding to upper limits on IDR for Immediate Occupancy (IO; IDR=0.007), Life Safety (LS; IDR=0.025), and Collapse Prevention (CP; IDR=0.05) performance levels. These performance levels are adopted from the "Prestandard and Commentary for the Seismic Rehabilitation of Buildings [5]" published by the Federal Emergency Management Agency (FEMA). In addition, contours corresponding to peak transient IDRs of 0.075 and 0.100 are also shown. In thousands of collapse analyses conducted by the authors on models such as the ones considered in this study, a large percentage of models lose stability (i.e., stiffness matrix ill-conditioning) beyond peak transient IDRs of 0.10. Thus, peak transient IDRs greater than 0.10 would almost surely result in complete collapse. Given that the models do not include certain critical failure modes such as local buckling in column flanges, the peak transient IDR range of 0.075-0.100 (CO) may be indicative of partial to complete collapse (unstable). Models with intermediate peak transient IDRs in the range of 0.050-0.075 can be expected to be on the verge of collapse (neutrally stable) and hence may be red-tagged (RT). The structural performance levels are summarized in Table 3.1.

The following observations can be made from the results of the simulations:

1. In the frequency and amplitude bands of relevance to seismic ground motion, the peak transient IDR response is more or less monotonously increasing (or constant, but not decreasing) with increasing PGV at a given T level. The same is more or less true with increasing T at a given PGV level. This desirable feature in as far as identifying damaging features of ground motion is concerned is not necessarily true at given levels of peak ground displacement (PGD). For example, for two 3-cycle ground motion records with $PGD = 1.5m$, the peak transient IDR in the existing building with susceptible connections (Figure A.2(c)) points to collapse under the record with $PGV = 1.25m/s$, but only red-tagged under the record with $PGV = 2.25m/s$. This suggests that structural response can be more simply characterized using the PGV-T combination rather than the PGV-PGD combination.

2. The IO and LS regimes (peak transient IDR < 0.025) do not shrink significantly with increasing number of ground motion cycles (see Figures A.1, B.1, C.1, and D.1) . Plasticity levels, if at all yielding occurs, are quite low at these low IDRs (see Figures A.4, B.4, C.4, and D.4), showing peak residual IDR as a function of peak transient IDR). As a result, not much degradation is expected due to increased number of cycles. This holds true even for the existing building model with connections susceptible to fracture, perhaps because the susceptibility to fracture exists only in beams and not in columns of the model. Moreover, this susceptibility is quite low in the beam top flange and web (see Figure 1.6). Another factor may be that low-cycle fatigue is not considered in the modeling approach. There is some, although only mildly significant, shrinking in the CP regime with increasing number of cycles. The greatest change going from 1-cycle to 10-cycle excitation is the dramatic and progressive expansion of the collapse regime at the expense of the shrinking of the CP–CO regime. In other words, under multi-cycle excitation ($N > 2$), there is a steep gradient in the response surface going from collapse-safe performance to complete global collapse with small increases in the ground motion period and/or peak ground velocity. This is especially true in the long-period excitation regime ($T > T_1$, where T_1 is the fundamental natural period of the building), where there is little difference in PGV thresholds for CP, RT, and CO performance levels. This points to the extreme sensitivity of structural response to the velocity amplitude of long-period, long-duration ground motion. Performance can range from satisfactory to complete collapse with subtle differences in the PGV in the vicinity of the CP/RT/CO thresholds. The threshold values for the exceedance of the CP, RT, and CO performance levels of (a) idealized wave period at PGV of 2.5m/s and (b) PGV at period of 6s, for various number of idealized wave cycles, are listed in Table 3.2 for all four building models.

3. For near-certain complete collapse (peak transient IDR > 0.10) of buildings with perfect connections to occur under 1- or 2-cycle excitation (e.g., near-source records), the excitation period must exceed roughly the building fundamental period. For the existing building, the excitation period must exceed 4.5s, whereas, for the redesigned building, it must exceed 4.0s (compare Figures B.1(b) and D.1(b)). However, the PGV threshold for collapse of the redesigned building under 2-cycle excitation is higher (1.2 m/s from Figure D.8(b)) than that of the existing building (0.9 m/s from Figure B.8(b)). Furthermore, this intensity threshold holds steady for cycles with a wide range of periods (4s–6s) in the case of the redesigned building. It does not drop with increasing period as in the case of the existing building.

4. The PGV thresholds for near-certain complete collapse (peak IDR > 0.10) under 1-cycle to 10-cycle X direction excitation varies approximately from 1.575m/s to 0.5m/s for the existing building model with susceptible connections, from 1.9m/s to 0.5m/s for the existing building model with perfect connections, and from 1.9m/s to 0.8m/s for the redesigned building model with perfect connections (Table 3.2). These values apply to long-period ground motion ($T = 6s$).

5. Collapse risk is negligible/minor if ground motion $PGV < 0.5m/s$ or $T < 1.5s$ for $N \leq 5$ for all four building models (see Figures A.8, B.8, C.8, and D.8).

6. Partial (and perhaps complete) collapse (peak transient IDR > 0.075) is almost certain to occur in all four models if ground excitation has a period $T > 5s$, a velocity amplitude $PGV > 1m/s$, and has multiple cycles ($N > 1$).

7. While the areal coverage on the PGV-T plane of the "CP or worse" regime is about the same in both the existing and redesigned building models (both with perfect connections), the significantly higher PGV threshold for collapse of the redesigned building under long period ground motion ($T > 5s$) is the main benefit of the 1997 UBC design when compared to the 1982 UBC design. In addition, the PGV threshold for Life-Safe (LS) performance holds steady for the redesigned building model with increasing T, whereas it drops rapidly for the existing building model with increasing T. The stiffer, but stronger, redesigned building is thus more robust in its response to long period ground motion when compared against the more flexible, but weaker, existing building model. The same is generally true for high PGV-low T excitation as well with the redesigned building model outperforming the existing building model.

8. The effect of connection susceptibility to fracture in lowering the PGV threshold for collapse under long period ground excitation ($T > 5s$) is clear. This effect diminishes with increasing number of cycles. Under 10-cycle excitation, both the perfect and susceptible connection models have the same PGV threshold for collapse under the $T = 6s$ ground motion. However, for shorter period ground motion ($T = 3s$) the PGV threshold for collapse under 10-cycle ground motion is far greater (1.75m/s from Figure B.1(f)) for the perfect connection model than for the susceptible connection model (1.15m/s from Figure A.1(f)). As a result, the areal coverage of the collapse regime in the T-PGV plane is much greater for the fracture susceptible connection model when compared against the perfect connection model.

9. There are significant qualitative differences between the performance of the existing building model (perfect connections) under X and Y excitations. In the long period regime ($T > T_x$ or T_y), the PGV threshold for collapse in the Y direction is always (for all N) lower than that for collapse in the X direction by about 15%. On the other hand, the performance under short period ground motion in the Y direction is more robust than under X-direction motion. In the excitation period range of 1–2s, the peak transient IDR response of 0.03-0.04 dominates over 0.02-0.03 under X direction excitation, whereas the reverse is true for Y direction excitation.

10. Peak residual IDR occurs only beyond the LS performance level (peak transient IDR of 0.025) and grows linearly, but slowly until the CP performance level, then accelerates significantly. Beyond this level of performance, much of the transient IDR is not recovered and residual IDR forms a much greater percentage of the transient IDR (e.g., compare Figures A.1 and A.3 or see Figures A.4, B.4, C.4, and D.4). Iwata et al. [13] conducted a study of twelve steel structures damaged in the 1995 Kobe earthquake. Using the measured peak residual IDR and reported repair costs, they estimated a reparability limit of 0.015 for the peak residual IDR. However, there are two cases presented by them where buildings with peak residual IDR greater than 0.02 were successfully repaired. In most cases, this level of peak residual IDR is reached when the peak transient IDR exceeds 0.05, the CP performance level. Thus, while the structure may not have collapsed at this IDR level, it certainly becomes unusable at this stage. This lends credence to the red-tagging of these buildings beyond the peak transient IDR of 0.05 that is adopted in this study.

11. There is a high degree of correlation between the permanent roof drift (roof residual displacement normalized by building height) and the peak residual IDR as evidenced by the close correspondence between their relationships to the peak transient IDR (compare Figures A.6 and A.4, B.6 and B.4, C.6 and C.4, and D.6 and D.4). So the amount of lean (or tilt) following an earthquake can be used to reliably estimate the post-earthquake condition of the building.

12. The number of cycles of ground excitation has minimal impact in cases where peak transient IDR is below the CP limit. If the peak transient IDR exceeds the CP limit, degradation is swift with increasing number of cycles for both susceptible-connection as well as perfect-connection building models (Figures A.9 and B.9).

13. The story location of peak transient IDR closely tracks the ground excitation period T, steadily dropping from the top of the building with increasing T. The downward migration halts not at the bottom story, but slightly higher. This phenomenon and its implications for the mechanism of collapse of these building models will be closely examined in the next chapter.

14. Under short period excitation ($T < 1.5s$). the peak transient IDR saturates to a value below the CP limit with increasing PGV (e.g., Figure A.8). Under longer period ground motion, the peak transient IDR grows with PGV (linearly for moderate period excitation, more rapidly for long period excitation with $T > T_x$).

These observations can be qualitatively explained by way of the classical analysis of energy budget in multi-story buildings subjected to earthquake excitation [33, 34]. Starting from the governing differential equation of motion and integrating all terms with respect to the structural relative displacement vector, $\underline{v}$, the equation for energy balance can be written as:

$$E_k(t) + E_\xi(t) + E_a(t) = E_I(t) \tag{3.1}$$

Model	N	Thresholds for CP		Thresholds for RT		Thresholds for CO	
		PGV (m/s) @T = 6s	T (s) @PGV = 2.5m/s	PGV (m/s) @T = 6s	T (s) @PGV = 2.5m/s	PGV (m/s) @T = 6s	T (s) @PGV = 2.5m/s
Existing building (susceptible connections) X direction excitation	1	0.800	2.00	1.150	3.60	1.575	4.50
	2	0.625	1.75	0.750	3.60	0.900	4.50
	3	0.600	1.50	0.700	3.50	0.750	4.45
	4	0.600	1.40	0.625	2.35	0.625	4.00
	5	0.600	1.25	0.600	2.20	0.625	2.50
	10	0.500	1.00	0.500	1.35	0.500	1.50
Existing building (perfect connections) X direction excitation	1	0.810	2.10	1.250	4.50	1.900	5.63
	2	0.750	2.10	0.875	4.50	1.125	5.10
	3	0.690	2.10	0.800	4.25	0.875	4.75
	4	0.625	2.10	0.720	4.00	0.775	4.50
	5	0.600	2.10	0.650	3.75	0.720	4.25
	10	0.500	1.30	0.500	1.60	0.500	1.80
Existing building (perfect connections) Y direction excitation	1	0.860	1.90	1.180	4.50	1.650	5.40
	2	0.740	1.90	0.875	4.45	1.025	4.80
	3	0.650	1.90	0.750	4.30	0.850	4.50
	4	0.625	1.80	0.700	3.50	0.725	4.25
	5	0.600	1.60	0.625	2.30	0.625	3.40
	10	0.500	1.25	0.500	1.40	0.500	1.50
Redesigned building (perfect connections) X direction excitation	1	1.100	2.65	1.450	3.70	1.900	4.50
	2	0.950	2.20	1.130	3.15	1.350	3.70
	3	0.875	2.10	1.000	2.75	1.100	3.20
	4	0.850	2.05	0.900	2.50	0.975	2.80
	5	0.825	2.00	0.875	2.40	0.875	2.60
	10	0.750	1.75	0.800	2.05	0.800	2.08

Table 3.2: Peak ground velocity and period thresholds for the exceedance of the collapse prevention (CP), red-tagged (RT), and collapsed (CO) performance levels for all building models. N is the number of cycles of ground excitation.

where $E_k(t)$ is the instantaneous kinetic energy of the system, $E_\xi(t)$ is the energy dissipated by viscous forces until time t, $E_a(t)$ is the recoverable strain energy stored in the system plus the dissipated hysteretic energy until time t, and $E_I(t)$ is the energy imparted to the system by the input excitation until time t, given by

$$E_k(t) = \frac{1}{2}\sum_{i=1}^{N_f} m_i \dot{v_i^t}^2 \tag{3.2}$$

$$E_\xi(t) = \int \underline{f_D}^T d\underline{v} \tag{3.3}$$

$$E_a(t) = \int \underline{f_S}^T d\underline{v} = \sum_{i=1}^{N_f} \int f_{Si} dv_i \tag{3.4}$$

$$E_I(t) = \int \sum_{i=1}^{N_f} m_i \ddot{v_i^t} dv_g = \int \sum_{i=1}^{N_f} m_i \ddot{v_i} dv_g + \frac{1}{2}\sum_{i=1}^{N_f} m_i \dot{v_g}^2 \tag{3.5}$$

In the above equations, $\underline{f_D}$ is the damping force vector, $\underline{f_S}$ is the restoring force vector, m_i is the mass of floor i, v_i^t is the absolute displacement of floor i, N_f is the number of floors in the building, $\ddot{v_i^t}$ is the absolute acceleration of floor i, and v_g and $\dot{v_g}$ are the ground displacement and velocity, respectively. E_I is the total work done by all the inertial forces (base shear) on the foundation (displacing through a displacement equal to the ground displacement). In other words, it is the energy imparted to the structure during seismic shaking [2, 8, 23, 32]. If the input excitation period is much shorter than that of the structure, $v_i \approx -v_g$; as a result, $E_I \approx 0$. For the long-period buildings of this study, the energy imparted from short-period excitation is small and the peak transient IDR must consequently be quite small. If the input excitation period is much longer than that of the structure, $v_i \approx 0$, and $E_I \approx \frac{1}{2}\sum_{i=1}^{N_f} m_i \dot{v_g}^2$, i.e., the input excitation energy is proportional to the square of the ground velocity. It is clear from this analysis that for the long-period structures of this study, only long-period ground motion can induce a strong response. This explains why collapse-level response is induced only by ground motions with periods longer than the fundamental period of the building (for single-cycle excitation). Moreover, for long period motion, the structural response degrades rapidly with PGV due to the quadratic relationship between input energy and PGV. If the intensity of shaking (PGV) is very strong, then the period does not have to be as long to induce collapse-level response. Alternately, within certain limits, a longer period motion relative to the building fundamental period requires a smaller PGV to cause collapse-level response. This explains the lower PGV thresholds required for collapse-level IDR in the Y direction of the existing building (perfect connections) compared to the X direction ($T_y = 4.26s < T_x = 4.52s$). Of course, if ground motion period is too long (greater than, say, twice or thrice the fundamental period of the building), then loading is almost static and does not induce strong enough dynamic response. Finally, it should be noted that the energy balance analysis is not appropriate for excitation velocities that are extreme where conservation of momentum may be more applicable. However, peak ground velocity from earthquakes seldom exceeds

2.5m/s and energy balance would generally be applicable.

Chapter 4 Localization of Damage and Mechanism of Collapse

The comprehensive database described in the last chapter offers an opportunity to study and understand the nature of collapse in the tall steel moment frame building models considered. It was observed there that there is a steady downward migration of the story location of the peak transient IDR from the top of the building with increasing period of ground excitation. This migration is arrested between stories 4 and 7 in the collapse regime of response of the existing building, and at story 4 in the case of the redesigned building. What is the explanation for this behavior and what is its relationship to the mechanism of collapse? Is the mechanism of collapse dependent upon the nature of ground motion? These questions motivate this section of the study.

To first uncover the anatomy of a collapse mechanism, one instance of collapse is studied closely. The deformed shape of the structure as it is collapsing along with the plastic hinges on one of the frames are shown in Figure 4.1. The figure shows the formation of plastic hinges at the top of all columns in an upper story, at the bottom of all columns in a lower story, and at both ends of all beams in the intermediate stories. Such a pattern of hinging results in shear-like deformation in these stories, resembling plastic shear bands in ductile solids that are severely (shear) strained (e.g., [25]). We coin the term "quasi-shear band (QSB)" to refer to this yield localization region in moment frame buildings. Most of the lateral deformation due to seismic shaking is concentrated in this band. The severe plastic hinging causes it to be far more compliant than the overriding block of stories above and the supporting basal block of stories below. When the overturning 1^{st}-order and 2^{nd}-order ($P-\Delta$) moments from the inertia of the overriding block of stories exceeds the moment-carrying capacity of the quasi-shear band, it loses stability and collapses. This initiates gravity-driven progressive collapse of the overriding block of stories. Thus, the collapse mechanism initiates as a sidesway mechanism that is taken over by gravity once the quasi-shear band is destabilized. An idealized representation of the collapse mechanism is shown in Figure 4.2.

In structures where the moment frame is proportioned such that the panel zones are weaker than the beams, the quasi-shear band may start with yielding in the panel zones of the intermediate stories rather than at the ends of the beams. However, shear yielding of panel zones is quite a stable mode of deformation (note that the material model for panel shear stress-strain behavior in FRAME3D has no upper limit on the shear strain). Well before some form of instability sets in the panel zone region, there will typically be sufficient moment build-up in the beams to cause yielding. Since deterioration can be much faster in beams, the ultimate collapse mechanism will be due to excessive plastic rotations in the beams of the intermediate stories of the quasi-shear band.

In an N_s-story building, N_s 1-story quasi-shear bands are theoretically possible, (N_s-1) 2-story QSBs are possible, and so on. Thus, there are a total of $N_s(N_s+1)/2$ possible QSBs in either principal direction of the building as shown in Figure 4.3. During strong shaking one or more of these quasi-shear bands can

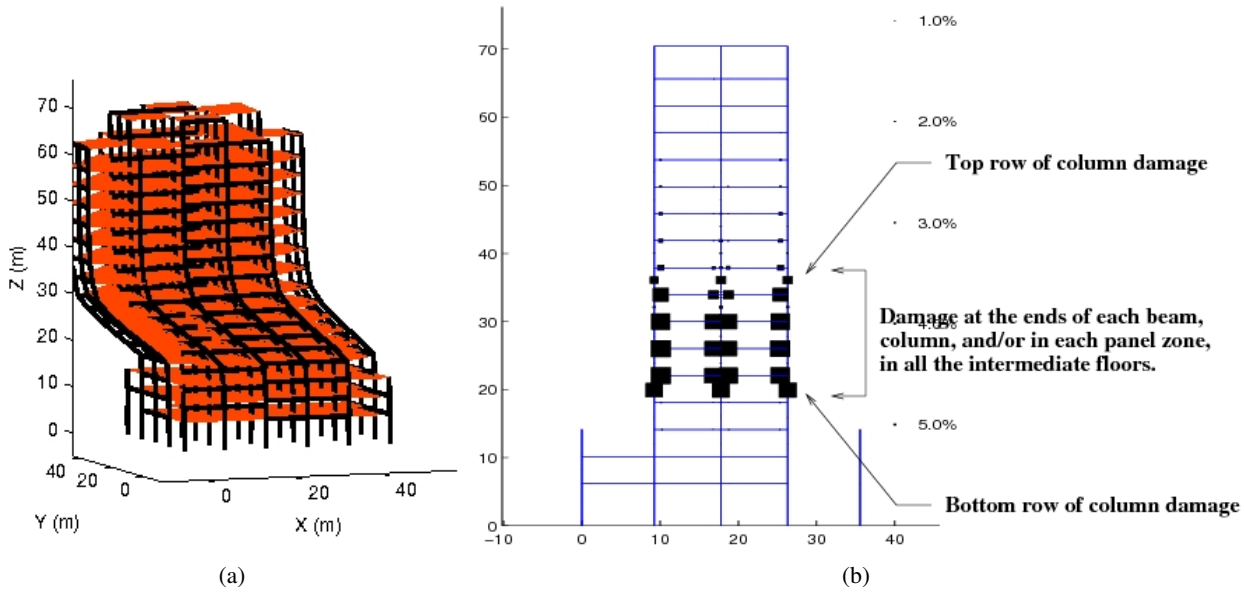

(a) (b)

Figure 4.1: Anatomy of a collapse mechanism: (a) Typical mechanism of collapse from the simulation of the existing building subjected to strong ground motion (synthetic 3-component motion at Northridge from an 1857-like $M_w = 7.9$ earthquake on the San Andreas fault). Deformations are scaled by a factor of 5 for visual clarity. (b) Plastic rotations in one of the frames oriented in the direction of sidesway collapse. The square markers indicate plastic rotations at the ends of beams and columns, with the size proportional to the amount of plastic deformation.

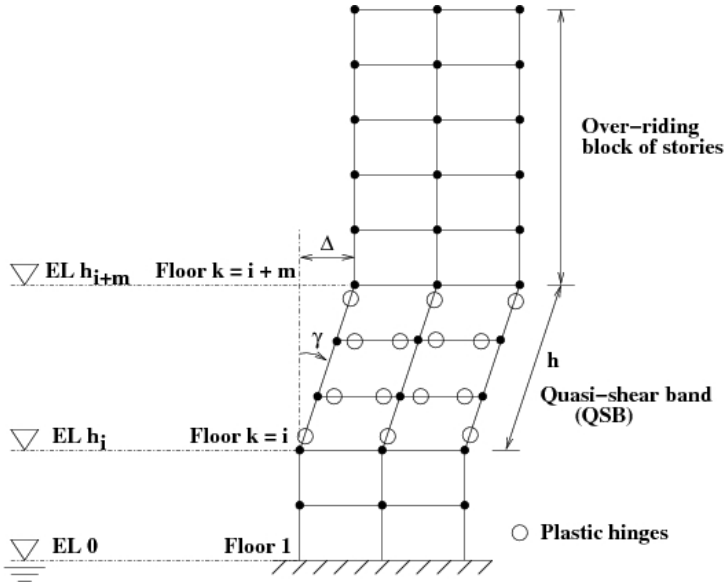

Figure 4.2: Simplified schematic of a sidesway-collapse mechanism.

form. It is reasonable to postulate that the most prominent of these bands, the "primary" quasi-shear band, will evolve into a sidesway collapse mechanism. Then, in order to help establish the relationship between the collapse mechanism of the buildings considered in this study and the ground motion parameters, T,

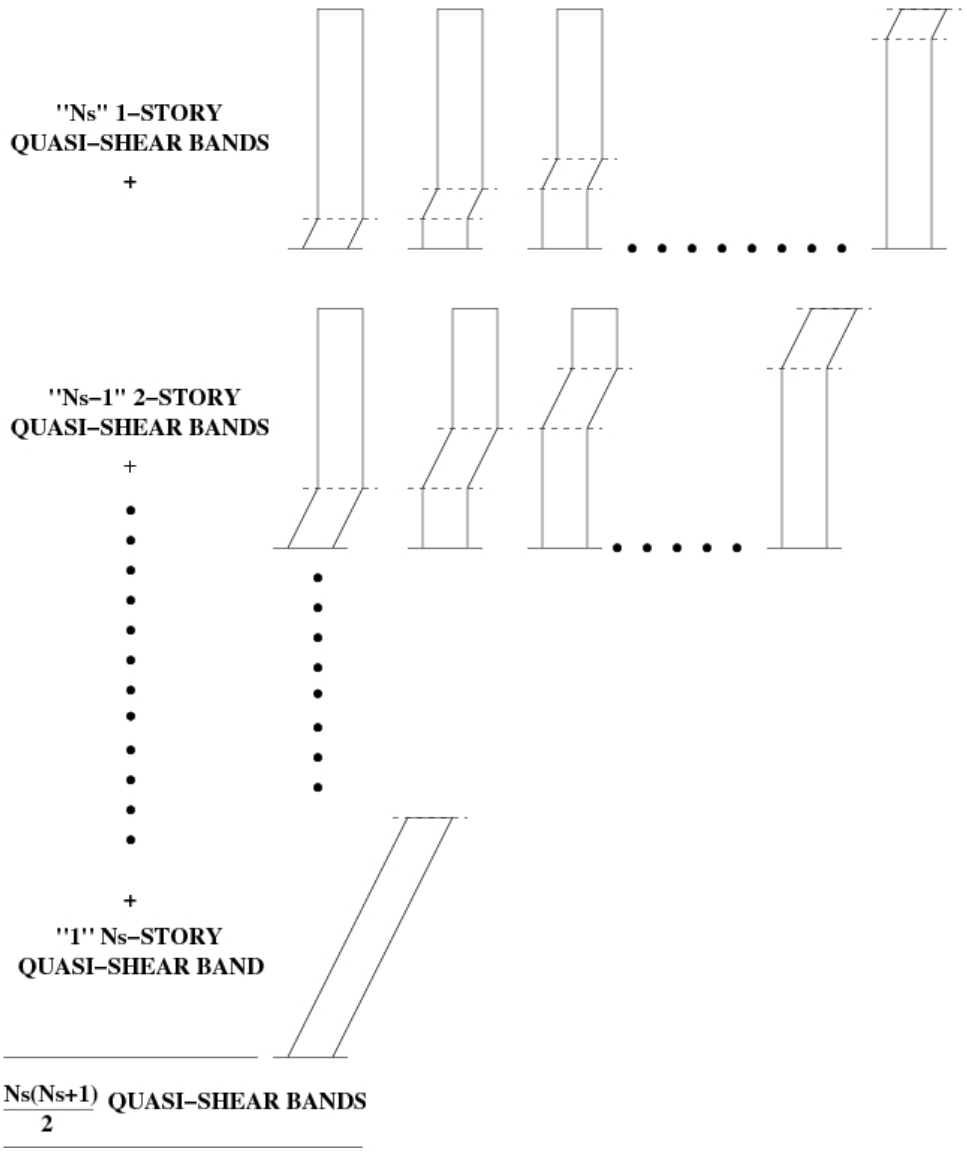

Figure 4.3: All possible quasi-shear bands (and hence sidesway-collapse mechanisms) for a building with N_s stories in one principal direction.

PGV, and N, the first step would be to identify the primary quasi-shear band in each of the analysis cases archived in the database of Chapter 3. This is accomplished by attributing and computing a damage index for each of the $N_s(N_s+1)/2$ possible quasi-shear bands. The band with the largest damage index is the "primary" quasi-shear band. This damage index is an aggregate of the damage indices (extent of plasticity) of all the components comprising the band. The following steps are involved in determining the quasi-shear band damage index:

1. **Component Damage Index:**

   (a) Fibers in the nonlinear end segments of elastofiber elements: The fiber damage index is the fiber plastic strain (ductility demand), $\epsilon - \epsilon_y$, normalized by the plastic strain to fiber rupture or

fracture, whichever is smaller ($min[\epsilon_r, \epsilon_{frac}] - \epsilon_y$). ϵ is the maximum fiber strain, ϵ_y is the fiber yield strain, ϵ_r is the fiber rupture strain, and ϵ_{frac} is the fiber fracture strain.

(b) Nonlinear end segments of elastofiber elements: The segment damage index is the average fiber damage index for the 20 fibers comprising the segment.

(c) Panel zone damage index: The panel zone damage index is the plastic shear strain, $\gamma - \gamma_y$, normalized by the plastic shear strain at ultimate shear stress, $\gamma_u - \gamma_y$. γ is the peak shear strain in panel, γ_y is the panel yield strain, and γ_u is the panel strain at ultimate shear stress.

2. **Joint Damage Index:** The component damage indices are used as is or combined into a joint damage index defined as the root-mean-square of the damage indices of all elements framing into the joint:

$$D_{joint,j} = \left[\frac{1}{N_{beam} + N_{col} + N_{pz}} \left(\sum_{i=1}^{N_{beam}} (D_{ef,i})^2 + \sum_{i=1}^{N_{col}} (D_{ef,i})^2 + \sum_{i=1}^{N_{pz}} (D_{pz,i})^2 \right) \right]^{\frac{1}{2}} \tag{4.1}$$

where $D_{joint,j}$ is the damage index of any joint j, $D_{ef,i}$ is the damage index of the i^{th} elastofiber element, $D_{pz,i}$ is the damage index of the i^{th} panel-zone element, N_{beam} is the number of beams framing into the joint in the direction of shear deformation of the quasi-shear band, N_{col} is the number of columns framing into the joint (typically one or two), and N_{pz} is the number of panel zones (typically one) at the joint in the direction of shear deformation of the QSB.

3. **Floor Damage Index (FDI):**

(a) The floor damage index of the top floor of the QSB is the average of the damage indices of the top nonlinear segments in all columns of the top story of the band. Similarly, the FDI of the bottom floor of the QSB is the average of the damage indices of the bottom nonlinear segments in all columns of the bottom story of the band.

(b) The FDI for each intermediate floor is the average of the joint damage indices of all joints on the floor.

4. **Quasi-Shear Band Damage Index:** The damage index for each quasi-shear band is the average of the FDIs of all floors within the band. The band with the largest damage index is the primary QSB in a given response history analysis case. If the extent of plasticity is severe enough to render this band unstable, it will evolve into a sidesway collapse mechanism driven by gravity to progressive global collapse of the structure.

Shown in Figure 4.4(a) is the variation of the three floor damage indices (average of column top damage, average of column bottom damage, and average of joint damage) over the height of the existing building (perfect connections) when subjected to strong 3-component ground motion simulated at a southern California site in the ShakeOut scenario earthquake [24]. Also shown is the primary quasi-shear band (red dashed line) as identified using the approach outlined above. It is clear from the actual distribution of frame plastic

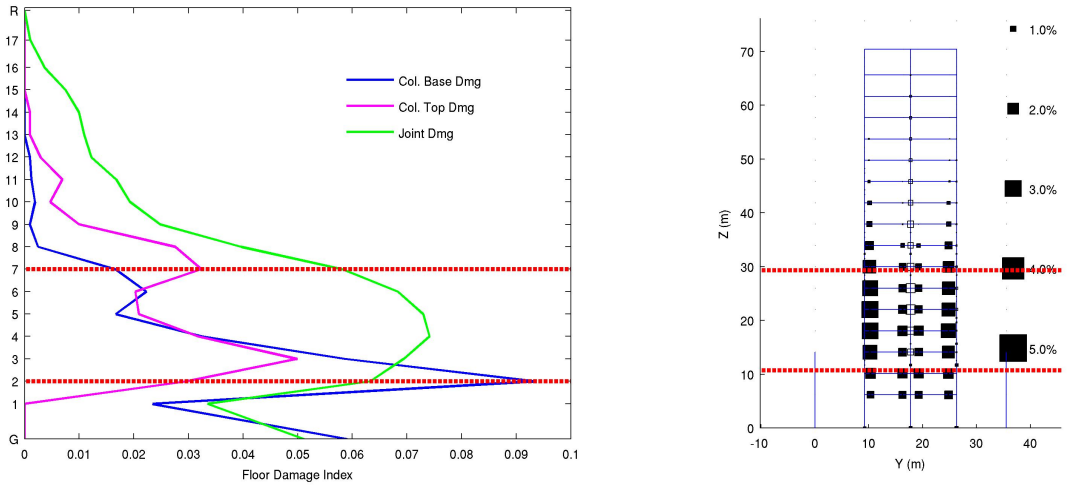

(a) (b)

Figure 4.4: (a) Identification of the primary quasi-shear band (QSB). (b) Comparison of the identified "primary QSB" against the actual distribution of plastic hinges in the existing building (perfect connections) when subjected to strong 3-component ground motion simulated at a southern California site in the ShakeOut scenario earthquake. Plastic rotation is proportional to size of square.

hinging, shown in Figure 4.4(b), that there is uniformly heavy yielding throughout the primary QSB. While there is some beam yielding above and below this band, collapse is not likely to extend beyond the stories within the selected band because significant column yielding has occurred only at the upper and lower limits of this band and not outside. This can be seen from Figure 4.4(a) which shows that the top and bottom of the primary QSB correspond to local maxima of the floor damage indices computed using the column top and bottom damage, respectively.

The aforementioned approach is used to identify the primary quasi-shear band in each analysis case for the four building models within the parametric study using the idealized ground motion waveforms presented in the last chapter. The results for the existing building (perfect connections) under 1-cycle X-direction excitation are shown in Figure 4.5. Shown there are bars indicating the location and extent of the primary quasi-shear band over the height of the building as a function of the excitation period T, for each PGV intensity. The fill color represents the peak transient IDR.

The following observations can be made:

1. There is no column damage when the pulse amplitude is less than or equal to 0.5 m/s for any pulse period in the range 0.5-6.0s. Hence, no quasi-shear band has formed and none could be identified in these cases.

2. For a given pulse in the relatively low amplitude regime (0.125-1.375 m/s), say with amplitude 1.25 m/s, the primary QSB is located at the top of the building for small pulse period and migrates down with increasing pulse period. This downward migration stops at the third or fourth floor for pulse periods longer than about the fundamental period of the building, with the location of the band becoming

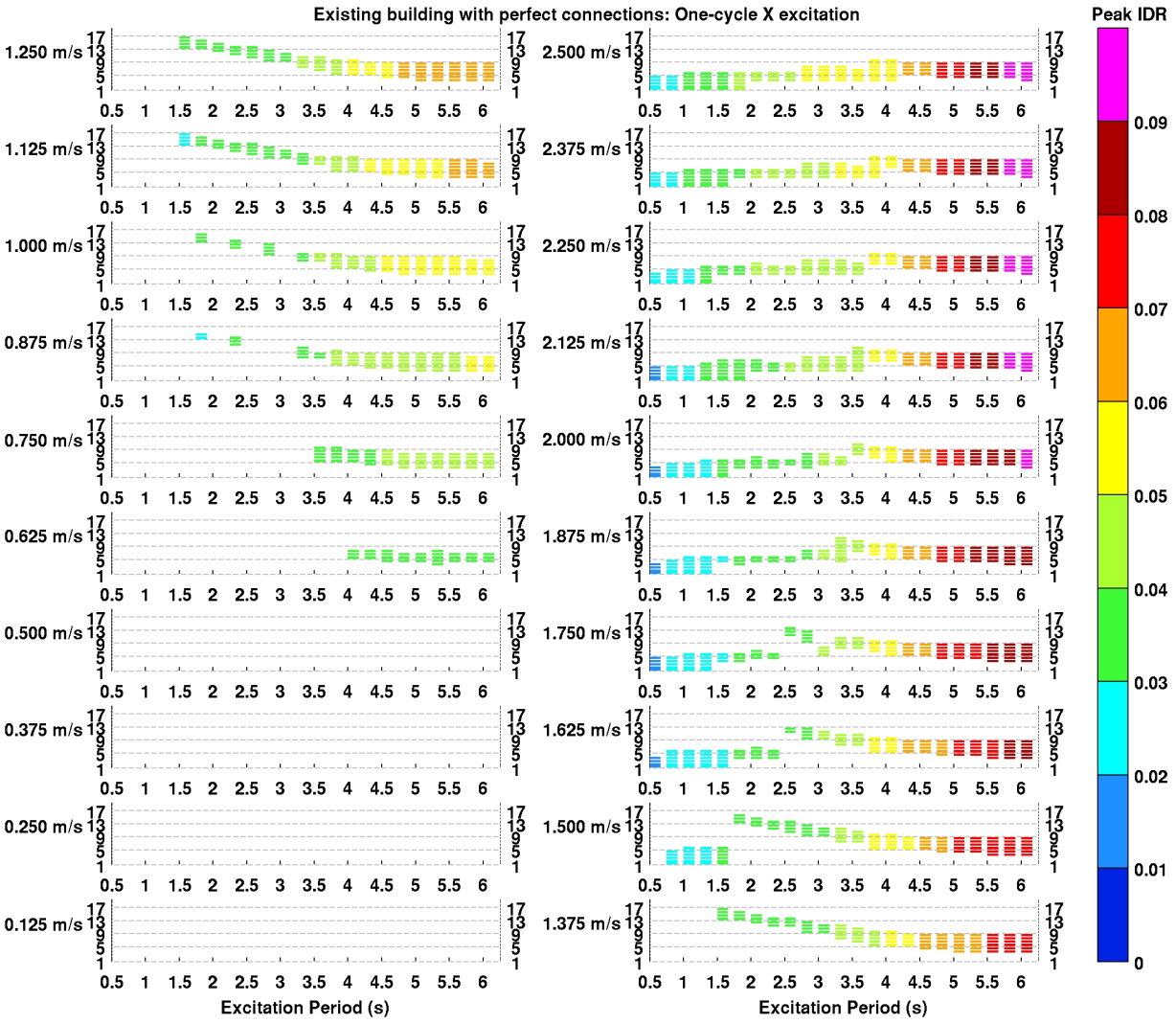

Figure 4.5: Primary quasi-shear band in the existing building (perfect connections) subjected to idealized single-cycle X direction excitation. Pulse period T varies from 0.5 seconds to 6 seconds; peak ground velocity PGV varies from 0.125 m/s to 2.5 m/s.

invariant with ground excitation period.

3. For a given pulse in the relatively large amplitude regime (1.875-2.5 m/s), say with amplitude 2.00 m/s, the primary quasi-shear band is located at the bottom of the building for small pulse period and migrates up with increasing pulse period until it coalesces nominally to the same invariant QSB location as for pulses in the low-amplitude, long-period excitation regime discussed above.

4. For a given pulse in the intermediate amplitude regime (1.50-1.75 m/s), say with amplitude 1.50 m/s, the primary QSB is located at the bottom stories for short periods, at the top stories for intermediate periods ($<$ building fundamental period) and migrating down with increasing period. The migration once again stops (when the pulse period roughly equals the fundamental period of the building) nominally at the same invariant QSB location as was observed for the low-amplitude and large-amplitude,

long period excitation regimes.

5. Figures similar to Figure 4.5 are given in Appendices A through D for all four building models (existing building with susceptible connections under X excitation, existing building with perfect connections under X and Y excitation, and redesigned building with perfect connections under X excitation) subjected to 1–5 cycle excitation. The observations 1–4 more or less hold true for all cases. There are subtle differences from one case to the next. However, under long period excitation in both the low amplitude and high amplitude regimes, the convergence of the primary quasi-shear band to one or two building-specific sets of stories holds true in majority of the cases. The results for multi-cycle excitation are quite similar to those under single-cycle excitation, except that the PGV thresholds demarcating low-, moderate-, and high-intensity ground motions are progressively lower with increasing number of cycles. The excitation period thresholds for collapse are lower as well. But, collapse continues to occur nominally in the same set of stories under multi-cycle excitation as for the single-cycle excitation (Figures A.11(b), A.12(b), A.13(b), A.14(b), A.15(b), B.11(b), B.12(b), B.13(b), B.14(b), B.15(b), C.11(b), C.12(b), C.13(b), C.14(b), C.15(b), D.11(b), D.12(b), D.13(b), D.14(b), D.15(b)).

6. Figures 4.6 and 4.7 show the primary quasi-shear band in the existing building (susceptible connections) and the redesigned building model (perfect connections), respectively, under 1-, 2-, 3-, 4-, 5-, and 10-cycle X excitation, re-arranged in the order of increasing peak interstory drift ratio (IDR). It is clear that with few exceptions total collapse (peak transient IDR > 0.100) occurs only in cases where the primary quasi-shear band has formed in the set of stories corresponding to the nominally invariant QSB observed in items 1–4 above. This suggests a characteristic mechanism or one or two preferred mechanisms of collapse for each building under all forms of earthquake excitation. For instance, there is a strong preference for collapse to occur between floors 3 and 9, floors 3 and 10, and floors 4 and 10 in the existing building (susceptible connections) under X direction excitation. There is a weaker preference for collapse to occur between floors 5 and 10, and 5 and 11. Thus, there are just five preferred mechanisms out of a total of 153 possible mechanisms . Similarly, there is a strong preference for collapse to occur between floors 3 and 8 in the redesigned building (perfect connections) under X excitation. There is a weak preference for collapse to occur between floors 4 and 9, floors 3 and 9, floors 3 and 6, and floors 3 and 7 (five preferred mechanisms out of $[N_s(N_s+1)/2 = 153]$ possible mechanisms). Note that the preferred collapse mechanisms are spatially clustered together with significant story-overlap. Collapse is restricted to occur in this narrow band of stories.

7. Figures 4.8 and 4.9 show the primary quasi-shear band in the existing building model (perfect connections) under X direction and Y direction excitations, respectively, with 1–5, and 10 cycles, rearranged in the order of increasing peak interstory drift ratio (IDR). The strongly preferred collapse mechanisms under X direction excitation occur between floors 3 and 9, and floors 4 and 9, while the weakly preferred collapse mechanisms occur between floors 3 and 8, and floors 4 and 8 (four preferred mechanisms out of 153 possible mechanisms, all clustered together within a narrow story zone). The strongly preferred collapse mechanisms under Y direction excitation occur between floors 3 and 9, floors 3 and 8, floors 4 and 8, and floors 4 and 9, while there is a weak preference for the

collapse mechanism to form between floors 5 and 9 (five preferred mechanisms out of 153 possible mechanisms, once again clustered together within a narrow story zone).

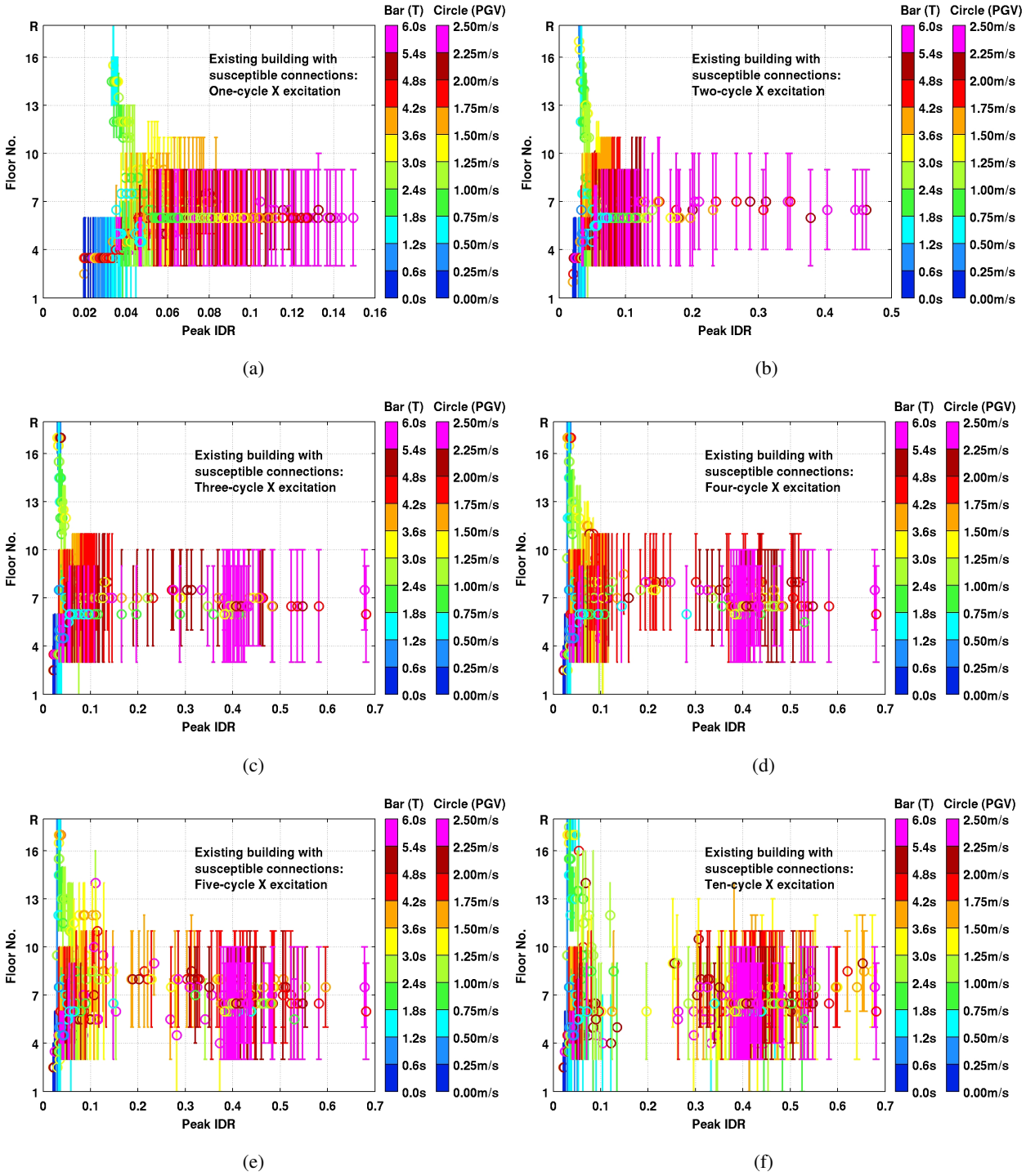

Figure 4.6: The location and extent of the primary quasi-shear band (QSB) plotted against peak transient interstory drift ratio (IDR) in the existing building model (susceptible connections) when subjected to idealized 1-, 2-, 3-, 4-, 5-, and 10-cycle X direction excitation. Pulse periods vary from 0.5s to 6s and amplitudes vary from 0.125 m/s to 2.5 m/s. Ground excitation period T and peak velocity PGV can be identified by the pen color of the bar and the circle, respectively. Note that peak transient IDR excess of 0.075 occurs only under long-period excitation (greater than the fundamental period of the building approximately), and that collapse occurs in a select few mechanisms that are clustered together.

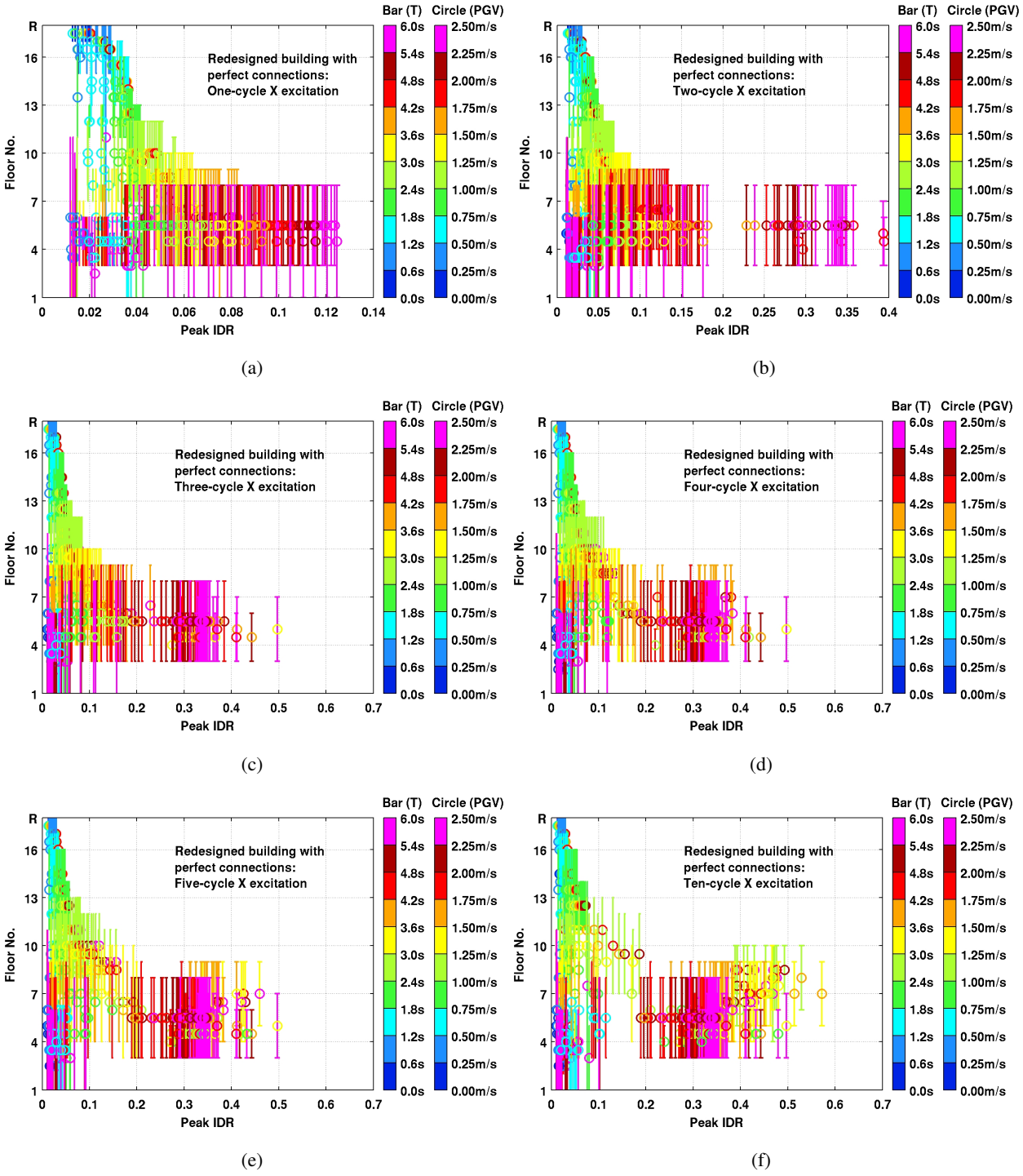

Figure 4.7: The location and extent of the primary quasi-shear band (QSB) plotted against peak transient interstory drift ratio (IDR) in the redesigned building model (perfect connections) when subjected to idealized 1-, 2-, 3-, 4-, 5-, and 10-cycle X direction excitation. Pulse periods vary from 0.5s to 6s and amplitudes vary from 0.125 m/s to 2.5 m/s. Ground excitation period T and peak velocity PGV can be identified by the pen color of the bar and the circle, respectively. Note that peak transient IDR excess of 0.075 occurs only under long-period excitation (greater than the fundamental period of the building approximately), and that collapse occurs in a select few mechanisms that are clustered together.

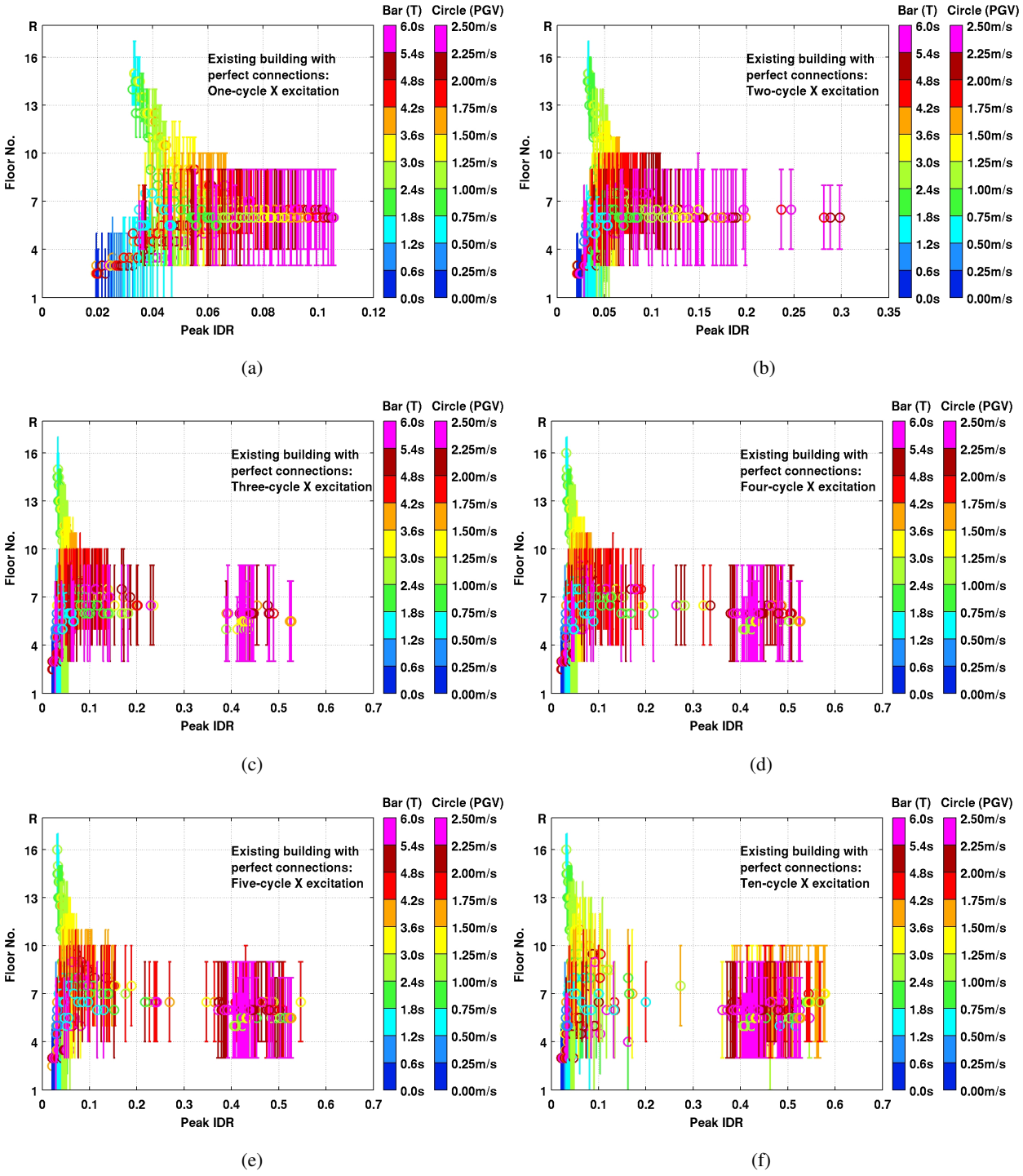

Figure 4.8: The location and extent of the primary quasi-shear band (QSB) plotted against peak transient interstory drift ratio (IDR) in the existing building model (perfect connections) when subjected to idealized 1-, 2-, 3-, 4-, 5-, and 10-cycle X direction excitation. Pulse periods vary from 0.5s to 6s and amplitudes vary from 0.125 m/s to 2.5 m/s. Ground excitation period T and peak velocity PGV can be identified by the pen color of the bar and the circle, respectively. Note that peak transient IDR excess of 0.075 occurs only under long-period excitation (greater than the fundamental period of the building approximately), and that collapse occurs in a select few mechanisms that are clustered together.

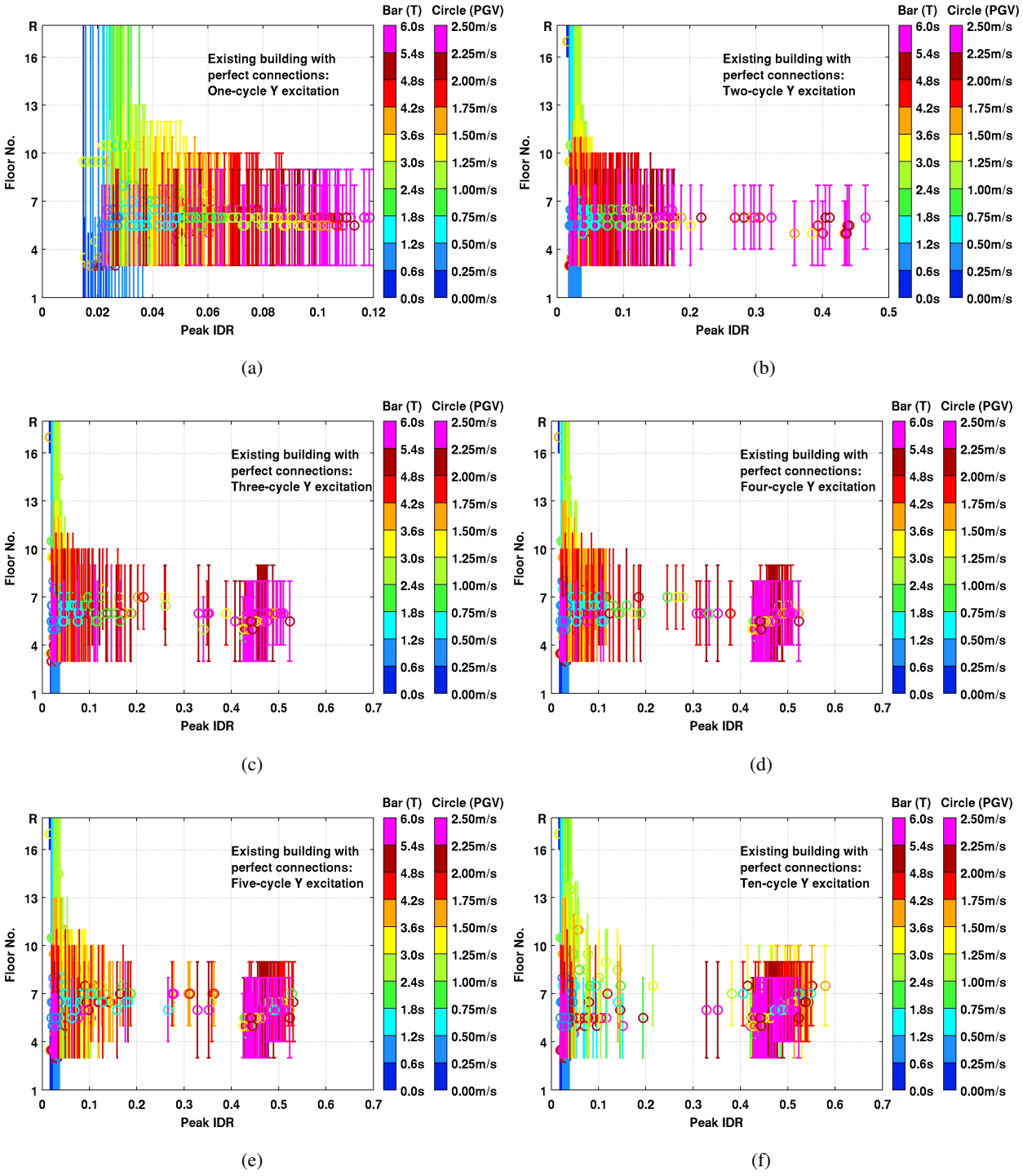

Figure 4.9: The location and extent of the primary quasi-shear band (QSB) plotted against peak transient interstory drift ratio (IDR) in the existing building model (perfect connections) when subjected to idealized 1-, 2-, 3-, 4-, 5-, and 10-cycle Y direction excitation. Pulse periods vary from 0.5s to 6s and amplitudes vary from 0.125 m/s to 2.5 m/s. Ground excitation period T and peak velocity PGV can be identified by the pen color of the bar and the circle, respectively. Note that peak transient IDR excess of 0.075 occurs only under long-period excitation (greater than the fundamental period of the building approximately), and that collapse occurs in a select few mechanisms that are clustered together.

4.1 Understanding quasi-shear band formation through the uniform shear-beam analogy

The distribution of moments in a steel moment frame subjected to lateral loads is such that it produces double curvature in all the columns and beams resulting in shear-racking of the frame [29]. Thus, in an overall sense, shear-beam-like behavior and not cantilever-like behavior dominates moment-frame response. This allows for the drawing of an analogy between steel moment frames excited by earthquake ground motion and a shear wave traveling through a uniform shear-beam [14, 12]. However, three significant differences exist between steel moment frame buildings and uniform shear-beams. First, the buildings are not uniform, there is typically stiffness and strength gradation as well as some mass variation over the height of the structure. Second, gravity is not usually considered in the uniform shear-beam, whereas it plays an important role in the collapse behavior of the building structure by causing second order ($P-\Delta$) effects associated with the self-weight of the structure acting through its deformed configuration under lateral loading. $P-\Delta$ effects, however, simply amplify the 1^{st} order overturning moments caused by the floor plate inertial forces. This amplification becomes perceptible only beyond peak transient IDRs of 0.04 (Figure E.1) and becomes significant beyond peak transient IDRs of 0.08 (evidence is presented in Appendix E). At the peak transient IDR level of 0.08, the primary quasi-shear band has coalesced and become invariant (Figures 4.6–4.9), suggesting that $P-\Delta$ effect has only a minor role to play in the formation of the quasi-shear band. Lastly, steel-frame buildings do exhibit low levels of damping which are not typically present in the uniform shear-beam. Damping has the effect of attenuating the response (which impacts the response to multi-pulse excitation more than single-pulse excitation) and lengthening the apparent period. But the low level of damping inherent in steel structures means that it plays a relatively minor role in the damage localization phenomenon. Thus, the differences in the building response and the analogous shear-beam response, if they exist, are attributable primarily to non-uniformity. The applicability of the uniform shear-beam analogy to these moment frame buildings must be investigated separately in the elastic and inelastic regimes of response. If the analogy holds, it can help explain quasi-shear band formation and its evolution into a sidesway-collapse mechanism.

4.1.1 Elastic response ($PGV < 0.25m/s$)

Consider a vertically standing uniform elastic shear-beam of height H, mass per unit volume ρ and shear modulus G, fixed at one end. The speed at which shear waves propagate through the beam is $C = \sqrt{G/\rho}$. When the fixed base of the beam is subjected to a support motion described by displacement $v_g(t)$, velocity $\dot{v_g}(t)$ and acceleration $\ddot{v_g}(t)$, the resulting shear strain in the beam, $\gamma(y,t)$ is given by

$$\gamma(y,t) = \frac{-\dot{v_g}(t - y/C)}{C} \tag{4.2}$$

which is a disturbance that travels along the height of the beam at the velocity C. The free end of the shear-beam must remain traction-free (zero strain). This causes the upward traveling shear-strain wave to be reflected off the free end with a change in sign. The fixity condition at the base of the beam requires the stress to be doubled in order to maintain continuity of tractions. So a downward traveling strain wave

must be reflected off the base with no change in sign. For the sawtooth-like velocity pulse input motion of Figure 2.1, when the first half of the velocity-proportional shear-strain wave (forward phase) is reflected with a change in sign, it interferes constructively with the upward traveling second half (reverse phase) of the incident wave. This results in a doubling of the shear strain at a distance $\lambda/4$ from the top of the beam, where $\lambda = CT$ is the wave-length. This is illustrated in Figure 4.10. Since the fundamental period of oscillation of the beam is given by $T_1 = 4H/C$, this implies that the location of maximum strain (measured from the top of the beam), given by HT/T_1, is proportional to the ratio of the pulse period to the fundamental period of the beam. The downward traveling forward phase then reflects off the base with no change in sign, once again causing strain doubling, but this time at the base of the beam. This phenomenon is numerically demonstrated by subjecting the base of a simple discretized uniform shear-beam model to the saw-tooth pulse of Figure 2.1 with a period of 1s. The model consists of 400 shear spring-mass elements (Figure 4.11). The mass m and the spring elastic shear stiffness coefficient k_1 are chosen to result in a fundamental period T_1 of 4s for the shear-beam model. First, the springs are modeled to remain elastic. The snapshots of strain distribution in the model at time intervals of 0.1s are shown in Figure 4.12(a). For comparison, the redesigned building model with perfect connections is subjected to the same pulse in the X direction. The period of the pulse is roughly one-quarter of the building's X-translation fundamental period of 4.06s, while its amplitude is small enough to keep the building elastic. The traveling wave is imaged through snapshots of the inter-story drift ratio at various times (Figure 4.12(b)). The IDR, being the difference in the displacements of the top and bottom of a given story normalized by its height, is approximately analogous to the shear strain observed in the uniform shear-beam. The IDR distribution tracks the strain in the shear-beam model very closely. The subtle differences in the locations of the peaks can be attributed to the non-uniformity of the steel building. From this example it is clear that the uniform shear-beam analogy to tall steel moment frame buildings holds quite well in the elastic regime of structural response.

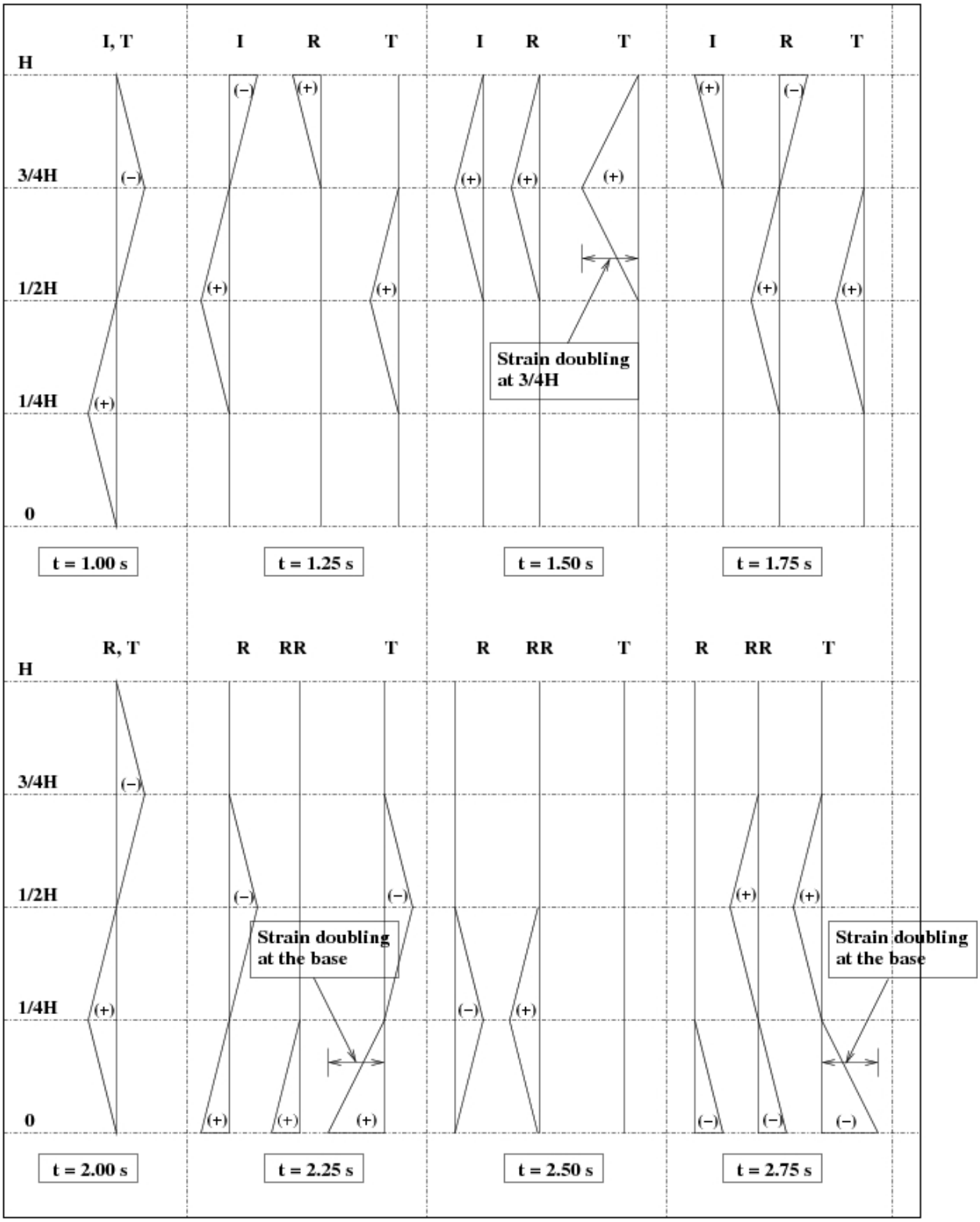

Figure 4.10: Example of strain-doubling in a shear-beam. The incident wave 'I' reflects off the free end of the beam as the reflected wave 'R'. Constructive interference of the 'I' and 'R' waves results in the total wave 'T' with strain doubling at 1/4 H from the free end. Strain-doubling also occurs at the base due to reflection off the fixed end.

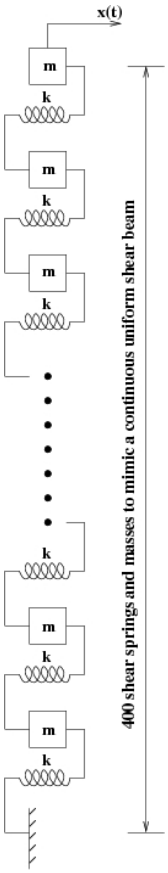

Figure 4.11: Schematic representation of the discretized uniform shear-beam model.

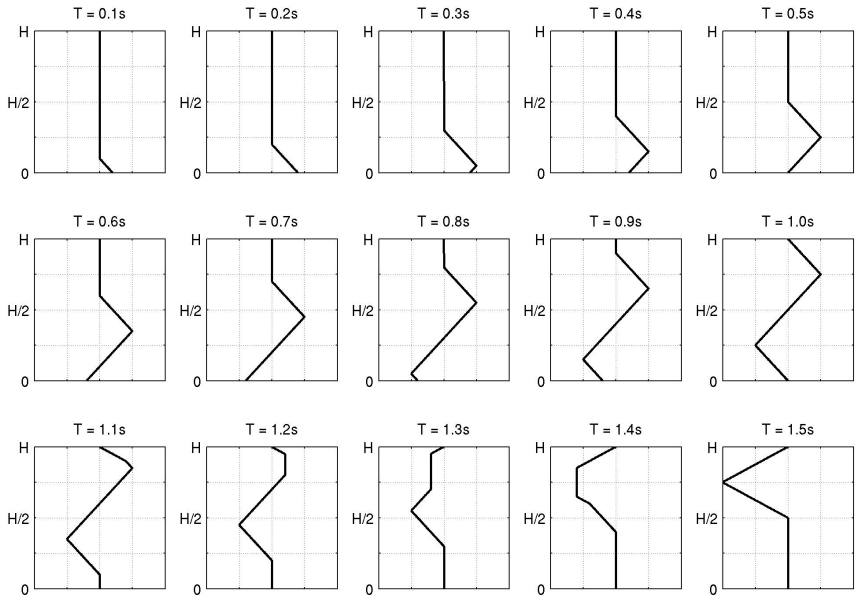

(a)

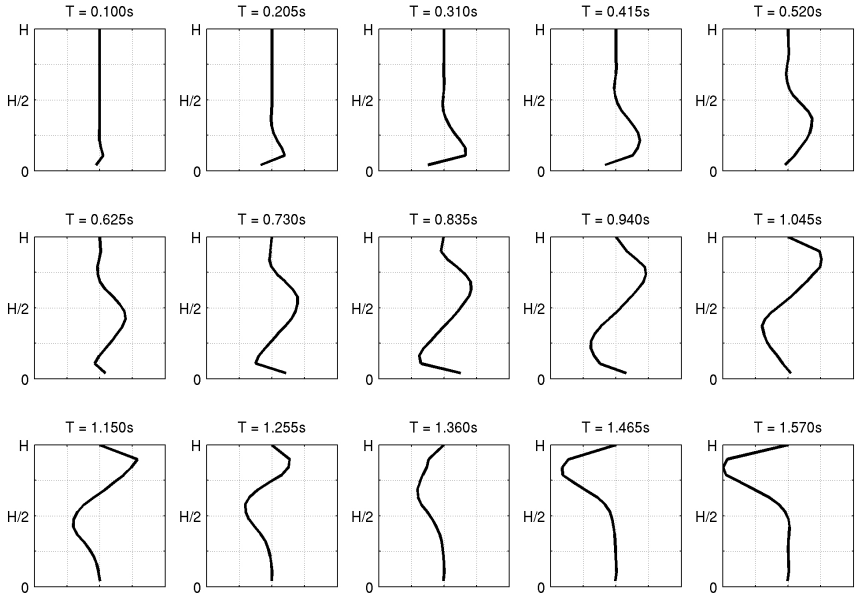

(b)

Figure 4.12: Comparison of (a) the strain response of an elastic discretized uniform shear-beam model to an incident pulse with a period equal to one-quarter of the fundamental period of the beam; and (b) the transient interstory drift ratio (IDR) response of the redesigned building to a low-intensity incident pulse with a period approximately equal to one-quarter of the fundamental period of the building. The pulse intensity is chosen such that it causes no yielding in the building. The evolution of the location of peak strain in the two cases are in good agreement.

4.1.2 Inelastic case ($PGV \geq 0.25m/s$)

If the shear-beam were to yield, the greatest amount of yielding can be expected to occur at locations where strain doubling occurs in the elastic case. To confirm this, the base of the discretized uniform shear-beam model is excited by pulses of the type shown in Figure 2.1 with periods 1 to 5s. Here, the spring restoring force is modeled in a nonlinear fashion and is hysteretic. The backbone curve is taken to be bilinear. The hysteretic rules are governed by an extended Masing hypothesis [15]. The post-yield stiffness coefficient k_2 is chosen to be 10% of the elastic stiffness coefficient k_1. Two possibilities exist for the occurrence of yielding: (a) the intensity of input motion is moderate enough to not yield the structure on its way up. But upon reflection off the roof, it causes yielding due to constructive interference of the reflected forward phase of the pulse and the upward traveling reverse phase; and (b) the input motion is strong enough to yield the structure on its way up.

Moderate intensity ($0.25m/s \leq PGV < 1.5m/s$) excitation: Yielding after reflection off the roof

Figure 4.13 shows the accumulated plastic strain in the discretized shear-beam resulting from 1-cycle pulses with periods of 1 to 5 seconds. The yield stress of the springs is chosen such that the pulse with PGV intensity of 1.5m/s does not yield the beam on its way up. Peak plastic strain occurs at $H/4$ from the free end of the shear-beam when excited by the 1s pulse (Figure 4.13(a)), at $H/2$ from the free end under the 2s pulse (Figure 4.13(b)), at $3H/4$ from the free end for the 3s pulse (Figure 4.13(c)), and at H from the free-end for the 4s pulse (Figure 4.13(d)), consistent with the location of the strain-doubling in the elastic case (HT/T_1 from the free end). For the 5s pulse with wavelength $5H$, strain doubling does not occur in the elastic case, but peak strain still occurs at the base when the incident part of the pulse entering the shear-beam interacts positively with the reflected part of the pulse arriving from the free-end of the model. In the nonlinear case, greatest yielding can be expected to occur at the base, and indeed this is the case as evident from the map of the accumulated plastic strain shown in Figure 4.13(e).

Figure 4.14 shows the distribution of plastic rotations in the beams, columns, and joints of the existing building (perfect connections), when subjected to 0.75m/s pulses with periods 1s-4s in the X direction. The pulse intensity is chosen such that it does not yield the building on its way up. Recall that the X direction fundamental period of the building is 4.52s. Overlaid on the plastic rotation maps are the theoretical locations of strain doubling under the elastic uniform shear-beam assumption (dashed red lines). Whereas the location of peak plastic rotation accumulation in the nonlinear uniform shear-beam coincided with the location of strain-doubling in the elastic uniform shear-beam, this is not true for the case of the building as a result of its non-uniformity. The yield localization region does migrate down from the top of the building with increasing period, but the migration slows down and gets arrested nominally between floors 3 and 9. This is unlike the corresponding inelastic uniform shear-beam where the peak strain continues to migrate to the very bottom. Going from the top of the building to the bottom, there is a gradual increase in the strength and stiffness of the structure. The stiffness of the structure affects only the speed of the traveling wave and does not affect the location of greatest yielding. However, the increased strength at the bottom of the structure does not allow yielding to permeate into those stories. Greatest yielding occurs a few stories above the base where the strength of the structure is low enough, yet there is sufficient, if not perfect, constructive

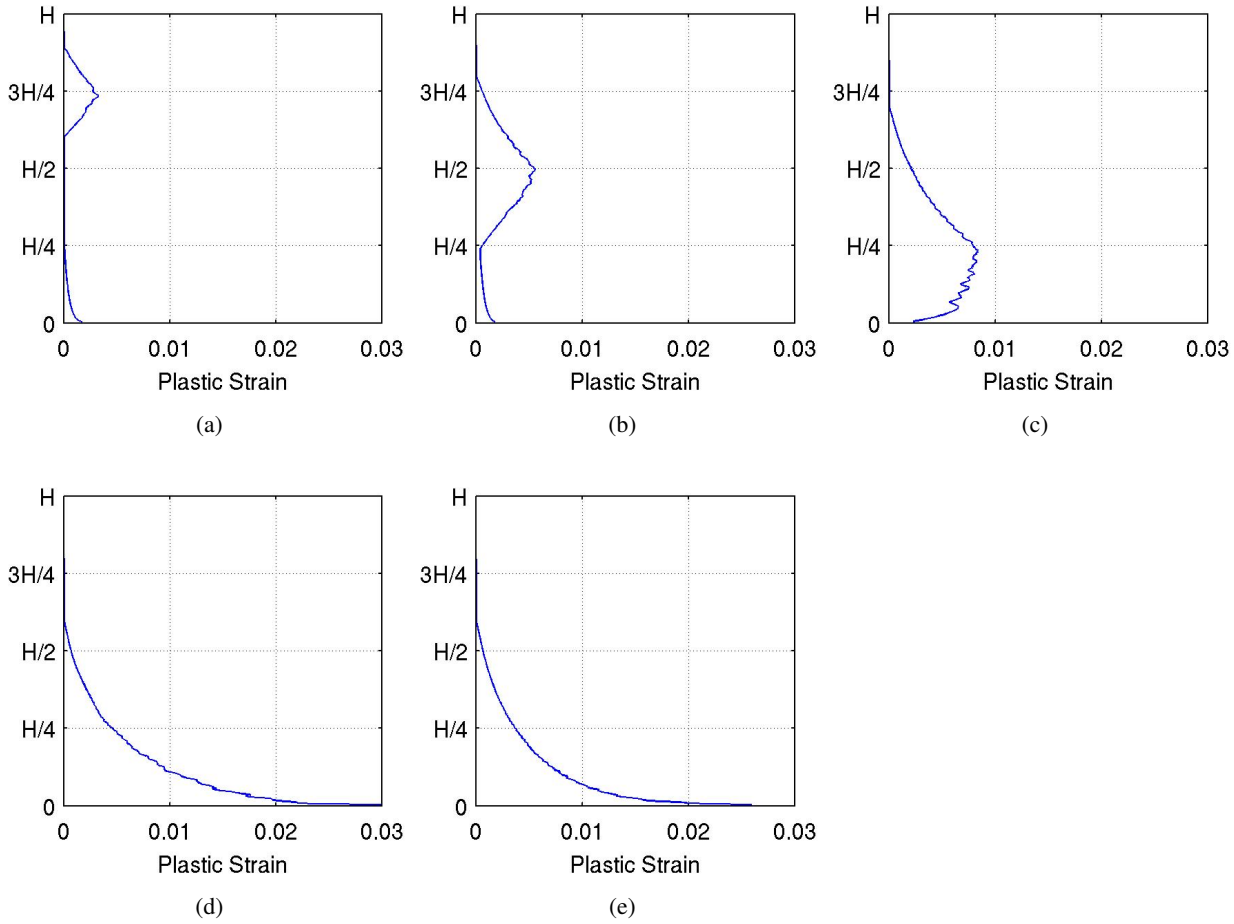

Figure 4.13: Accumulated plastic strain over the height of the discretized uniform shear-beam when subjected to 1-cycle velocity pulses with peak velocity of 1.5 m/s and periods varying from 1s-5s. Peak plastic strain occurs at a distance of $H/4$, $H/2$, $3H/4$, and H from the free end under excitation by pulses with periods 1s, 2s, 3s, and 4s, respectively. These match with the theoretically exact locations of strain-doubling in a uniform elastic shear beam due to propagating shear waves. For the 5s pulse loading, strain-doubling never occurs in the elastic beam, but the peak strain does occur at the fixed end. Peak plastic strain occurs at the fixed end in the nonlinear case as well.

interference of the incident and reflected waves. The long wavelengths at these long periods ensure that the superposition is fairly positive and peak strain is not that far off from the maximum possible strain from the uniform shear-beam analogy. This explains why the downward migration of the quasi-shear band with increasing T is arrested a few stories from the base of the building in Figure 4.14 as well as the parametric analysis presented in Chapter 3.

Under moderate PGV levels, the primary quasi-shear band will evolve into a collapse mechanism if and only if the input energy of excitation is large enough. It was shown at the end of the last chapter that at moderate PGV levels, only long-period motions have the ability to impart enough energy to these tall buildings to induce collapse-level responses. From the above analysis, under these long-period motions, the primary quasi-shear band must form in the vicinity of the stories where the downward migration of QSBs

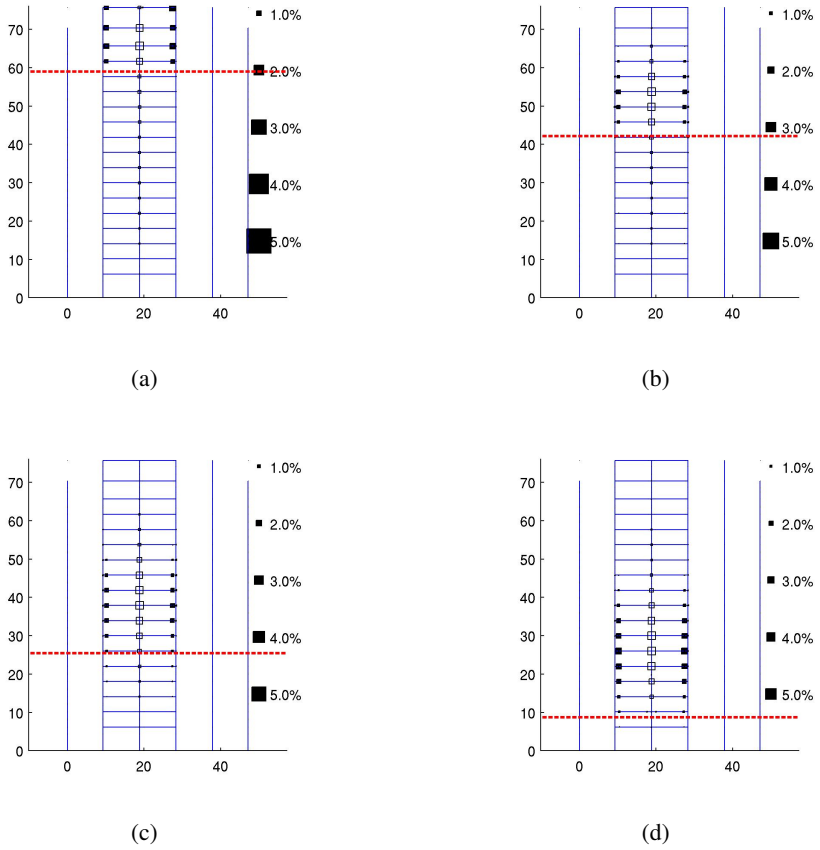

Figure 4.14: Plastic hinge rotations in the existing building (perfect connections) resulting from single-cycle ($PGV = 0.75m/s$) X-direction excitation with periods of (a) 1s, (b) 2s, (c) 3s, and (d) 4s. The dashed lines indicate the predicted location for the peak shearing force in an elastic shear-beam and based on Figure 4.13, the peak strain in an inelastic shear-beam with the same fundamental period as the building model.

is arrested. It is thus in this special region that collapse can occur. The implication of this finding is that there may be a small set of preferred mechanisms of collapse, that are clustered together, under moderate intensity excitations.

High intensity ($PGV \geq 1.5m/s$) excitation: Yielding on the way up

If the incident pulse has a large enough amplitude relative to the yield strength of various parts of the structure it may cause yielding to occur in the building on its way up. To demonstrate this, the responses of the existing building model (perfect connections) under two single-cycle waveforms with identical period ($T = 2.25s$), but different PGVs (0.5m/s and 1.5m/s) are compared. Shown in Figure 4.15 is the strain of a fiber in a beam at each floor of the model for the two cases. If fiber has not yielded, its response is shown using a dashed line-style. Once the fiber yields, the line-style is changed to solid. It is quite clear that under the moderate level excitation of 0.5m/s the fiber yields only after the wave reflects off the roof. On the other hand, the 1.5m/s pulse is strong enough to yield the fibers on its way up. The plastic strain is

not greatest at the base, but between floors 3 and 9 for the existing building. This is a direct consequence of the non-uniformity of the strength of the building over its height. The strength of the building drops as the pulse travels up the building. However, inertial forces drop as well, as a result of fewer stories above contributing to the mass. There exists a narrow band of stories with an optimal combination of low-enough strength and high-enough inertia where peak yielding occurs and the primary quasi-shear band forms. This optimal region is nominally between floors 3 and 9 in the existing building model, identical to the location of the preferred collapse mechanism under moderate intensity excitation.

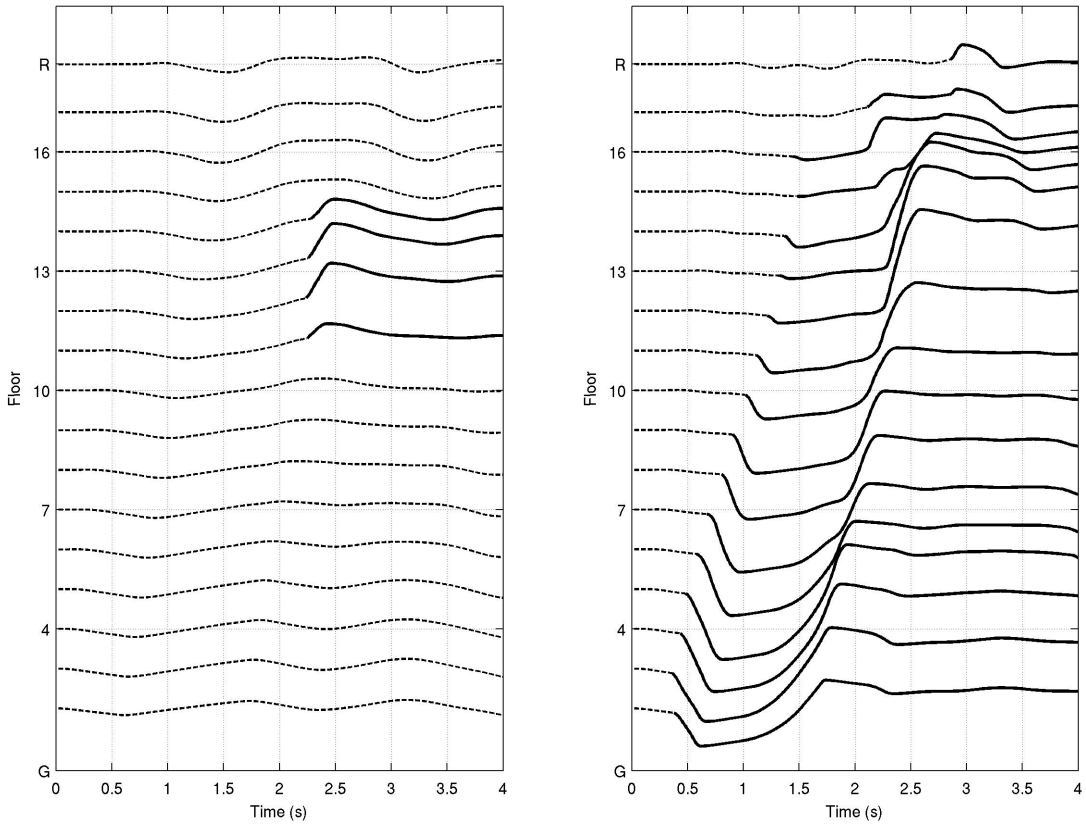

Figure 4.15: Strain of a fiber in a beam at each floor of the existing building (perfect connections) for an incident pulse with a period of 2.25s and amplitudes of (a) 0.5 m/s and (b) 1.5 m/s. The dashed lines indicate pre-yield response, the heavy solid lines indicate post-yield response (if any).

After yielding the structure on its way up, the pulse gets reflected off the roof and the reflected phase of the pulse constructively interferes with the incident phase to produce yielding in the upper stories. The post-reflection yielding in this case occurs in the upper stories because the pulse-period (2.25s) is not long enough relative to the fundamental period of the building in the X direction (4.52s). Thus, under intense, but short-period motions, two distinct quasi-shear bands form in the structure, one in the lower stories and

the other in the upper stories. But yielding is not great enough at either locations to cause collapse since the input excitation energy is not large enough. For high-intensity motions to cause collapse, the period of excitation does not need to be as long as for moderate-intensity motions. However, it still needs to be sizable enough relative to the fundamental period of structure. If not, the input energy of excitation will not be large enough as shown in the previous chapter. As the period of the incident pulse is increased, the post-reflection quasi-shear band converges toward the pre-reflection quasi-shear band. This can be explained through the uniform shear-beam analogy in the same way as the post-reflection yielding under moderate-intensity loading. If the period of the pulse is long enough, then post-reflection yielding will occur in the same region as the pre-reflection yielding. Thus, under both large-amplitude motion with moderately long periods as well as moderate PGV motion with long periods, there is a propensity for the primary quasi-shear band to form in an optimal set of stories governed by the mass and strength distribution of the building over its height. These are characteristics solely of the structure and not of the ground motion. When T and PGV are large enough, it is this band that evolves into a collapse mechanism. This points to the existence of a "characteristic" collapse mechanism or only a few preferred collapse mechanisms (out of the $\frac{N_s(N_s+1)}{2}$ possible mechanisms) in either principal direction of the building. If multiple preferred collapse mechanisms exist, they would be clustered together with significant story-overlap amongst them.

This explains the occurrence of just 1–5 preferred collapse mechanisms that are clustered together in the simulations of all four models under idealized ground motion waveforms.

4.2 Identifying the characteristic collapse mechanism using the Principle of Virtual Work

If the non-uniformity in strength is the primary reason for the existence of a characteristic collapse mechanism for tall steel moment frame buildings, it must be possible to identify this mechanism using an energy principle such as the Principle of Virtual Work (PVW). The PVW can be applied to each of the $N_s(N_s+1)/2$ possible quasi-shear bands in either principal direction of building (Figure 4.3), at the instant that the QSB has been fully plasticized. Using the notation in Figure 4.2, the PVW for the fully plasticized quasi-shear band that extends from floor i to floor $i+m$, with height $h = h_{i+m} - h_i$, can be written as:

$$\ddot{v}_{cr}^{t}\Delta \sum_{k=i+m}^{N_f} m_k + (h - h\cos\gamma) \sum_{k=i+m}^{N_f} P_k = \sum_{k=i,j=1}^{k=i+m,j=N_j} M_p^{(k,j)}\gamma \tag{4.3}$$

where γ is the plastic rotation at each joint under sidesway or the shear strain in the quasi-shear band, $\Delta = h\sin\gamma$, $N_f = N_s + 1$ is the number of floors in the building, N_j is the number of joints in each floor, P_k and m_k are the weight and mass of the k^{th} floor, respectively, and $\ddot{v}_{cr}^{t}$ is the critical absolute acceleration of the over-riding block above the quasi-shear band that fully plasticizes the band. For $k = i$ (the bottom floor of the quasi-shear band) and $k = i + m$ (the top floor of the QSB), $M_p^{k,j}$ refers to the column plastic moment capacity (suitably reduced by the factor $\left[1 - \frac{P_{col}}{P_{col,y}}\right]$ to account for the column axial compressive load P_{col}; $P_{col,y}$ is the column axial yield force). For the joints on the intermediate stories, $M_p^{k,j}$ refers to the minimum of (a) the column plastic moment capacity in the excitation direction, (b) the sum of the plastic moment capacities of the beams framing into the joint in the excitation direction, and (c) the panel zone plastic moment capacity.

For small γ (a reasonable approximation for collapse initiation), Eq. 4.3 reduces to:

$$\ddot{v}_{cr}^{t}h \sum_{k=i+m}^{N_f} m_k = \sum_{k=i,j=1}^{k=i+m,j=N_j} M_p^{(k,j)} \tag{4.4}$$

and the critical acceleration of the overriding block at which the quasi-shear band fully plasticizes is given by:

$$\ddot{v}_{cr}^{t} = \frac{\sum_{k=i,j=1}^{k=i+m,j=N_j} M_p^{(k,j)}}{h \sum_{k=i+m}^{N_f} m_k} \tag{4.5}$$

$$= g \frac{\sum_{k=i,j=1}^{k=i+m,j=N_j} M_p^{(k,j)}}{h \sum_{k=i+m}^{N_f} P_k} \tag{4.6}$$

where g is the acceleration due to gravity. From plastic analysis principles, the quasi-shear band that becomes unstable (completely plasticizes) at the lowest acceleration of the over-riding block is the characteristic mechanism of collapse. Note that since this approach does not account for fracture, it will predict the same collapse mechanism for buildings with susceptible connections and perfect connections alike. Also, note that the inertial forces from the floors within the quasi-shear band are neglected in the above formulation. If these forces are included, the relative and absolute accelerations of the over-riding block must be treated separately, breaking down the simplicity of the solution. The following additional term will appear on the left hand side of Eq. 4.3: $\sum_{k=i}^{k=i+m} m_k \left[\frac{h_i - h_k}{h} \ddot{v}_{cr} + \ddot{v}_g \right] \left(\frac{h_i - h_k}{h} \right) \Delta$, where $\ddot{v}_{cr}$ is the critical relative acceleration of the over-riding block above the quasi-shear band, h_i is the elevation of floor i, and $\ddot{v}_g$ is the ground acceleration.

The critical (in units of "g") acceleration for plasticizing each of the $N_s(N_s+1)/2$ possible quasi-shear bands of the existing and redesigned buildings in the X and Y directions, determined using this approach, are given below in matrix form. The row number represents the bottom floor whereas the column number represents the top floor of the QSB. Thus, the ij^{th} element of the matrix, $\ddot{v}_{cr}^{t,ij}$, corresponds to the quasi-shear band that extends from floor i up to floor j. The penthouse is excluded from this calculation in both buildings.

Existing building, X direction

		Top floor of quasi-shear band																	
		1	2	3	4	5	6	7	8	9	10	11	12	13	14	15	16	17	18
	1	0	0.291	0.220	0.164	0.149	0.138	0.135	0.133	0.137	0.140	0.148	0.158	0.174	0.194	0.228	0.278	0.373	0.581
	2	0	0	0.486	0.250	0.197	0.168	0.157	0.150	0.150	0.150	0.158	0.165	0.181	0.201	0.235	0.284	0.379	0.588
	3	0	0	0	0.327	0.202	0.157	0.142	**0.132**	**0.131**	**0.130**	0.136	0.142	0.156	0.172	0.202	0.243	0.326	0.505
	4	0	0	0	0	0.344	0.202	0.166	**0.146**	**0.140**	**0.136**	0.141	0.145	0.158	0.174	0.203	0.243	0.325	0.502
	5	0	0	0	0	0	0.321	0.203	0.161	0.148	**0.139**	**0.142**	0.144	0.156	0.170	0.197	0.236	0.315	0.484
Bottom	6	0	0	0	0	0	0	0.352	0.213	0.176	0.157	0.154	0.154	0.164	0.176	0.203	0.241	0.320	0.489
floor	7	0	0	0	0	0	0	0	0.347	0.222	0.177	0.166	0.160	0.168	0.178	0.204	0.240	0.316	0.481
of	8	0	0	0	0	0	0	0	0	0.387	0.235	0.199	0.181	0.184	0.190	0.214	0.249	0.326	0.492
QSB	9	0	0	0	0	0	0	0	0	0	0.382	0.249	0.204	0.198	0.198	0.219	0.251	0.326	0.487
	10	0	0	0	0	0	0	0	0	0	0	0.435	0.270	0.236	0.223	0.239	0.268	0.343	0.506
	11	0	0	0	0	0	0	0	0	0	0	0	0.439	0.295	0.251	0.257	0.278	0.350	0.508
	12	0	0	0	0	0	0	0	0	0	0	0	0	0.516	0.333	0.307	0.314	0.382	0.541
	13	0	0	0	0	0	0	0	0	0	0	0	0	0	0.538	0.382	0.351	0.409	0.557
	14	0	0	0	0	0	0	0	0	0	0	0	0	0	0	0.670	0.467	0.489	0.625
	15	0	0	0	0	0	0	0	0	0	0	0	0	0	0	0	0.749	0.606	0.690
	16	0	0	0	0	0	0	0	0	0	0	0	0	0	0	0	0	1.066	0.895
	17	0	0	0	0	0	0	0	0	0	0	0	0	0	0	0	0	0	1.406

Existing building, Y direction

		Top floor of quasi-shear band																	
		1	2	3	4	5	6	7	8	9	10	11	12	13	14	15	16	17	18
	1	0	0.283	0.221	0.170	0.155	0.144	0.141	0.140	0.143	0.147	0.155	0.165	0.182	0.204	0.240	0.293	0.392	0.610
	2	0	0	0.471	0.252	0.200	0.172	0.161	0.154	0.154	0.155	0.162	0.171	0.187	0.208	0.243	0.294	0.393	0.609
	3	0	0	0	0.277	0.177	0.141	0.129	**0.122**	**0.122**	0.123	0.129	0.135	0.149	0.166	0.194	0.236	0.316	0.491
	4	0	0	0	0	0.294	0.179	0.149	**0.133**	**0.130**	0.128	0.133	0.138	0.151	0.167	0.195	0.236	0.315	0.488
	5	0	0	0	0	0	0.277	0.180	0.146	**0.136**	0.130	0.133	0.137	0.149	0.163	0.190	0.229	0.305	0.471
Bottom	6	0	0	0	0	0	0	0.303	0.189	0.159	0.144	0.143	0.144	0.155	0.168	0.194	0.232	0.309	0.474
floor	7	0	0	0	0	0	0	0	0.302	0.197	0.162	0.153	0.150	0.158	0.170	0.195	0.231	0.305	0.466
of	8	0	0	0	0	0	0	0	0	0.335	0.210	0.180	0.166	0.171	0.179	0.203	0.238	0.313	0.474
QSB	9	0	0	0	0	0	0	0	0	0	0.336	0.223	0.186	0.183	0.186	0.207	0.240	0.312	0.470
	10	0	0	0	0	0	0	0	0	0	0	0.381	0.242	0.215	0.207	0.224	0.253	0.326	0.484
	11	0	0	0	0	0	0	0	0	0	0	0	0.384	0.264	0.231	0.239	0.262	0.331	0.484
	12	0	0	0	0	0	0	0	0	0	0	0	0	0.449	0.300	0.280	0.291	0.357	0.510
	13	0	0	0	0	0	0	0	0	0	0	0	0	0	0.476	0.345	0.324	0.380	0.524
	14	0	0	0	0	0	0	0	0	0	0	0	0	0	0	0.589	0.421	0.447	0.579
	15	0	0	0	0	0	0	0	0	0	0	0	0	0	0	0	0.661	0.544	0.632
	16	0	0	0	0	0	0	0	0	0	0	0	0	0	0	0	0	0.931	0.802
	17	0	0	0	0	0	0	0	0	0	0	0	0	0	0	0	0	0	1.233

Redesigned building, X direction

		Top floor of quasi-shear band																	
		1	2	3	4	5	6	7	8	9	10	11	12	13	14	15	16	17	18
	1	0	0.305	0.226	0.158	0.152	0.149	0.153	0.154	0.162	0.173	0.187	0.204	0.227	0.259	0.306	0.374	0.498	0.760
	2	0	0	0.505	0.243	0.203	0.185	0.181	0.177	0.182	0.191	0.204	0.220	0.243	0.275	0.323	0.392	0.520	0.790
	3	0	0	0	0.215	0.160	**0.143**	**0.142**	**0.139**	**0.145**	0.154	0.167	0.181	0.202	0.230	0.272	0.332	0.441	0.672
	4	0	0	0	0	0.232	0.168	0.156	0.146	**0.150**	0.158	0.170	0.183	0.203	0.230	0.272	0.330	0.438	0.666
	5	0	0	0	0	0	0.238	0.181	0.156	0.156	0.162	0.172	0.184	0.204	0.230	0.271	0.327	0.433	0.657
Bottom	6	0	0	0	0	0	0	0.263	0.181	0.169	0.170	0.178	0.188	0.206	0.231	0.271	0.326	0.431	0.651
floor	7	0	0	0	0	0	0	0	0.219	0.176	0.169	0.175	0.182	0.199	0.222	0.261	0.312	0.412	0.621
of	8	0	0	0	0	0	0	0	0	0.247	0.195	0.190	0.191	0.205	0.226	0.263	0.313	0.411	0.617
QSB	9	0	0	0	0	0	0	0	0	0	0.268	0.217	0.203	0.213	0.230	0.266	0.313	0.408	0.609
	10	0	0	0	0	0	0	0	0	0	0	0.308	0.234	0.229	0.240	0.272	0.316	0.409	0.605
	11	0	0	0	0	0	0	0	0	0	0	0	0.294	0.244	0.242	0.269	0.307	0.395	0.581
	12	0	0	0	0	0	0	0	0	0	0	0	0	0.348	0.281	0.293	0.320	0.405	0.586
	13	0	0	0	0	0	0	0	0	0	0	0	0	0	0.374	0.325	0.331	0.407	0.578
	14	0	0	0	0	0	0	0	0	0	0	0	0	0	0	0.468	0.380	0.437	0.596
	15	0	0	0	0	0	0	0	0	0	0	0	0	0	0	0	0.461	0.450	0.578
	16	0	0	0	0	0	0	0	0	0	0	0	0	0	0	0	0	0.655	0.664
	17	0	0	0	0	0	0	0	0	0	0	0	0	0	0	0	0	0	0.893

Redesigned building, Y direction

		Top floor of quasi-shear band																	
		1	2	3	4	5	6	7	8	9	10	11	12	13	14	15	16	17	18
	1	0	0.295	0.224	0.162	0.157	0.156	0.160	0.162	0.171	0.182	0.198	0.215	0.240	0.274	0.325	0.399	0.532	0.814
	2	0	0	0.487	0.243	0.206	0.191	0.187	0.184	0.190	0.200	0.214	0.230	0.255	0.289	0.341	0.416	0.553	0.842
	3	0	0	0	0.235	0.174	0.157	0.155	0.152	0.159	0.168	0.182	0.196	0.219	0.250	0.296	0.362	0.482	0.736
	4	0	0	0	0	0.247	0.182	0.168	0.158	0.162	0.171	0.184	0.197	0.219	0.249	0.294	0.359	0.477	0.726
	5	0	0	0	0	0	0.252	0.192	0.167	0.167	0.173	0.185	0.196	0.217	0.246	0.291	0.354	0.469	0.713
Bottom	6	0	0	0	0	0	0	0.277	0.194	0.181	0.182	0.191	0.200	0.220	0.248	0.291	0.353	0.467	0.707
floor	7	0	0	0	0	0	0	0	0.239	0.190	0.183	0.189	0.195	0.213	0.240	0.282	0.340	0.449	0.679
of	8	0	0	0	0	0	0	0	0	0.268	0.212	0.206	0.205	0.220	0.244	0.285	0.342	0.450	0.677
QSB	9	0	0	0	0	0	0	0	0	0	0.298	0.238	0.220	0.229	0.250	0.290	0.344	0.450	0.672
	10	0	0	0	0	0	0	0	0	0	0	0.341	0.253	0.247	0.261	0.297	0.348	0.452	0.670
	11	0	0	0	0	0	0	0	0	0	0	0	0.313	0.260	0.261	0.292	0.337	0.435	0.641
	12	0	0	0	0	0	0	0	0	0	0	0	0	0.370	0.304	0.319	0.353	0.448	0.650
	13	0	0	0	0	0	0	0	0	0	0	0	0	0	0.419	0.363	0.374	0.460	0.653
	14	0	0	0	0	0	0	0	0	0	0	0	0	0	0	0.522	0.431	0.495	0.675
	15	0	0	0	0	0	0	0	0	0	0	0	0	0	0	0	0.534	0.518	0.662
	16	0	0	0	0	0	0	0	0	0	0	0	0	0	0	0	0	0.754	0.760
	17	0	0	0	0	0	0	0	0	0	0	0	0	0	0	0	0	0	1.022

The characteristic mechanism of collapse for the existing building in the X direction, predicted using this approach, extends from floor 3 to floor 10, with an $\ddot{v}_{cr}^{t}$ of $0.130g$. Since the $\ddot{v}_{cr}^{t}$ for QSBs that run from floors 3 to 9 and floors 3 to 8 are not too different (they are within a couple of percentage points–$0.131g$ and $0.132g$, respectively), these QSBs could evolve into collapse mechanisms as well. Thus, three preferred mechanisms may be predicted using this approach. Shown underlined and in bold are the strongly preferred collapse mechanisms in the perfect- and susceptible-connection models of the existing building under X direction excitation (discussed previously; see Figures 4.6 and 4.8). It is clear that the strongly preferred mechanisms from the simulations are very well predicted by this minimization approach. Shown in bold, but not underlined, are the weakly preferred mechanisms. The $\ddot{v}_{cr}^{t}$ for the weakly preferred mechanisms occurring between floors 4 and 9, and floors 4 and 10 is within 10% of the minimum value. However, they are higher than the $\ddot{v}_{cr}^{t}$ values for mechanisms between floors 1 and 7, and floors 1 and 8. These mechanisms are subsets of the two most critical mechanisms between floors 3 and 9, and 3 and 10. Collapse after initiating between floors 3 and 9, and 3 and 10, could localize further during the collapse process. Thus, the observation of collapse between floors 4 and 9, and 4 and 10 despite other mechanisms having smaller $\ddot{v}_{cr}^{t}$ does not debunk this minimization approach. The collapse mechanisms which are subsets of the preferred collapse mechanisms predicted by this approach should also be considered possible.

In the Y direction, the predicted characteristic collapse mechanism for the existing building extends from floor 3 to floor 8 or 9. Both QSBs have a $\ddot{v}_{cr}^{t}$ of $0.122g$. The simulations of the existing building model with perfect connections show a strong preference for collapse to occur exactly between these floors as well as within two subsets of stories (floors 4 and 8, and floors 4 and 9). The ability of the PVW-plastic analysis approach to robustly predict the preferred collapse mechanisms is clear.

The best results are obtained for the redesigned building under X direction loading. Collapse is predicted to occur between floors 3 and 8 ($\ddot{v}_{cr}^{t} = 0.139g$). Collapse occurs between these floors in majority of the cases (refer to earlier discussion and Figure 4.7). The weakly preferred mechanisms between floors 3 and 6, 3 and 7, and 3 and 9 in the simulations have the next smallest $\ddot{v}_{cr}^{t}$ (within 5% of the minimum $\ddot{v}_{cr}^{t}$ of $0.139g$ for the critical mechanism between floors 3 and 8). The other weakly preferred mechanism between floors 4 and 9 is a subset of the mechanism between floors 3 and 9. It is clear from this discussion that if one

or more mechanisms have a $\ddot{v}_{cr}^{t}$ very close (say within 5%) to the minimum $\ddot{v}_{cr}^{t}$, the characteristic collapse mechanism may be non-unique. Collapse may occur in one of these preferred mechanisms. In general, the collapse mechanisms for 10-cycle loading are not as well predicted by this approach.

To confirm that these findings are not limited to idealized single-component motions, but applicable equally to 3-component earthquake excitation, three of the models (existing building with perfect and susceptible connections, and redesigned building with perfect connections) are analyzed under a suite of 636 3-component earthquake excitations. These are synthetic waveforms computed at 636 sites in southern California from the simulation of an 1857-like earthquake ($M_w = 7.9$) on the San Andreas fault [21, 22]. The East component of horizontal motion is oriented in the building X direction. While the East component is the stronger component in majority of the 636 sites, the North component is stronger at some of the locations. The primary quasi-shear band in each building at each of the 636 analysis is shown plotted against the peak transient IDR (taken to be the maximum IDR in either direction) on Figure 4.16. For the existing building with perfect or susceptible connections, the primary QSB coalesces between floors 3 and 10, with mechanisms forming between floors 3 and 8, 3 and 9, 3 and 10, 4 and 9, as well as 4 and 10 in equal measure. This is consistent with the predictions using the Principle of Virtual Work, where these five mechanisms had the lowest critical over-riding block accelerations for collapse in either direction (within a few percentage points of each other). Given the complexity associated with 3-component ground motion and the torsional eccentricity in this building, this is more than satisfactory. Likewise, the collapse mechanism in the redesigned occurs between floors 3 and 8 in majority of the cases. In a few cases, it forms between floors 3 and 6, 3 and 7, 3 and 9, and 4 and 8. This is consistent with the $\ddot{v}_{cr}^{t}$ values for these mechanisms being close to (within a few percentage points of) the minimum $\ddot{v}_{cr}^{t}$ value corresponding to the mechanism between floors 3 and 8 for collapse in either direction. Thus, the findings of the possible existence of preferred (characteristic) collapse mechanism(s) in these buildings hold true for earthquake excitation as well. It should be mentioned, however, that the synthetic waveforms from the San Andreas earthquake are not broadband in character. They are lowpass-filtered through a Butterworth filter with a corner at 2s. This is because the velocity model characterizing the earth structure is not well-resolved to reliably propagate high-frequency waves. Having said this, the soft lower cutoff of 2s for the seismic wave period is well below the fundamental periods of both buildings. Hence, the band-limited nature of the ground motions does not diminish the value of using these synthetic waveforms in lieu of recorded waveforms for the validation of this study.

The above plastic analysis approach which quantifies the relative propensity for all the possible collapse mechanisms to occur could possibly be used in the optimal design of moment frame systems. The objective could be to size the members in such a way as to maximize the number of preferred mechanisms ($\ddot{v}_{cr}^{t}$ for all these mechanisms would have to be similar). It may not be feasible to make all mechanisms equally plausible; getting collapses in upper stories is hard in general, as sufficient mass will not be present in the stories overriding the quasi-shear band. However, one could aim to maximize the number of preferred mechanisms by boosting the $\ddot{v}_{cr}^{t}$ for the lower story mechanisms.

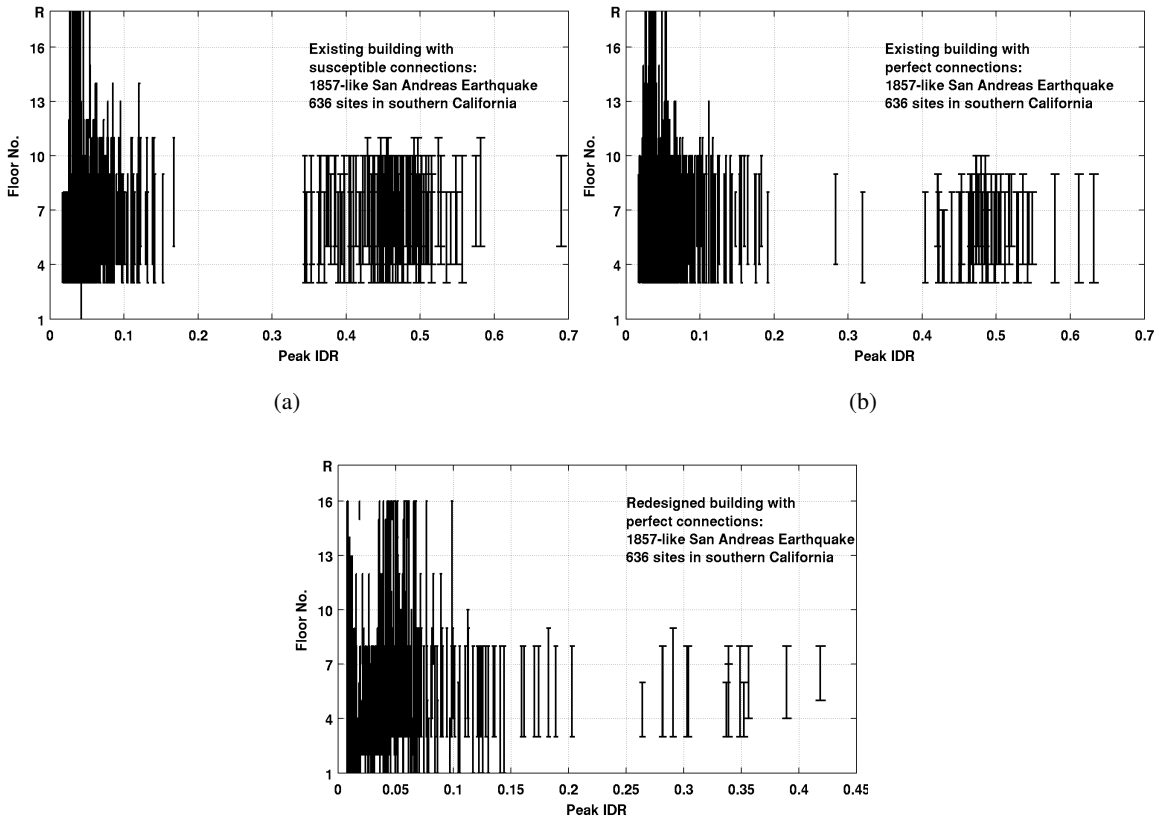

Figure 4.16: The location and extent of the primary quasi-shear band (QSB) plotted against peak transient interstory drift ratio (IDR) in three of the building models when subjected to synthetic 3-component excitation at 636 sites in southern California from an 1857-like magnitude 7.9 earthquake on the San Andreas fault: (a) existing building (susceptible connections); (b) existing building (perfect connections); and (c) redesigned building (perfect connections). Note that the primary quasi-shear band (QSB) coalesces to a narrow band of stories in each of the three cases, agreeing well with the predictions using the Principle of Virtual Work.

Chapter 5 Rapid Estimation of Response

Weeks after the 2010 Haiti earthquake which caused wide-spread damage, engineers world-over were comparing pre-earthquake and post-earthquake satellite images to identify collapsed and extensively damaged buildings for rescue and rehabilitation. Past experience suggests that the chances of finding people alive buried under rubble diminishes rapidly in the hours following the disaster. It is absolutely crucial to not only know the extent of regional damage, but also identify the exact location of collapsed structures so that rescue operations could be prioritized and launched swiftly. With the near certain failure of communication, power, and transportation networks, rapid damage estimation tools could serve as the eyes and ears for emergency response and management to augment information from the USGS ShakeMap and ShakeCast products. Databases of the kind described in Chapter 3 can be used effectively for this purpose in the immediate aftermath of an earthquake. When (and if) recorded waveforms at various locations become available after the earthquake, the closest surrogate to each of the recorded waveforms can be determined. For swift disaster response, the damage to tall buildings at these locations can then be rapidly estimated using a table look-up approach, thus by-passing time-history analyses using recorded motions and building models. The same approach can be used for ball-park estimation of structural response under any given earthquake record, in lieu of comprehensive nonlinear analysis. For this estimation methodology to produce reliable results, the idealized representation of the ground motion must be such that the response of tall buildings under the true waveforms is similar to that under their idealized representations. The ground motion representation described in Chapter 3 has been shown to satisfy this condition for the buildings considered in this study. Thus, the proposed rapid estimation approach can be verified on these target building models.

On January 9, 1857, a large earthquake of magnitude 7.9 occurred on the San Andreas fault, with rupture initiating at Parkfield in Central California and propagating in a southeasterly direction over a distance of more than 360km. Such a unilateral rupture produces significant directivity toward the San Fernando and Los Angeles basins. Indeed, newspaper reports of sloshing observed in the Los Angeles river point to long-duration (1–2 min) and long-period (2–8 s) shaking. If such an earthquake were to happen today, it could impose significant seismic demand on many present-day tall buildings. In 2005-06, using state-of-the-art computational tools in seismology and structural engineering, validated using data from the January 17, 1994, magnitude 6.7 Northridge earthquake, the damage to the existing (susceptible connections) and redesigned (perfect connections) buildings was simulated at 636 sites in southern California due to ground motion from an 1857-like hypothetical magnitude 7.9 earthquake on the San Andreas fault [21, 22]. The study indicated that serious damage occurs in these buildings at many locations in the region in the north-to-south rupture scenario. The peak velocity simulated was of the order of 1 m/s in the Los Angeles basin, including downtown Los Angeles, and 2m/s in the San Fernando valley, while the peak displacements were of the order of 1m and 2m in the Los Angeles basin and San Fernando valley, respectively. Whereas the east component was the stronger component at many locations (e.g., West Los Angeles; see Figure 5.1), the north component was stronger at some locations (e.g., Downey).

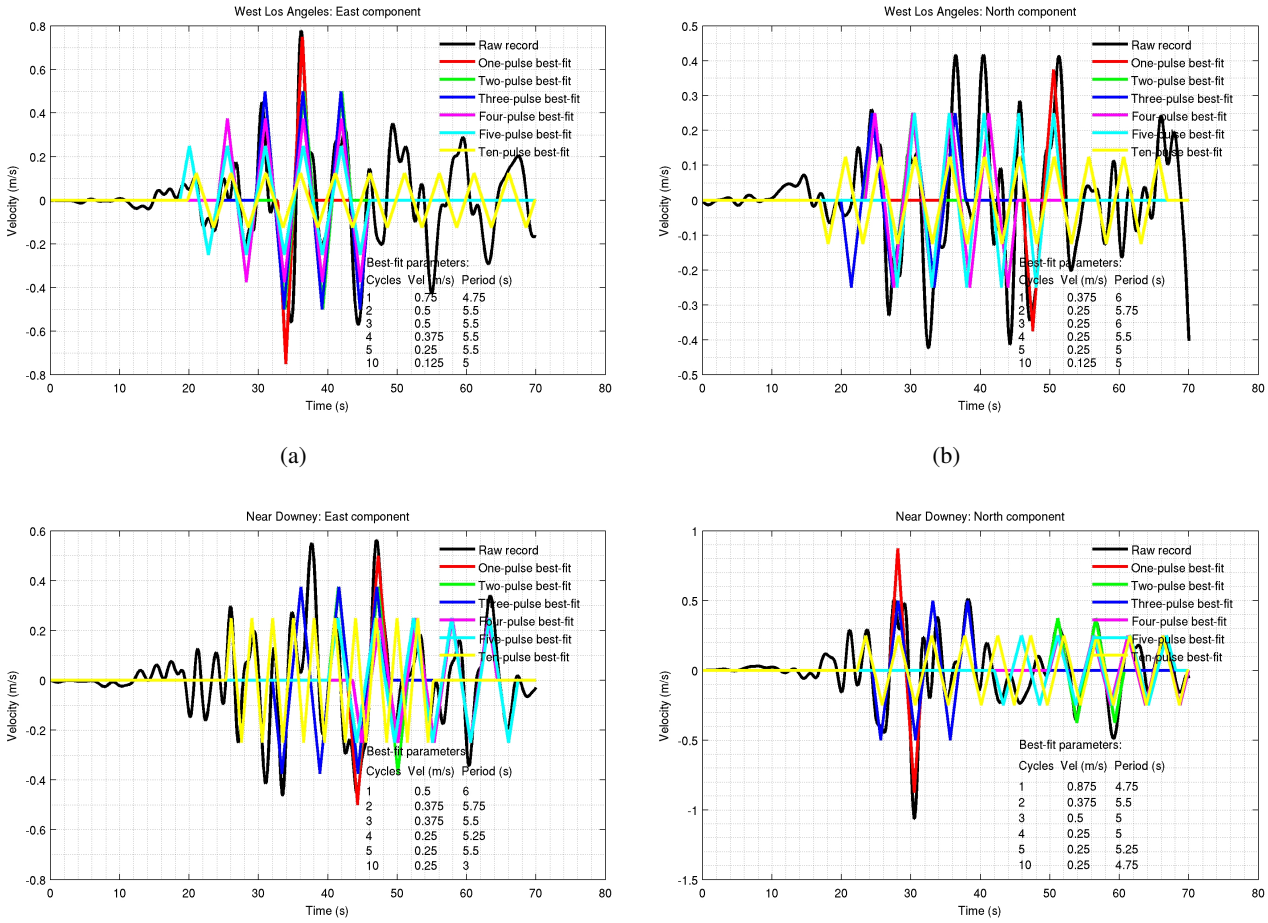

Figure 5.1: Synthetic velocity waveforms at sites in West Los Angeles [(a) east component; (b) north component] and Downey [(c) east component; (d) north component] from a simulated 1857-like San Andreas fault earthquake. Also shown are the idealized 1-, 2-, 3-, 4-, 5-, and 10-cycle wave-trains with the least absolute deviation (L_1 norm) from the corresponding record.

Here, the existing building (perfect connections) model is analyzed under the 636 three-component synthetic motions (lowpass-filtered at a corner at 2s). The building's X direction is oriented in the geographical east direction. The peak transient IDR at all the locations is shown on a regional map in Figure 5.2(a). To see whether this regional damage map could be estimated using the proposed rapid estimation approach outlined above, the best-fit 1-, 2-, 3-, 4-, and 5-cycle surrogate idealized waveforms (five idealized representations) for the two horizontal components of the 636 three-component ground motion histories are first determined. The L_1 norm (least absolute deviation) is used for this optimization. In the first attempt, the peak transient IDR at each location in either direction is estimated as the maximum of that under each of the five best-fit 1-, 2-, 3-, 4-, and 5-cycle waveforms from the structural response database. For the east component idealization, the database corresponding to the response of the existing building (perfect connections) to X-direction excitation is used. For the north component idealization, the database corresponding to the response of the existing building (perfect connections) to Y-direction excitation is used. Typical buildings are provided with lateral force-resisting systems in two mutually orthogonal directions to counter the two horizontal components of ground shaking. For rapid estimation purposes, the responses in the two directions are assumed to be independent. Needless to say, torsional effects cannot be accurately captured by this estimation procedure. The results of the estimation are given in Figure 5.2. This "direct" approach to response estimation resulted in under-estimation at many locations. The Gaussian mean estimation error in the interstory drift ratio is 0.0075 and the standard deviation is 0.0190.

The lower estimates for IDR from the "direct" approach occur at locations where the ground motion strong component waveform has one big pulse followed by a trailing wave-train with somewhat lower, but not insignificant, amplitudes. For example, consider the hypothetical velocity history shown in Figure 5.3. It has one very strong pulse followed by two trailing pulses that are relatively weaker, yet quite strong. The 1-cycle best-fit idealization has an amplitude of 1.625m/s, while the 3-cycle best-fit idealization has an amplitude of 1.25m/s (the amplitudes differ by a moderate 0.375m/s). This implies that the waveform has one pulse with a nominal amplitude of 1.625m/s and two other pulses with an average nominal amplitude of 1.0625m/s $\left(Note: \frac{2*1.0625+1.625}{3} = 1.25\right)$. The best-fit 1-cycle idealization captures the first peak well, but misses out on the trailing two pulses, whose effects are then left out resulting in response under-estimation. The best-fit 3-cycle idealization has an amplitude that is closer to the amplitude of the trailing two pulses. As a result, the effect of the strong first peak is not captured, once again resulting in under-estimation. A modified approach to estimating the peak transient interstory drift ratio (IDR) becomes necessary for such cases. Given the strength of the largest pulse, it may be assumed that the entire transient interstory drift from this pulse is permanent (plastic) in nature. If the story location of the peak transient IDR under the 3-cycle idealization matches that under the 1-cycle idealization, the peak transient IDR under the true waveform can be estimated as the peak transient IDR from the first strong cycle plus the peak transient IDR under the trailing 2-cycle excitation. As shown in the figure, the amplitude of the best-fit to the two trailing pulses can be deduced to be $\frac{3*PGV_3-1*PGV_1}{3-1}$. Here, PGV_3 is the amplitude of the 3-cycle best-fitting waveform and PGV_1 is the amplitude of the 1-cycle best-fitting waveform.

The outline of the "modified" rapid estimation approach is as follows (the first two steps constitute the "direct approach"):

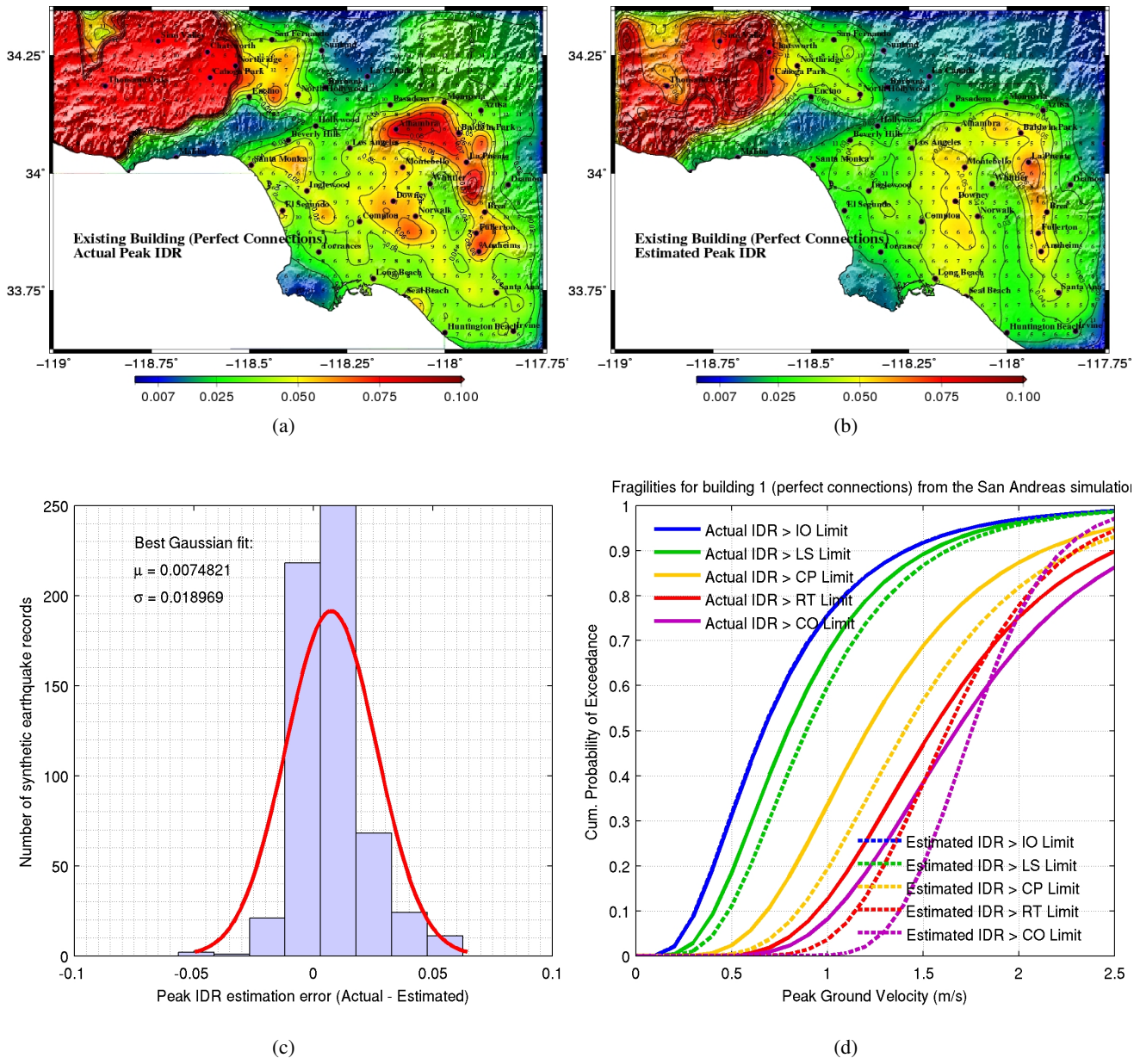

Figure 5.2: (a) Map of peak transient interstory drift ratio (IDR) in the existing building (perfect connections) computed using synthetic 3-component waveforms at 636 sites from the 1857-like San Andreas earthquake simulation (b) The corresponding map of estimated peak transient IDR computed using the best-fitting idealized saw-tooth waveforms to the horizontal components of the synthetic motion. (c) Histogram of the estimation error and the best Gaussian fit. (d) Comparison of fragilities determined using computed responses in (a) and the estimated responses in (b). These are results obtained using the "direct" rapid estimation approach.

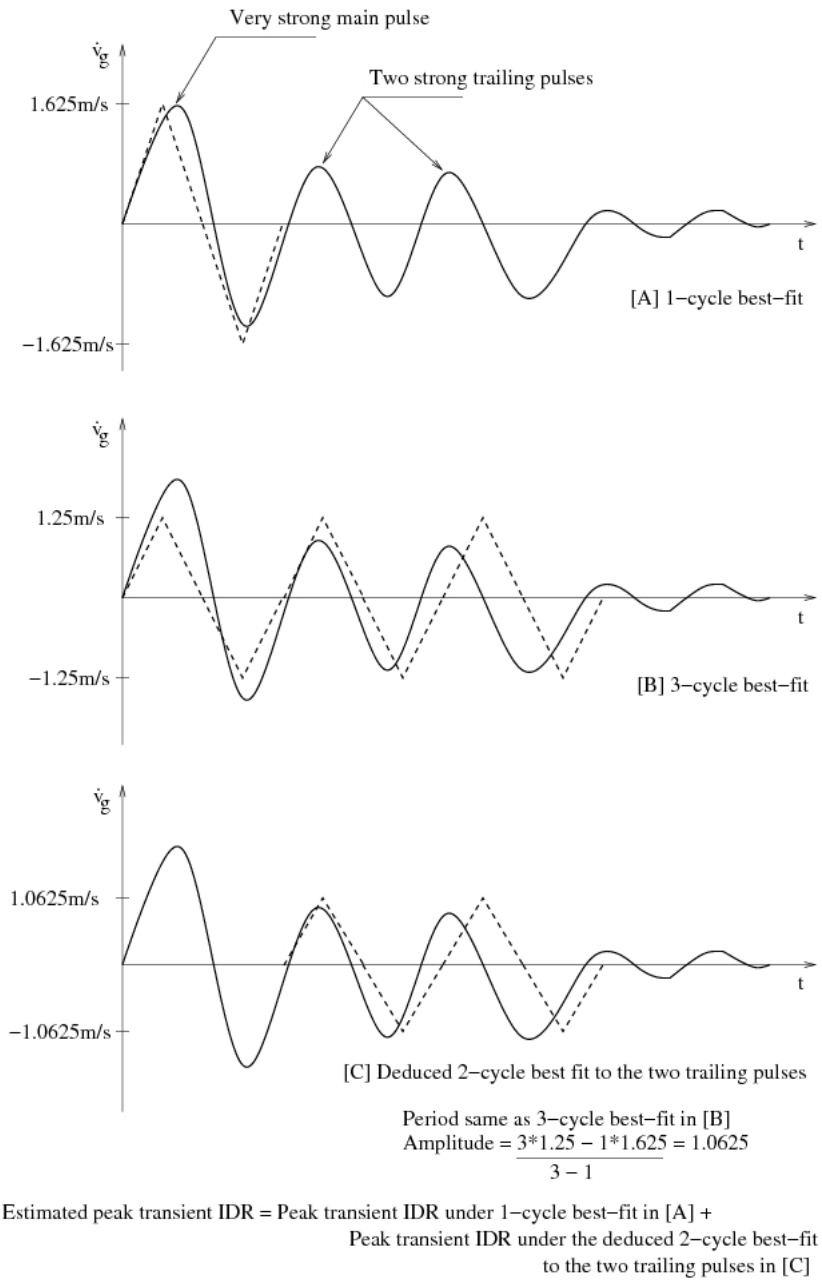

Figure 5.3: Hypothetical velocity history with one very strong pulse followed by two weaker, yet quite significant, trailing pulses. Neither the best-fit 1-cycle pulse nor the best-fit 3-cycle pulse is able to capture the structural response effectively. A modified approach to estimate the peak transient interstory drift ratio (IDR) is employed in such cases. It involves deducing the amplitude of the best-fit 2-cycle waveform to the two trailing pulses using the best-fit 1-cycle and 3-cycle waveforms. The peak transient IDR is then estimated as the sum of the peak transient IDRs under the best-fit 1-cycle waveform and the best-fitting 2-cycle waveform to the two trailing pulses.

1. The best-fitting 1-, 2-, 3-, 4-, and 5-cycle waveforms to the two horizontal components of the measured or synthetic record are determined.

2. The structure response database is queried for the peak transient IDR under each of the ten best-fit

idealized waveforms (1–5 cycles and two components), with due consideration to the building orientation relative to the azimuth of the two ground motion components. In the San Andreas example, the X direction database is used to estimate the peak transient IDR under the east component idealizations, while the Y direction database is used for IDR estimation under the north component idealizations. The peak transient IDR is the maximum of the 10 IDRs resulting from the database queries, with the following exceptions.

3. The PGV of the 5-cycle ($I = 5$) idealized waveform is compared against the PGV of the 1-cycle, 2-cycle, 3-cycle, and 4-cycle ($J = 1, 2, 3, 4$) waveforms. If, for any J, the difference is 0.25m/s or 0.375m/s, then the response is estimated by superposing the response under the J-cycle idealization and the best-fitting waveform for the trailing $[I - J]$-cycle waveform. The amplitude of the trailing $[I - J]$-cycle waveform is taken to be $\frac{I*PGV_I - J*PGV_J}{I-J}$ and its period is taken to be identical to the original I-cycle best-fit. Here, PGV_I is the amplitude of the I-cycle best-fitting waveform and PGV_J is the amplitude of the J-cycle best-fitting waveform. The process is repeated for $I = 4, 3, 2$ with J varying from 1 to I-1. The largest IDR that results from these computations is taken to be the best estimate of structural response to the ground motion waveform under consideration.

The pseudocode for the rapid damage estimation procedure is outlined in Figure 5.4. The peak transient IDR response of the existing building (perfect connections) under the synthetic ground motion from the 1857-like San Andreas earthquake at each of the 636 analysis sites is estimated using this procedure. The results are shown in Figure 5.5(b) for convenient comparison against the actual values shown in Figure 5.5(a). The actual and estimated values for all analysis sites are shown plotted against each other in Figures 5.6(a) and 5.6(b). The errors are also quantified in the histogram and its best-fit Gaussian distribution in Figure 5.6(c). They have a Gaussian mean of 0.0011 and standard deviation of 0.021 which is somewhat high. To understand the effectiveness of the rapid estimation procedure, the IDRs must be related to useful damage measures or performance levels which can be used in the decision-making process for disaster response. Recall that the IDR limits for the IO, LS, CP, RT, and CO performance levels (Table 3.1) are 0.007, 0.025, 0.05, 0.075, and 0.100 respectively. Clearly, the standard deviation of the rapid damage estimation procedure is roughly equivalent to one performance level. In other words, estimated IDR with an error of one-σ will be off the mark by one performance level, for instance, if the true performance level is RT, the prediction may be either CP or CO. Of course, on the average, the rapid estimation procedure performs rather well. Shown in Figure 5.6(d) are the fragilities for each of the performance levels (cumulative probability of exceedance of a given performance level as a function of PGV), computed using the actual and estimated IDRs. The IO, LS and CP fragilities derived using estimated IDRs agree very well with those derived using actual IDRs, with probability of exceedance not differing by more that 3%. The estimation procedure over-predicts the probability of exceedance of the RT and CO performance levels by up to 10%.

Finally, the estimation of IDR under the near-source records described earlier is revisited using the modified rapid damage estimation procedure adopted for the San Andreas study. The results are summarized in Figure 5.7. The error in IDR now has a Gaussian mean of -0.0014 and a standard deviation of 0.0086, both being marginally worse than the original estimation procedure. It may be prudent to classify records as near-source or otherwise prior to adopting one estimation procedure or the other.

```
INITIATE T = 0.50s : 0.25s : 6.00s
INITIATE PGV = 0.125m/s : 0.125m/s : 2.500m/s
INITIATE N = 1 : 1 : 5
GENERATE IDEALIZED WAVES USING ALL [Ti, PGVj, Nk] COMBINATIONS

FOR EACH Ni, FIND THE [To, PGVo] COMBINATION WITH THE LEAST ABSOLUTE DEVIATION BETWEEN
THE IDEALIZED WAVE AND EACH HORIZONTAL COMPONENT OF THE GROUND MOTION RECORD

FOR EACH [Ti, PGVi, Ni] COMBINATION (i=1:5), DETERMINE PEAK IDR & LOCATION FROM STRUCTURAL
RESPONSE DATABASE. DO THIS STEP FOR BOTH HORIZONTAL COMPONENTS. THE ABSOLUTE MAXIMUM OF
ALL THESE IDRs IS THE CURRENT ESTIMATE OF THE PEAK TRANSIENT IDR

FOR i=1:5
  FOR j=1:i–1
    IF 0.125 < (PGVj–PGVi) < 0.500
      PGVi (TRAILING) = (i*PGVi–j*PGVj)/(i–j)
      PKIDR1 = PKIDR(Tj, PGVj, Nj)
      LOC1 = LOC(Tj, PGVj, Nj)
      PKIDR2 = PKIDR(Ti, PGVi (TRAILING), Ni–Nj)
      LOC2 = LOC(Ti, PGVi (TRAILING), Ni–Nj)
      IF LOC1==LOC2
        CURRENT ESTIMATE OF PEAK IDR = MAX(CURRENT ESTIMATE OF PEAK IDR, PKIDR1+PKIDR2)
```

Figure 5.4: Pseudocode for the rapid damage estimation procedure.

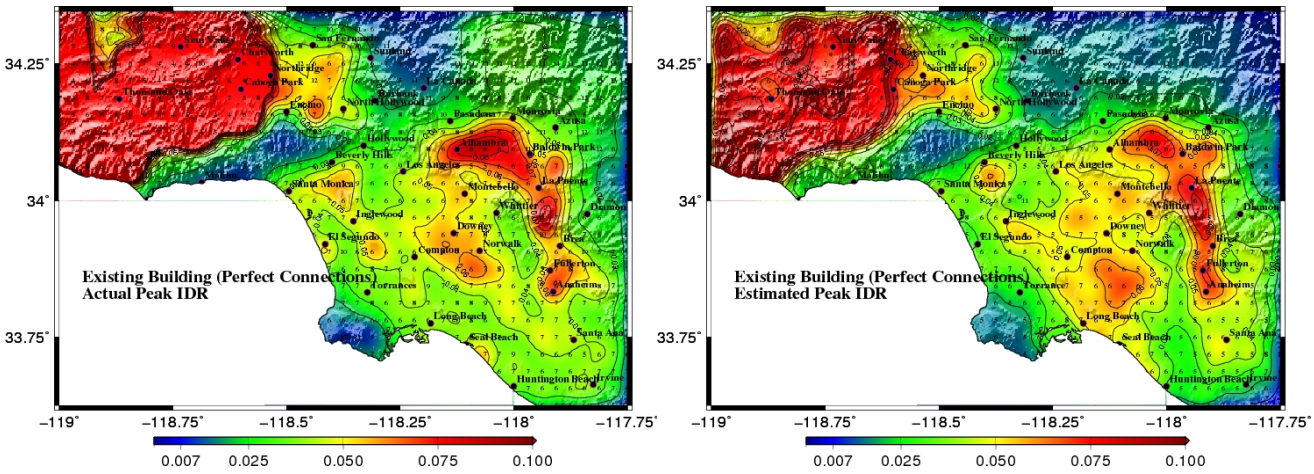

Figure 5.5: (a) Map of peak transient interstory drift ratio (IDR) in the existing building (perfect connections) computed using synthetic 3-component waveforms at 636 sites from the 1857-like San Andreas earthquake simulation (b) The corresponding map of estimated peak transient IDR computed with the "modified" rapid estimation approach using the best-fitting idealized saw-tooth waveforms to the horizontal components of the synthetic motion.

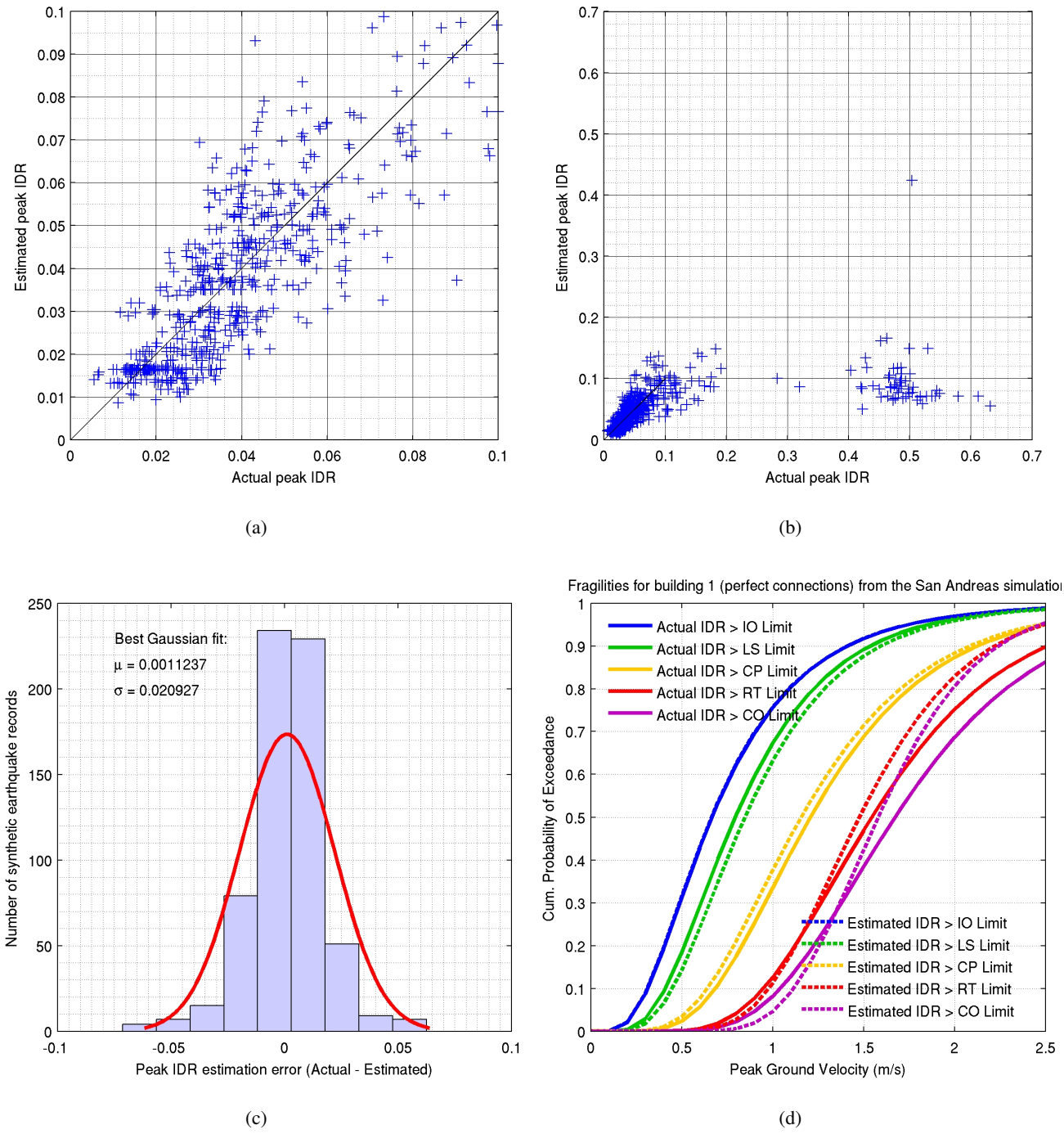

Figure 5.6: (a) and (b) The values of estimated and actual peak interstory drift ratios (IDRs) at each of the 636 southern Californian sites from Figure 5.5 plotted against each other. (c) Histogram of the estimation error and the best Gaussian fit. (d) Comparison of fragilities determined using computed responses in Figure 5.5(a) and the estimated responses in Figure 5.5(b). These are results obtained using the "modified" rapid estimation approach.

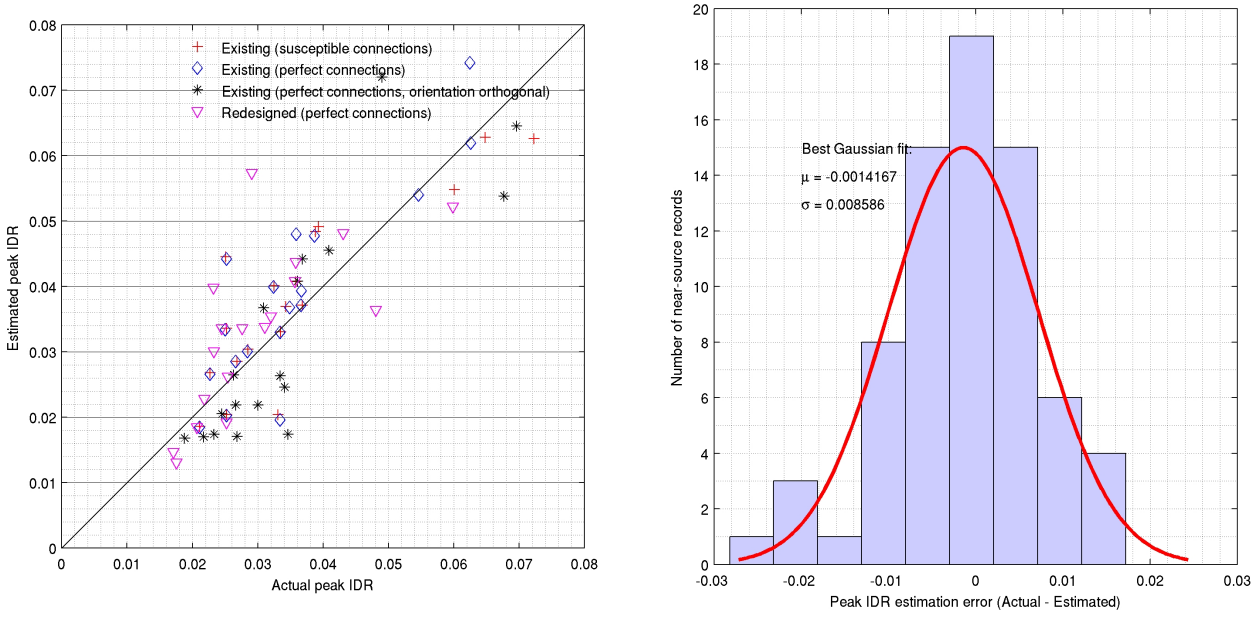

(a) (b)

Figure 5.7: (a) Peak transient interstory drift ratio (IDR) computed using all near-source records plotted against that computed using not the best-fit idealized 1-cycle saw-tooth waveforms as in Figure 2.7, but the rapid estimation methodology adopted for the San Andreas case: All buildings. The diagonal line represents identical results from the two analyses. (b) Histogram of the error in determining the peak transient IDR from the idealized waveform representation as opposed to the actual record. The best-fit Gaussian is also shown.

Chapter 6 Limitations of the Study

1. The findings of the study are based on analyses of just two moment frame buildings in the 20-story class. These buildings cannot be realistically considered to cover the entire class of steel moment frame buildings. Having said this, the periods and strengths of these two buildings are significantly different, the existing building has a prominent torsional eccentricity whereas this is eliminated in the redesigned building, and different levels of vulnerability to fracture have been considered. Thus, the models analyzed do cover a broad spectrum of features within this class of structures. Furthermore, the sensitivity of structural response of these models is consistent with theoretical energy balance predictions, and the existence of preferred collapse mechanisms is deduced from the simple uniform shear-beam analogy after correcting for the non-uniform nature of the buildings. The strong theoretical basis for the findings suggest that they are robust and may be broadly applicable to the entire class of tall steel moment frame buildings. However, further studies are needed to confirm this.

2. The findings of the study related to the mechanism of collapse are limited to regular buildings that do not have discontinuities in the vertical load-carrying system (in the moment frame or the gravity columns). For instance, say a column carrying gravity load of many upper floors is terminated at a lower floor and its load is transferred to two adjacent columns through a transfer beam. In this case, if the transfer beam fails during earthquake excitation, then there could be a rapid vertical progressive collapse similar to an implosion, not the progressive collapse initiated by sidesway destabilization of the QSB.

3. The parametric analyses are conducted using single component excitation. The results are thus applicable to ground motions with the strong component oriented in either one of the two principal directions of the buildings (or lateral force-resisting system). If the strongest shaking is at a 45° angle with respect to either principal direction of the building the peak transient IDR response of the structure may be estimated as the sum of the square root of the squares of peak transient IDR from the two components of ground motion in the building principal directions. If the preferred collapse mechanisms are significantly different in the two directions of the building (unlike the buildings considered here), then collapse will still occur in one of the preferred mechanisms in either direction. Other factors such as subtle contributions to stiffness or strength from non-structural components, and construction variability between the two directions, may determine the direction in which the structure collapses.

4. Ground velocity waveforms that have positive and negative phases with different amplitudes or that have an unequal number of positive and negative phases have not been considered in the parametric analyses.

5. The rapid estimation procedure is tested on a single scenario earthquake. Evaluating its robustness and

quantifying the errors associated with the procedure requires its application to a significantly greater number of earthquake scenarios. In this context, the use of other ground motion idealization schemes and optimization schemes need to be investigated.

6. As with any modeling techniques, the FRAME3D models of the buildings have limitations too:

   (a) Composite action of moment-frame beams has not been included. Moment-frame beams are connected to the concrete slab on metal deck through shear connectors (studs). This leads to some part of the slab in the vicinity of the beam to act as being part of the beam, leading to increased stiffness and strength. The effect of this is two-fold. Firstly, it could make the moment-frames stiffer attracting greater seismic forces, but this could be partly offset by the increased strength from composite action. In addition, since this would make the beams stronger in relation to the columns, it could have the effect of pushing the location of plastic yielding into the columns.

   (b) Damage to floor slabs is not modeled.

   (c) Floor framing beams that support the dead weight of the floors are not modeled. While they are typically assumed pin-connected, in reality they do offer partial restraint. Of course, the sections are much shallower and smaller than the moment frame beams. This factor, in conjunction with the fact that only partial restraint is offered by the connections, implies that their contribution may be quite small relative to the moment frame beams.

   (d) Some critical failure modes such as local flange buckling of I-sections are not included in the structural modeling.

   (e) Column splices have not been modeled. Column splices are typically located three feet above the floor slab with the intention of locating them away from the high-moment (high flexural stress) regions near beam-column joints. In the absence of axial load, the theoretical point of contraflexure (zero moment) is at mid-height of the column. In the case of columns, axial load does exist and buckling failure could occur at mid-height (first mode buckling). So the splice location of three feet above the floor slab is chosen to avoid the most vulnerable locations of the column. These splices are weak points and could fail especially if the column goes into tension during the earthquake.

   (f) Stiffness of partitions, and stair & elevator enclosures is not included.

   (g) The structure foundations have not been included in the structural models. Soil-structure interaction (SSI, e.g., [27, 7, 28, 30, 31]) is not included in the analyses.

Chapter 7 Conclusions

1. Parametric analysis of two steel moment frame buildings and their variants are conducted to study their sensitivity to ground motion features. The two buildings are an existing 18-story steel moment frame building ($T_x = 4.52s, T_y = 4.26s, T_\phi = 2.69s$) designed according to the 1982 UBC and a building with the same configuration, but redesigned according to the 1997 UBC ($T_{x+y-} = 4.05s, T_{x+y+} = 3.85s, T_\phi = 2.60s$). Four cases are considered – existing building with susceptible connections excited in the X direction, existing building with perfect connections excited separately in X and Y directions, and redesigned building with perfect connections excited in the X direction. Ground motion velocity waveforms are idealized as sawtooth-like wave-trains, characterized by three parameters- a period T, an amplitude PGV (peak ground velocity), and a duration represented by the number of cycles N. The structural response under a suite of real records matches closely with the response under the corresponding best-fitting idealized waveforms. The four building models are analyzed under a suite of idealized ground motion waveforms applied in either direction and the results are stored in a database. T is varied between 0.5s–6.0s, PGV is varied between 0.125m/s–2.5m/s and N is varied between 1–5. 1-cycle (near-source) ground motion with pulse-periods longer than 4.5s and PGV greater than 1.625m/s, and 3-cycle motion with cycle-periods longer than 3.25s and PGV greater than 0.75m/s cause collapse in the buildings considered in this study. Under short period excitation ($T < 1.5s$). the peak transient interstory drift ratio (IDR) saturates to a value below the collapse prevention (CP) performance limit with increasing PGV, i.e., collapse can only be caused by long-period ground motion. Under longer period ground motion, the peak transient IDR grows with PGV (linearly for moderately long-period excitation, more rapidly for long-period excitation with $T > T_x$). Collapse risk is negligible/minor if ground motion $PGV < 0.5m/s$ or $T < 1.5s$ for $N \leq 5$ for all four building models. Partial (and perhaps complete) collapse is almost certain to occur in all four models if ground excitation has a period $T > 5s$, a velocity amplitude $PGV > 1m/s$, and has more than one cycle ($N > 1$). These findings are qualitatively explained using a classical energy balance analysis for multi-story buildings under earthquake excitation. The number of cycles of ground excitation has minimal impact in cases where peak transient IDR is below the CP limit. If the peak transient IDR exceeds the CP limit, degradation is swift with increasing number of cycles for both susceptible-connection as well as perfect-connection building models.

2. Collapse occurs due to the formation of a quasi-shear band consisting of plastic hinges at the top of all columns in the uppermost story of the band, at the bottom of all columns in the lowermost story of the band, and at both ends of all beams in the intermediate stories. The location of the primary quasi-shear band QSB (the shear band with the greatest plastic strains) as a function of the input excitation period largely follows that of the region of greatest yield in a uniform shear-beam. The greater the period of input excitation, the lower the location of the band. In the uniform shear beam, yielding would migrate all the way to the base for pulse periods exceeding the beam period. However, because the buildings

are non-uniform in strength, the downward migration of the primary QSB with increasing pulse period is arrested a few stories above the base. Combined with the fact that collapse can occur only under long-period motions, this implies that there must exist a characteristic mechanism of collapse or a few preferred mechanisms of collapse for these buildings– sidesway collapse initiated by shear instability in the primary quasi-shear band a few stories above the base.

3. To predict the preferred mechanisms of collapse in these buildings a plastic analysis approach is developed. In this approach, the Principle of Virtual Work is applied to to all possible quasi-shear bands in the building. The band whose capacity is exceeded under the smallest absolute acceleration ($\ddot{v}_{cr}^{t}$) of the over-riding block of stories is identified as the characteristic collapse mechanism. If one or more mechanisms have a $\ddot{v}_{cr}^{t}$ very close (say within 5%) to the minimum $\ddot{v}_{cr}^{t}$, the characteristic collapse mechanism may be non-unique. Collapse may occur in one of these preferred mechanisms. The results from this approach agree well with the simulations of all four building models under idealized ground motion waveforms where collapse occurs. The simulations do not show the formation of a single (unique) collapse mechanism. However, in each model only one to five collapse mechanisms occur out of a possible 153 mechanisms in each principal direction of the building.

4. The plastic analysis approach to identify the preferred collapse mechanisms can alternately be used to develop an improved design of the building that would be close to optimal, where yielding occurs all over, by proportioning the system to make all collapse mechanisms equally likely.

5. An efficient rapid structural response estimation procedure has been developed. It utilizes the database of structural responses under idealized ground motion waveforms compiled for the sensitivity study. For the estimation of structural response under a measured ground motion record, the 1-, 2-, 3-, 4-, and 5-cycle idealized waveforms that have the least absolute deviation from the two horizontal components of the record are determined. The peak transient IDR under the measured ground motion is estimated as the greatest of the peak transient IDRs under each of the five best-fit idealized waveforms. These IDRs are rapidly determined by querying the structural response database. A modified approach is necessary to account for special cases involving a few big pulses, followed by a few moderately strong pulses.

Appendix A Existing (UBC 1982) Building with Susceptible Connections: Archive of Response Parameters Under Idealized-Waveform Shaking in X Direction

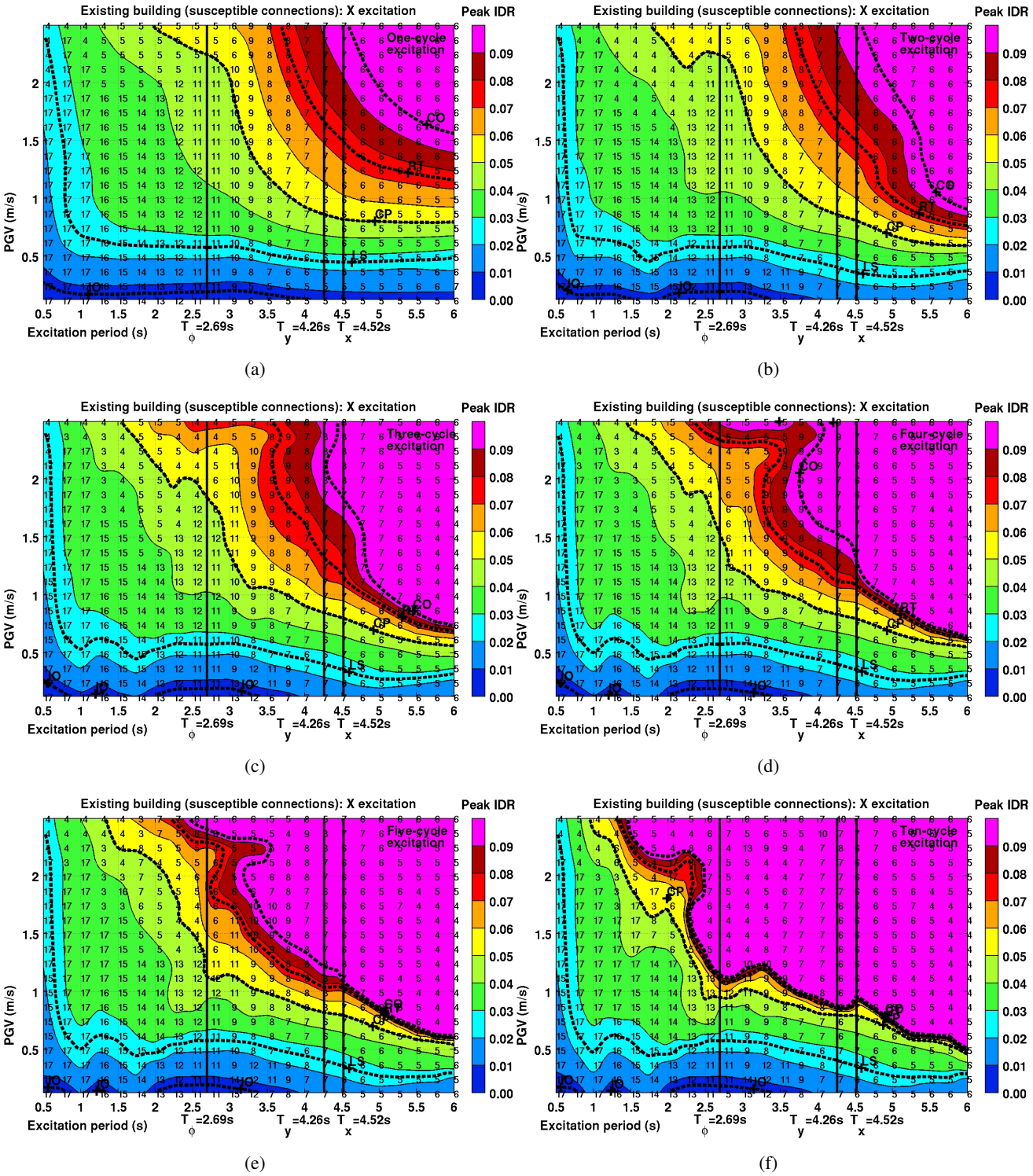

Figure A.1: Peak transient interstory drift ratio (IDR) maps for the existing building (susceptible connections) as a function of idealized saw-tooth waveform excitation parameters, period T, peak ground velocity PGV, and number of cycles N. The one-component ground motion is applied in the building X direction. The story location where the peak occurs is labeled at each of the 460 [T,PGV] combinations for which analyses were performed. Contours corresponding to empirical performance levels of immediate occupancy (IO), life-safety (LS), collapse prevention (CP), red-tagged (RT), and collapsed (CO), are shown in bold font. The principal direction building fundamental periods are indicated for reference.

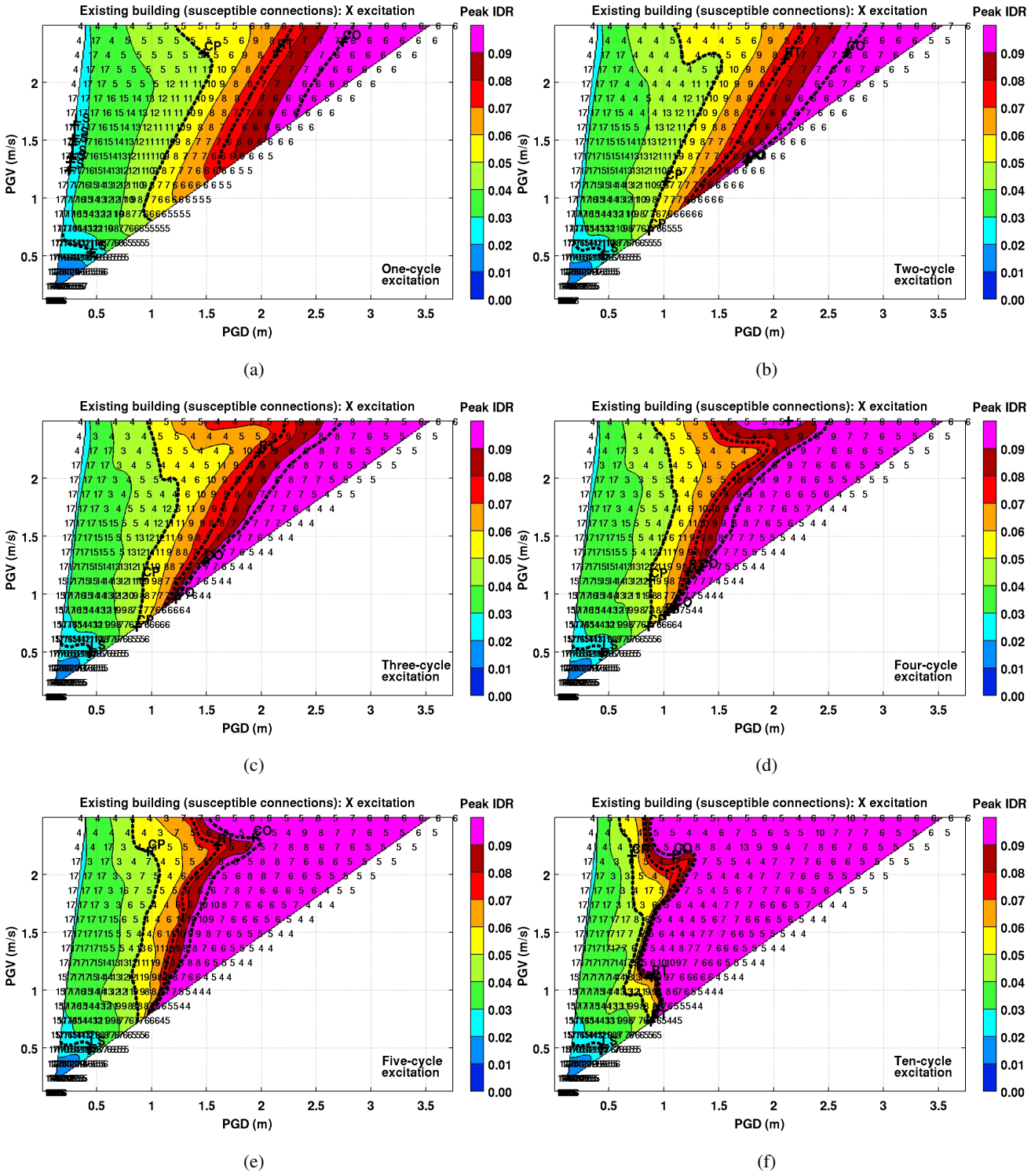

Figure A.2: The peak transient interstory drift ratio (IDR) maps for the existing building (susceptible connections) from Figure A.1 transformed to the peak ground displacement (PGD) - peak ground velocity (PGV) plane. The story location where the peak occurs is labeled at each of the 460 [T,PGV] combinations for which analyses were performed. Contours corresponding to the empirical IO, LS, CP, RT, and CO performance levels are also transformed and shown in bold font.

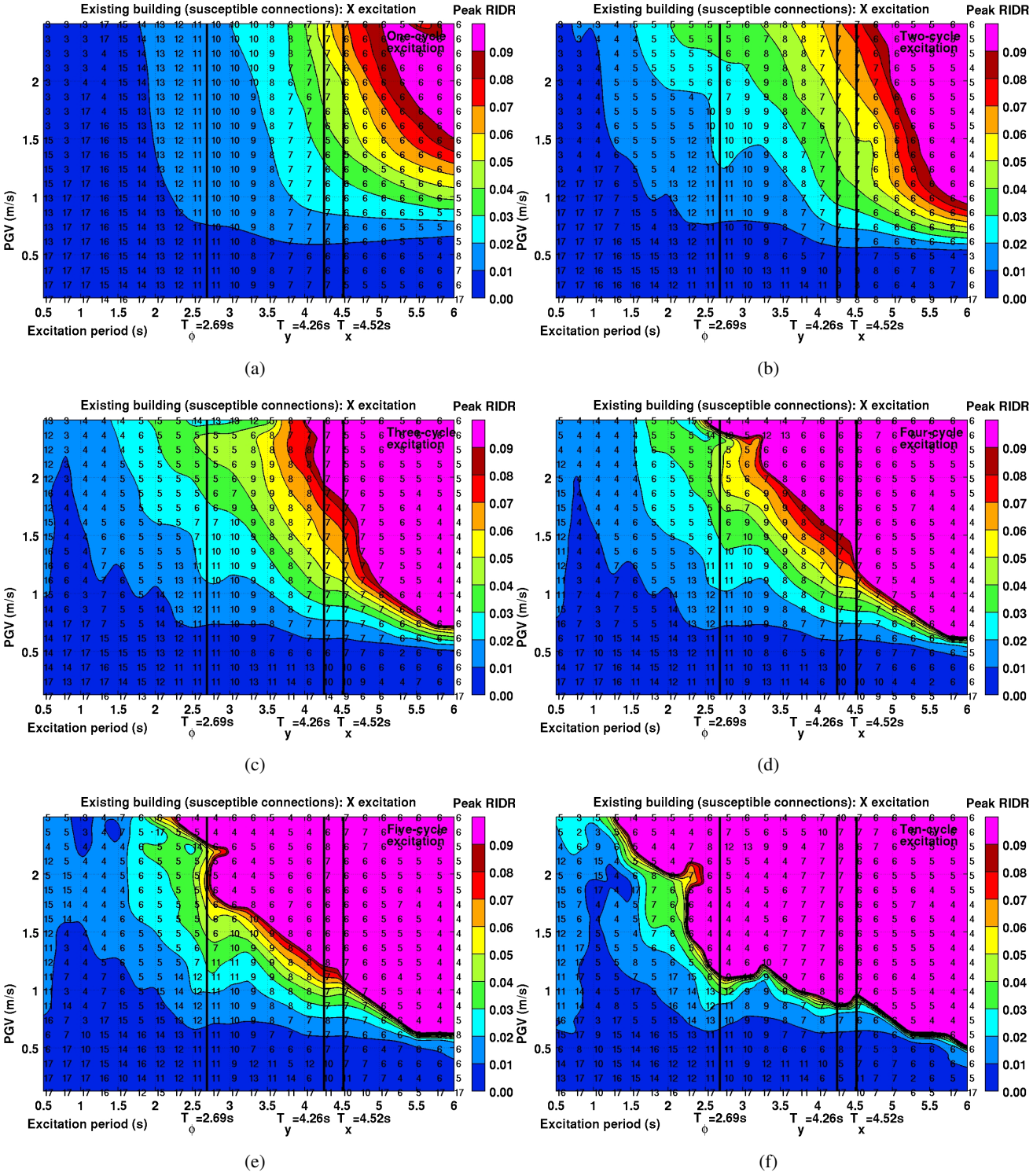

Figure A.3: Peak residual interstory drift ratio (RIDR) maps for the existing building (susceptible connections) as a function of idealized saw-tooth waveform excitation parameters, period T, peak ground velocity PGV, and number of cycles N. The one-component ground motion is applied in the building X direction. The story location where the peak occurs is labeled at each of the 460 [T,PGV] combinations for which analyses were performed. The principal direction building fundamental periods are indicated for reference.

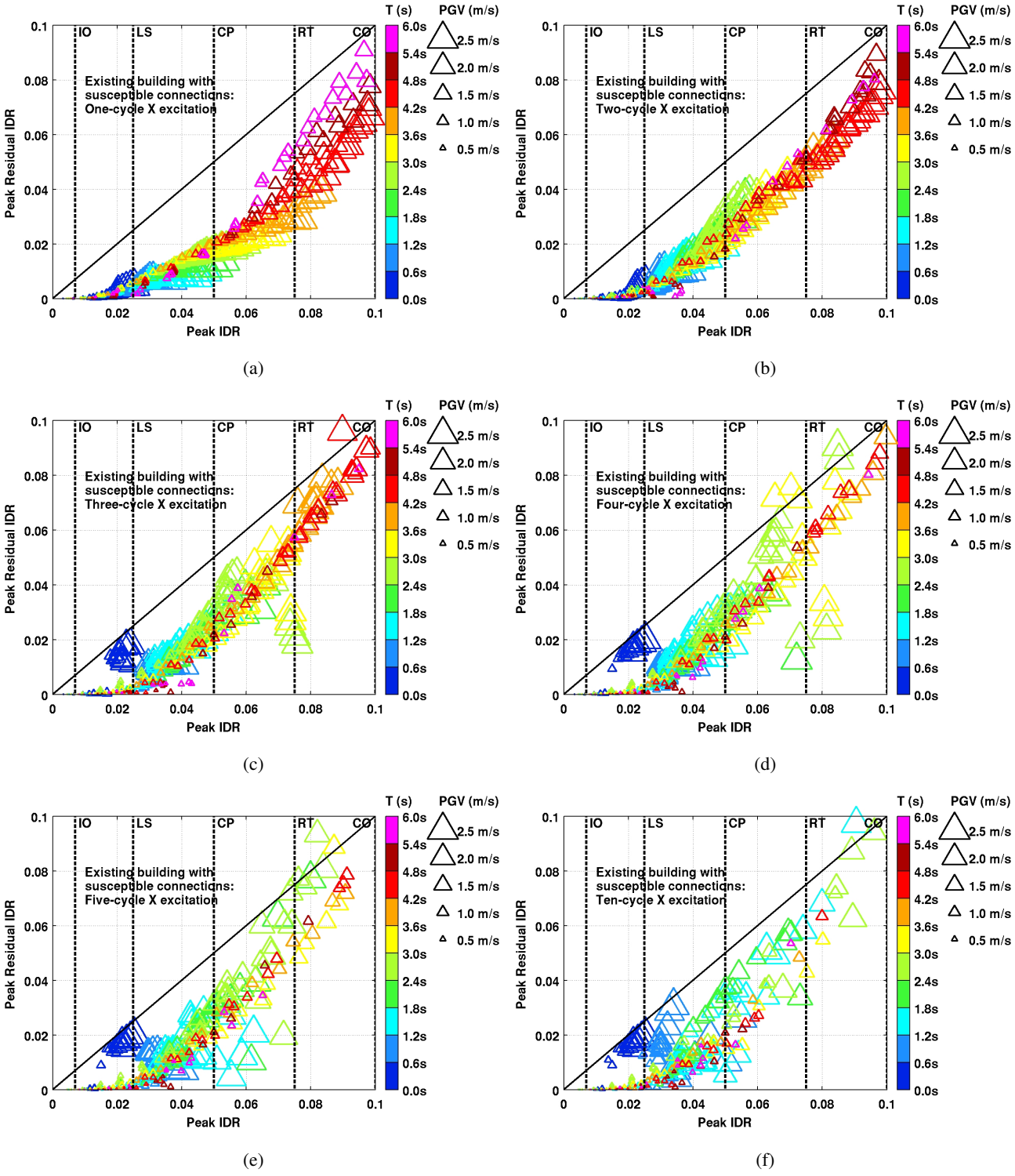

Figure A.4: Peak residual interstory drift ratio (RIDR) in the existing building (susceptible connections) plotted as a function of the peak transient IDR under idealized saw-tooth waveform excitation. The results for 1-, 2-, 3-, 4-, 5-, and 10-cycle excitations are shown separately. The one-component ground motion is applied in the building X direction. Points corresponding to peak transient IDR > 0.10 are indicative of near-certain collapse; residual IDR is no longer meaningful. Hence, these points are not shown. The empirical immediate occupancy (IO), life-safety (LS), collapse prevention (CP), red-tagged (RT), and collapsed (CO) performance levels are marked on the IDR axis.

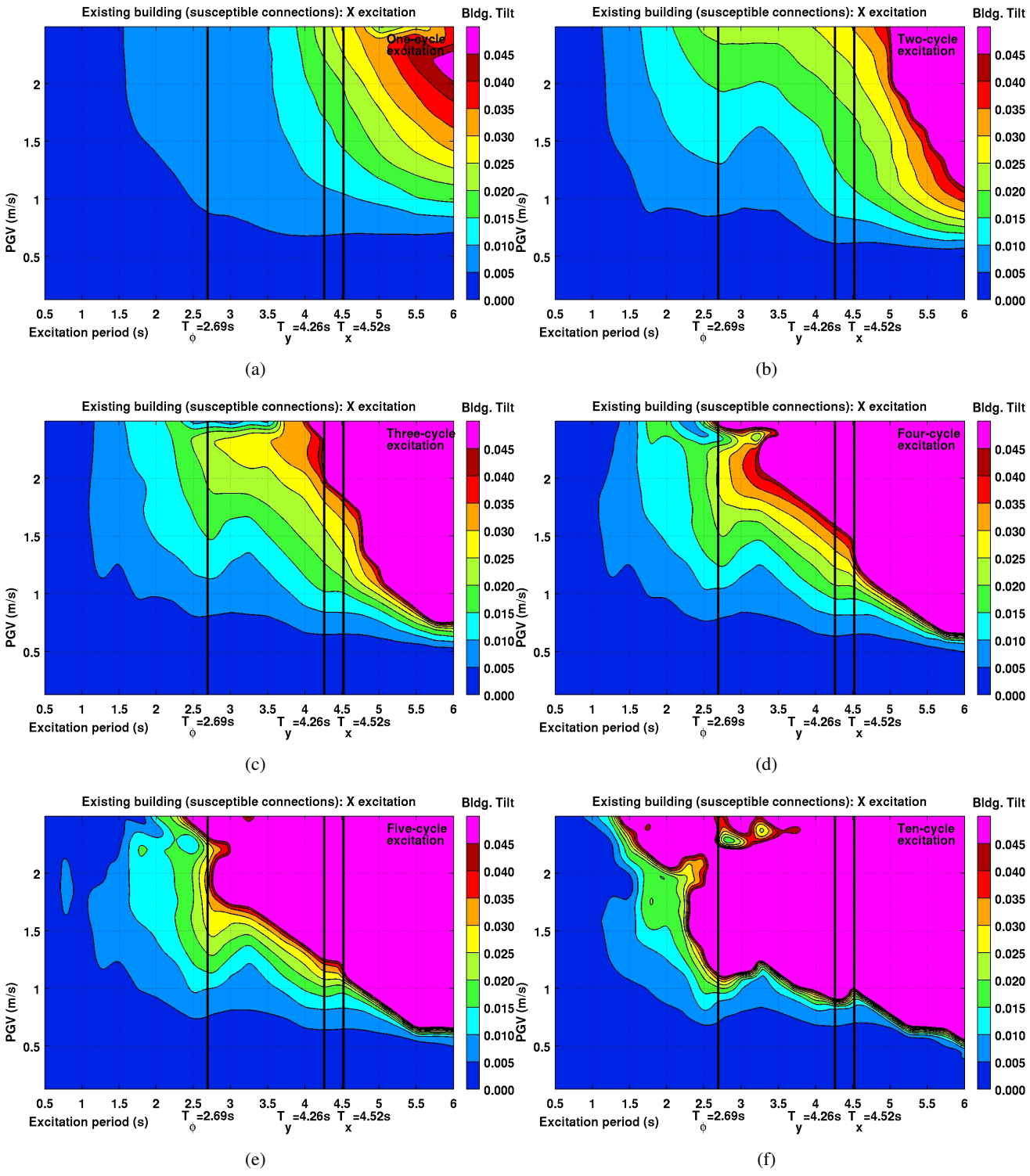

Figure A.5: Permanent roof drift (roof residual displacement normalized by building height) in the existing building (susceptible connections) as a function of idealized saw-tooth waveform excitation parameters, period T, peak ground velocity PGV, and number of cycles N. The one-component ground motion is applied in the building X direction. The principal direction building fundamental periods are indicated for reference.

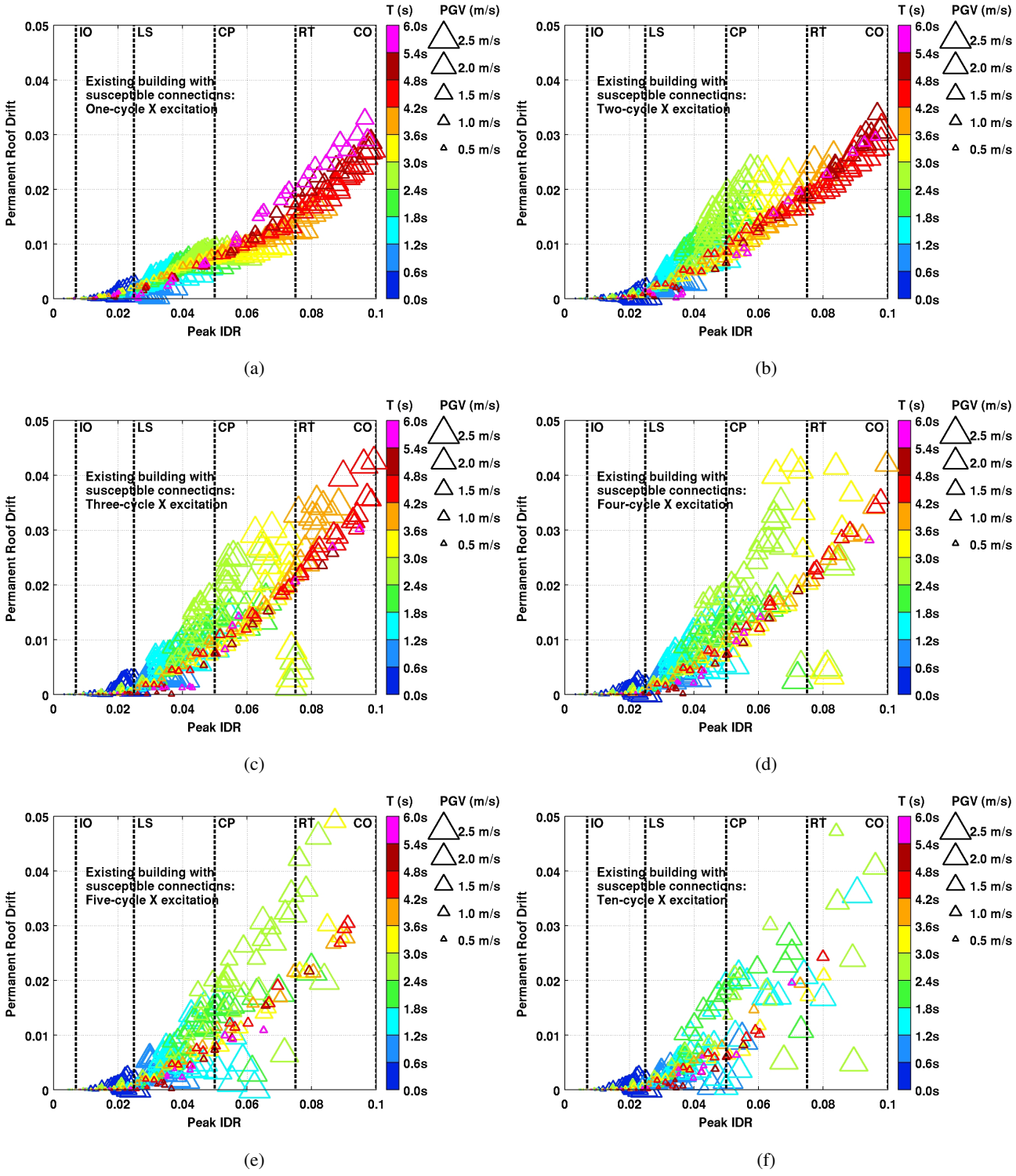

Figure A.6: Permanent roof drift (roof residual displacement normalized by building height) in the existing building (susceptible connections) plotted as a function of the peak transient interstory drift ratio (IDR) under idealized saw-tooth waveform excitation. The results for 1-, 2-, 3-, 4-, 5-, and 10-cycle excitations are shown separately. The one-component ground motion is applied in the building X direction. Points corresponding to peak transient IDR > 0.10 are indicative of near-certain collapse; permanent roof drift is no longer meaningful. Hence, these points are not shown. The empirical immediate occupancy (IO), life-safety (LS), collapse prevention (CP), red-tagged (RT), and collapsed (CO) performance levels are marked on the IDR axis.

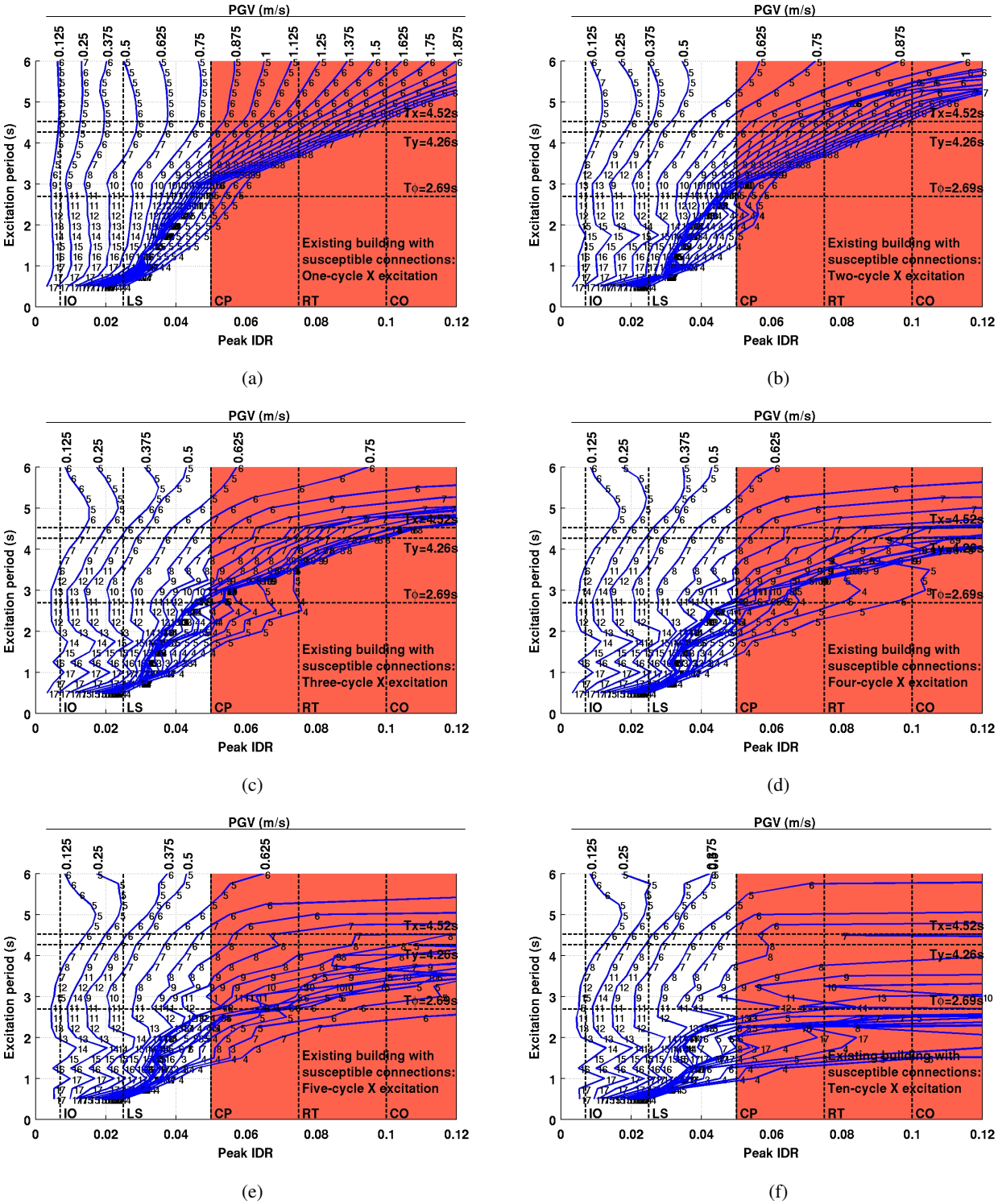

Figure A.7: Peak transient interstory drift ratio (IDR) is shown plotted against the idealized saw-tooth waveform excitation period (T) for the existing building (susceptible connections) at various levels of peak ground velocity (PGV). Each subfigure corresponds to a different number of excitation cycles. The one-component ground motion is applied in the building X direction. The story location where the peak occurs is labeled at each of the 460 [T,PGV] combinations for which analyses were performed. The empirical immediate occupancy (IO), life-safety (LS), collapse prevention (CP), red-tagged (RT), and collapsed (CO) performance levels are marked on the IDR axis. The principal direction building fundamental periods are indicated for reference.

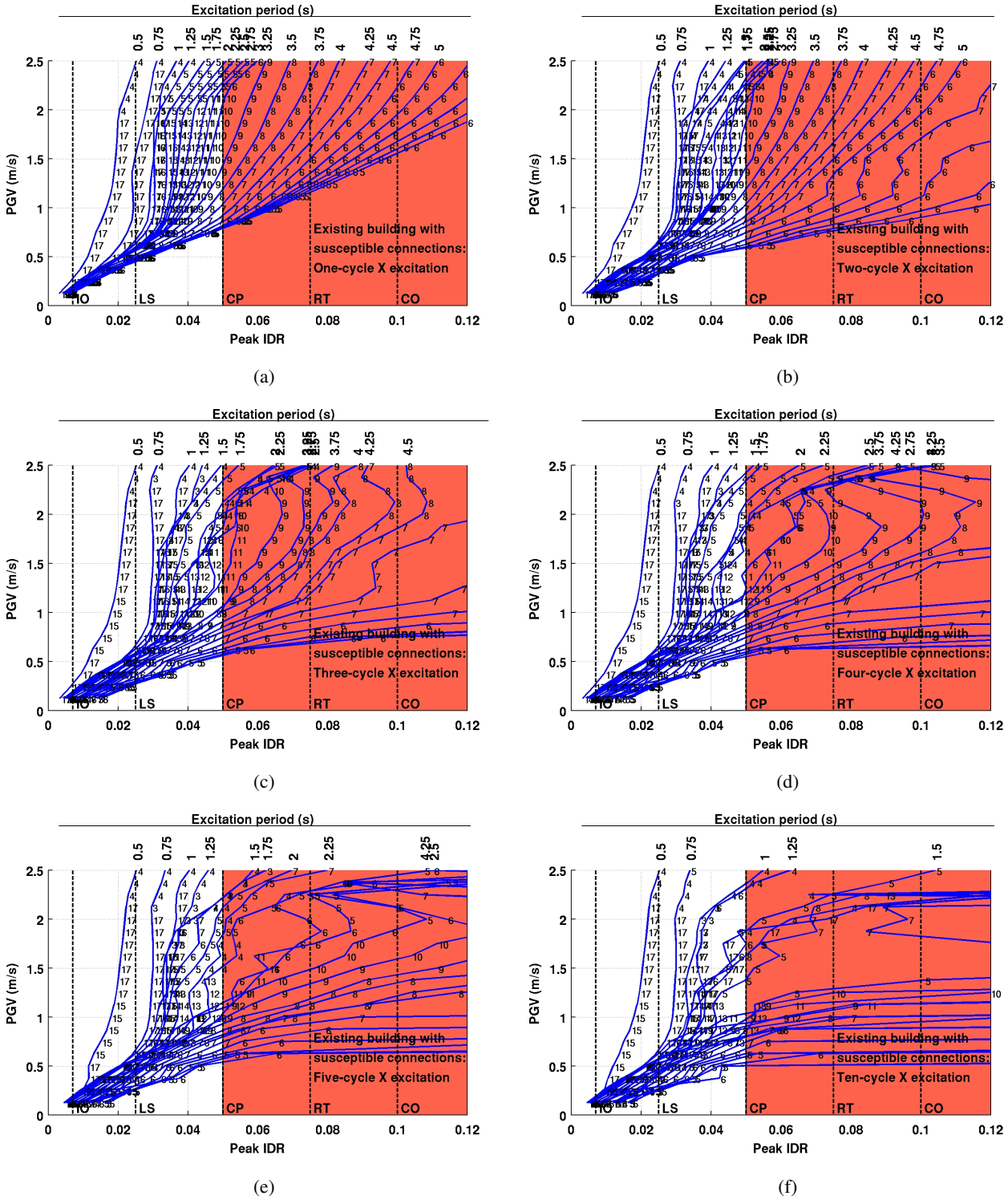

Figure A.8: Peak transient interstory drift ratio (IDR) is shown plotted against the idealized saw-tooth waveform excitation peak ground velocity (PGV) for the existing building (susceptible connections) at various levels of waveform periods (T). Each subfigure corresponds to a different number of excitation cycles. The one-component ground motion is applied in the building X direction. The story location where the peak occurs is labeled at each of the 460 [T,PGV] combinations for which analyses were performed. The empirical immediate occupancy (IO), life-safety (LS), collapse prevention (CP), red-tagged (RT), and collapsed (CO) performance levels are marked on the IDR axis.

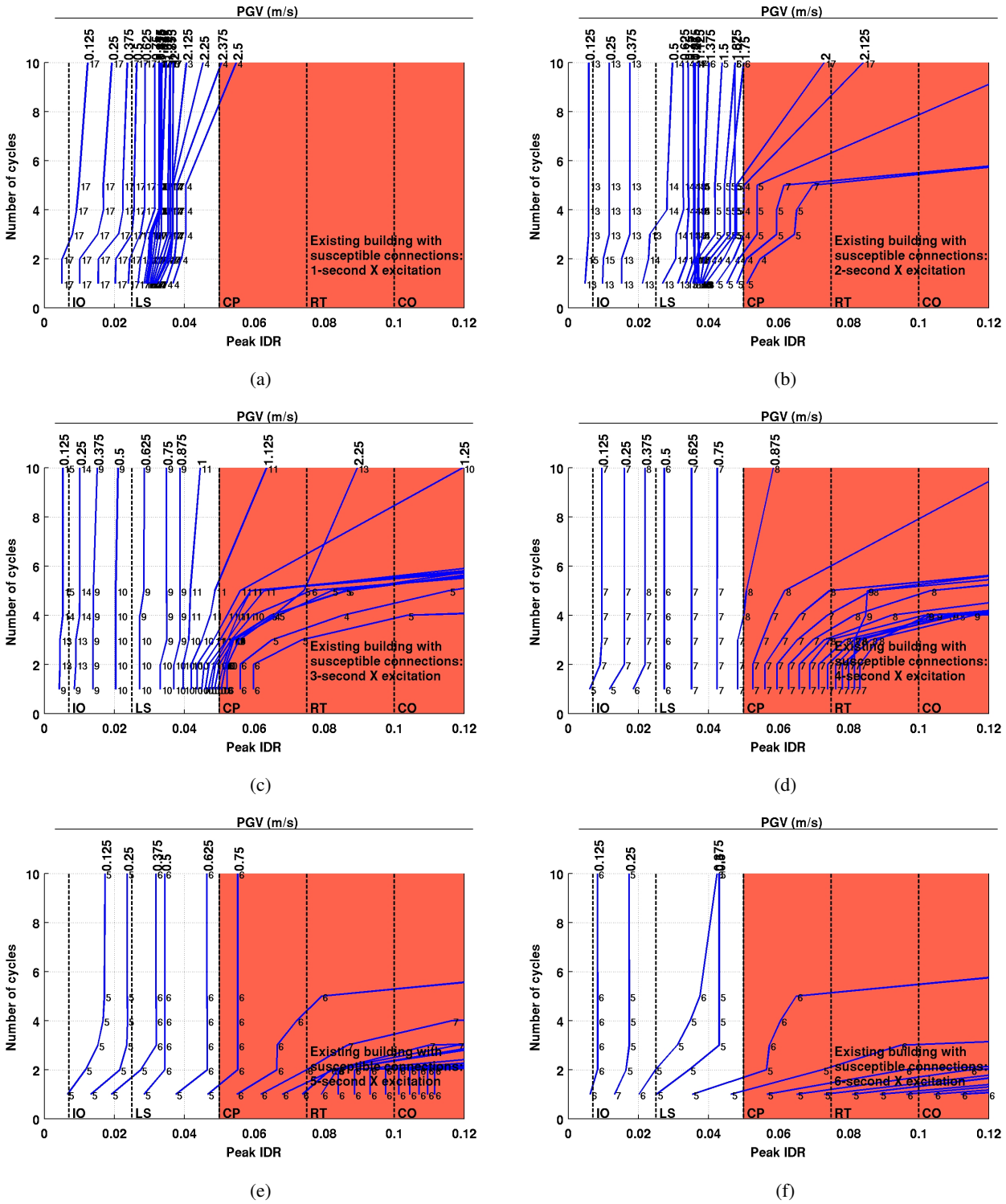

Figure A.9: Peak transient interstory drift ratio (IDR) is shown plotted against the number of cycles (N) in the idealized saw-tooth waveform excitation for the existing building (susceptible connections) at various levels of peak ground velocity (PGV). Each subfigure corresponds to a different excitation period (1s–6s). The one-component ground motion is applied in the building X direction. The story location where the peak occurs is labeled at each of the 460 [T,PGV] combinations for which analyses were performed. The empirical immediate occupancy (IO), life-safety (LS), collapse prevention (CP), red-tagged (RT), and collapsed (CO) performance levels are marked on the IDR axis.

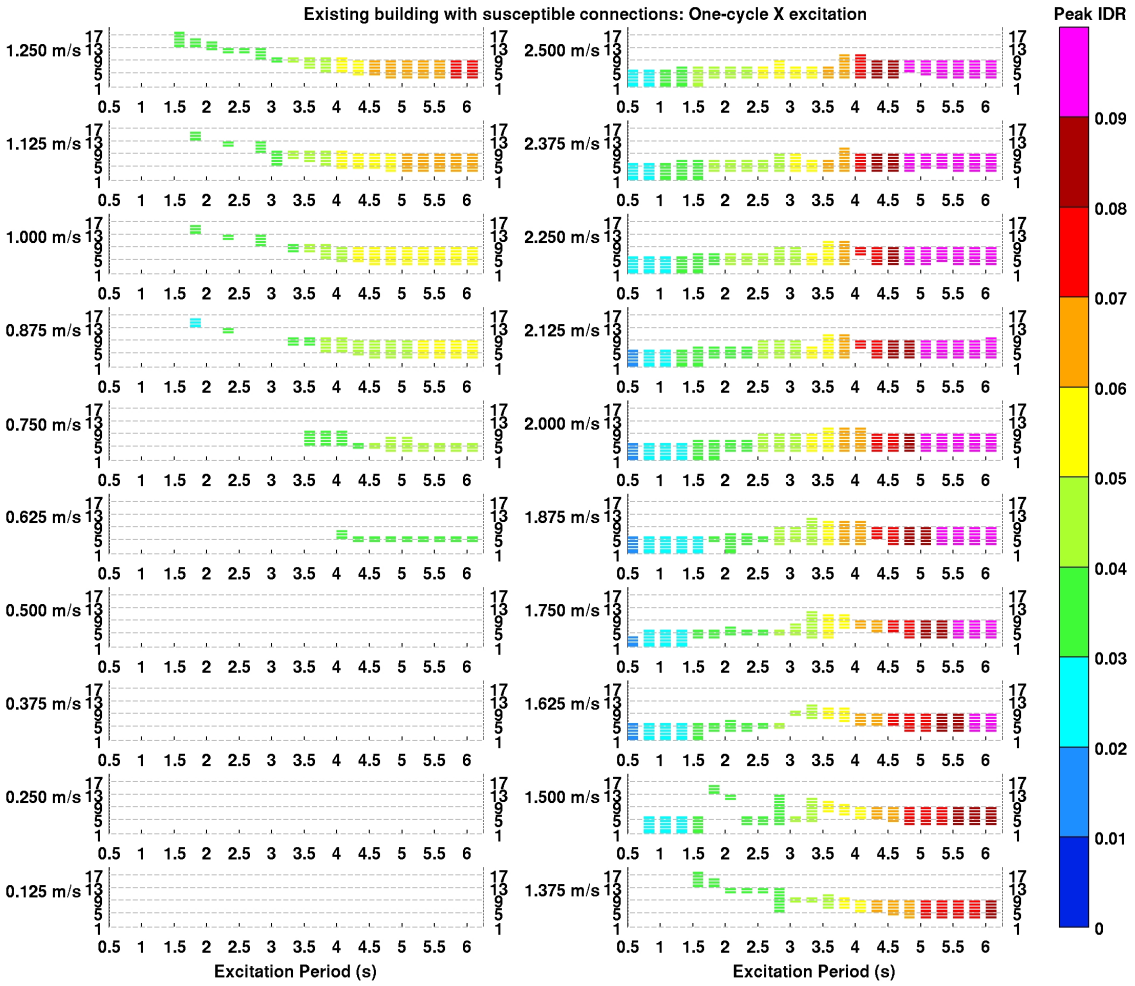

(a) Story extent of band for each (T,PGV) combination.

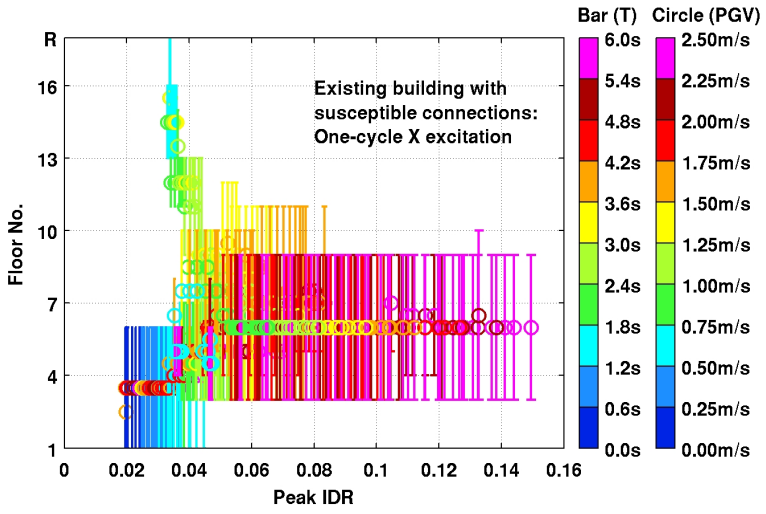

(b) Story extent of bands for all (T,PGV) combinations. Bar color identifies the excitation period and circle color identifies the peak ground velocity.

Figure A.10: Principal quasi-shear bands in the existing building (susceptible connections) subjected to one-cycle idealized waveforms in the X direction.

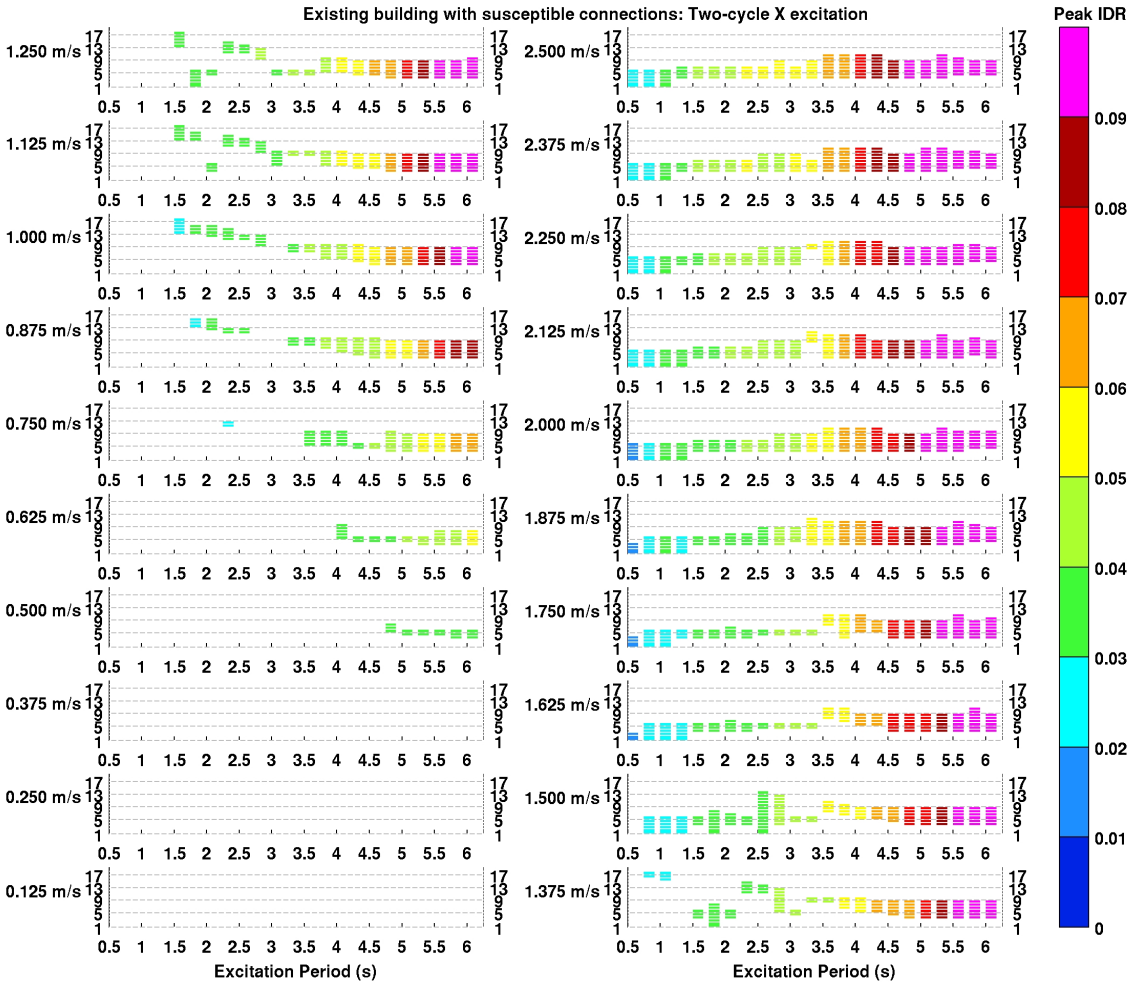

(a) Story extent of band for each (T,PGV) combination.

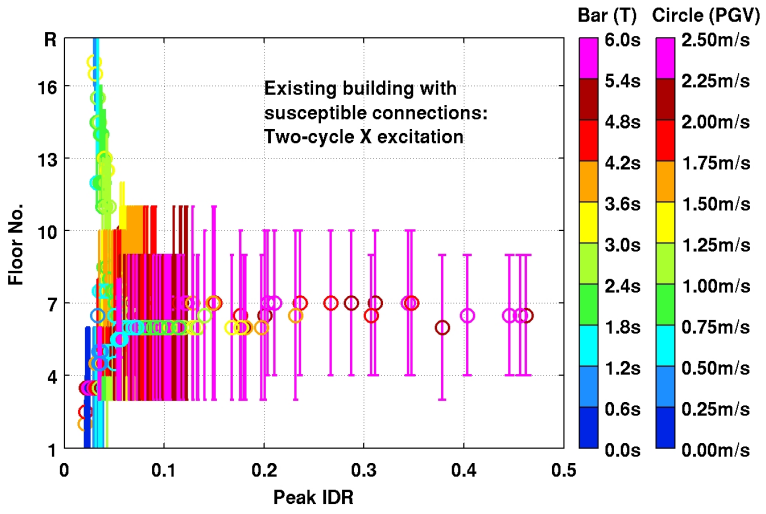

(b) Story extent of bands for all (T,PGV) combinations. Bar color identifies the excitation period and circle color identifies the peak ground velocity.

Figure A.11: Principal quasi-shear bands in the existing building (susceptible connections) subjected to two-cycle idealized waveforms in the X direction.

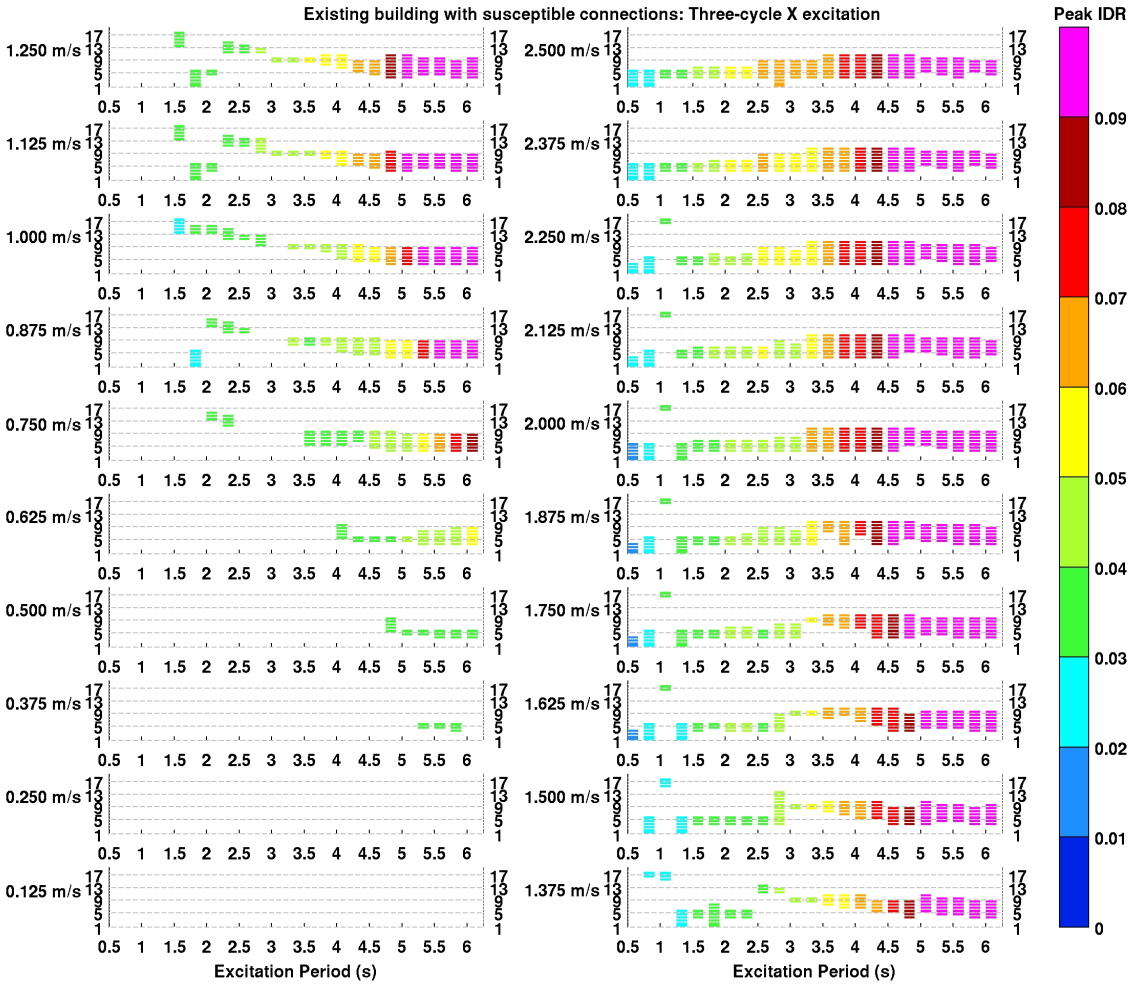

(a) Story extent of band for each (T,PGV) combination.

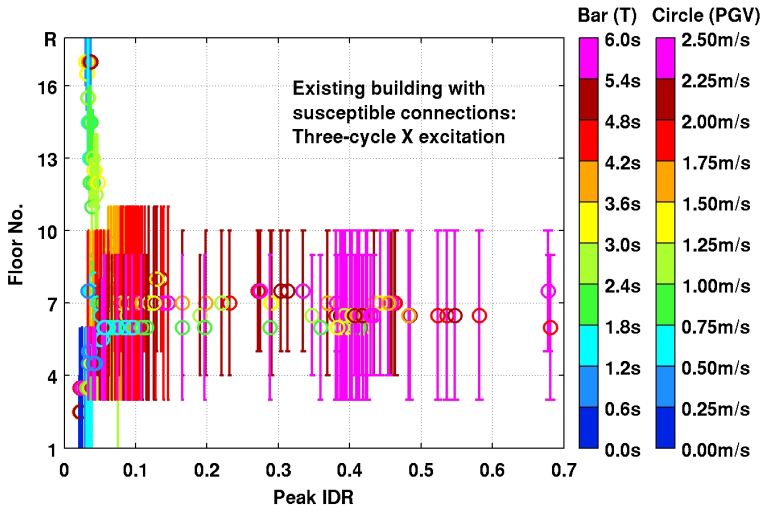

(b) Story extent of bands for all (T,PGV) combinations. Bar color identifies the excitation period and circle color identifies the peak ground velocity.

Figure A.12: Principal quasi-shear bands in the existing building (susceptible connections) subjected to three-cycle idealized waveforms in the X direction.

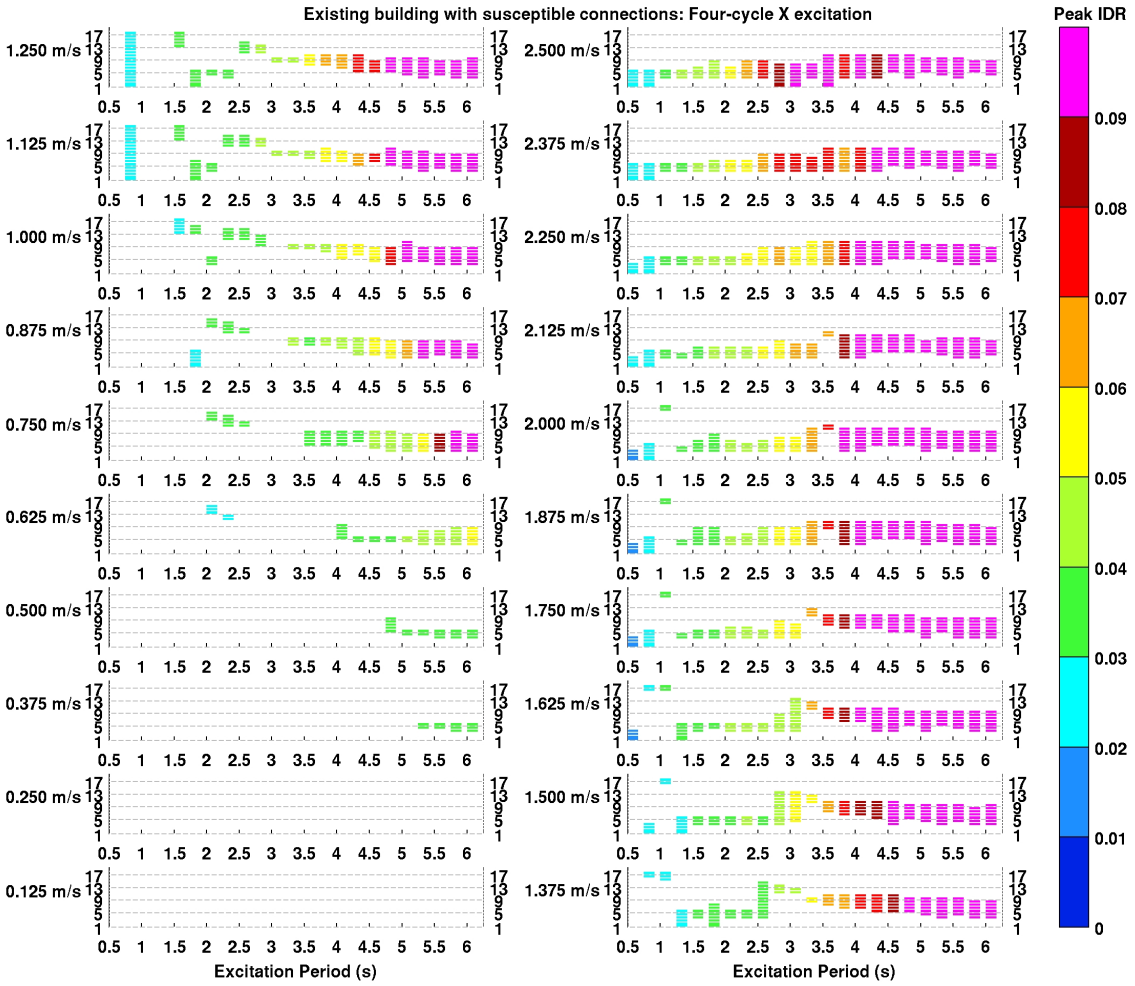

(a) Story extent of band for each (T,PGV) combination.

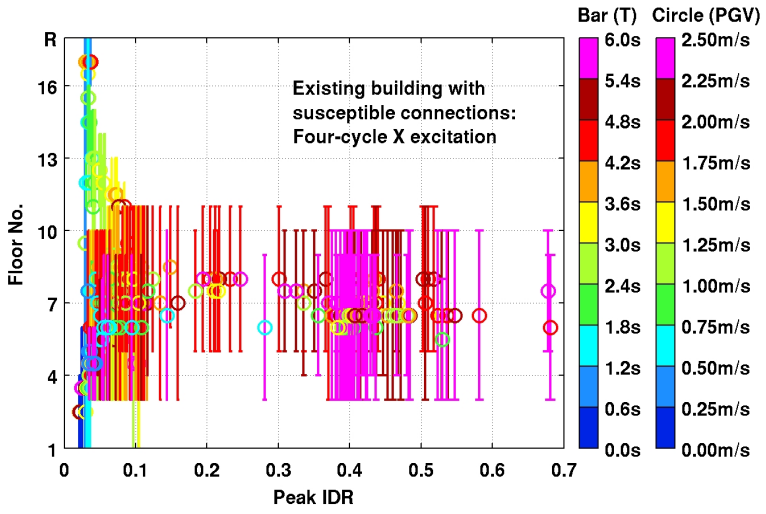

(b) Story extent of bands for all (T,PGV) combinations. Bar color identifies the excitation period and circle color identifies the peak ground velocity.

Figure A.13: Principal quasi-shear bands in the existing building (susceptible connections) subjected to four-cycle idealized waveforms in the X direction.

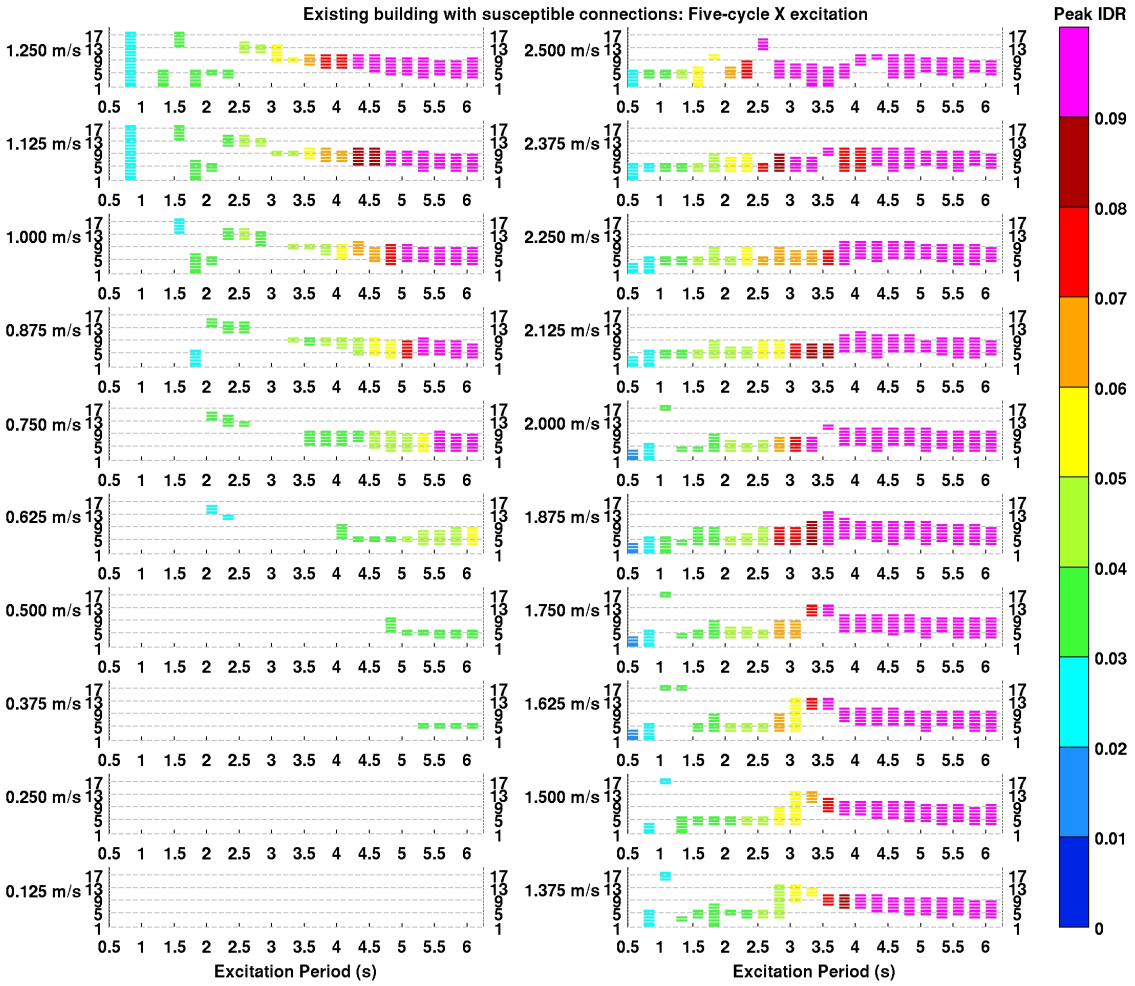

(a) Story extent of band for each (T,PGV) combination.

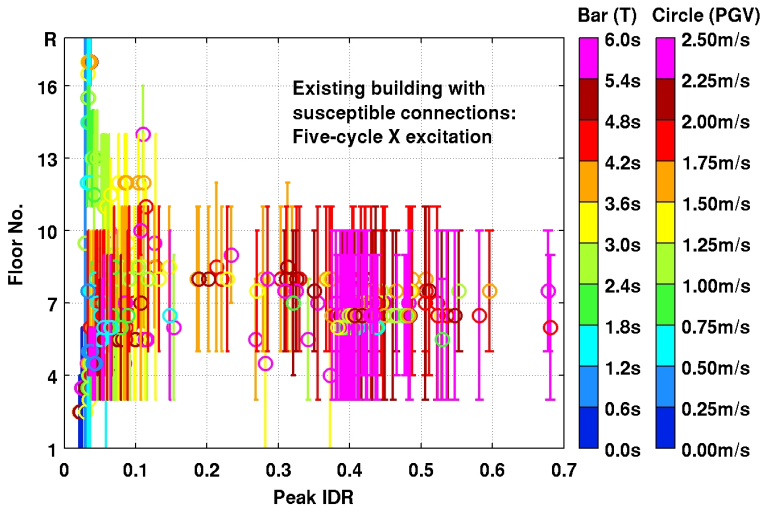

(b) Story extent of bands for all (T,PGV) combinations. Bar color identifies the excitation period and circle color identifies the peak ground velocity.

Figure A.14: Principal quasi-shear bands in the existing building (susceptible connections) subjected to five-cycle idealized waveforms in the X direction.

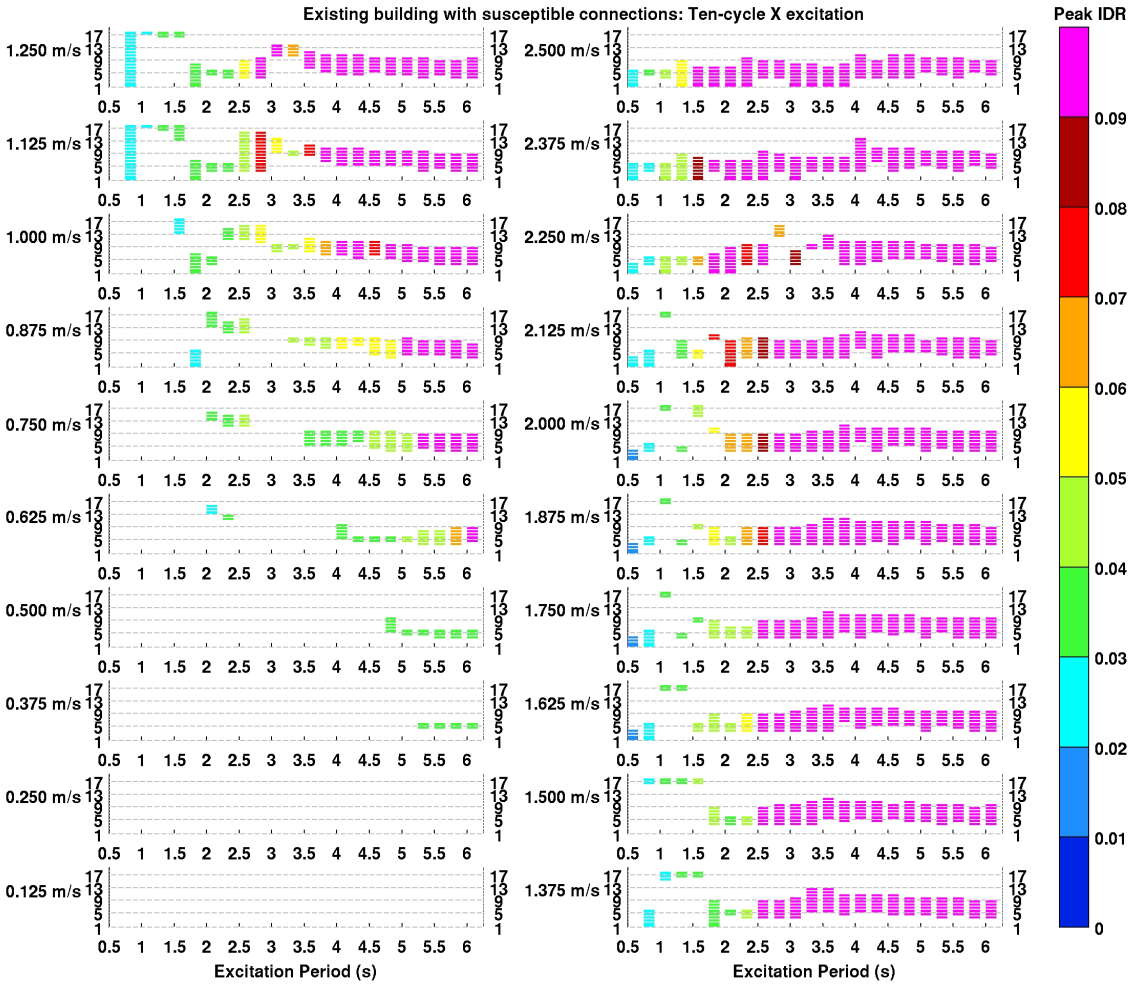

(a) Story extent of band for each (T,PGV) combination.

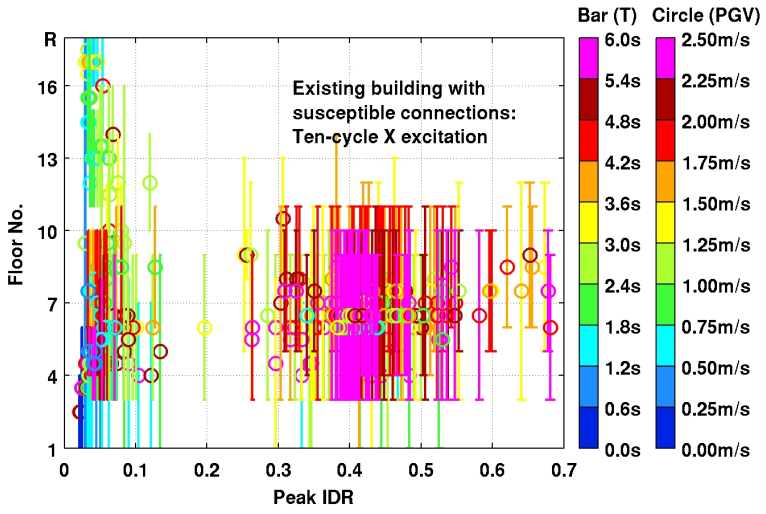

(b) Story extent of bands for all (T,PGV) combinations. Bar color identifies the excitation period and circle color identifies the peak ground velocity.

Figure A.15: Principal quasi-shear bands in the existing building (susceptible connections) subjected to ten-cycle idealized waveforms in the X direction.

Appendix B Existing (UBC 1982) Building with Perfect Connections: Archive of Response Parameters Under Idealized-Waveform Shaking in X Direction

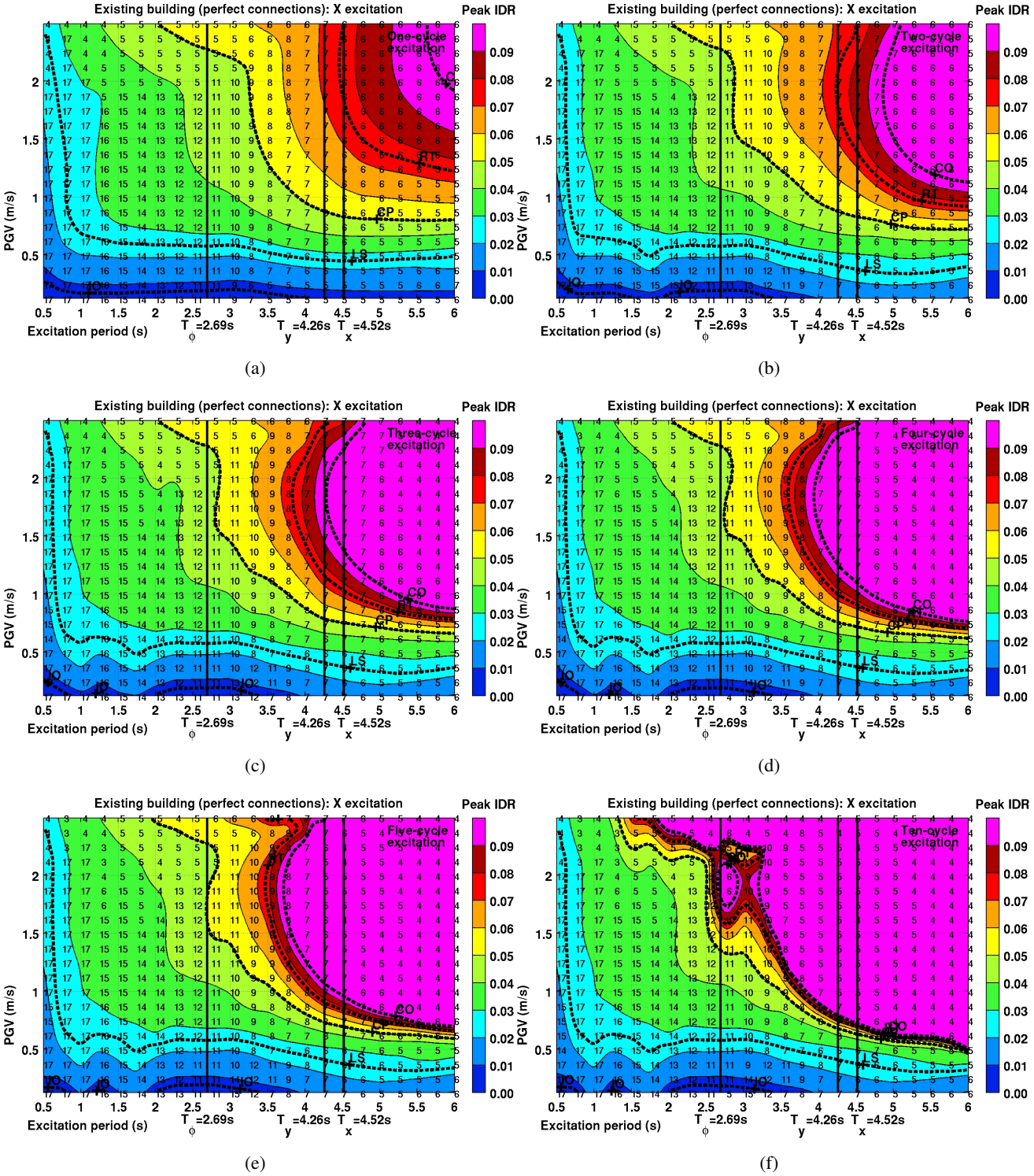

Figure B.1: Peak transient interstory drift ratio (IDR) maps for the existing building (perfect connections) as a function of idealized saw-tooth waveform excitation parameters, period T, peak ground velocity PGV, and number of cycles N. The one-component ground motion is applied in the building X direction. The story location where the peak occurs is labeled at each of the 460 [T,PGV] combinations for which analyses were performed. Contours corresponding to the empirical immediate occupancy (IO), life-safety (LS), collapse prevention (CP), red-tagged (RT), and collapsed (CO) performance levels are shown in bold font. The principal direction building fundamental periods are indicated for reference.

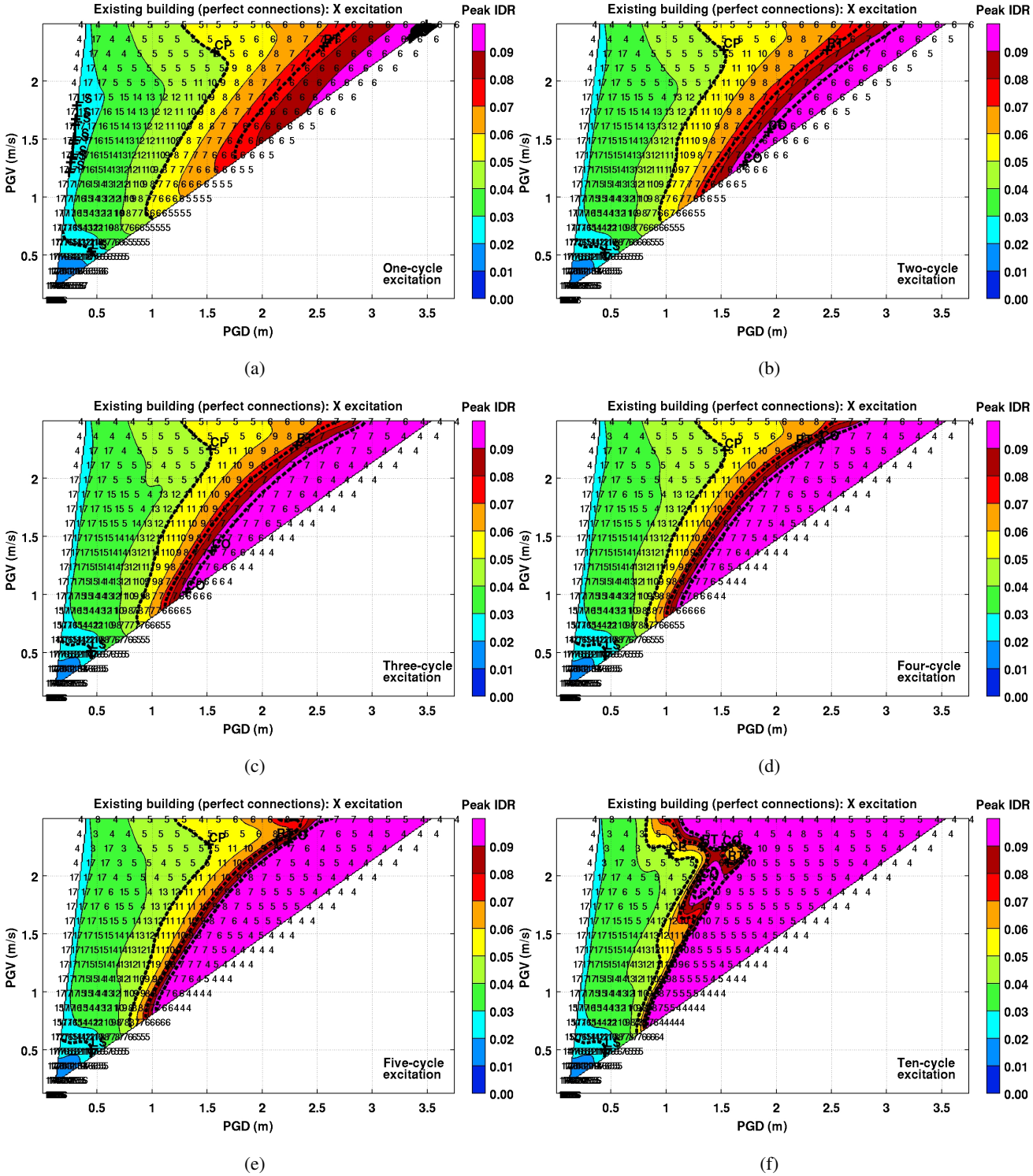

Figure B.2: The peak transient interstory drift ratio (IDR) maps for the existing building (perfect connections) from Figure B.1 transformed to the peak ground displacement (PGD) - peak ground velocity (PGV) plane. The story location where the peak occurs is labeled at each of the 460 [T,PGV] combinations for which analyses were performed. Contours corresponding to the empirical immediate occupancy (IO), life-safety (LS), collapse prevention (CP), red-tagged (RT), and collapsed (CO) performance levels are also transformed and shown in bold font.

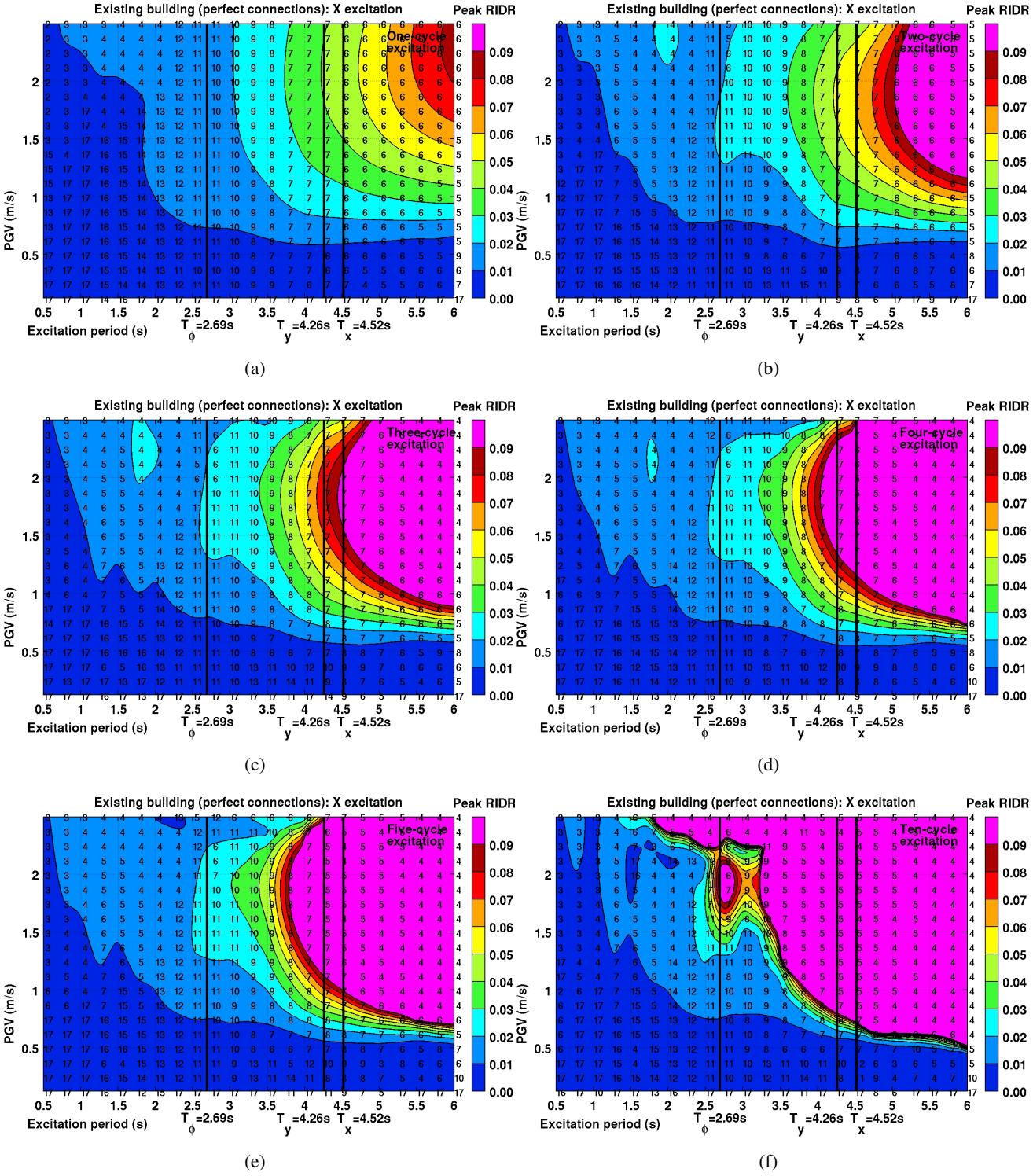

Figure B.3: Peak residual interstory drift ratio (RIDR) maps for the existing building (perfect connections) as a function of idealized saw-tooth waveform excitation parameters, period T, peak ground velocity PGV, and number of cycles N. The one-component ground motion is applied in the building X direction. The story location where the peak occurs is labeled at each of the 460 [T,PGV] combinations for which analyses were performed. The principal direction building fundamental periods are indicated for reference.

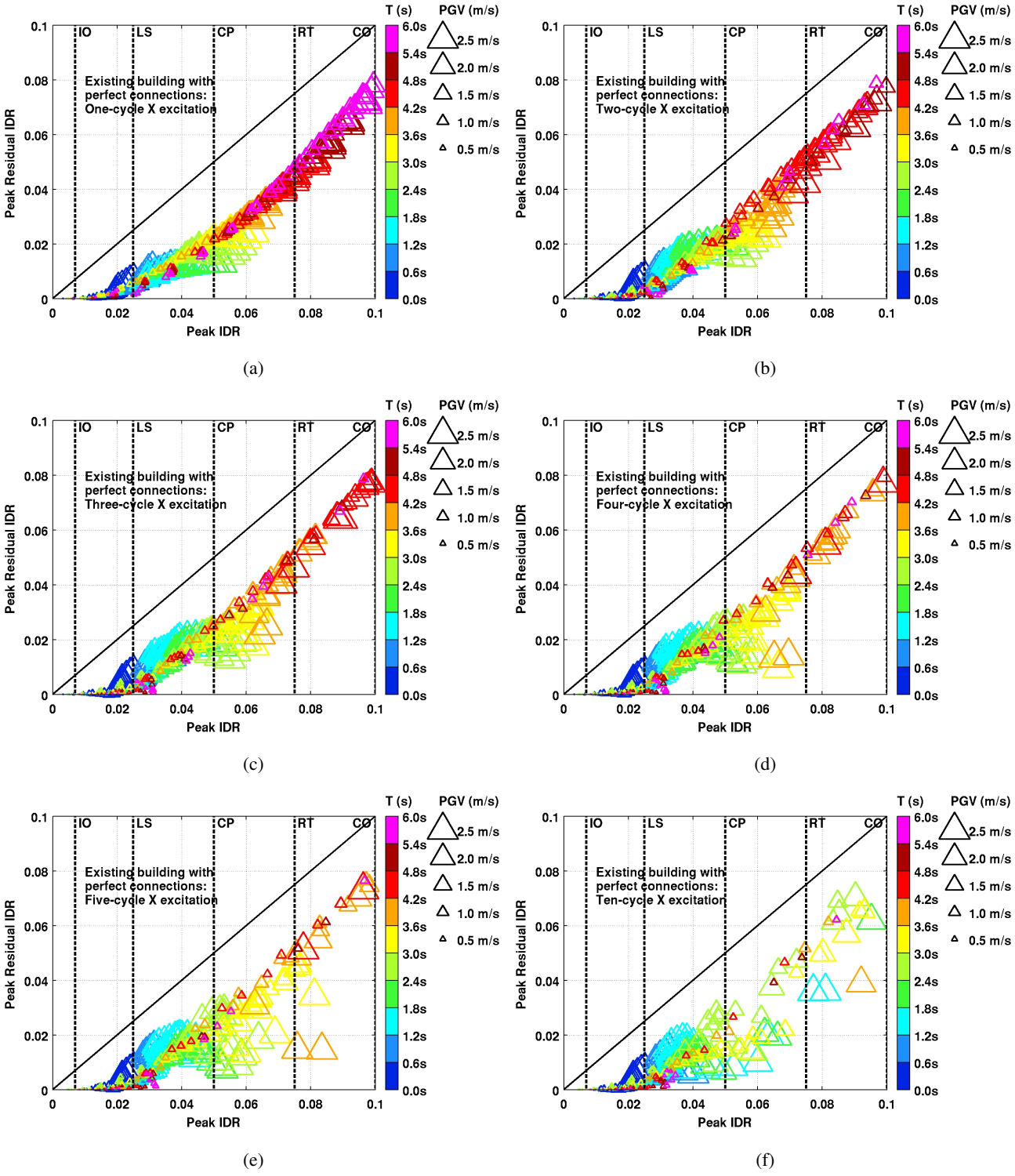

Figure B.4: Peak residual interstory drift ratio (RIDR) in the existing building (perfect connections) plotted as a function of the peak transient IDR under idealized saw-tooth waveform excitation. The results for 1-, 2-, 3-, 4-, 5-, and 10-cycle excitations are shown separately. The one-component ground motion is applied in the building X direction. Points corresponding to peak transient IDR > 0.10 are indicative of near-certain collapse; residual IDR is no longer meaningful. Hence, these points are not shown. The empirical immediate occupancy (IO), life-safety (LS), collapse prevention (CP), red-tagged (RT), and collapsed (CO) performance levels are marked on the IDR axis.

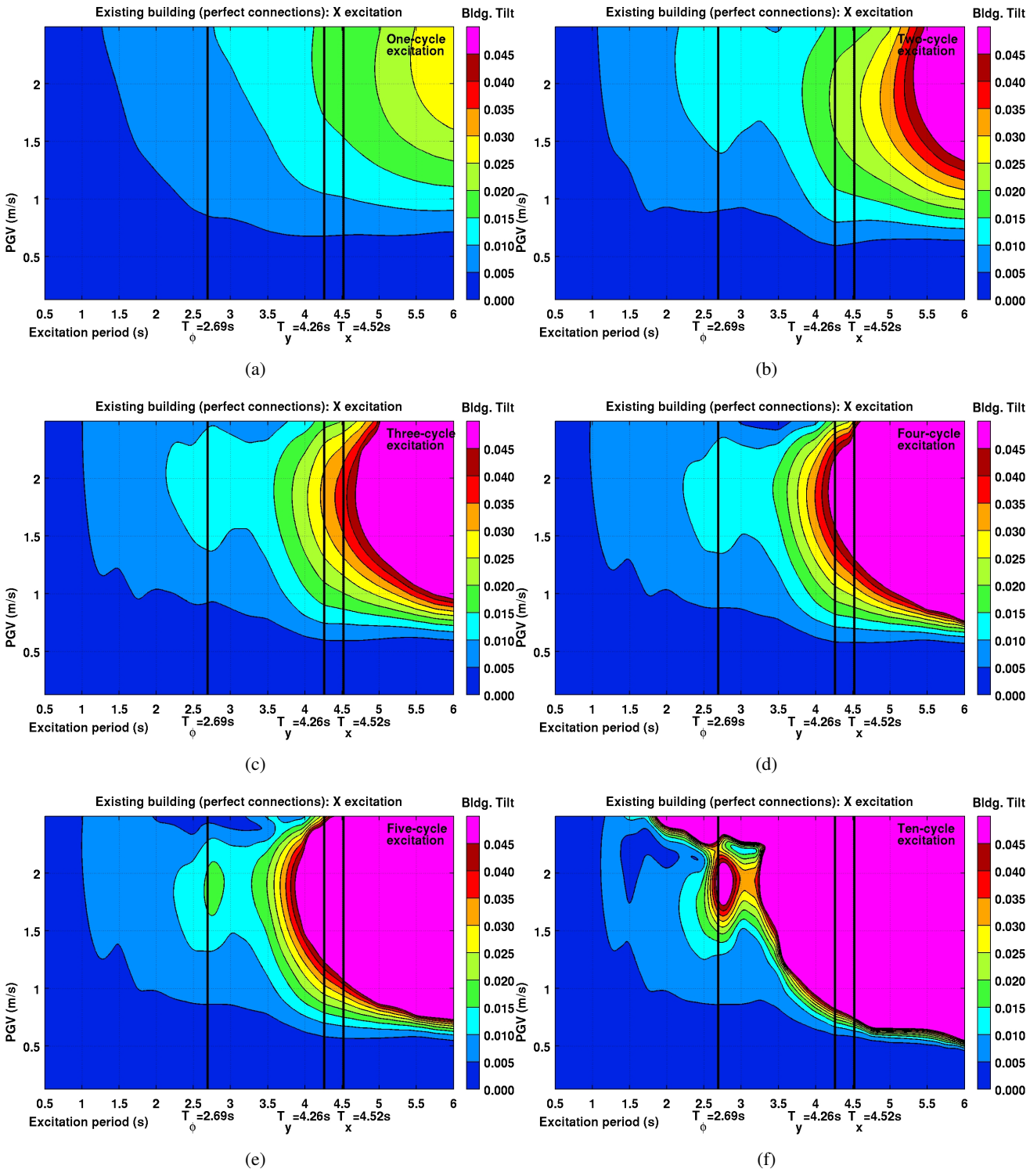

Figure B.5: Permanent roof drift (roof residual displacement normalized by building height) in the existing building (perfect connections) as a function of idealized saw-tooth waveform excitation parameters, period T, peak ground velocity PGV, and number of cycles N. The one-component ground motion is applied in the building X direction. The principal direction building fundamental periods are indicated for reference.

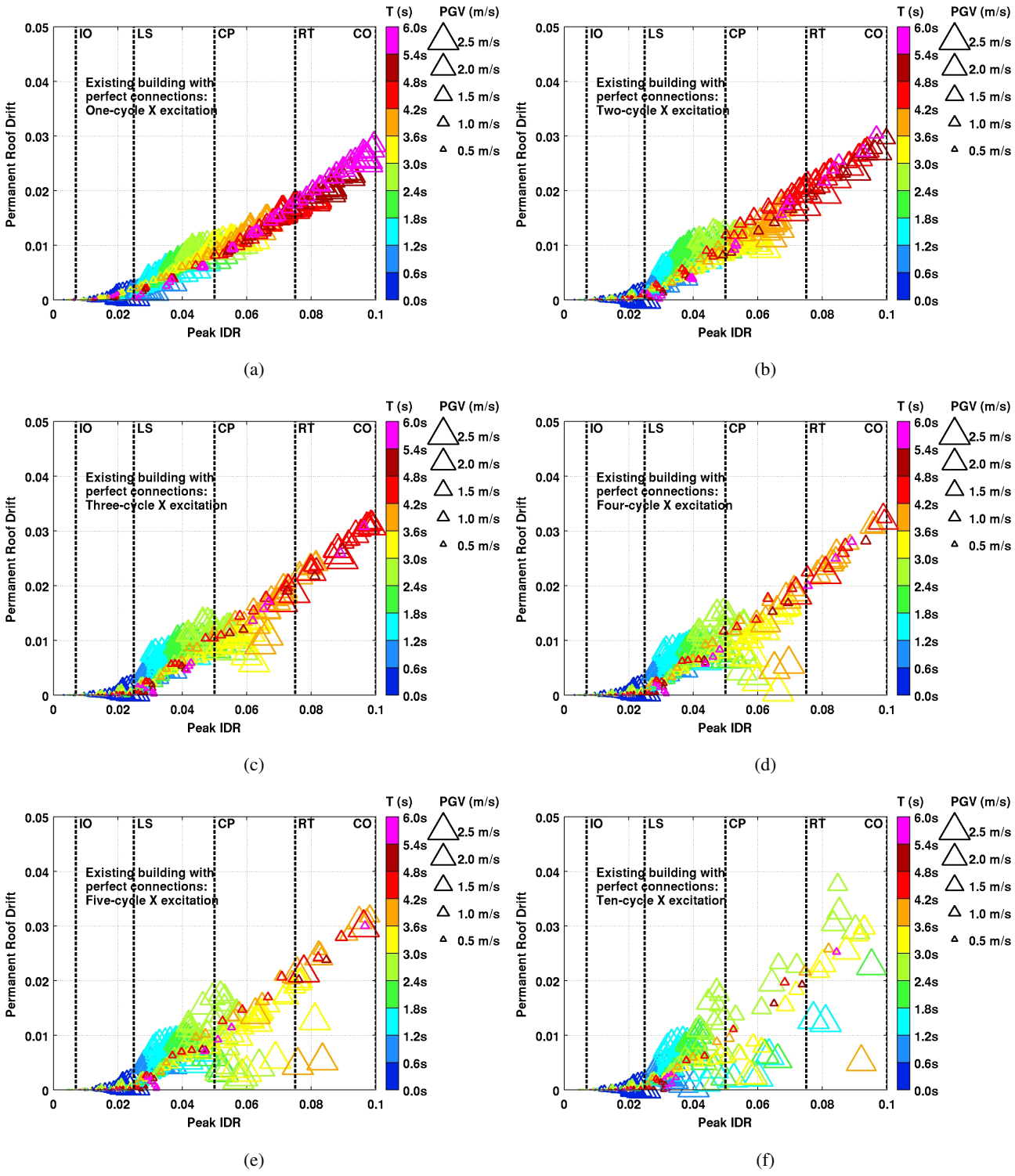

Figure B.6: Permanent roof drift (roof residual displacement normalized by building height) in the existing building (perfect connections) plotted as a function of the peak transient interstory drift ratio (IDR) under idealized saw-tooth waveform excitation. The results for 1-, 2-, 3-, 4-, 5-, and 10-cycle excitations are shown separately. The one-component ground motion is applied in the building X direction. Points corresponding to peak transient IDR > 0.10 are indicative of near-certain collapse; permanent roof drift is no longer meaningful. Hence, these points are not shown. The empirical immediate occupancy (IO), life-safety (LS), collapse prevention (CP), red-tagged (RT), and collapsed (CO) performance levels are marked on the IDR axis.

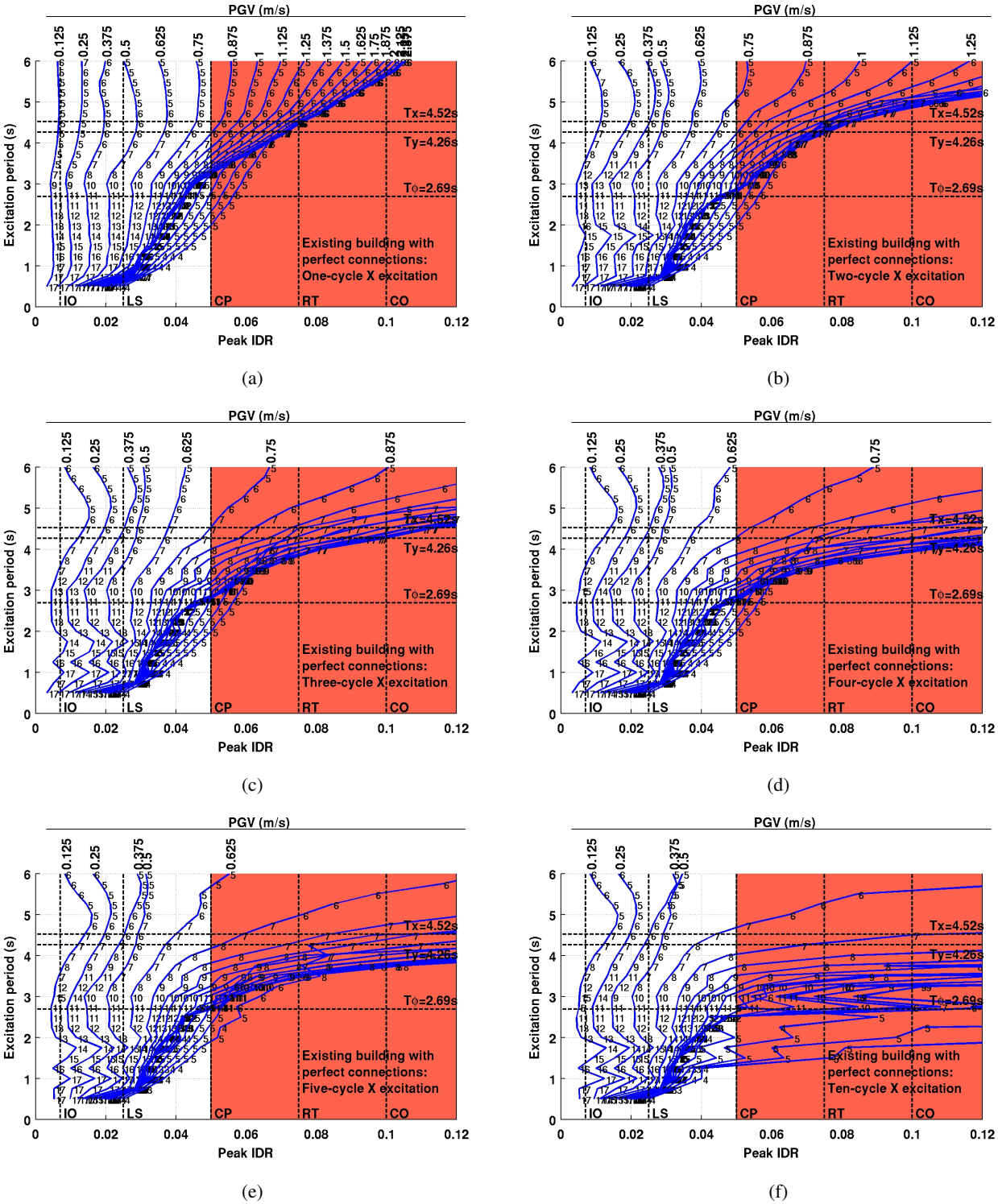

Figure B.7: Peak transient interstory drift ratio (IDR) is shown plotted against the idealized saw-tooth waveform excitation period (T) for the existing building (perfect connections) at various levels of peak ground velocity (PGV). Each subfigure corresponds to a different number of excitation cycles. The one-component ground motion is applied in the building X direction. The story location where the peak occurs is labeled at each of the 460 [T,PGV] combinations for which analyses were performed. The empirical immediate occupancy (IO), life-safety (LS), collapse prevention (CP), red-tagged (RT), and collapsed (CO) performance levels are marked on the IDR axis. The principal direction building fundamental periods are indicated for reference.

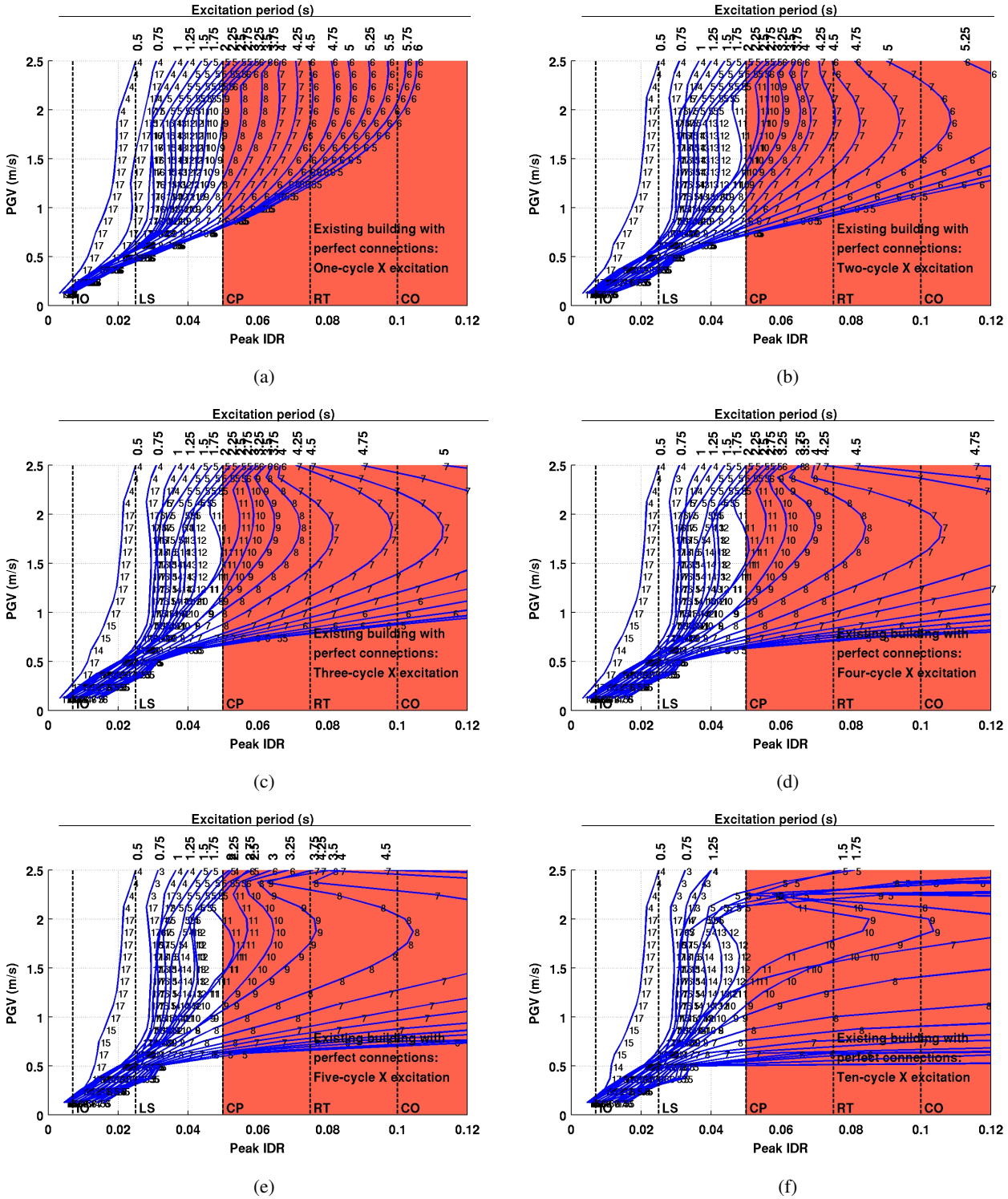

Figure B.8: Peak transient interstory drift ratio (IDR) is shown plotted against the idealized saw-tooth waveform excitation peak ground velocity (PGV) for the existing building (perfect connections) at various levels of waveform periods (T) . Each subfigure corresponds to a different number of excitation cycles. The one-component ground motion is applied in the building X direction. The story location where the peak occurs is labeled at each of the 460 [T,PGV] combinations for which analyses were performed. The empirical immediate occupancy (IO), life-safety (LS), collapse prevention (CP), red-tagged (RT), and collapsed (CO) performance levels are marked on the IDR axis.

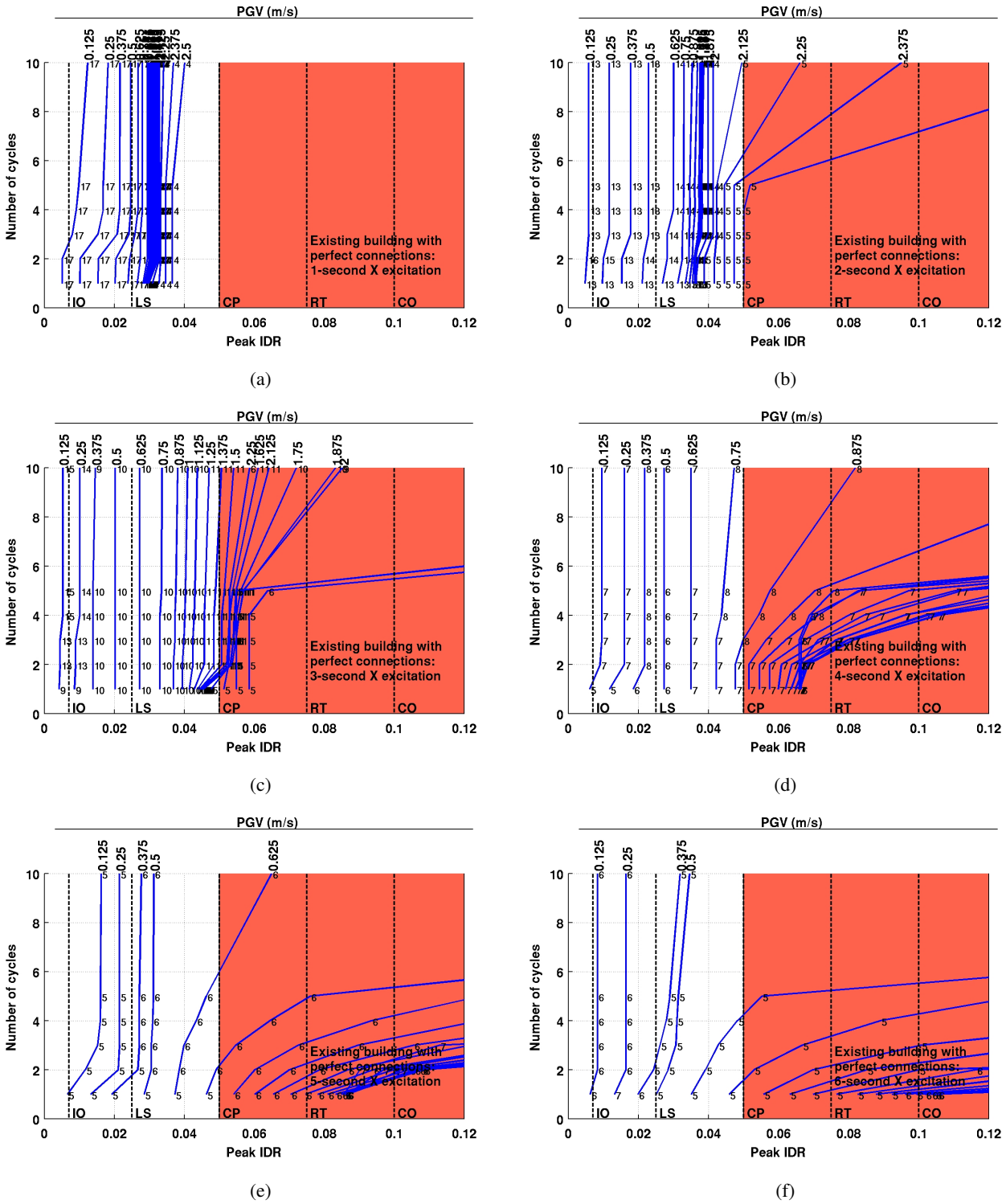

Figure B.9: Peak transient interstory drift ratio (IDR) is shown plotted against the number of cycles (N) in the idealized saw-tooth waveform excitation for the existing building (perfect connections) at various levels of peak ground velocity (PGV). Each subfigure corresponds to a different excitation period (1s–6s). The one-component ground motion is applied in the building X direction. The story location where the peak occurs is labeled at each of the 460 [T,PGV] combinations for which analyses were performed. The empirical immediate occupancy (IO), life-safety (LS), collapse prevention (CP), red-tagged (RT), and collapsed (CO) performance levels are marked on the IDR axis.

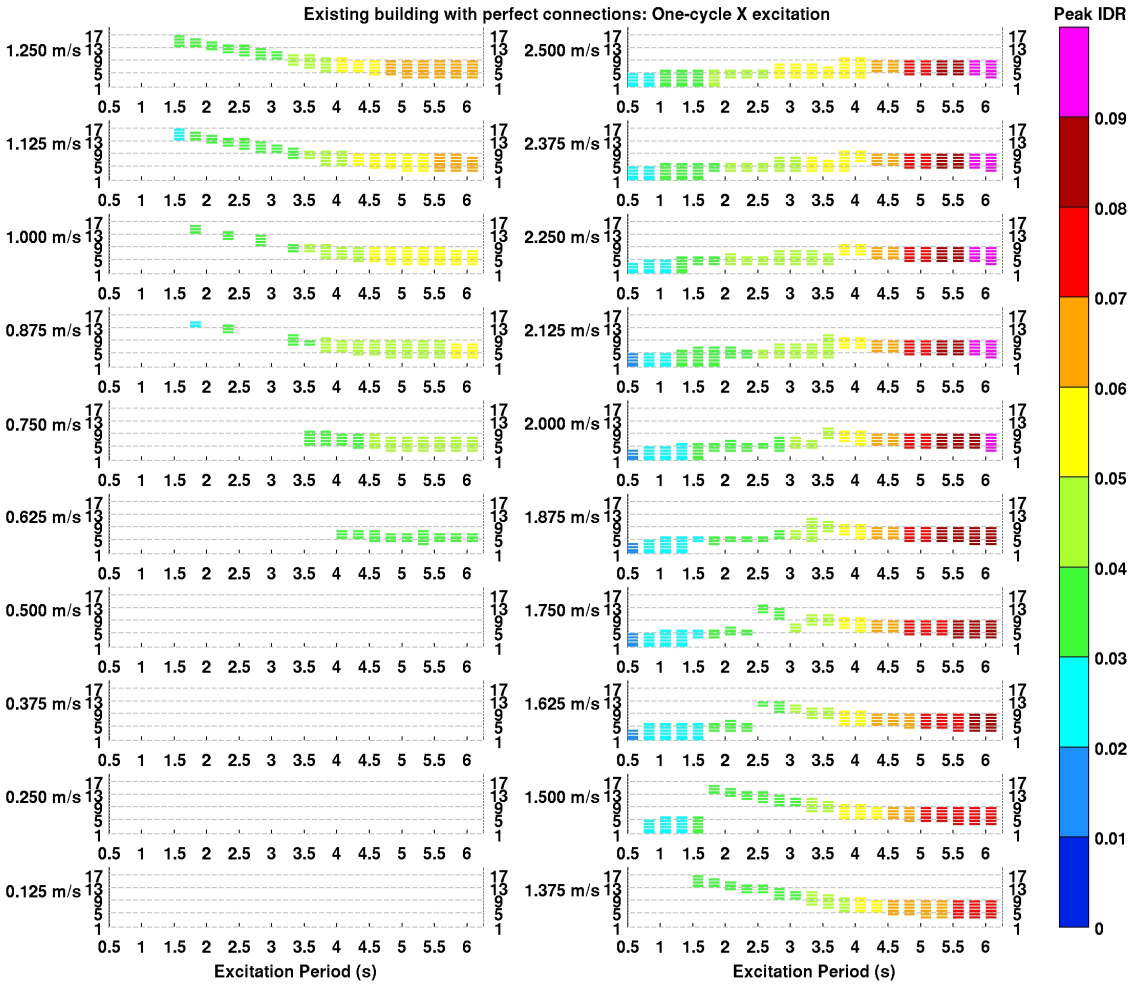

(a) Story extent of band for each (T,PGV) combination.

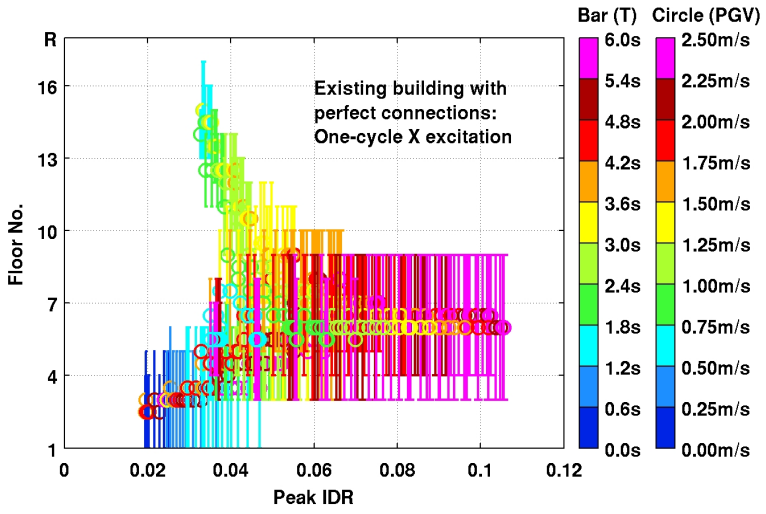

(b) Story extent of bands for all (T,PGV) combinations. Bar color identifies the excitation period and circle color identifies the peak ground velocity.

Figure B.10: Principal quasi-shear bands in the existing building (perfect connections) subjected to one-cycle idealized waveforms in the X direction.

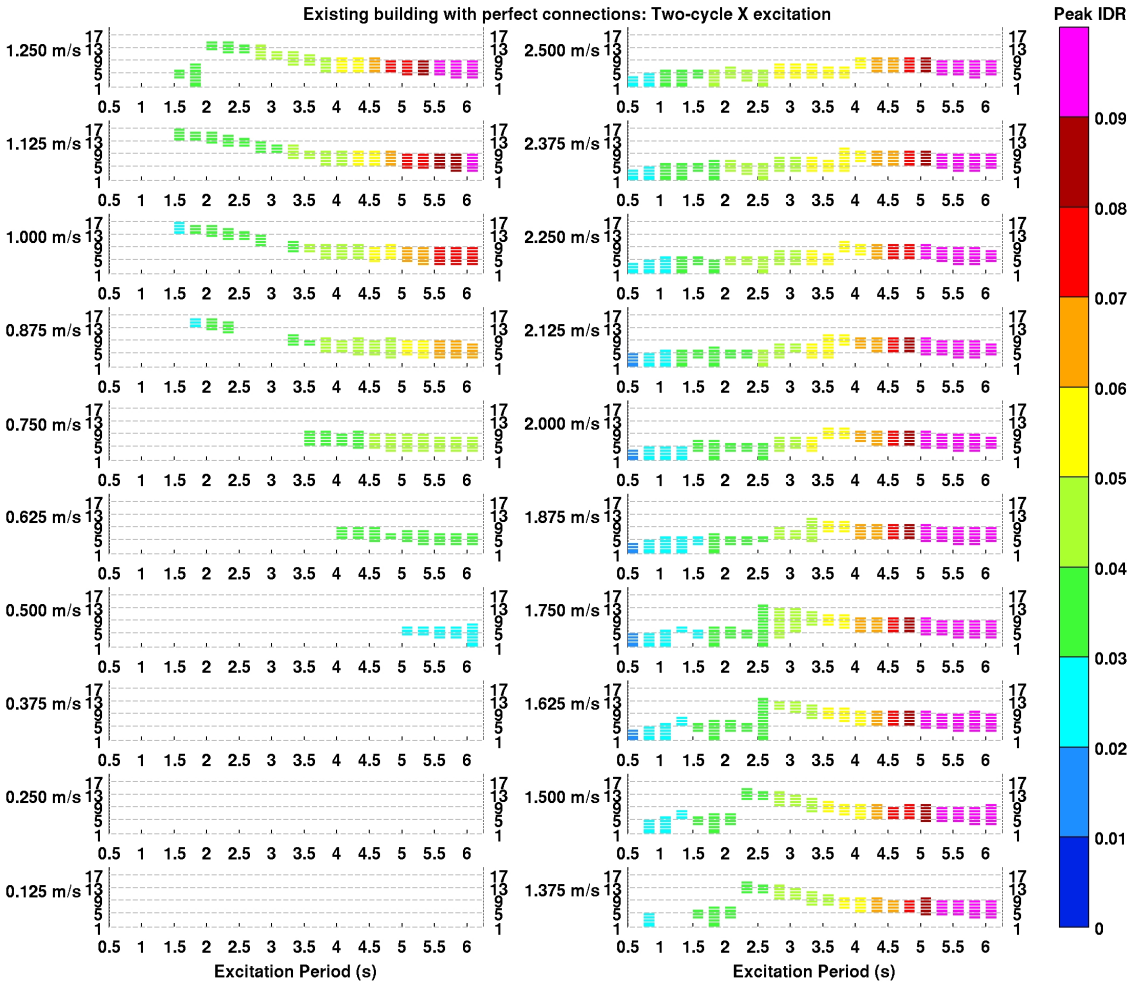

(a) Story extent of band for each (T,PGV) combination.

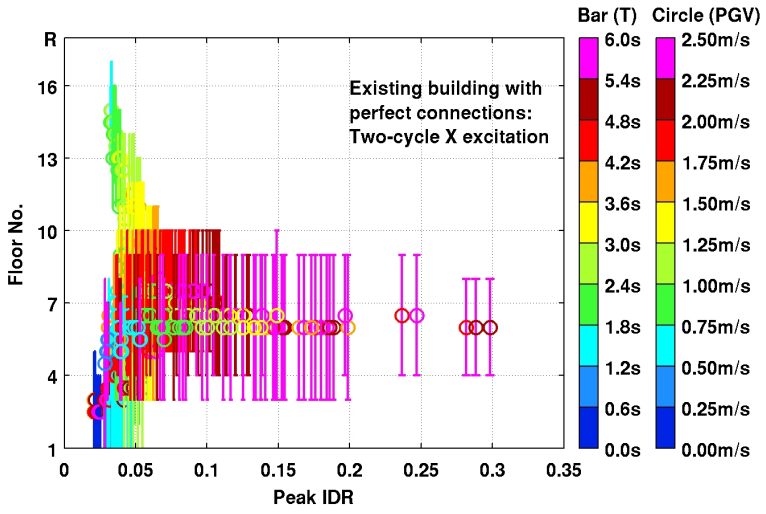

(b) Story extent of bands for all (T,PGV) combinations. Bar color identifies the excitation period and circle color identifies the peak ground velocity.

Figure B.11: Principal quasi-shear bands in the existing building (perfect connections) subjected to two-cycle idealized waveforms in the X direction.

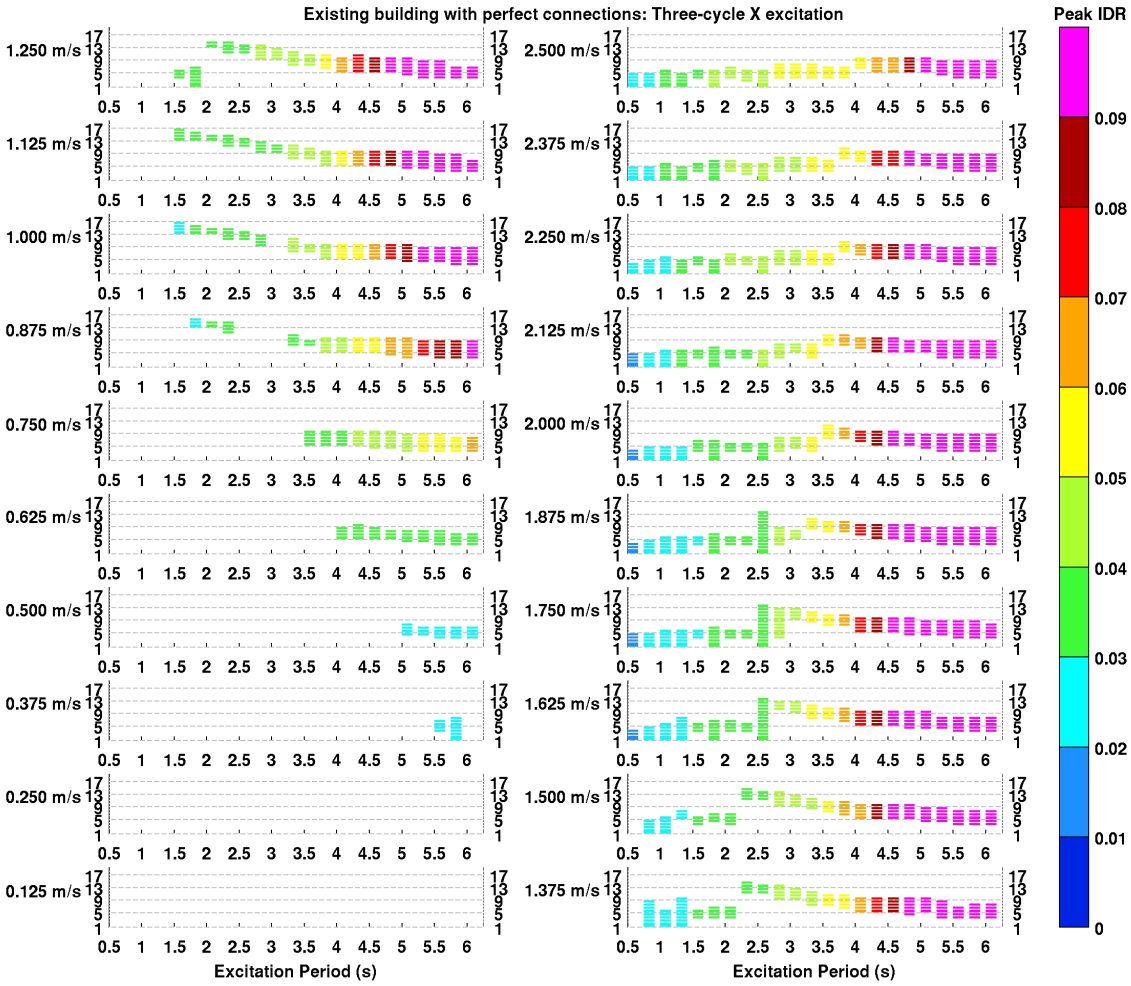

(a) Story extent of band for each (T,PGV) combination.

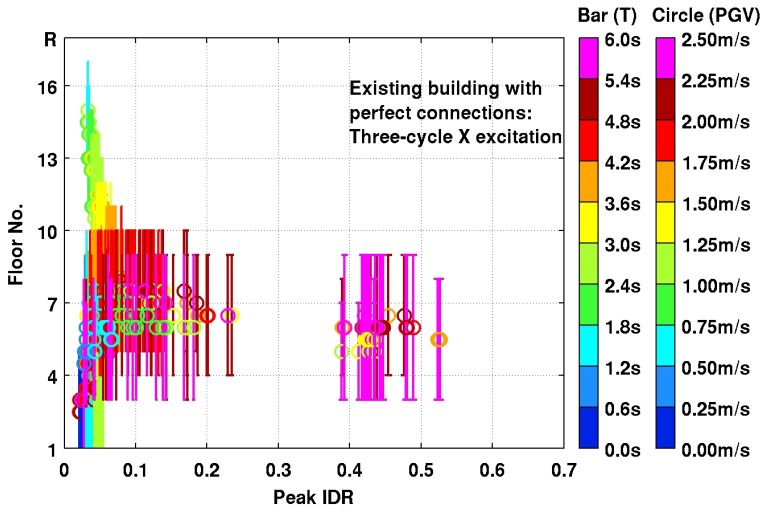

(b) Story extent of bands for all (T,PGV) combinations. Bar color identifies the excitation period and circle color identifies the peak ground velocity.

Figure B.12: Principal quasi-shear bands in the existing building (perfect connections) subjected to three-cycle idealized waveforms in the X direction.

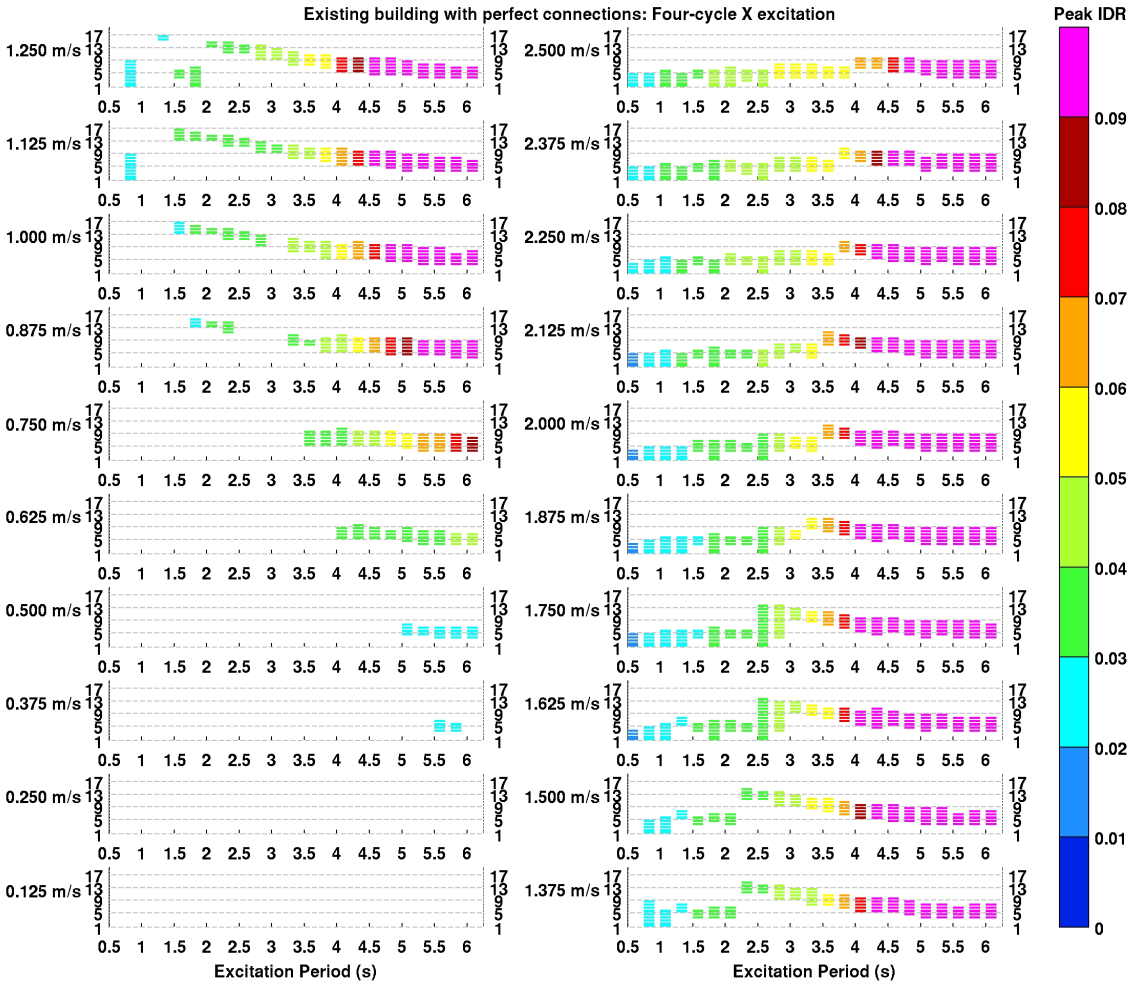

(a) Story extent of band for each (T,PGV) combination.

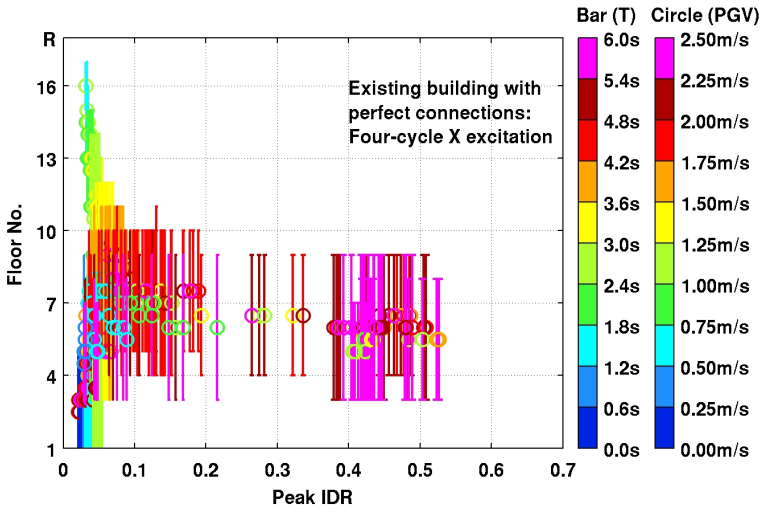

(b) Story extent of bands for all (T,PGV) combinations. Bar color identifies the excitation period and circle color identifies the peak ground velocity.

Figure B.13: Principal quasi-shear bands in the existing building (perfect connections) subjected to four-cycle idealized waveforms in the X direction.

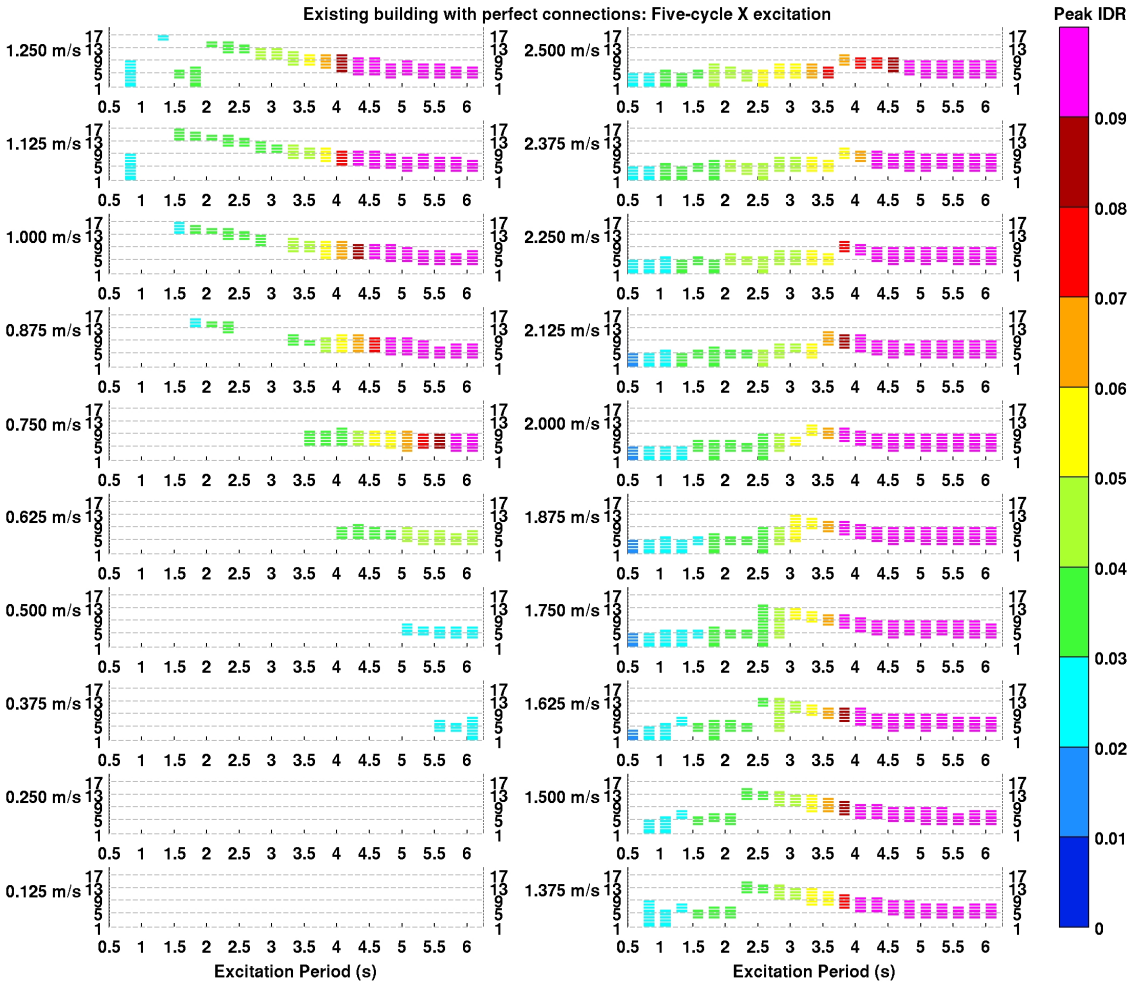

(a) Story extent of band for each (T,PGV) combination.

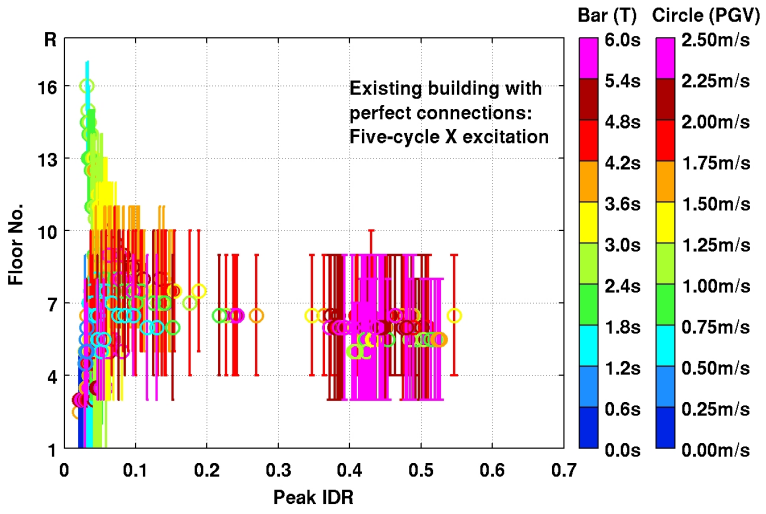

(b) Story extent of bands for all (T,PGV) combinations. Bar color identifies the excitation period and circle color identifies the peak ground velocity.

Figure B.14: Principal quasi-shear bands in the existing building (perfect connections) subjected to five-cycle idealized waveforms in the X direction.

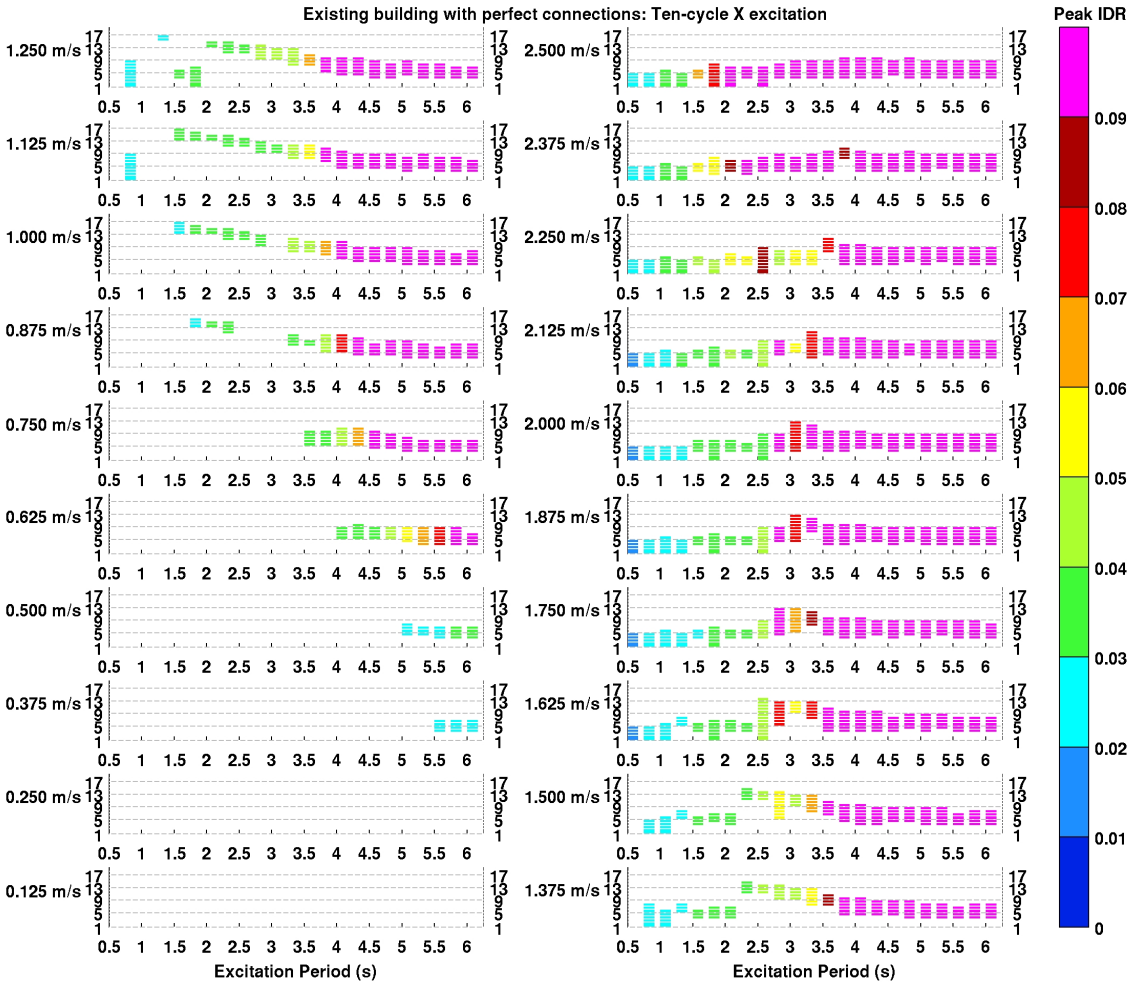

(a) Story extent of band for each (T,PGV) combination.

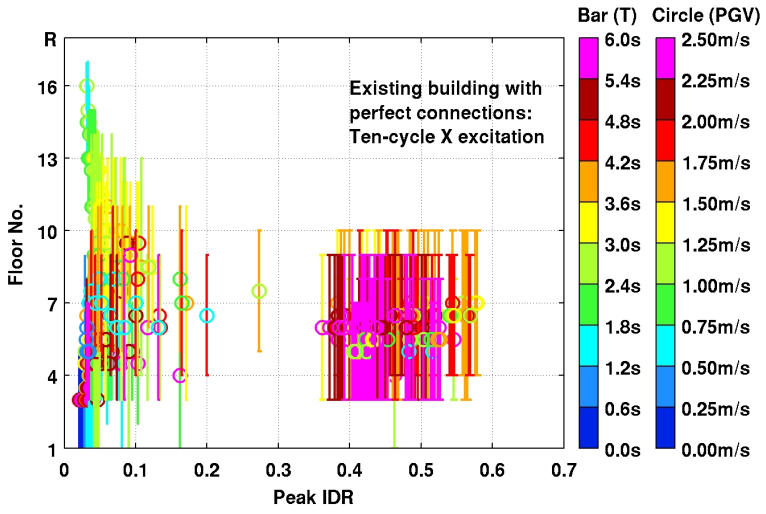

(b) Story extent of bands for all (T,PGV) combinations. Bar color identifies the excitation period and circle color identifies the peak ground velocity.

Figure B.15: Principal quasi-shear bands in the existing building (perfect connections) subjected to ten-cycle idealized waveforms in the X direction.

Appendix C Existing (UBC 1982) Building with Perfect Connections: Archive of Response Parameters Under Idealized-Waveform Shaking in Y Direction

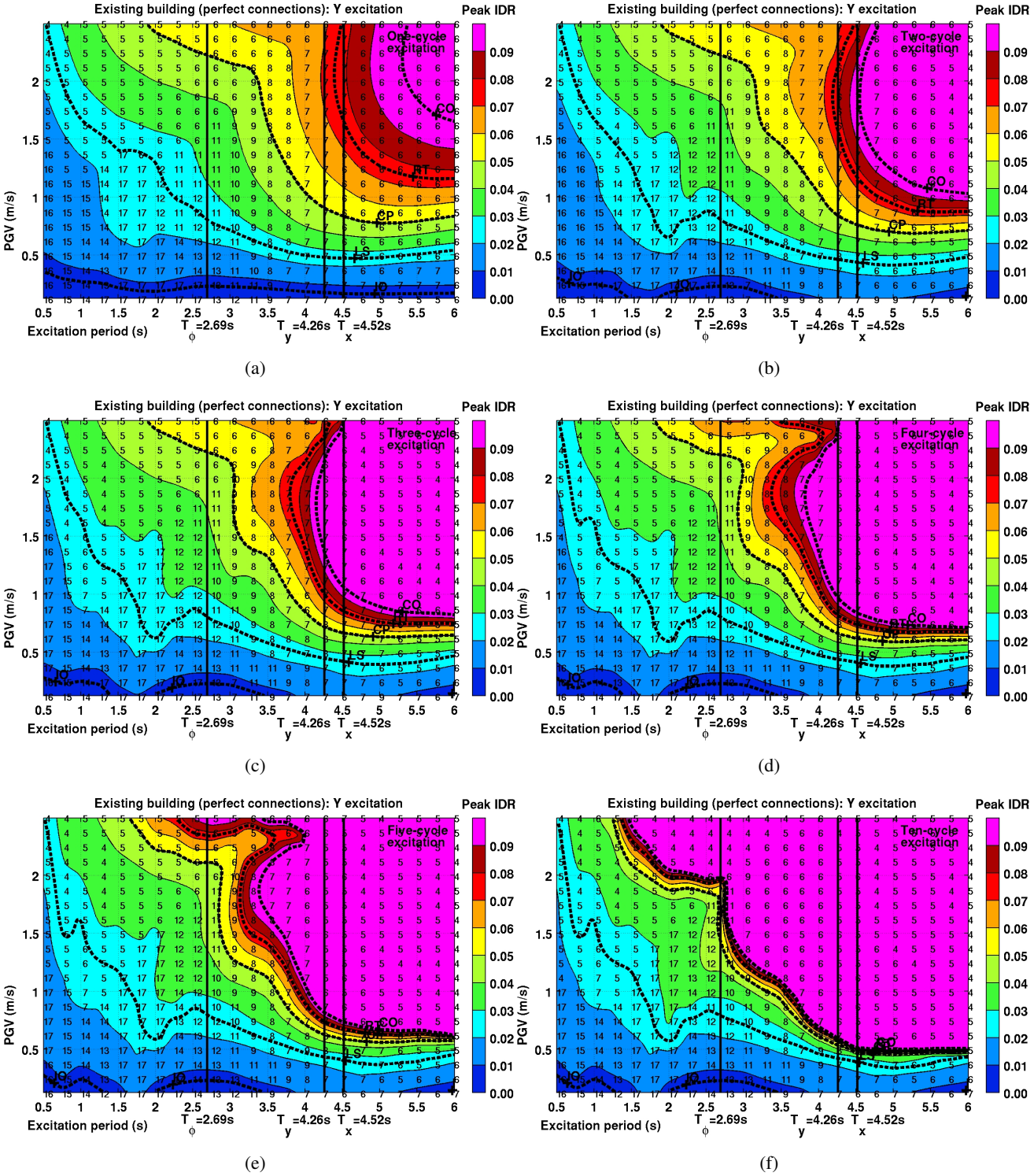

Figure C.1: Peak transient interstory drift ratio (IDR) maps for the existing building (perfect connections) as a function of idealized saw-tooth waveform excitation parameters, period T, peak ground velocity PGV, and number of cycles N. The one-component ground motion is applied in the building Y direction. The story location where the peak occurs is labeled at each of the 460 [T,PGV] combinations for which analyses were performed. Contours corresponding to the empirical immediate occupancy (IO), life-safety (LS), collapse prevention (CP), red-tagged (RT), and collapsed (CO) performance levels are shown in bold font. The principal direction building fundamental periods are indicated for reference.

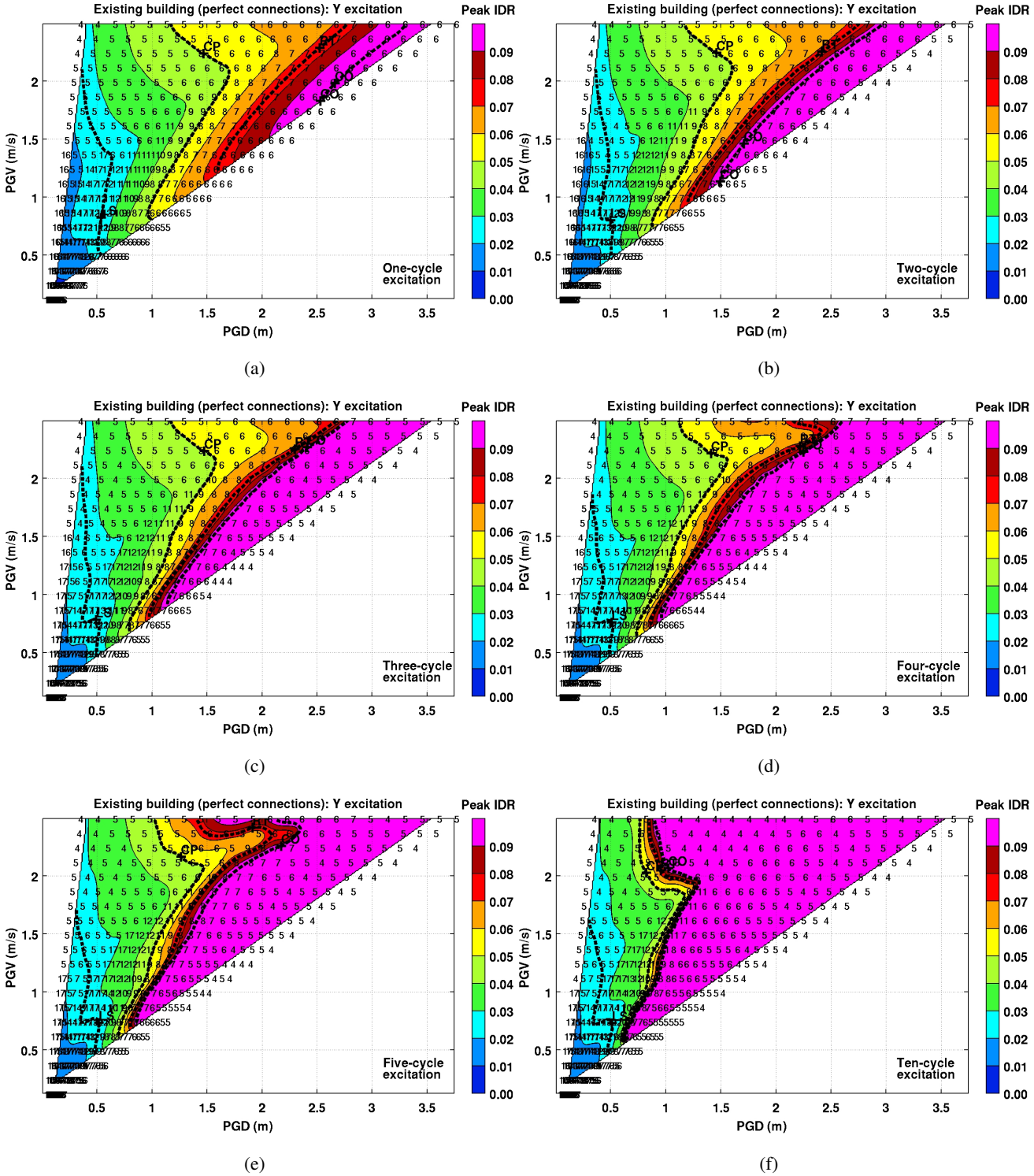

Figure C.2: The peak transient interstory drift ratio (IDR) maps for the existing building (perfect connections) from Figure C.1 transformed to the peak ground displacement (PGD) - peak ground velocity (PGV) plane. The story location where the peak occurs is labeled at each of the 460 [T,PGV] combinations for which analyses were performed. Contours corresponding to the empirical immediate occupancy (IO), life-safety (LS), collapse prevention (CP), red-tagged (RT), and collapsed (CO) performance levels are also transformed and shown in bold font.

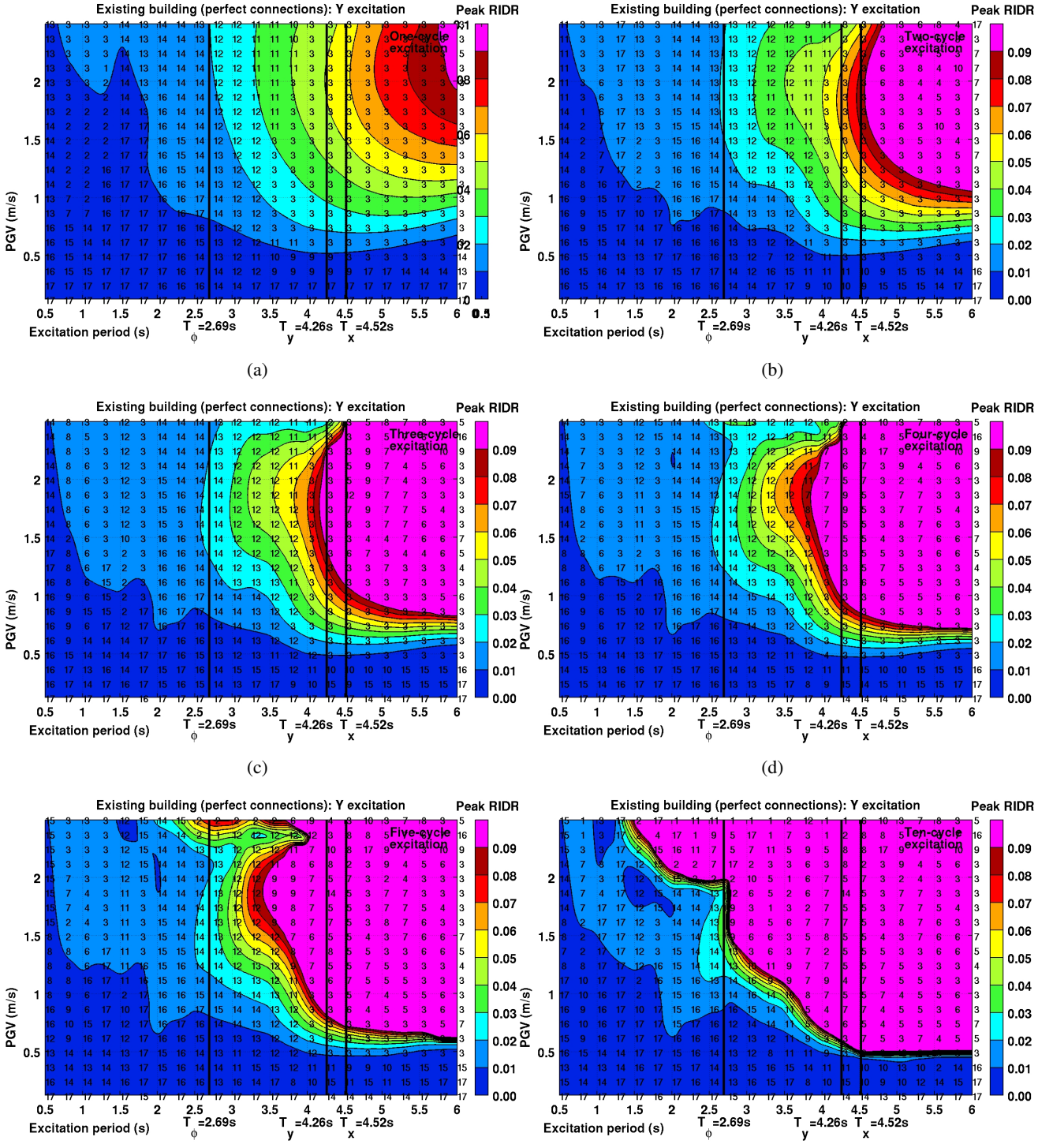

Figure C.3: Peak residual interstory drift ratio (RIDR) maps for the existing building (perfect connections) as a function of idealized saw-tooth waveform excitation parameters, period T, peak ground velocity PGV, and number of cycles N. The one-component ground motion is applied in the building Y direction. The story location where the peak occurs is labeled at each of the 460 [T,PGV] combinations for which analyses were performed. The principal direction building fundamental periods are indicated for reference.

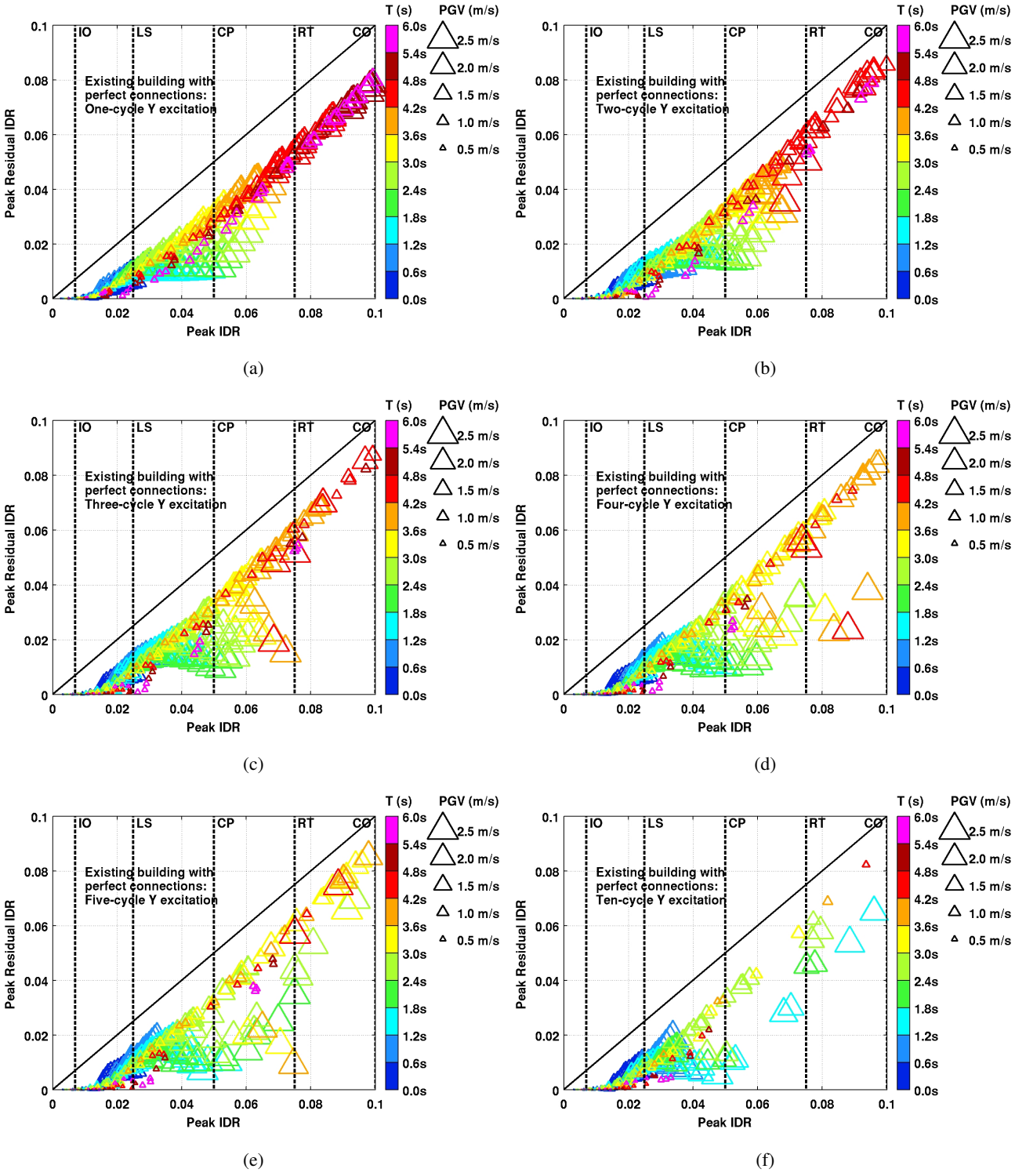

Figure C.4: Peak residual interstory drift ratio (RIDR) in the existing building (perfect connections) plotted as a function of the peak transient IDR under idealized saw-tooth waveform excitation. The results for 1-, 2-, 3-, 4-, 5-, and 10-cycle excitations are shown separately. The one-component ground motion is applied in the building Y direction. Points corresponding to peak transient IDR > 0.10 are indicative of near-certain collapse; residual IDR is no longer meaningful. Hence, these points are not shown. The empirical immediate occupancy (IO), life-safety (LS), collapse prevention (CP), red-tagged (RT), and collapsed (CO) performance levels are marked on the IDR axis.

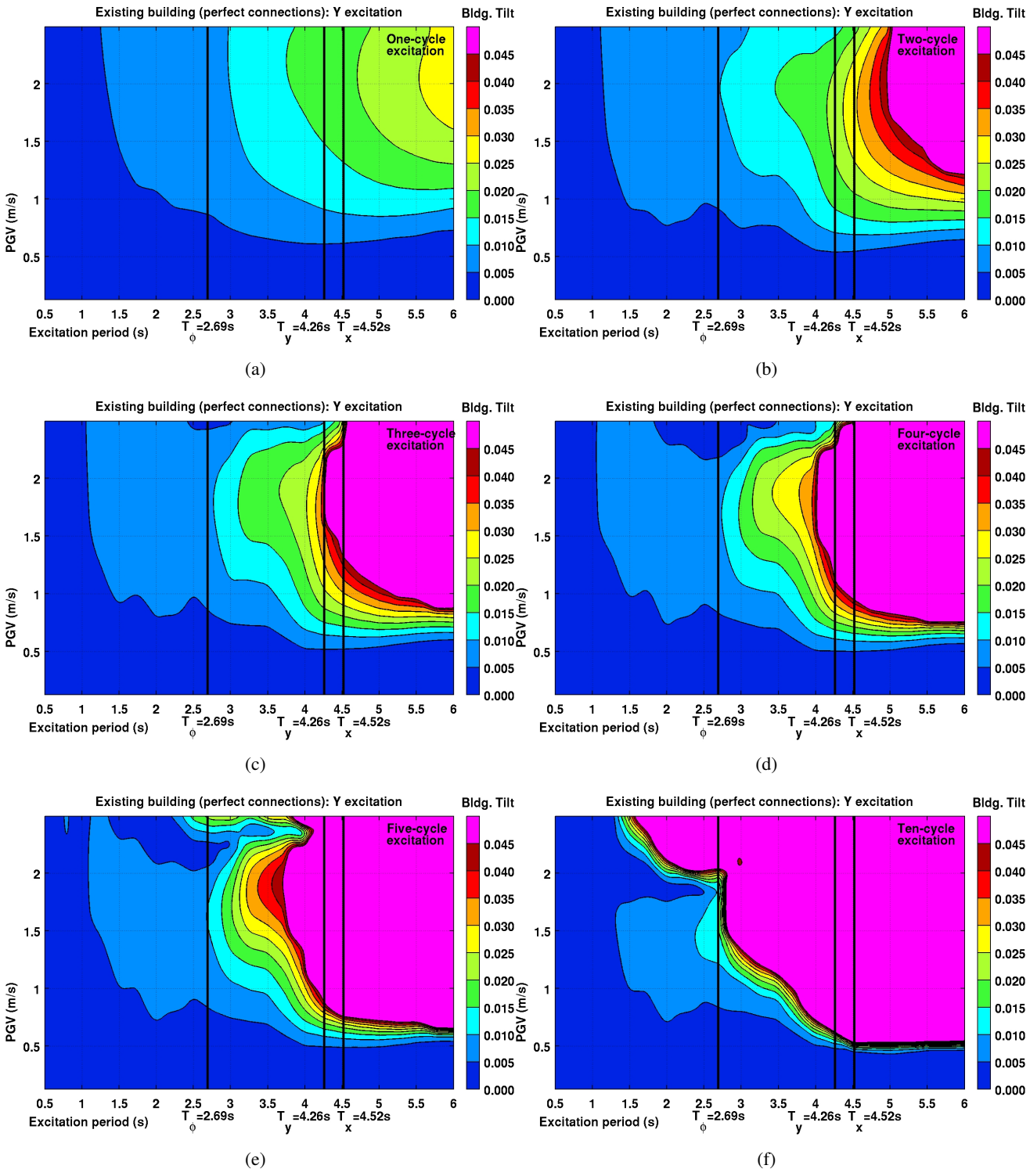

Figure C.5: Permanent roof drift (roof residual displacement normalized by building height) in the existing building (perfect connections) as a function of idealized saw-tooth waveform excitation parameters, period T, peak ground velocity PGV, and number of cycles N. The one-component ground motion is applied in the building Y direction. The principal direction building fundamental periods are indicated for reference.

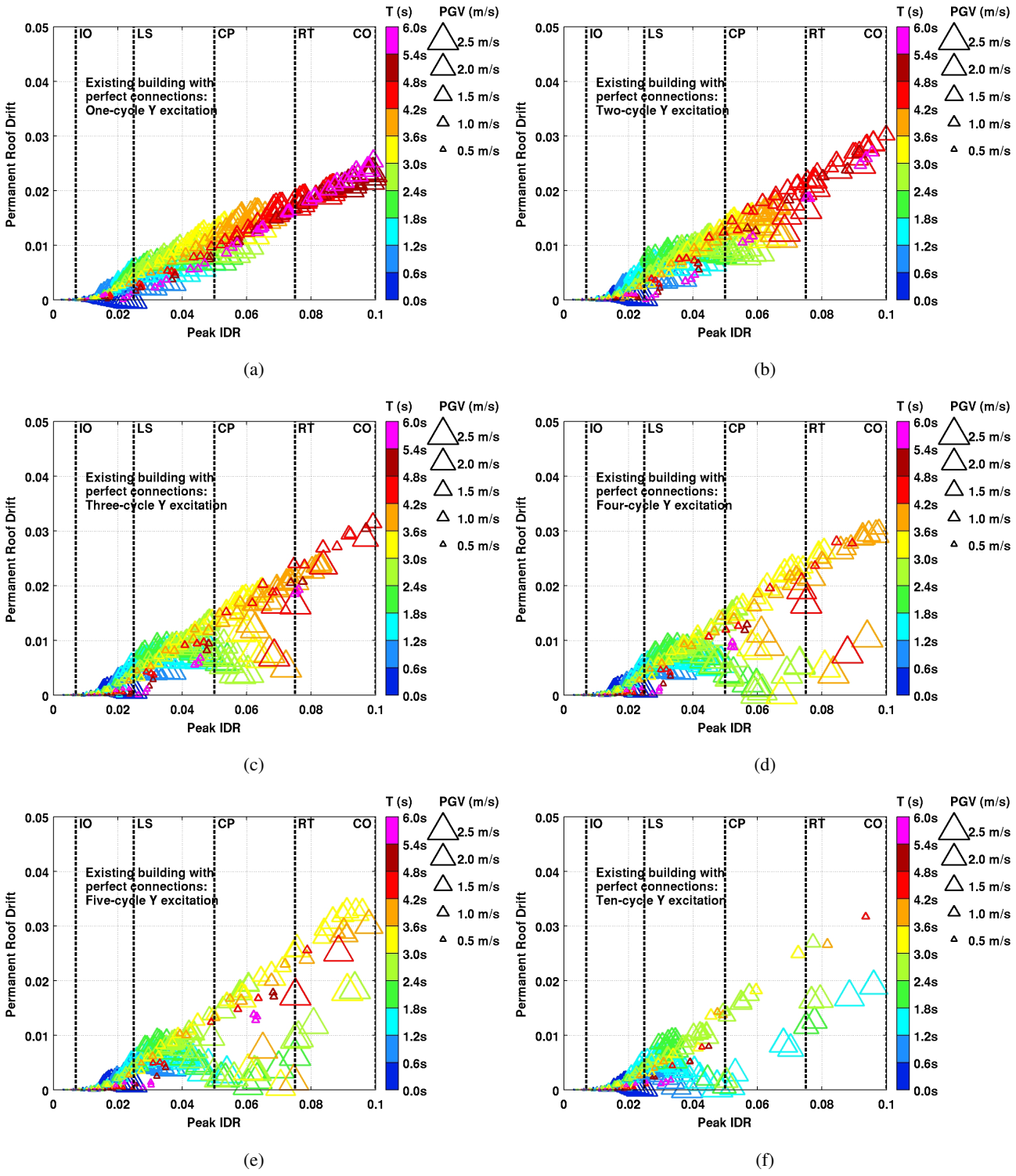

Figure C.6: Permanent roof drift (roof residual displacement normalized by building height) in the existing building (perfect connections) plotted as a function of the peak transient IDR under idealized saw-tooth waveform excitation. The results for 1-, 2-, 3-, 4-, 5-, and 10-cycle excitations are shown separately. The one-component ground motion is applied in the building Y direction. Points corresponding to peak transient IDR > 0.10 are indicative of near-certain collapse; permanent roof drift is no longer meaningful. Hence, these points are not shown. The empirical immediate occupancy (IO), life-safety (LS), collapse prevention (CP), red-tagged (RT), and collapsed (CO) performance levels are marked on the IDR axis.

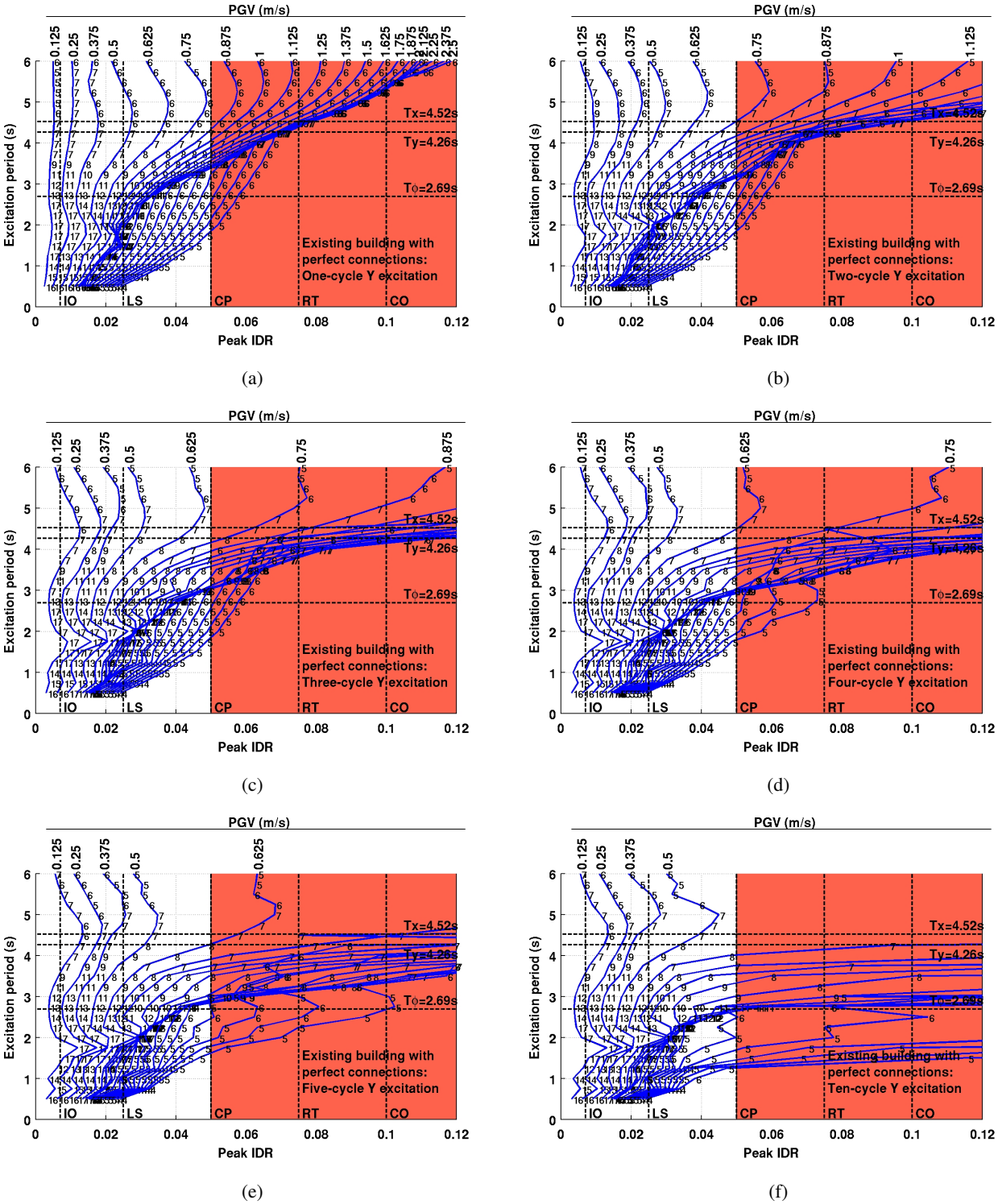

Figure C.7: Peak transient interstory drift ratio (IDR) is shown plotted against the idealized saw-tooth waveform excitation period (T) for the existing building (perfect connections) at various levels of peak ground velocity (PGV). Each subfigure corresponds to a different number of excitation cycles. The one-component ground motion is applied in the building Y direction. The story location where the peak occurs is labeled at each of the 460 [T,PGV] combinations for which analyses were performed. The empirical immediate occupancy (IO), life-safety (LS), collapse prevention (CP), red-tagged (RT), and collapsed (CO) performance levels are marked on the IDR axis. The principal direction building fundamental periods are indicated for reference.

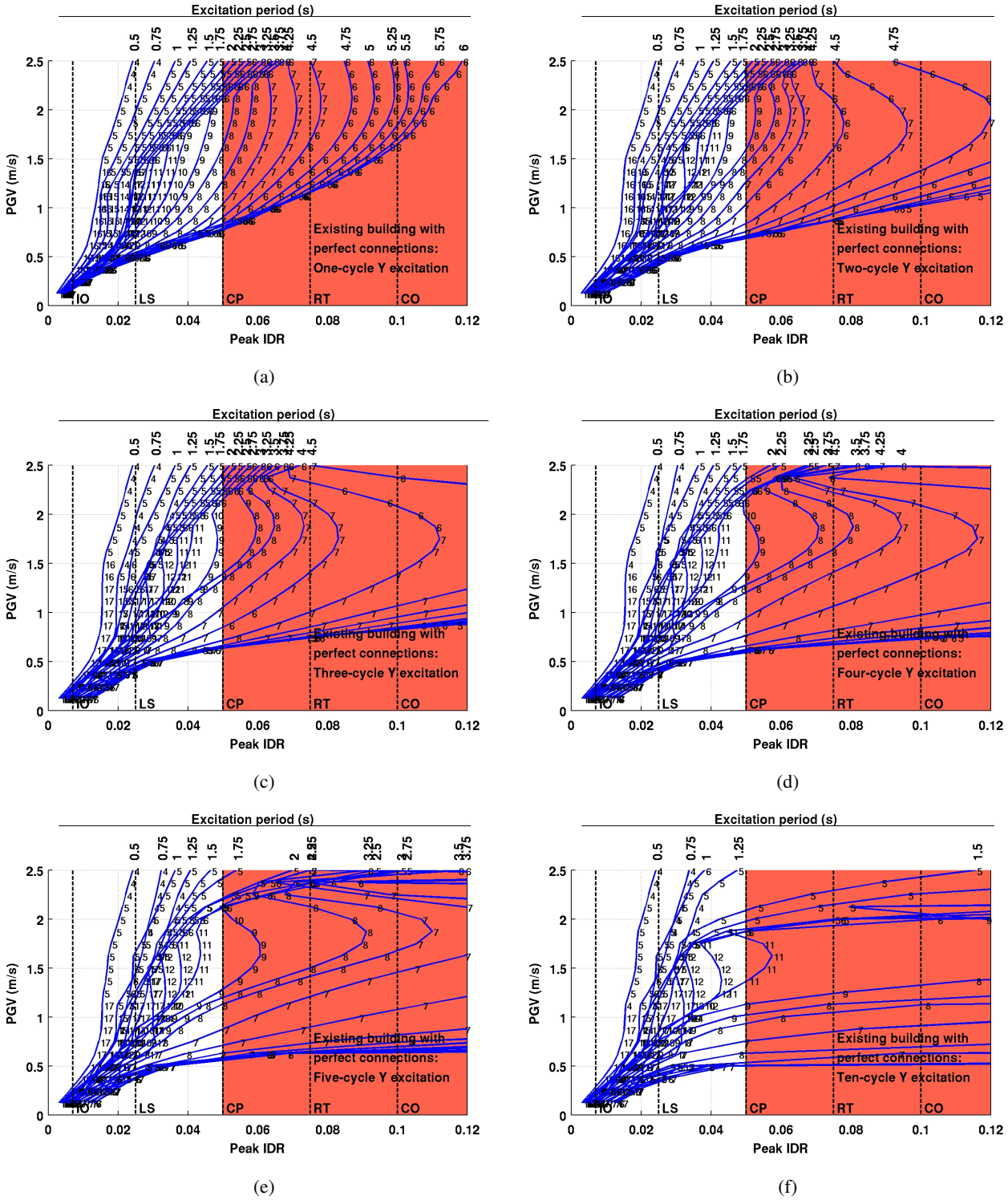

Figure C.8: Peak transient interstory drift ratio (IDR) is shown plotted against the idealized saw-tooth waveform excitation peak ground velocity (PGV) for the existing building (perfect connections) at various levels of waveform periods (T). Each subfigure corresponds to a different number of excitation cycles. The one-component ground motion is applied in the building Y direction. The story location where the peak occurs is labeled at each of the 460 [T,PGV] combinations for which analyses were performed. The empirical immediate occupancy (IO), life-safety (LS), collapse prevention (CP), red-tagged (RT), and collapsed (CO) performance levels are marked on the IDR axis.

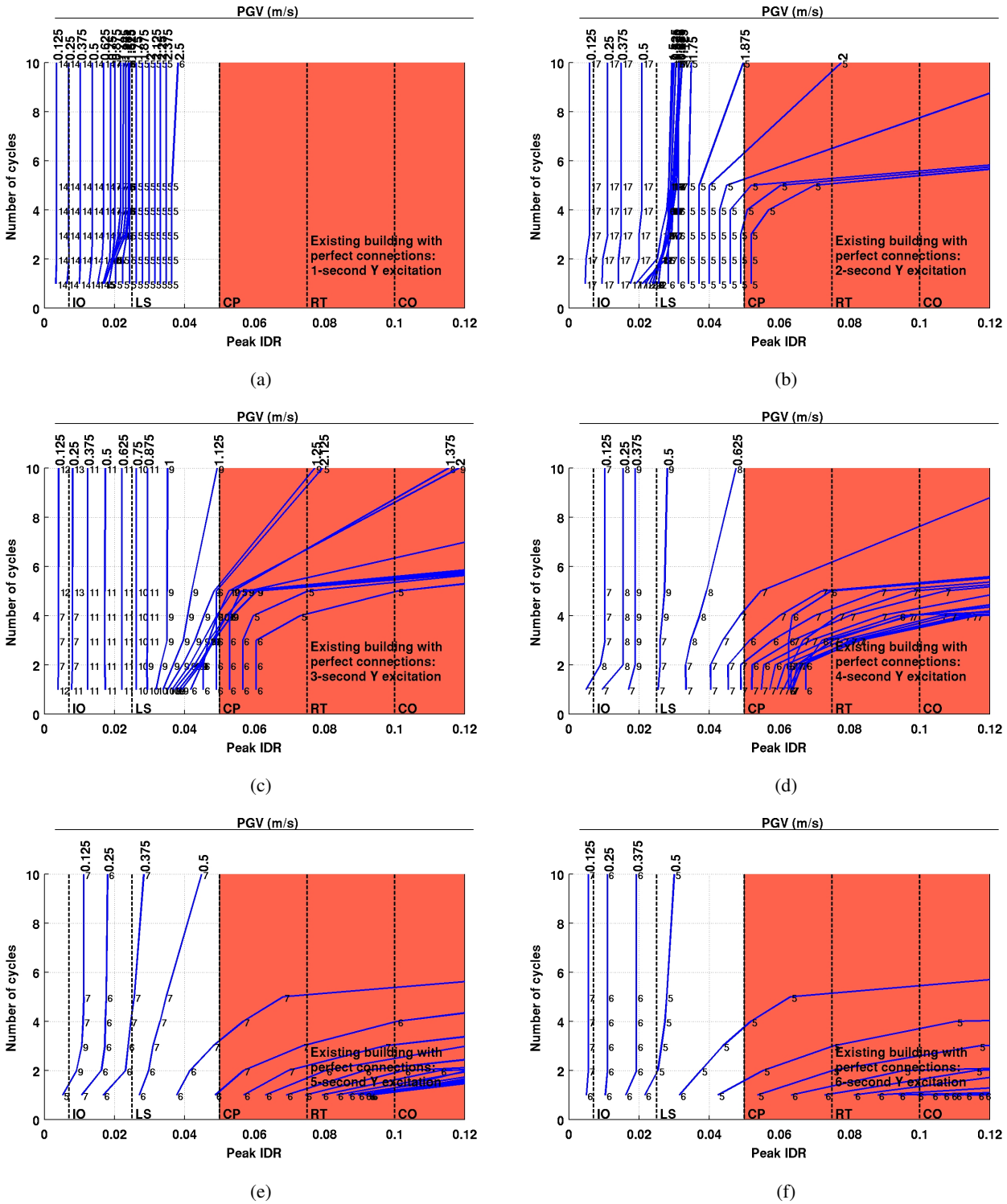

Figure C.9: Peak transient interstory drift ratio (IDR) is shown plotted against the number of cycles (N) in the idealized saw-tooth waveform excitation for the existing building (perfect connections) at various levels of peak ground velocity (PGV). Each subfigure corresponds to a different excitation period (1s–6s). The one-component ground motion is applied in the building Y direction. The story location where the peak occurs is labeled at each of the 460 [T,PGV] combinations for which analyses were performed. The empirical immediate occupancy (IO), life-safety (LS), collapse prevention (CP), red-tagged (RT), and collapsed (CO) performance levels are marked on the IDR axis.

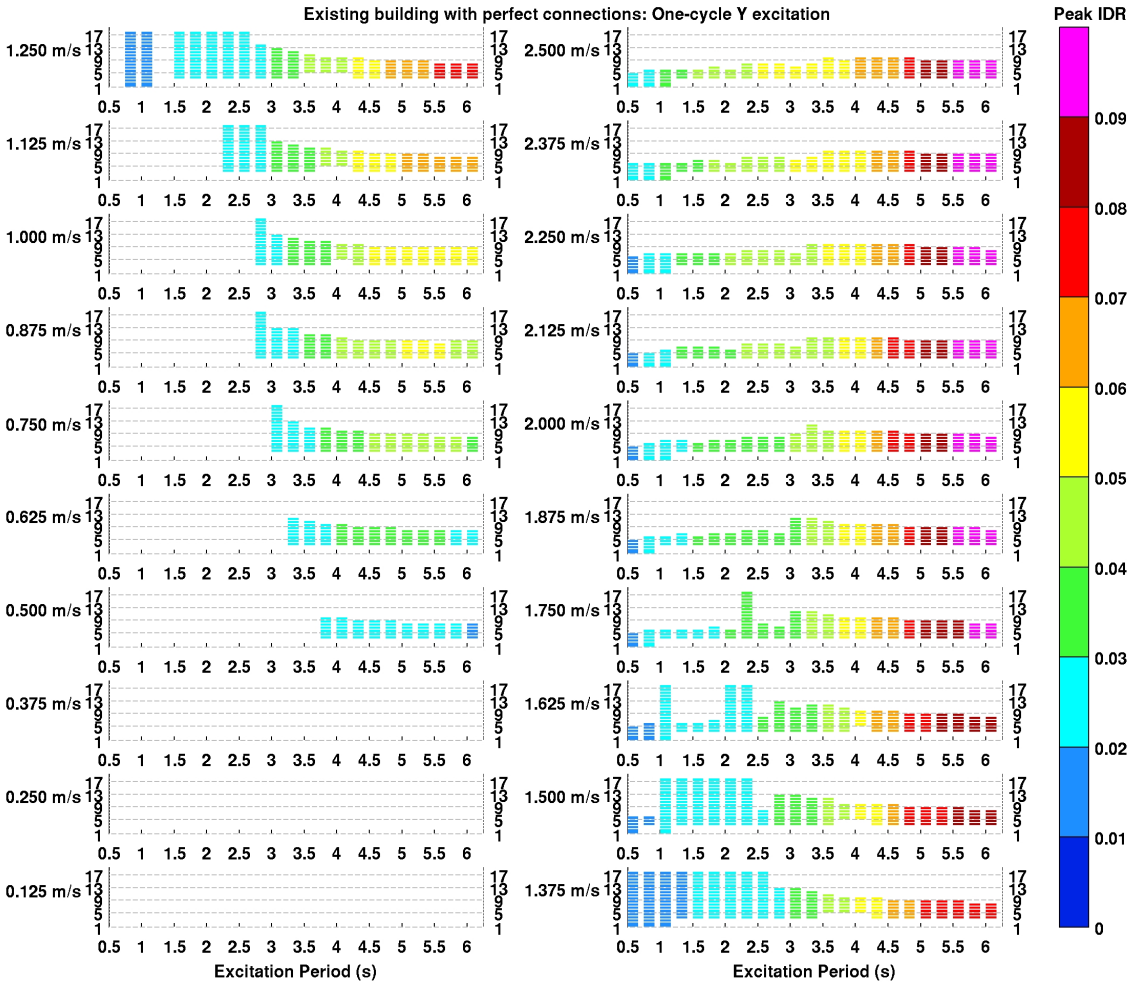

(a) Story extent of band for each (T,PGV) combination.

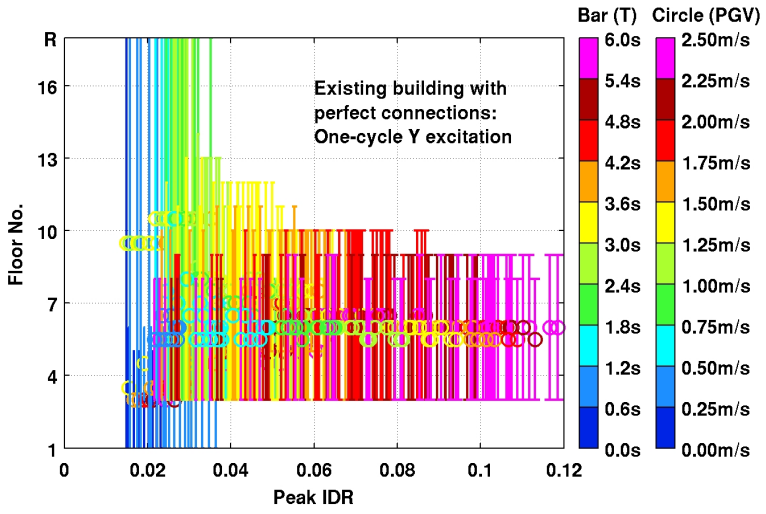

(b) Story extent of bands for all (T,PGV) combinations. Bar color identifies the excitation period and circle color identifies the peak ground velocity.

Figure C.10: Principal quasi-shear bands in the existing building (perfect connections) subjected to one-cycle idealized waveforms in the Y direction.

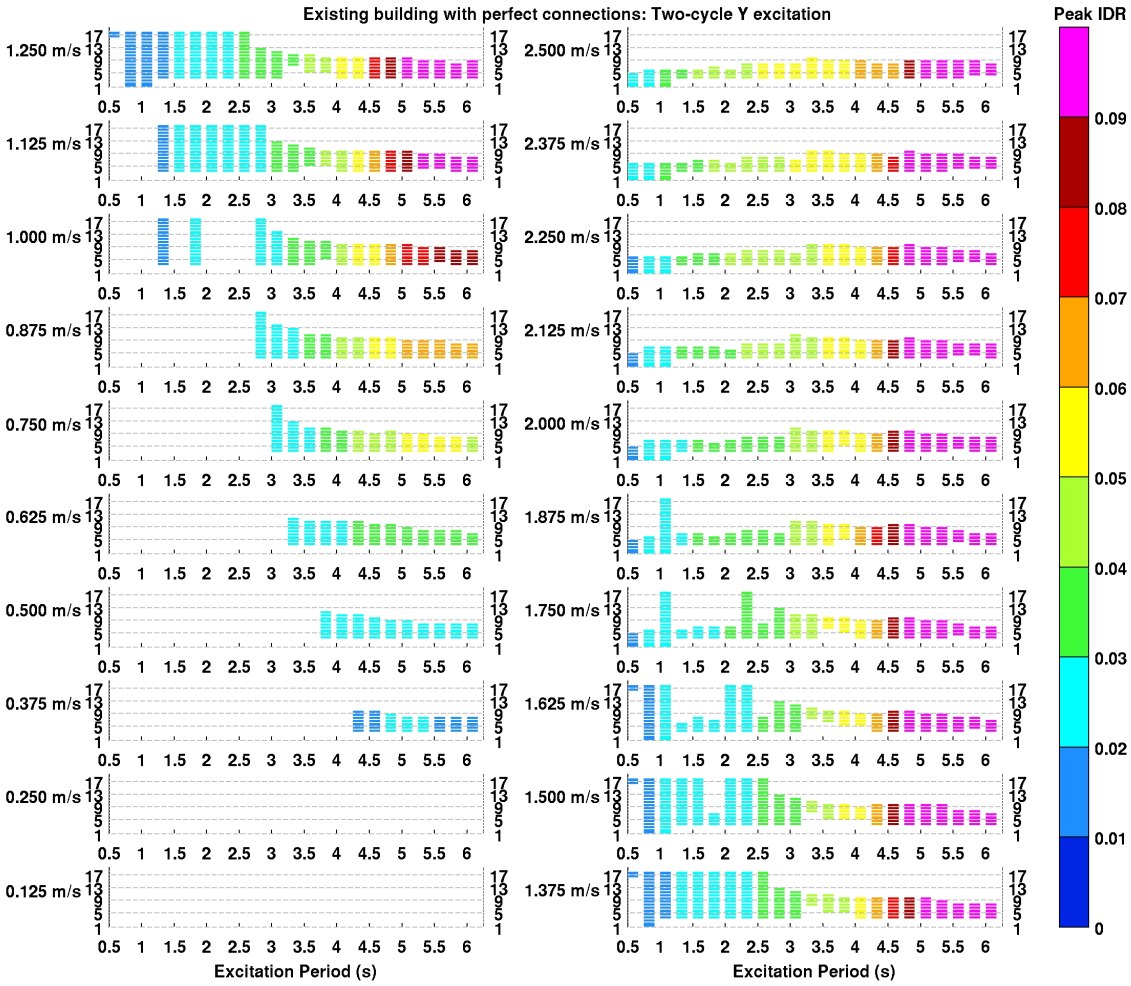

(a) Story extent of band for each (T,PGV) combination.

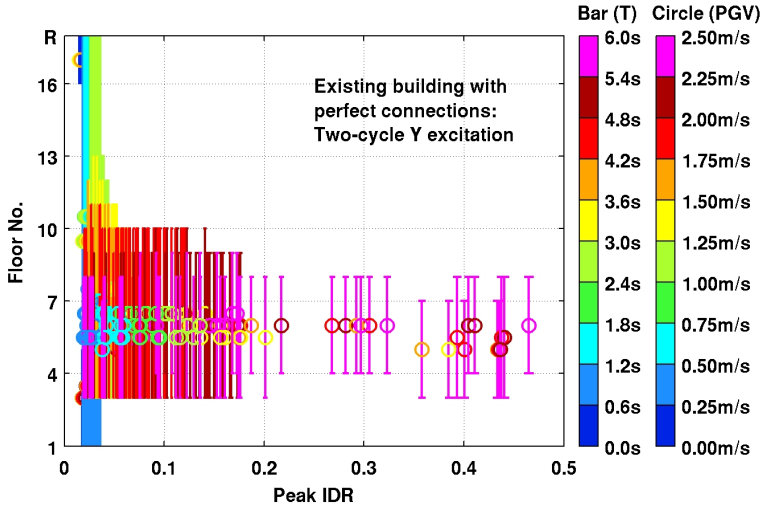

(b) Story extent of bands for all (T,PGV) combinations. Bar color identifies the excitation period and circle color identifies the peak ground velocity.

Figure C.11: Principal quasi-shear bands in the existing building (perfect connections) subjected to two-cycle idealized waveforms in the Y direction.

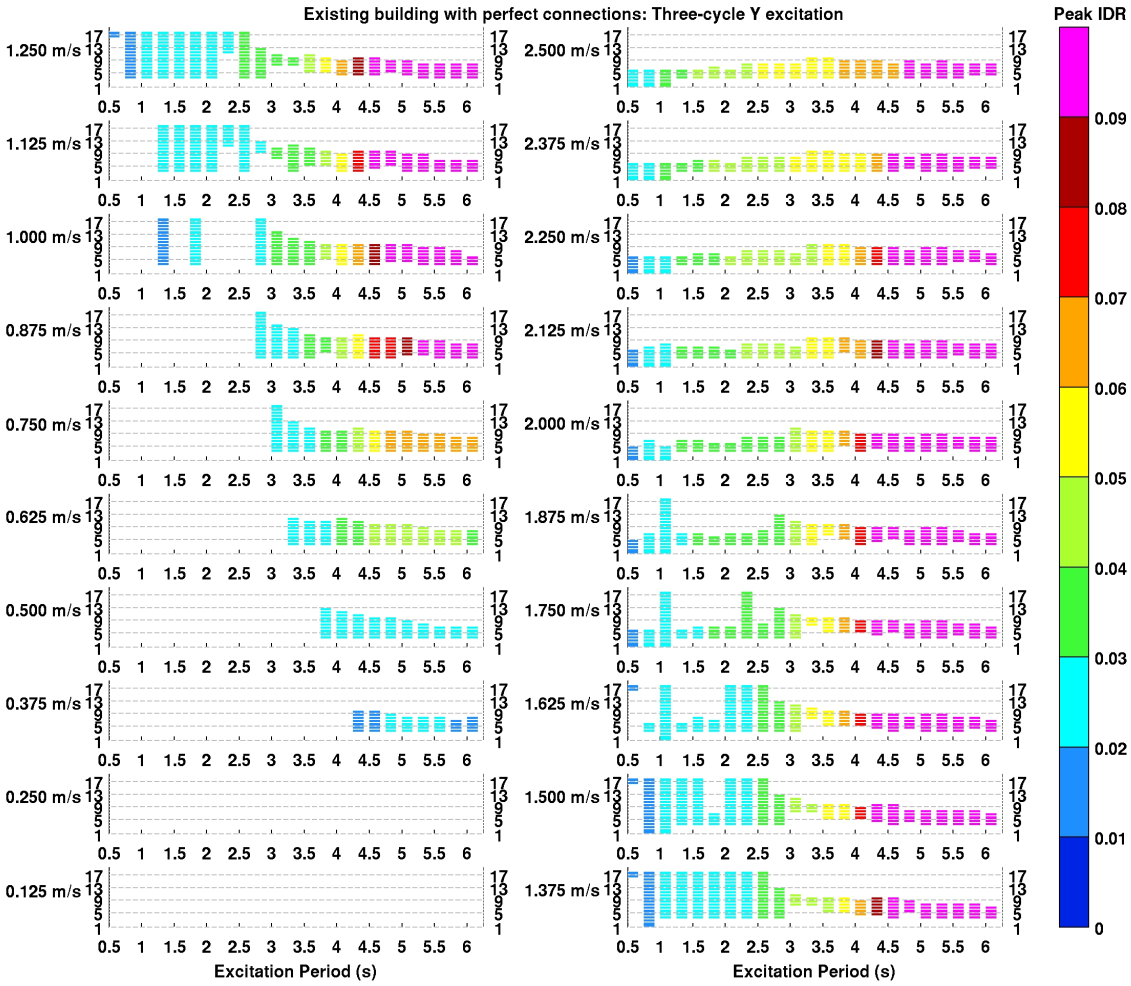

(a) Story extent of band for each (T,PGV) combination.

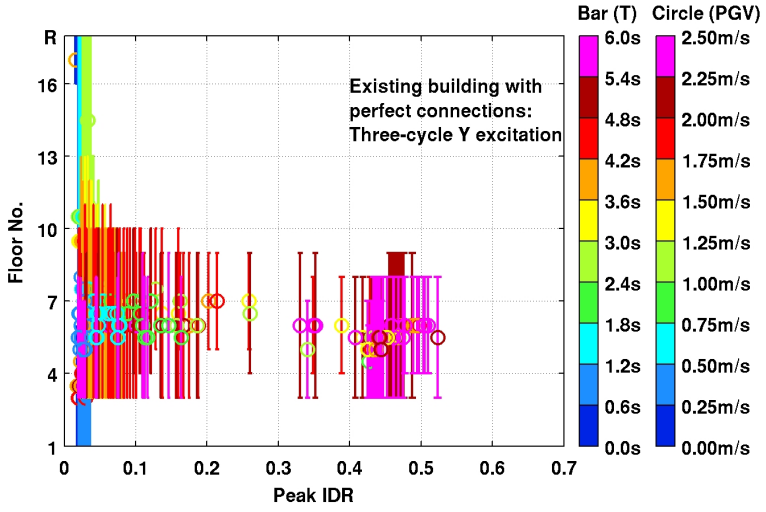

(b) Story extent of bands for all (T,PGV) combinations. Bar color identifies the excitation period and circle color identifies the peak ground velocity.

Figure C.12: Principal quasi-shear bands in the existing building (perfect connections) subjected to three-cycle idealized waveforms in the Y direction.

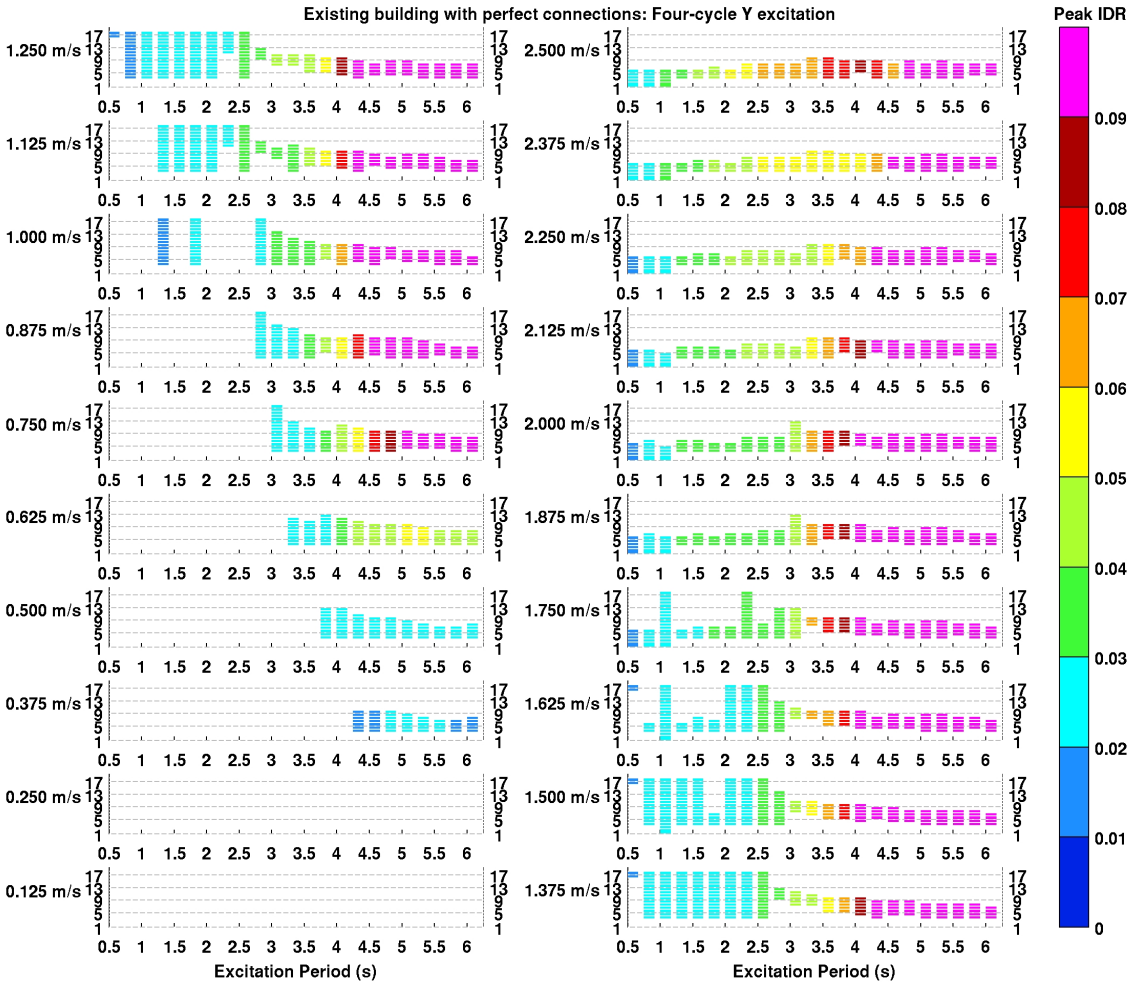

(a) Story extent of band for each (T,PGV) combination.

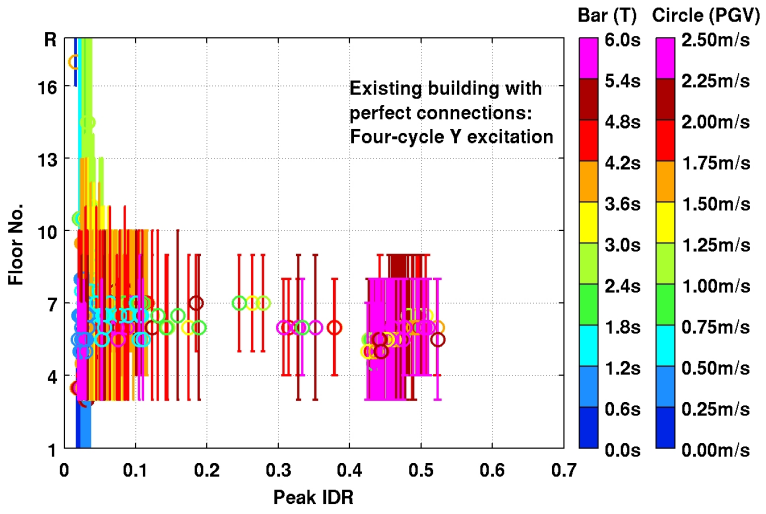

(b) Story extent of bands for all (T,PGV) combinations. Bar color identifies the excitation period and circle color identifies the peak ground velocity.

Figure C.13: Principal quasi-shear bands in the existing building (perfect connections) subjected to four-cycle idealized waveforms in the Y direction.

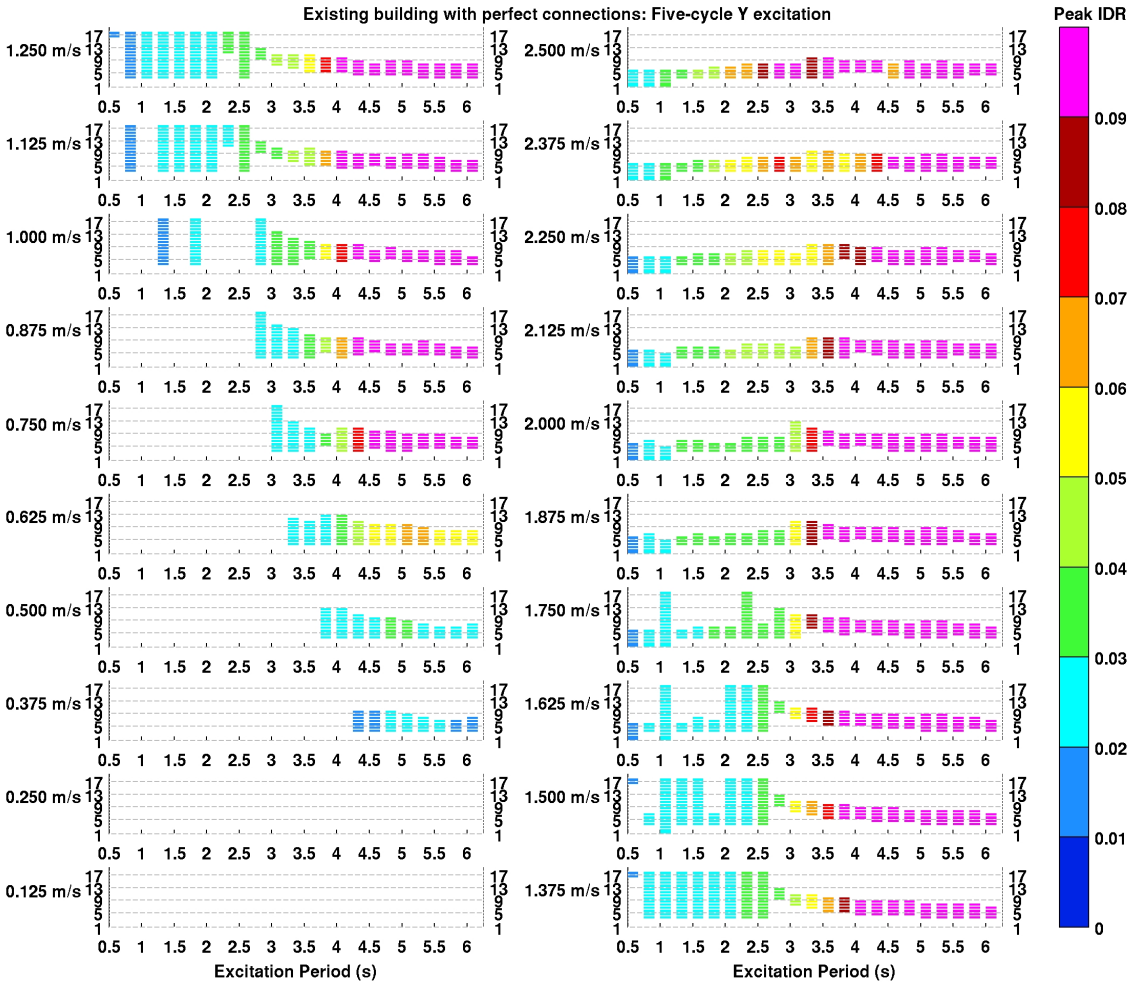

(a) Story extent of band for each (T,PGV) combination.

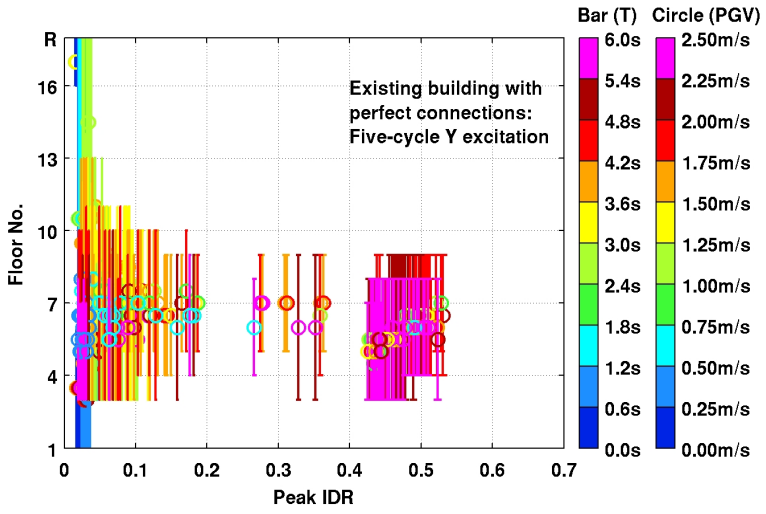

(b) Story extent of bands for all (T,PGV) combinations. Bar color identifies the excitation period and circle color identifies the peak ground velocity.

Figure C.14: Principal quasi-shear bands in the existing building (perfect connections) subjected to five-cycle idealized waveforms in the Y direction.

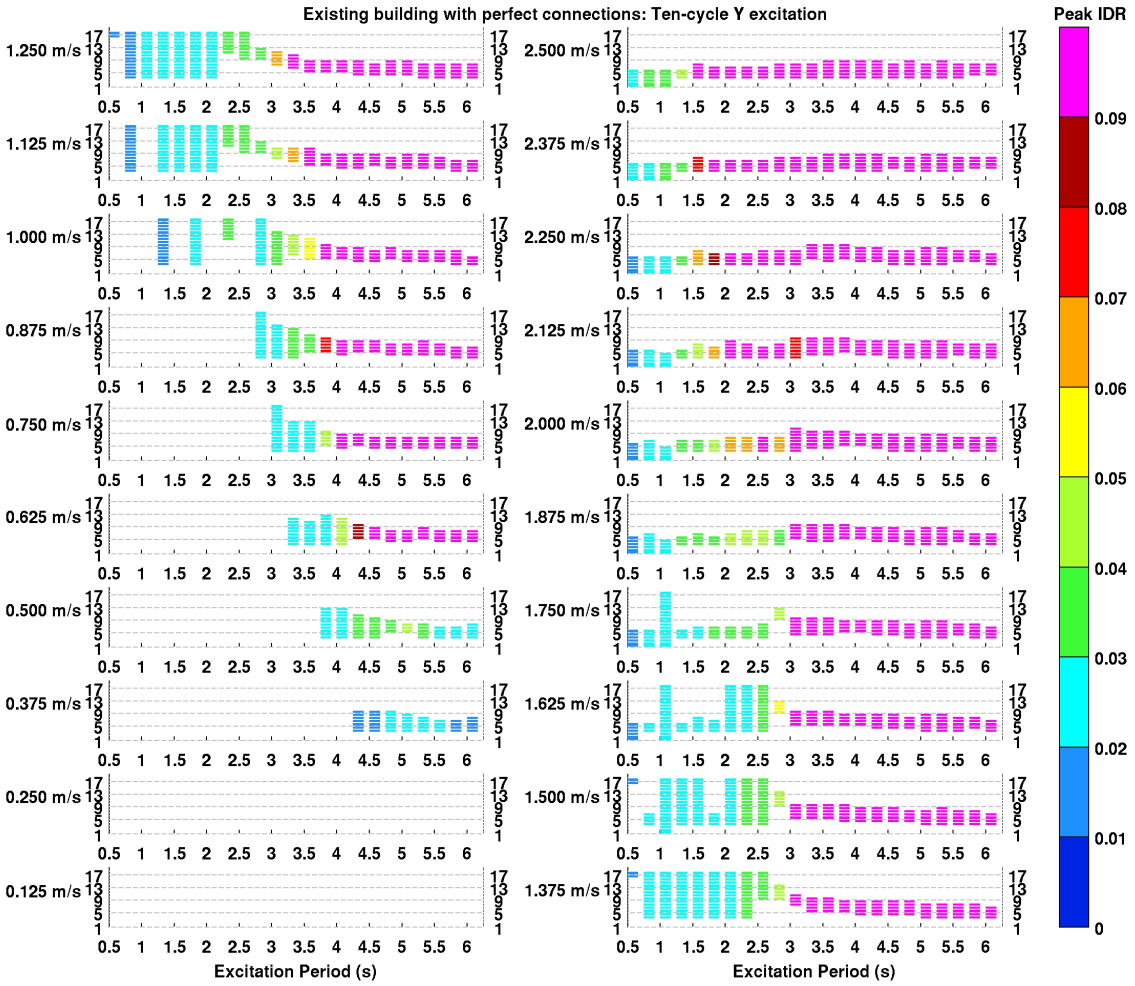

(a) Story extent of band for each (T,PGV) combination.

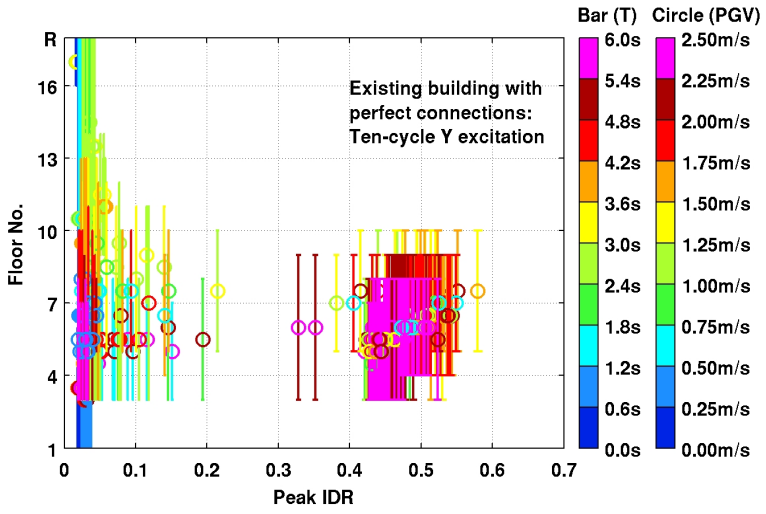

(b) Story extent of bands for all (T,PGV) combinations. Bar color identifies the excitation period and circle color identifies the peak ground velocity.

Figure C.15: Principal quasi-shear bands in the existing building (perfect connections) subjected to ten-cycle idealized waveforms in the Y direction.

Appendix D Redesigned (UBC 1997) Building with Perfect Connections: Archive of Response Parameters Under Idealized-Waveform Shaking in X Direction

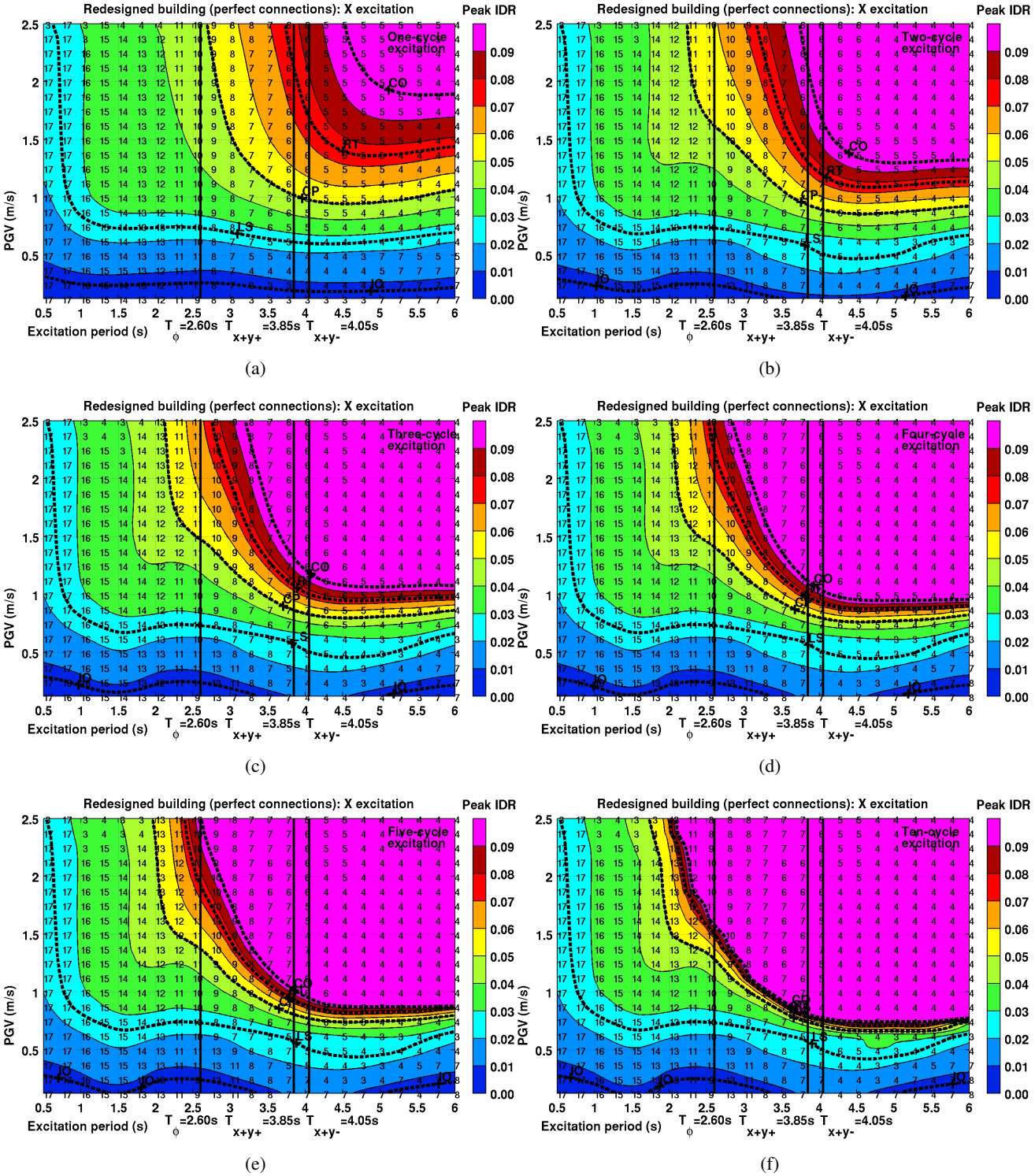

Figure D.1: Peak transient interstory drift ratio (IDR) maps for the redesigned building (perfect connections) as a function of idealized saw-tooth waveform excitation parameters, period T, peak ground velocity PGV, and number of cycles N. The one-component ground motion is applied in the building X direction. The story location where the peak occurs is labeled at each of the 460 [T,PGV] combinations for which analyses were performed. Contours corresponding to the empirical immediate occupancy (IO), life-safety (LS), collapse prevention (CP), red-tagged (RT), and collapsed (CO) performance levels are shown in bold font. The principal direction building fundamental periods are indicated for reference.

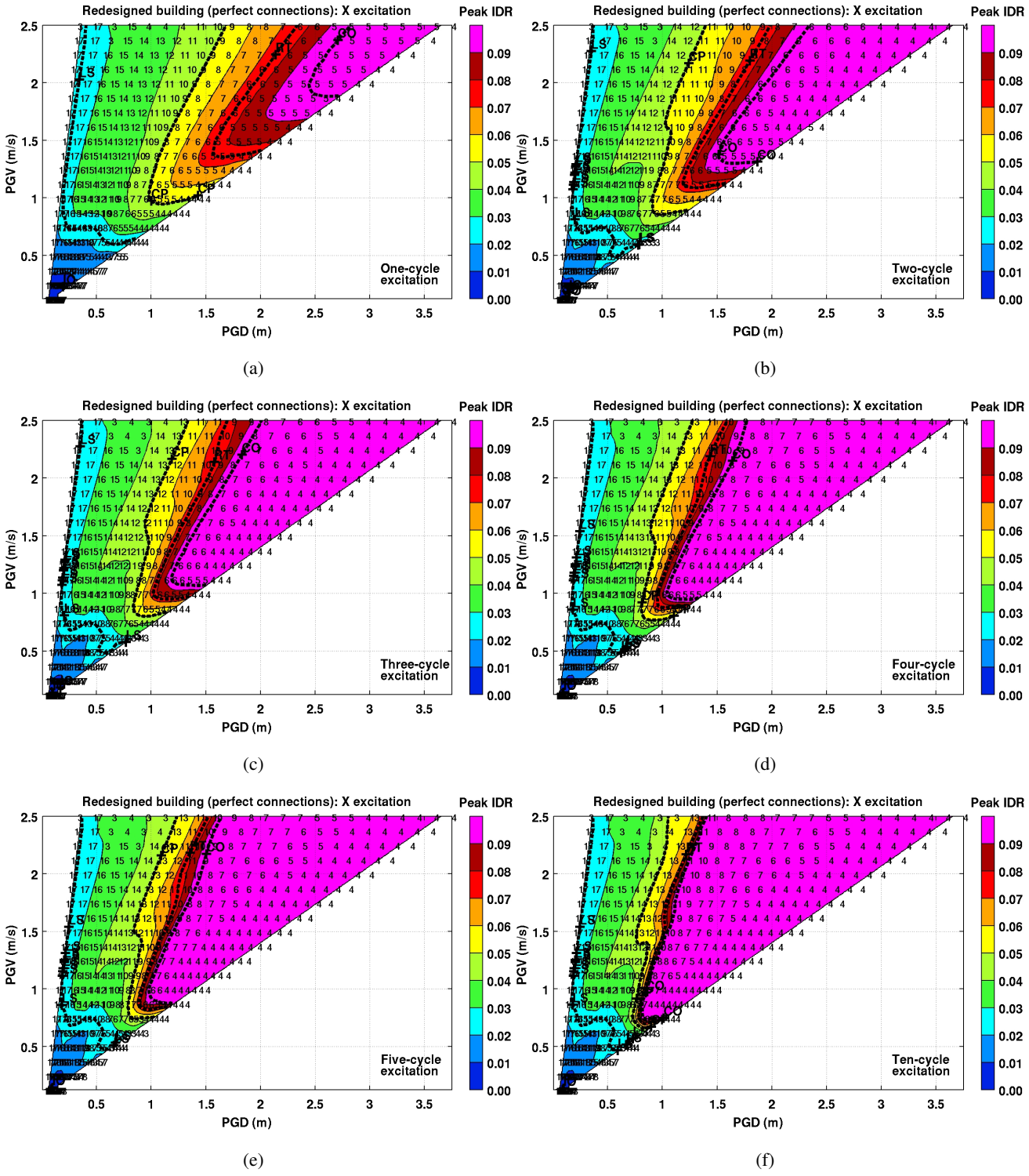

Figure D.2: The peak transient interstory drift ratio (IDR) maps for the redesigned building (perfect connections) from Figure D.1 transformed to the peak ground displacement (PGD) - peak ground velocity (PGV) plane. The story location where the peak occurs is labeled at each of the 460 [T,PGV] combinations for which analyses were performed. Contours corresponding to the empirical immediate occupancy (IO), life-safety (LS), collapse prevention (CP), red-tagged (RT), and collapsed (CO) performance levels are shown in bold font.

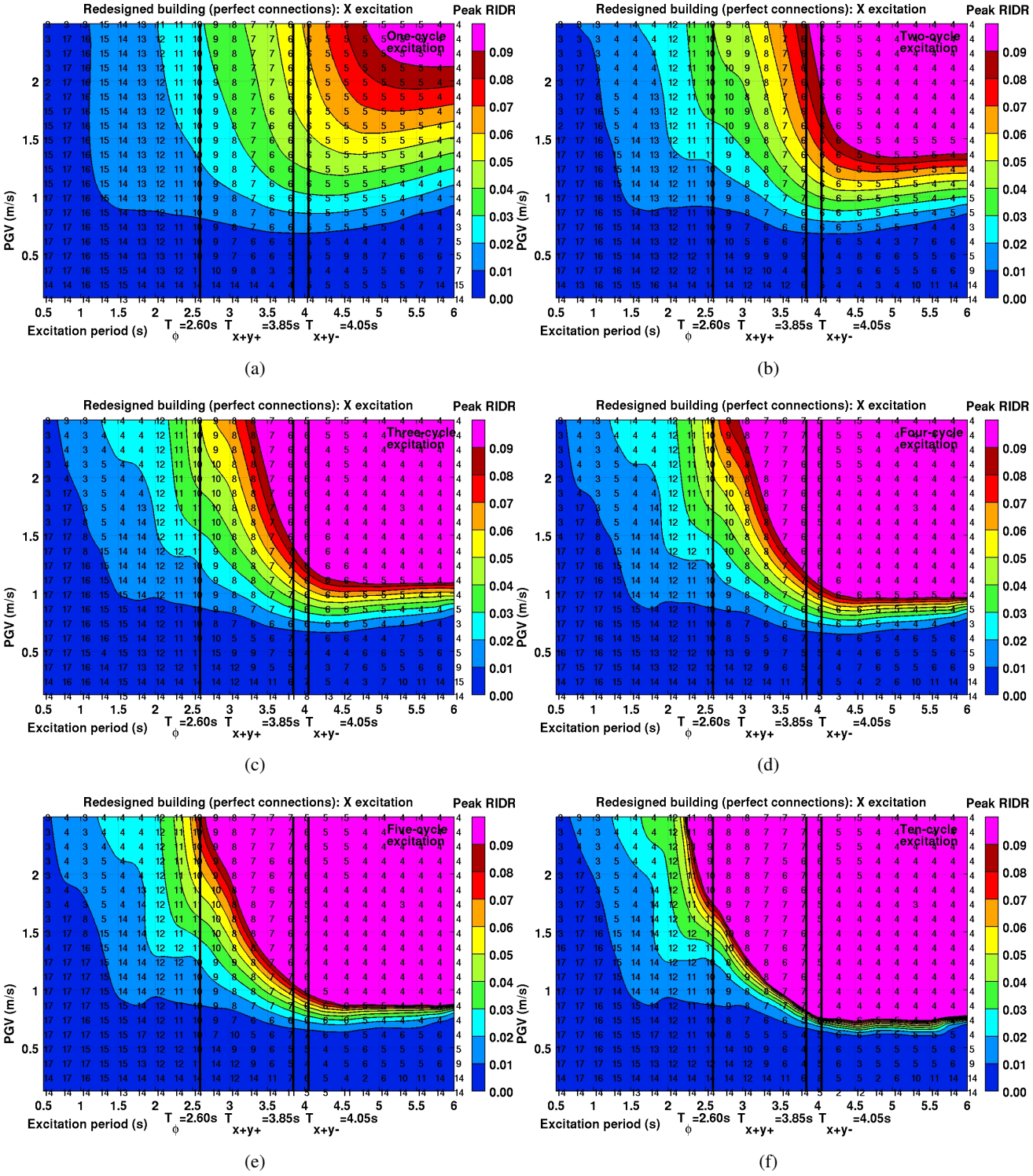

Figure D.3: Peak residual interstory drift ratio (RIDR) maps for the redesigned building (perfect connections) as a function of idealized saw-tooth waveform excitation parameters, period T, peak ground velocity PGV, and number of cycles N. The one-component ground motion is applied in the building X direction. The story location where the peak occurs is labeled at each of the 460 [T,PGV] combinations for which analyses were performed. The principal direction building fundamental periods are indicated for reference.

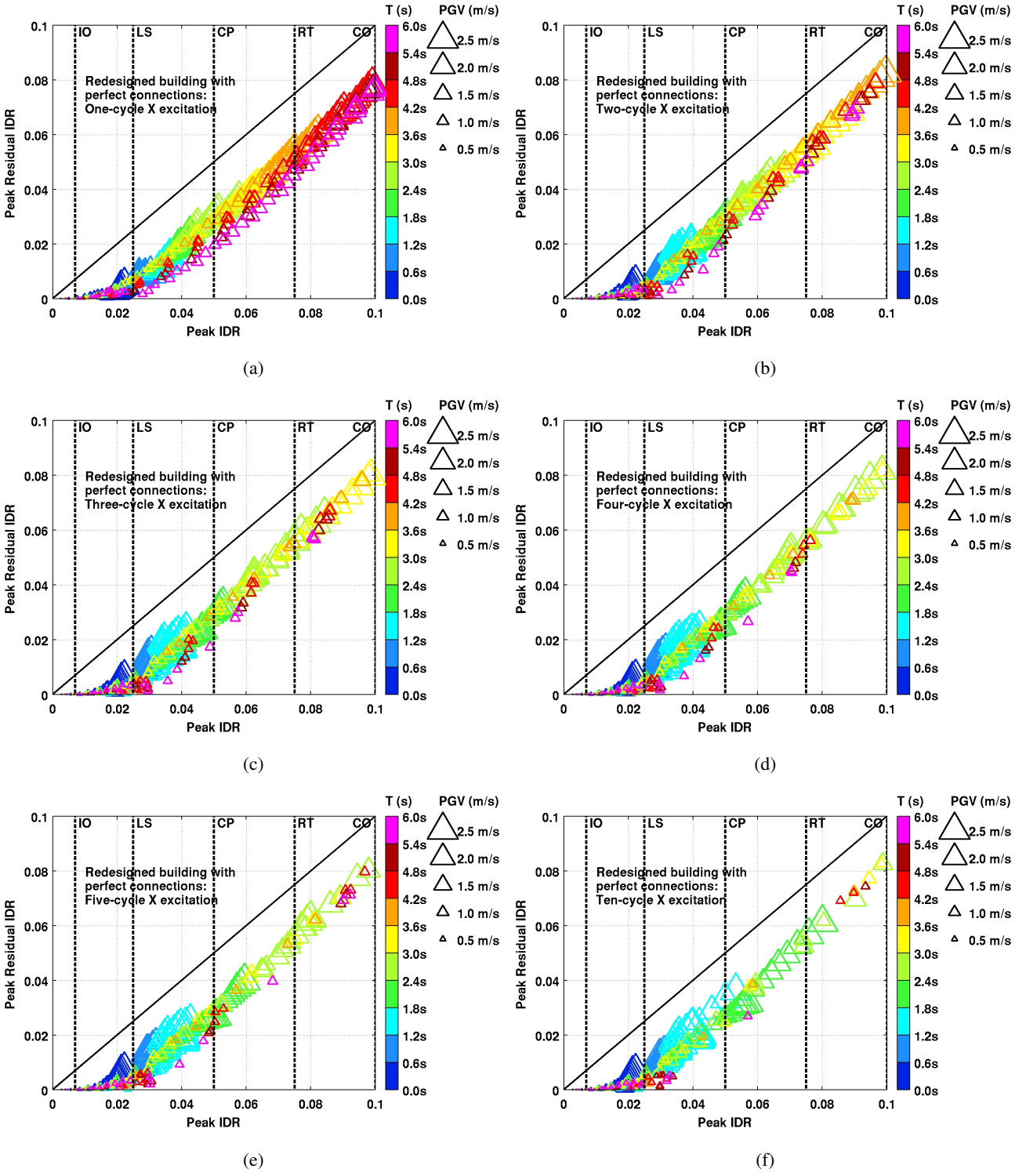

Figure D.4: Peak residual interstory drift ratio (RIDR) in the redesigned building (perfect connections) plotted as a function of the peak transient IDR under idealized saw-tooth waveform excitation. The results for 1-, 2-, 3-, 4-, 5-, and 10-cycle excitations are shown separately. The one-component ground motion is applied in the building X direction. Points corresponding to peak transient IDR > 0.10 are indicative of near-certain collapse; residual IDR is no longer meaningful. Hence, these points are not shown. The empirical immediate occupancy (IO), life-safety (LS), collapse prevention (CP), red-tagged (RT), and collapsed (CO) performance levels are marked on the IDR axis.

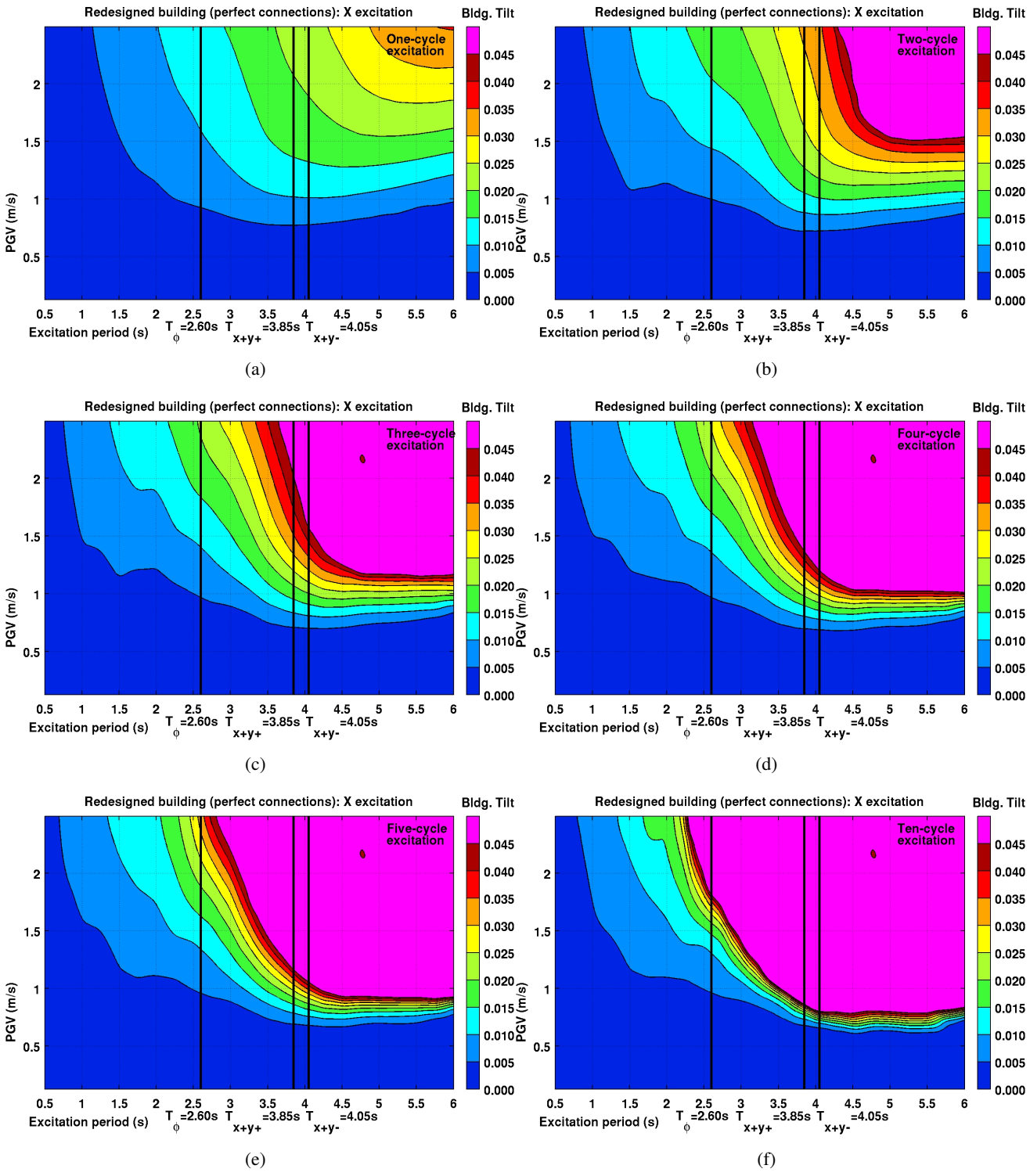

Figure D.5: Permanent roof drift (roof residual displacement normalized by building height) in the redesigned building (perfect connections) as a function of idealized saw-tooth waveform excitation parameters, period T, peak ground velocity PGV, and number of cycles N. The one-component ground motion is applied in the building X direction. The principal direction building fundamental periods are indicated for reference.

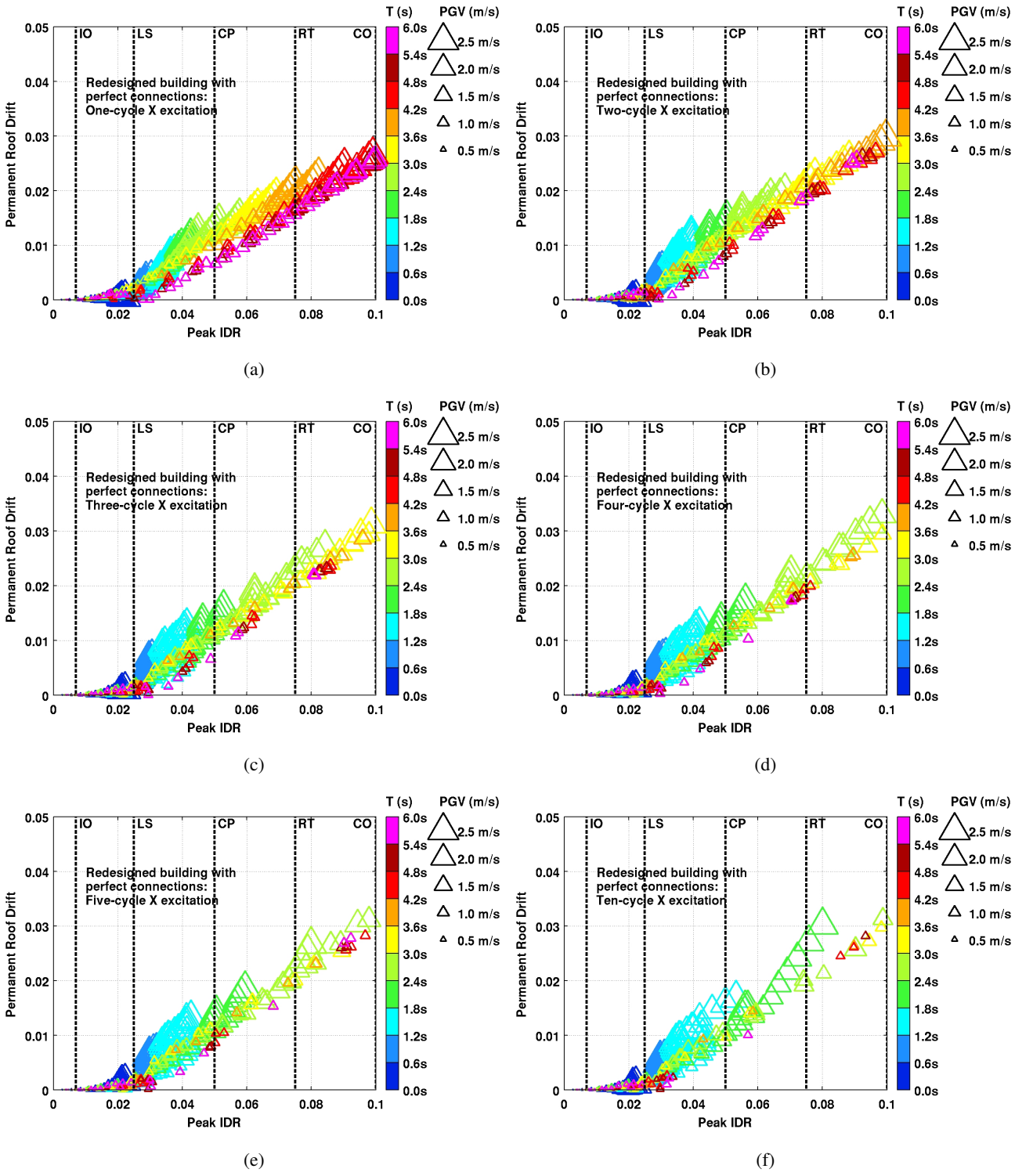

Figure D.6: Permanent roof drift (roof residual displacement normalized by building height) in the redesigned building (perfect connections) plotted as a function of the peak transient IDR under idealized saw-tooth waveform excitation. The results for 1-, 2-, 3-, 4-, 5-, and 10-cycle excitations are shown separately. The one-component ground motion is applied in the building X direction. Points corresponding to peak transient IDR > 0.10 are indicative of near-certain collapse; permanent roof drift is no longer meaningful. Hence, these points are not shown. The empirical immediate occupancy (IO), life-safety (LS), collapse prevention (CP), red-tagged (RT), and collapsed (CO) performance levels are marked on the IDR axis.

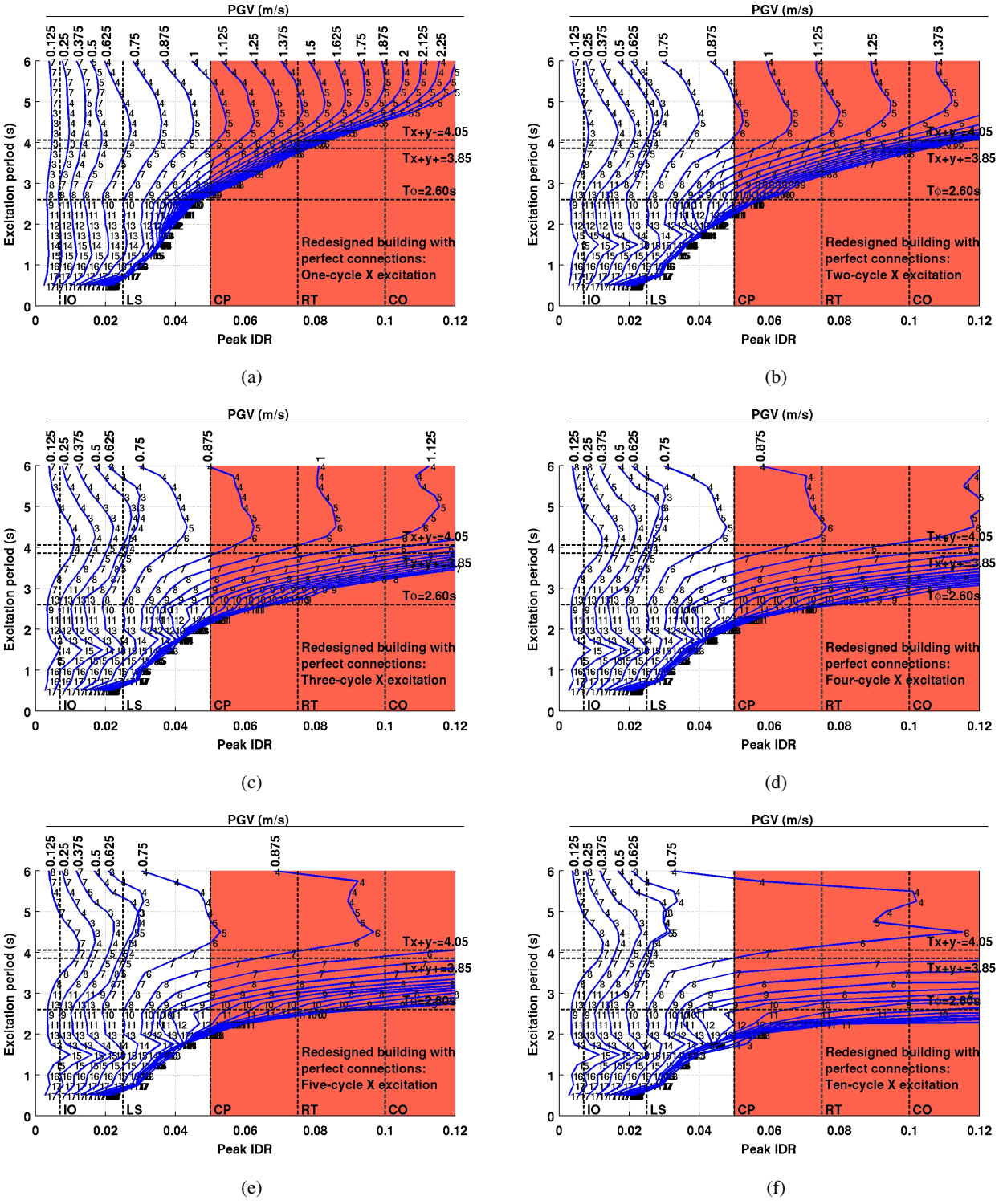

Figure D.7: Peak transient interstory drift ratio (IDR) is shown plotted against the idealized saw-tooth waveform excitation period (T) for the redesigned building (perfect connections) at various levels of peak ground velocity (PGV). Each subfigure corresponds to a different number of excitation cycles. The one-component ground motion is applied in the building X direction. The story location where the peak occurs is labeled at each of the 460 [T,PGV] combinations for which analyses were performed. The empirical immediate occupancy (IO), life-safety (LS), collapse prevention (CP), red-tagged (RT), and collapsed (CO) performance levels are marked on the IDR axis. The principal direction building fundamental periods are indicated for reference.

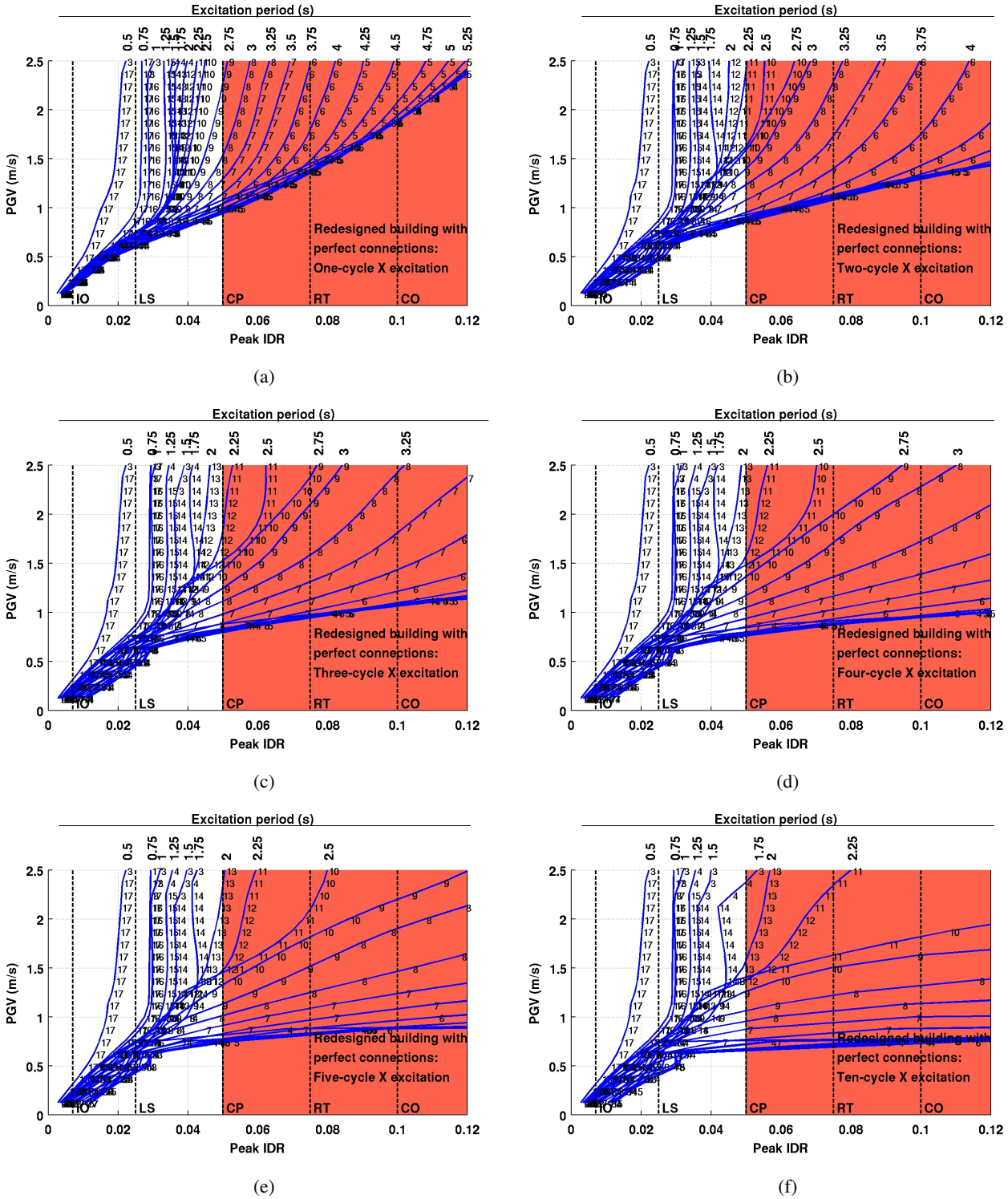

Figure D.8: Peak transient interstory drift ratio (IDR) is shown plotted against the idealized saw-tooth waveform excitation peak ground velocity (PGV) for the redesigned building (perfect connections) at various levels of wave-train periods (T). Each subfigure corresponds to a different number of excitation cycles. The one-component ground motion is applied in the building X direction. The story location where the peak occurs is labeled at each of the 460 [T,PGV] combinations for which analyses were performed. The empirical immediate occupancy (IO), life-safety (LS), collapse prevention (CP), red-tagged (RT), and collapsed (CO) performance levels are marked on the IDR axis.

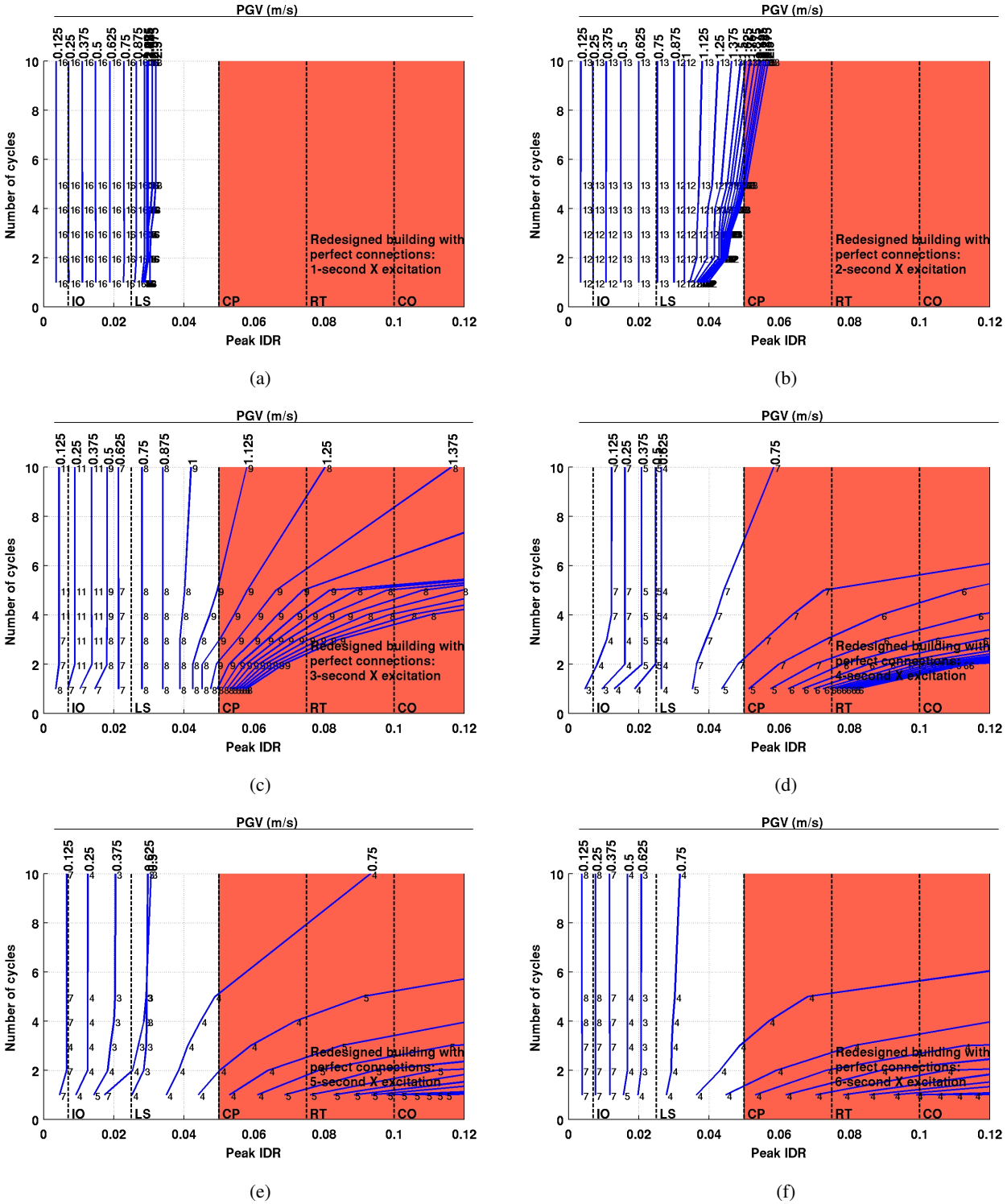

Figure D.9: Peak transient interstory drift ratio (IDR) is shown plotted against the number of cycles (N) in the idealized saw-tooth waveform excitation for the redesigned building (perfect connections) at various levels of peak ground velocity (PGV). Each subfigure corresponds to a different excitation period (1s–6s). The one-component ground motion is applied in the building X direction. The story location where the peak occurs is labeled at each of the 460 [T,PGV] combinations for which analyses were performed. The empirical immediate occupancy (IO), life-safety (LS), collapse prevention (CP), red-tagged (RT), and collapsed (CO) performance levels are marked on the IDR axis.

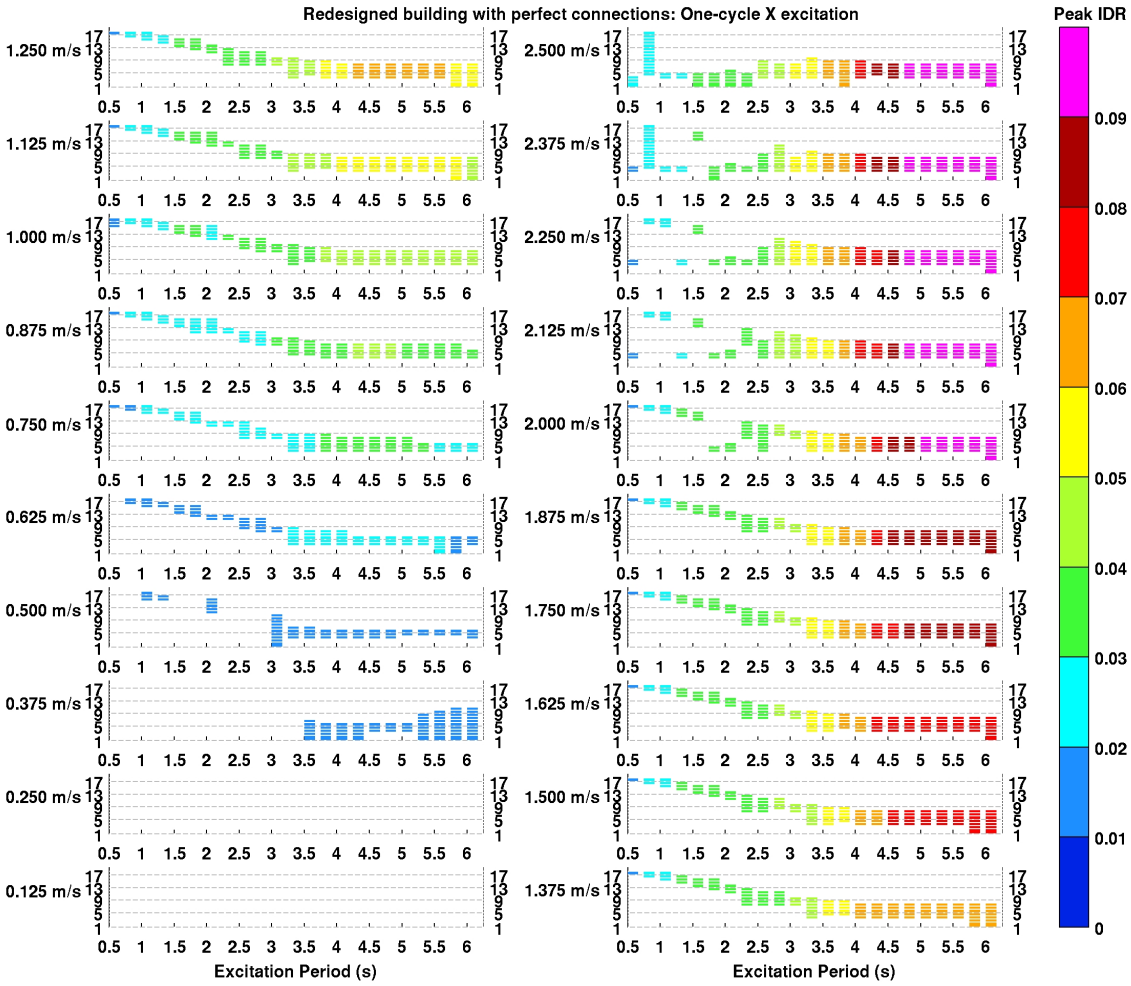

(a) Story extent of band for each (T,PGV) combination.

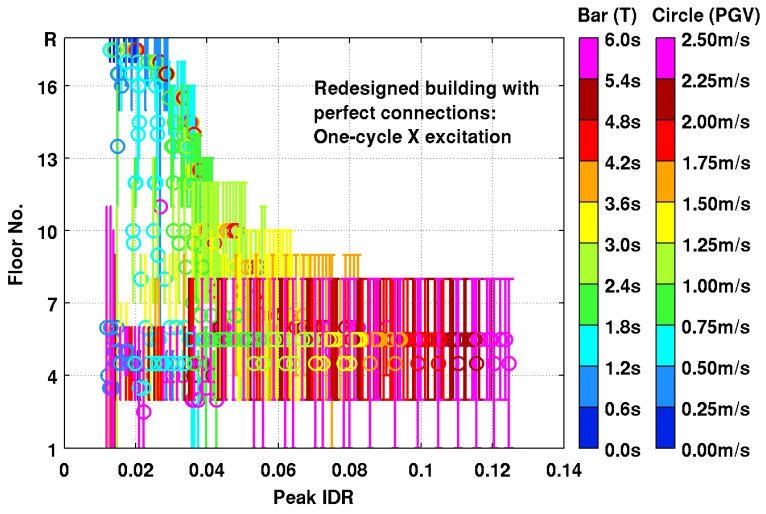

(b) Story extent of bands for all (T,PGV) combinations. Bar color identifies the excitation period and circle color identifies the peak ground velocity.

Figure D.10: Principal quasi-shear bands in the redesigned building (perfect connections) subjected to one-cycle idealized waveforms in the X direction.

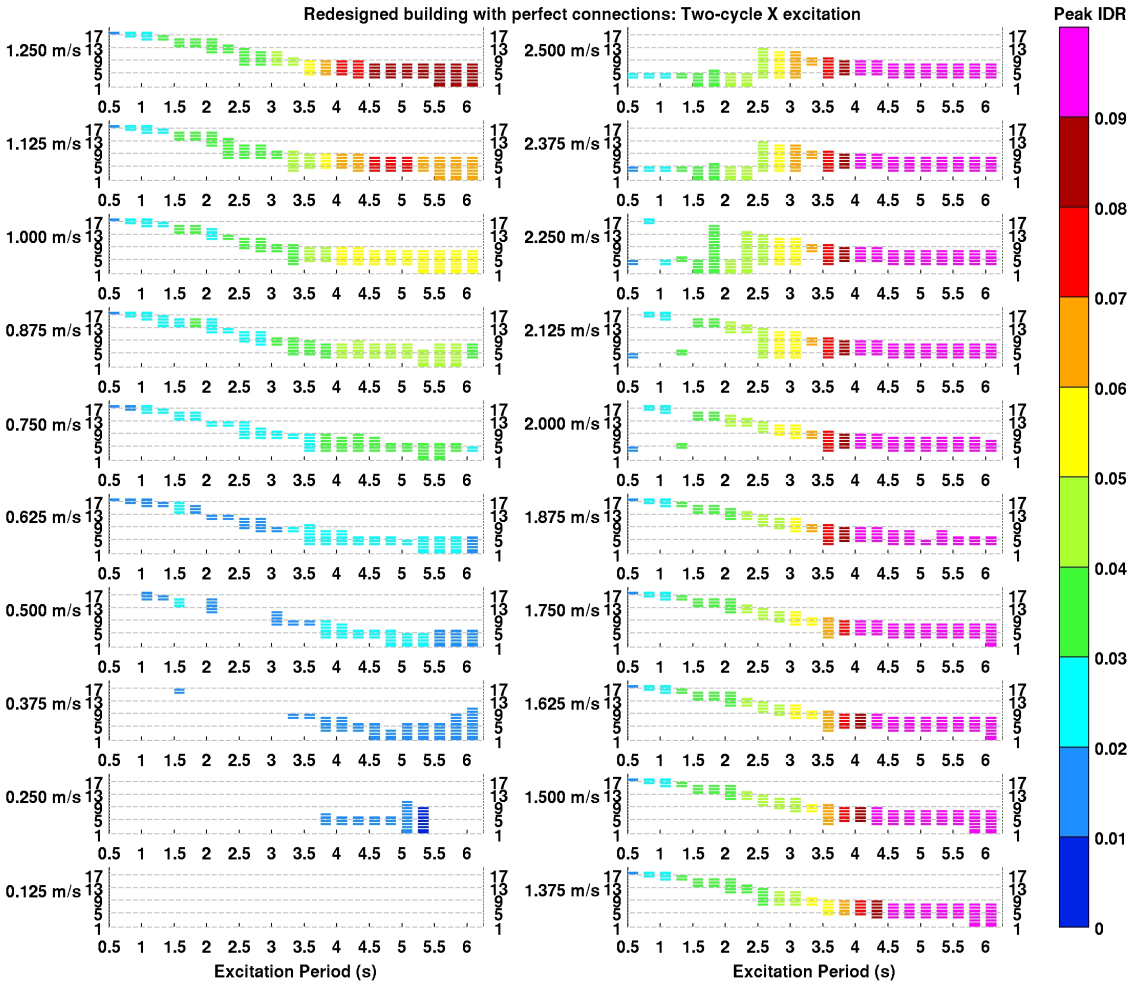

(a) Story extent of band for each (T,PGV) combination.

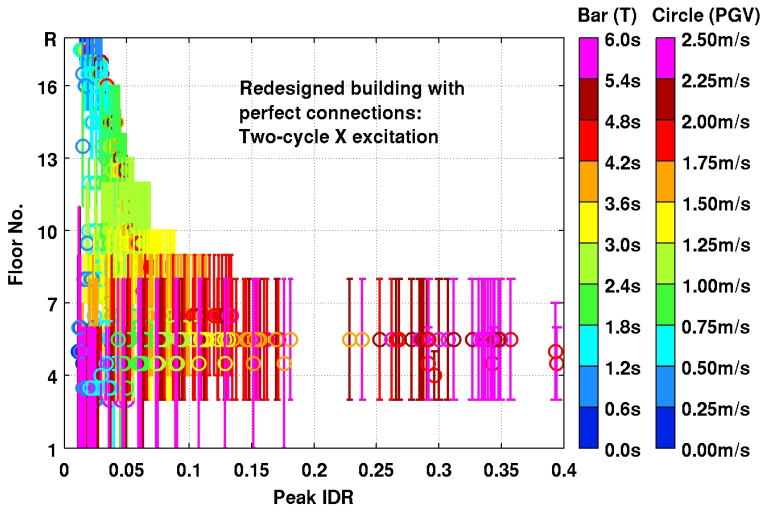

(b) Story extent of bands for all (T,PGV) combinations. Bar color identifies the excitation period and circle color identifies the peak ground velocity.

Figure D.11: Principal quasi-shear bands in the redesigned building (perfect connections) subjected to two-cycle idealized waveforms in the X direction.

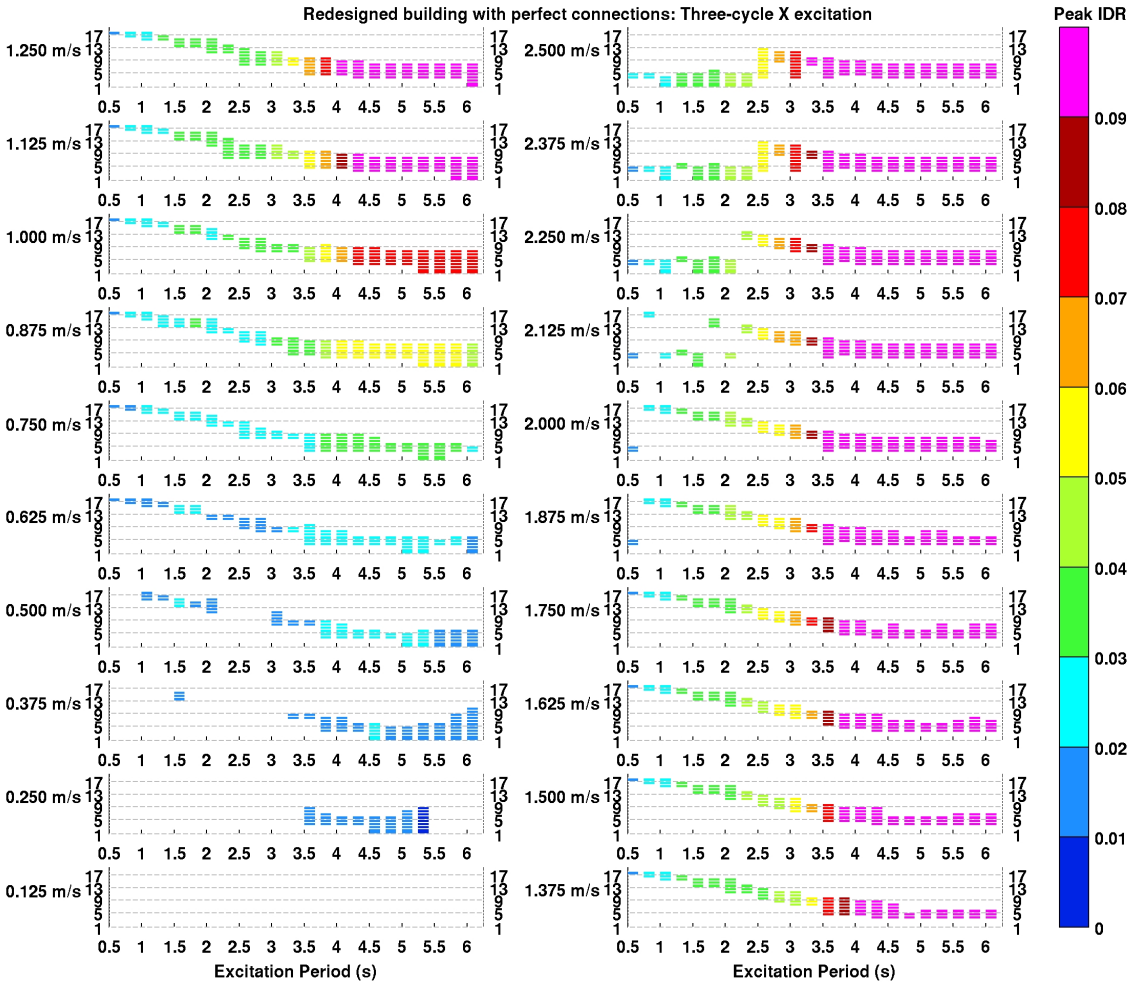

(a) Story extent of band for each (T,PGV) combination.

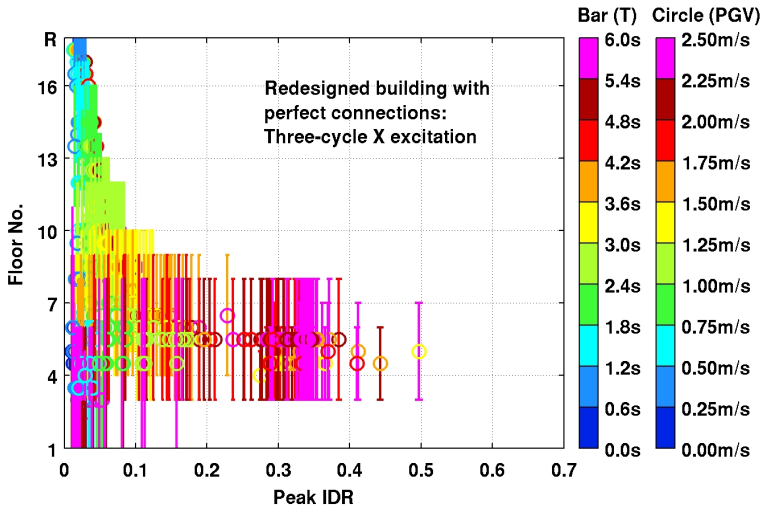

(b) Story extent of bands for all (T,PGV) combinations. Bar color identifies the excitation period and circle color identifies the peak ground velocity.

Figure D.12: Principal quasi-shear bands in the redesigned building (perfect connections) subjected to three-cycle idealized waveforms in the X direction.

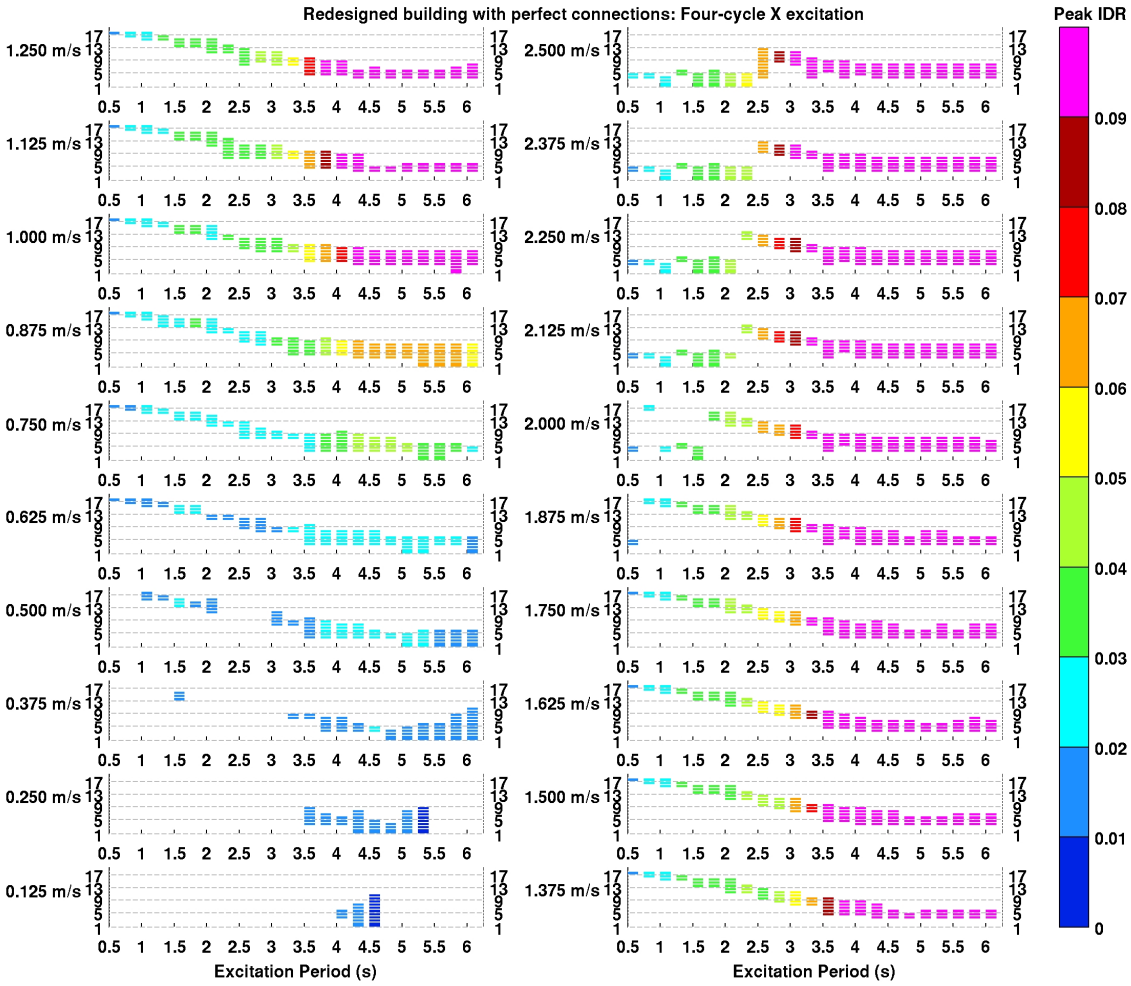

(a) Story extent of band for each (T,PGV) combination.

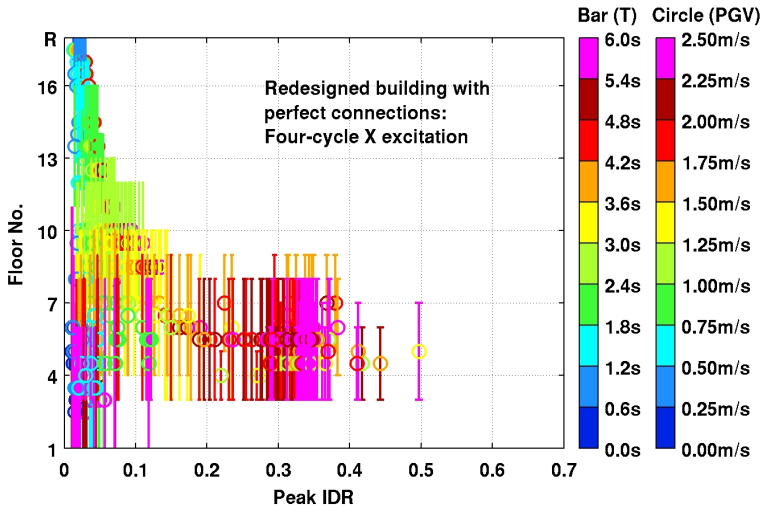

(b) Story extent of bands for all (T,PGV) combinations. Bar color identifies the excitation period and circle color identifies the peak ground velocity.

Figure D.13: Principal quasi-shear bands in the redesigned building (perfect connections) subjected to four-cycle idealized waveforms in the X direction.

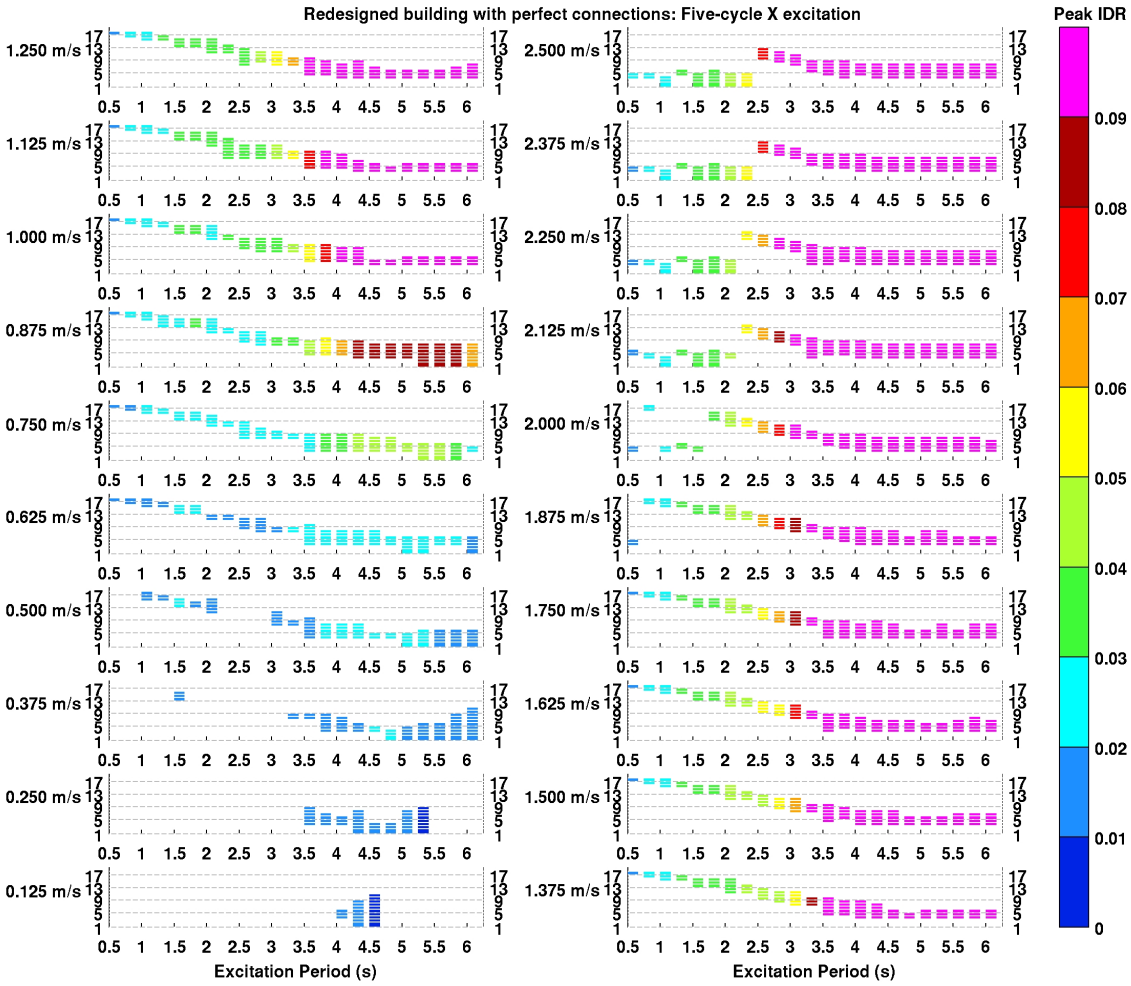

(a) Story extent of band for each (T,PGV) combination.

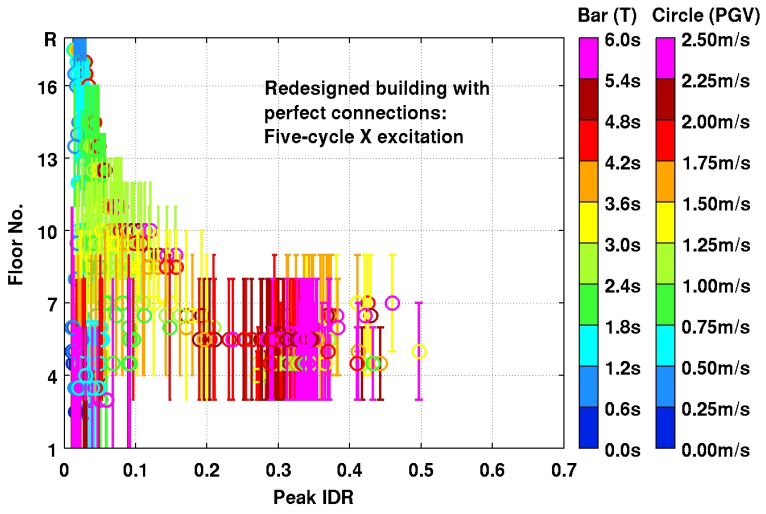

(b) Story extent of bands for all (T,PGV) combinations. Bar color identifies the excitation period and circle color identifies the peak ground velocity.

Figure D.14: Principal quasi-shear bands in the redesigned building (perfect connections) subjected to five-cycle idealized waveforms in the X direction.

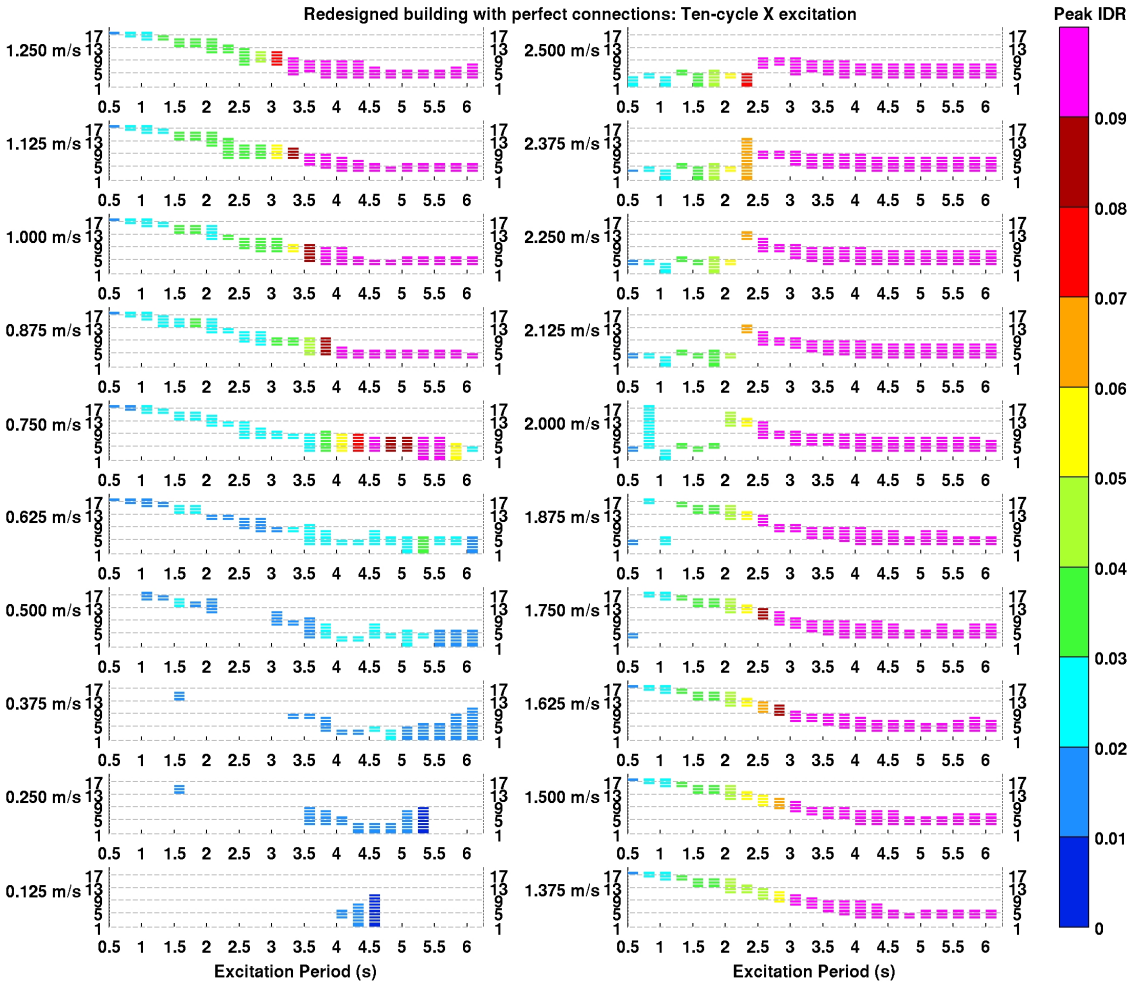

(a) Story extent of band for each (T,PGV) combination.

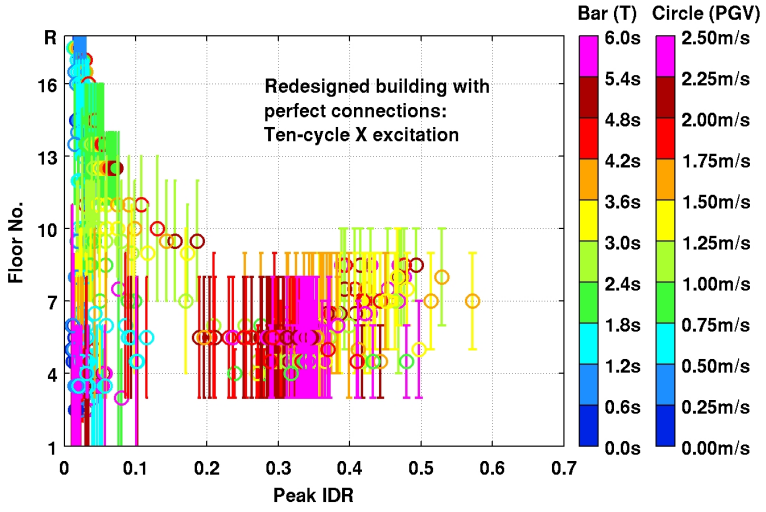

(b) Story extent of bands for all (T,PGV) combinations. Bar color identifies the excitation period and circle color identifies the peak ground velocity.

Figure D.15: Principal quasi-shear bands in the redesigned building (perfect connections) subjected to ten-cycle idealized waveforms in the X direction.

Appendix E Regime of Significance of $P - \Delta$ Effects

The existing and redesigned buildings with perfect connections are analyzed under a suite of 13 ground motion records from the September 21, 1999, magnitude 7.7 Chi-Chi earthquake in Taiwan, and the September 25, 2003, magnitude 8.3 Tokachi-Oki earthquake in Japan. Only the north component of these records is used to excite the models. Response spectra of these records are given in [22]. The ground motion records are scaled by factors ranging from 0.125 to 3.000 at 0.125 intervals, and 4.000 to 24.000 at 1.000 intervals, for a total of 585 excitation time-histories. Thus, the number of analysis cases for all 23 models amounts to 13,455. For each of these cases, nonlinear analyses are conducted with and without consideration of P-Δ effects. FRAME3D accounts for P-Δ effects by updating the structural geometry at each step, and ensuring force equilibrium in the deformed configuration. This feature is "turned off" to simulate structural response in the absence of P-Δ effects. The FRAME3D models are the same as those used in the parametric study of Chapter 3, except that panel zones are assumed rigid here. Joint element response is intimately tied into coordinate updating, especially of the beam-to-column attachment points, with the panel zone strain being determined by changes in the coordinates of the attachment points [18, 19]. So "turning off" coordinate updating to preclude P-Δ will result in joint element response differences that cannot be traced to P-Δ, and hence corrupt the results. The two models are analyzed, with and without P-Δ effects, under the same suite of scaled ground motion records as the SDOF systems, except that all three components are used to excite them. The peak transient IDR from the analysis including P-Δ is shown plotted against that from the analysis neglecting P-Δ in Figure E.1. Each point represents the response for a certain scaled ground motion record. Results are shown for both buildings. Also shown are quadratic relations that fit the data the best. It is quite clear that $P - \Delta$ effects become perceptible only beyond peak transient IDRs of 0.04 and become significant only beyond IDRs of 0.08 in both building models.

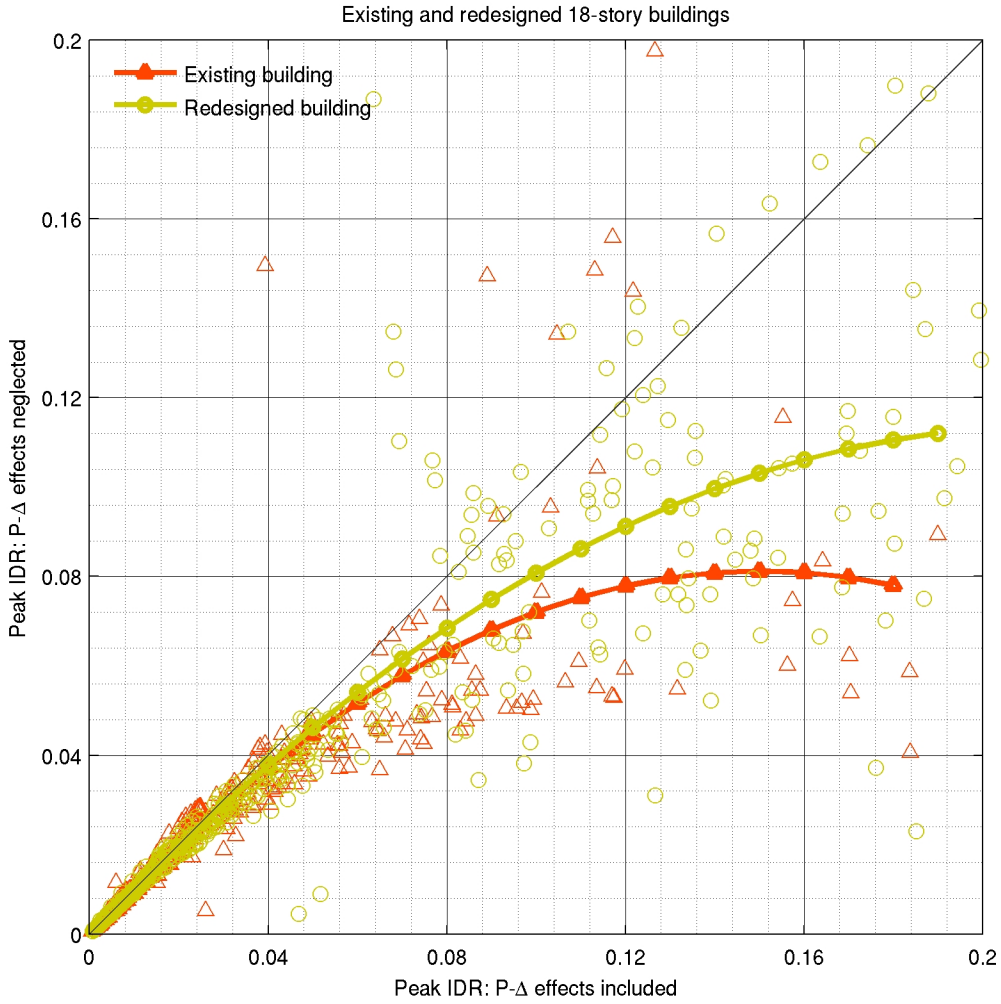

Figure E.1: Peak transient interstory drift ratio (IDR) in the two 18-story steel moment frame buildings under 13 ground motion records, scaled by factors ranging from 0.125 to 24.000, with and without P-Δ effects plotted against each other. The diagonal line is indicative of no contribution to the IDR response from P-Δ effects.

Bibliography

[1] BECK, J. L., AND HALL, J. F. Structural damage in Mexico city. *Geophysical Research Letters 13* (1986), 589–592.

[2] BERG, G. V., AND THOMAIDES, S. S. Energy consumption by structures in strong-motion earthquakes. In *Proceedings of the 2nd World Conference on Earthquake Engineering, Tokyo, Japan* (1960), pp. 681–696.

[3] CHALLA, V. R. M. Nonlinear seismic behavior of steel planar moment-resisting frames. Tech. Rep. EERL 92-01, Earthquake Engineering Research Laboratory, California Institute of Technology, Pasadena, California, 1992.

[4] CLOUGH, R. W., AND PENZIEN, J. *Dynamics of Structures (Second Edition)*. McGraw-Hill, Inc., 1993.

[5] FEMA. *Prestandard and Commentary for the Seismic Rehabilitation of Buildings*. FEMA-356. Federal Emergency Management Agency, USA, 2000.

[6] FEMA. *Recommended Specifications and Quality Assurance Guidelines for Steel Moment Frame Construction for Seismic Applications*. FEMA-353. Federal Emergency Management Agency, USA, 2000.

[7] FENVES, G. L., AND SERINO, G. Soil-structure interaction in buildings from earthquake records. *Earthquake Spectra 6*, 4 (1990), 641–655.

[8] GOEL, S. C., AND BERG, G. V. Inelastic earthquake response of tall steel frames. *Journal of the Structural Division, ASCE 94*, 8 (1968), 1834–1907.

[9] HALL, J. F. Parameter study of the response of moment-resisting steel frame buildings to near-source ground motions. Tech. Rep. EERL 95-08, Earthquake Engineering Research Laboratory, California Institute of Technology, Pasadena, California, 1995.

[10] HALL, J. F. Seismic response of steel frame buildings to near-source ground motions. *Earthquake Engineering and Structural Dynamics 27*, 12 (1998), 1445–1464.

[11] HALL, J. F., AND CHALLA, V. R. M. Beam-column modeling. *Journal of Engineering Mechanics 121*, 12 (1995), 1284–1291.

[12] HALL, J. F., HEATON, T. H., HALLING, M. W., AND WALD, D. J. Near-source ground motion and its effects on flexible buildings. *Earthquake Spectra 11*, 4 (1995), 569–605.

[13] IWATA, Y., SUGIMOTO, H., AND KUWAMURA, H. Reparability limit of steel structural buildings based on the actual data of hyogoken-nanbu earthquake. *Technical Memorandum of Public Works Research Institute 4022* (2006), 86–95.

[14] JACOBSEN, L. S. Vibrational transfer from shear buildings to ground. *Journal of Engineering Mechanics Division, ASCE 90*, 3 (1964), 21–38.

[15] JAYAKUMAR, P. Modeling and identification in structural dynamics. Tech. Rep. EERL 1987-01, Earthquake Engineering Research Laboratory, California Institute of Technology, Pasadena, California, USA, 1987.

[16] KRISHNAN, S. FRAME3D – A program for three-dimensional nonlinear time-history analysis of steel buildings: User guide. Tech. Rep. EERL 2003-03, Earthquake Engineering Research Laboratory, California Institute of Technology, Pasadena, California, USA, 2003.

[17] KRISHNAN, S. Three-dimensional nonlinear analysis of tall irregular steel buildings subject to strong ground motion. Tech. Rep. EERL 2003-01, Earthquake Engineering Research Laboratory, California Institute of Technology, Pasadena, California, USA, 2003.

[18] KRISHNAN, S., AND HALL, J. F. Modeling steel frame buildings in three dimensions – Part I: Panel zone and plastic hinge beam elements. *Journal of Engineering Mechanics 132*, 4 (2006), 345–358.

[19] KRISHNAN, S., AND HALL, J. F. Modeling steel frame buildings in three dimensions – Part II: Elastofiber beam element and examples. *Journal of Engineering Mechanics 132*, 4 (2006), 359–374.

[20] KRISHNAN, S., JI, C., KOMATITSCH, D., AND TROMP, J. Performance of 18-story steel moment frame buildings during a large San Andreas earthquake – a Southern California-wide end-to-end simulation. Tech. Rep. EERL 2005-01, http://caltecheerl.library.caltech.edu, Earthquake Engineering Research Laboratory, California Institute of Technology, Pasadena, California, USA, 2005.

[21] KRISHNAN, S., JI, C., KOMATITSCH, D., AND TROMP, J. Case studies of damage to tall steel moment frame buildings in southern California during large San Andreas earthquakes. *Bulletin of the Seismological Society of America 96*, 4 (2006), 1523–1537.

[22] KRISHNAN, S., JI, C., KOMATITSCH, D., AND TROMP, J. Performance of two 18-story steel moment frame buildings in southern California during two large simulated San Andreas earthquakes. *Earthquake Spectra 22*, 4 (2006), 1035–1061.

[23] MAHIN, S. A., AND LIN, J. Construction of inelastic response spectrum for single degree of freedom system. Tech. Rep. UCB/EERC-83-17, Earthquake Engineering Research Center, University of California, Berkeley, California, 1983.

[24] MUTO, M., AND KRISHNAN, S. Hope for the best, prepare for the worst: Response of tall steel buildings to the shakeout scenario earthquake. *Earthquake Spectra 27*, 2 (2011).

[25] RICE, J. R. The localization of plastic deformation. In *Proceedings of the 14th International Congress on Theoretical and Applied Mechanics, Volume 1* (1976), W. T. Koiter, Ed., North-Holland Publishing Co., Delft, pp. 207–220.

[26] SAC. Analytical and field investigations of buildings affected by the Northridge earthquake of January 17, 1994 – Part 1. Tech. Rep. SAC 95-04, Part 1, Structural Engineers Association of California, Applied Technology Council, and California Universities for Research in Earthquake Engineering, USA, 1995.

[27] SERINO, G. Dynamic soil-structure interaction in building response from earthquake records. Tech. Rep. UCB/SEMM-1989/01, Department of Civil Engineering, University of California, Berkeley, California, USA, 1989.

[28] STEWART, J. P., SEED, R. B., AND FENVES, G. L. Empirical evaluation of inertial soil-structure interaction effects. Tech. Rep. PEER-98/07, Pacific Earthquake Engineering Center, University of California, Berkeley, California, USA, 1998.

[29] TARANATH, B. S. *Wind and Earthquake Resistant Buildings*. Marcel Dekker, New York, NY, 2005.

[30] TRIFUNAC, M., HAO, T., AND TODOROVSKA, M. Response of a 14-story reinforced concrete structure to nine earthquakes: 61 years of observation in the Hollywood storage building. Tech. Rep. CE 01-02, Department of Civil Engineering, University of Southern California, Los Angeles, California, USA, 2001.

[31] TRIFUNAC, M. D., TODOROVSKA, M. I., AND HAO, T. Y. Full-scale experimental studies of soil-structure interaction – a review. In *Proceedings of the Second US–Japan Workshop on Soil-Structure Interaction, Tsukuba City, Japan, 52 pages (published on CD-ROM)* (2001).

[32] UANG, C.-M., AND BERTERO, V. V. Earthquake simulation tests and associated studies of a 0.3-scale model of a six-story concentrically braced structure. Tech. Rep. UCB/EERC-86-10, Earthquake Engineering Research Center, University of California, Berkeley, California, 1986.

[33] UANG, C.-M., AND BERTERO, V. V. Use of energy as a design criterion in earthquake-resistant design. Tech. Rep. UCB/EERC-88-18, Earthquake Engineering Research Center, University of California, Berkeley, California, 1988.

[34] UANG, C.-M., AND BERTERO, V. V. Evaluation of seismic energy in structures. *Earthquake Engineering and Structural Dynamics 19*, 1 (1990), 77–90.